

INCLUSIVE PARTICLE DISTRIBUTIONS
FROM THE PSI AND PSI PRIME DECAYS

Kirk A. Shinsky

A DISSERTATION
PRESENTED TO THE
FACULTY OF PRINCETON UNIVERSITY
IN CANDIDACY FOR THE DEGREE
OF DOCTOR OF PHILOSOPHY

RECOMMENDED FOR ACCEPTANCE BY THE
DEPARTMENT OF PHYSICS

June 1978

INCLUSIVE PARTICLE DISTRIBUTIONS FROM THE ψ AND ψ' DECAYS

ABSTRACT

This work presents the results of an experiment performed at the electron-positron storage ring SPEAR in the Stanford Linear Accelerator Center which studied the inclusive distribution of particles produced from the $\psi(3095)$ and $\psi'(3684)$ decays. To study the charged particle spectra, a single-arm magnetic spectrometer was employed which identified the species of each particle that triggered it over the entire momentum range as well as determining the momentum of the particle to about $1.7 \cdot p\%$, for the momentum, p , in GeV/c. Thus, the distributions for the different species of stable, charged hadrons, i.e. π^+ , K^+ , and p and \bar{p} , are presented and constitute the major portion of this work. A comparison is made between the inclusive hadron distributions from the resonance decays and from non-resonant e^+e^- annihilation. There is evidence for a purely statistical emission process for the resonance decays, while the non-resonance data appear similar to the resonance decays in the low momentum range of the distributions and diverge from them above about 1 GeV/c.

The charged multiplicity distributions associated with the hadrons in the magnetic spectrometer are presented as

well as the correlation of the averaged multiplicity with the spectrometer particle's momentum.

The SU(3) character of the resonances is assessed by observing their two and quasi-two body decays. Possible evidence for new high mass narrow resonances is seen, though at a low statistical significance.

Also, the production of free, fractionally-charged quarks is investigated, with a subsequent 90% C.L. upper limit on the decay of the psions into free quarks of about 0.06% if they are weakly interacting, or 0.1% if they have nuclear interactions similar to antiprotons.

The spectra of gamma rays produced in association with a particle in the spectrometer are presented. Evidence is seen for the decays of the ψ' to lower energy states and the subsequent radiative decay of these states to the ψ . This spectrum is compared with the inclusively measured gamma ray spectrum. There is also evidence for a low energy monochromatic photon of about 75 MeV from the decays of the ψ' in the spectrometer particle associated spectrum. The statistical significance of this state is, however, poor.

This work is dedicated to my late grandfather, Alfred Demkee,
who taught me the reality of dreams.

Knowing accurately every portion, they will not be struck so much by the accuracy of the description, as annoyed by its omissions,...What is told they depreciate as insignificant or besides the purpose; what is omitted they desiderate as vital to the question: their object to appear to know more than the writer. But a good critic should not judge a writer by what he leaves unsaid, but what he says: if he detects mis-statement in the latter, he may then feel certain that ignorance accounts for the former; but if what he says is accurate, his omissions ought to be attributed to deliberate judgement and not to ignorance.

Polybius VI.11

(trans. by E.S. Shuckburg)

ACKNOWLEDGEMENTS

To express gratitude to each of the dozens of people who made these experiments possible would be a difficult and risky task. From the army of support people to the experimentors themselves, their dedication and willingness to initiate and maintain the experimental equipment in spite of seemingly overpowering difficulties was truly remarkable. In particular, I'd like to especially thank Willie Werosta for his technical expertise in transforming concepts on paper into working pieces of equipment. His services to the success of this and past experiments of the O'Neill group at Princeton are deeply appreciated by all who were involved with them. The Experimental Facilities Department at the Stanford Linear Accelerator Center provided an impressive amount of support in installing this experiment. For instance, the equipment for the gamma ray detector was designed and installed within a six week period; an nearly impossible task without the willing support of this department. Further, the Computations Group of SLAC provided nearly inexhaustable resources for the analysis of this experiment. The operators of SPEAR also did an outstanding job of running that machine and were very patient in putting up with our sometimes impossible requests. Finally, a deep appreciation is extended to the

directorship of SLAC and the NSF for approving and funding this experiment.

As for the experimentors, appreciation is extended to the group from the University of Pavia, Italy in the persons of Gorgio Goggi, Fernanda Pastore, Michele Livan, Bruno Rossini, Fillipo Impellizeri, and Matteo Cavalli-Sforza, now at Princeton, for their fine work in constructing the large proportional chambers and the electronics of the triggering logic; to Gus Zorn, Bruce Barnett, Lew Jones and David Badtke from the University of Maryland for their expertise in constructing the shower, the Cherenkov, the time-of-flight and the range counters as well as a large portion of the analysis programs; to Lew Keller of SLAC for coordinating much of the interaction between this experiment and the management of SLAC as well as providing valuable effort in running the experiment; to Don Groom from the University of Utah whose ingenious solutions to difficult problems were crucial to the success of this project; and to Gerard O'Neill, David Aschman, Don Coyne and Hartmut Sadrozinski who provided most of the data-acquisition system as well as the spectrometer magnet and several proportional chambers, including the polymeeter. In particluar, I'd like to thank Don Coyne and Hartmut Sadrozinski for collectively acting as

my advisors and providing tremendous amounts of inspiration in the time I've been associated with them. Their warm friendship and congenial support soften the roughest of difficulties. Finally, a special thanks is due to Gerry O'Neill for providing the initial impetus for this experiment as well as a firm, guiding hand during its sometimes stormy course. His contributions are priceless.

For the construction, maintenance, and analysis of the gamma ray spectrometer and the data from it, I thank the group from the University of California at San Diego under George Masek and the group from the High Energy Physics Laboratory of Stanford University under Barrie Hughes and Robert Hofstaeder for their enthusiastic cooperation.

Finally, I'd like to thank Nancy Moore for tireless support in typing and proofing parts of this work as well as for countless other reasons.

TABLE OF CONTENTS

ABSTRACT.....	ii
PREFACE.....	xvii
INTRODUCTION.....	1
A. The Recent History of the New Particles	
1. The Discoveries.....	2
2. Properties of the New Resonances.....	7
B. The Apparatus.....	9
REFERENCES.....	14
CHAPTER I: THE APPARATUS.....	16
A. The Storage Ring.....	16
B. The Polymeter and Central Detector.....	17
C. Gamma Ray Spectrometer.....	18
D. Magnetic Spectrometer	21
1. Track Chambers	24
2. Cherenkov Counter.....	24
3. Magnet Proportional Chambers	26
4. Time-of-flight System	29
5. Shower Counter.....	30
6. Range Counter.....	31
7. Trigger System	33
8. Data Acquisition System	36
REFERENCES	41
CHAPTER II: DATA ACQUISITION AND ANALYSIS	42
A. Data Accumulation	42
B. Event Selection and Filtering	42
C. Event Reconstruction in the Spectrometer	
1. Incident Track Finding	44
2. Momentum Analysis	45
3. Further Event Selection	49
REFERENCES	51
CHAPTER III: PARTICLE IDENTIFICATION	52
A. Selection of Clean Particle Samples	52
1. Introduction	52
2. Devices Used in Particle	
Identification	54
3. Selection of a Representative	
Electron Sample	55
4. Selection of a Representative Muon	
Sample	61
5. Muons' Momentum Spectra	64
6. Selection of a Representative	
Sample of Hadrons	66

B. Tests of the Particle Identifiers	69
1. Generation of the Complete Probability Distributions	69
2. Response of the Shower Counter	72
3. Response of the Conjugate Side NaI Array	83
4. Response of the Cherenkov Counter...	88
5. Response of the Range Counter.....	91
6. Response of the Time-of-Flight System	94
C. Separation of Electrons, Muons, and Hadrons	100
1. Identification of Muons	100
2. Separation of Hadrons and Electrons	103
3. Separation of Pions, Kaons, and Protons	105
Separation with the TOF System	106
Separation with the Cherenkov Counter	109
REFERENCES.....	115
CHAPTER IV: CORRECTIONS APPLIED TO THE DATA....	116
A. General Considerations	116
B. The Monte Carlo Simulation of the Data..	117
C. Corrections for the Angular Acceptance..	119
D. Corrections for Nuclear Interaction Effects	121
E. Corrections for Reconstruction Failure Due to Decay	121
F. Corrections for Particle Misidentifi- cation.....	126
G. Corrections for Background Events in the Data	129
H. Corrections to the Momentum for Energy Losses	137
I. Normalization of the Data Via the Luminosity	137
REFERENCES.....	142
CHAPTER V: RESULTS AND DISCUSSION.....	143
A. Introduction.....	143
B. Models for Hadron Production from e^+e^- Collisions.....	143
C. Inclusive Momentum Spectra for Hadrons..	148
D. Invariant Cross Sections.....	154

E.	Particle Fractions.....	167
F.	Multiplicity Distributions.....	174
G.	Two-Body Decays.....	190
H.	A Search for Quarks.....	199
I.	Gamma Ray Distributions.....	207
	1. Introduction.....	207
	2. Inclusive Photon Spectra.....	208
	3. Photon Spectra for Spectrometer Triggers.....	215
	4. Discussion.....	223
J.	Conclusions.....	226
	REFERENCES.....	229
APPENDIX A: PROPERTIES OF CHARMONIUM.....		231
	REFERENCES.....	235
APPENDIX B: DIMENSIONS OF THE APPARATUS.....		236
APPENDIX C: NUCLEAR ABSORPTION CORRECTIONS.....		238
	REFERENCES.....	243

LIST OF ILLUSTRATIONS

Figure		Page
INTRODUCTION		
0-1	OZI Decays of the ϕ and ψ	4
0-2	Charmonium Level Diagram	5
0-3a	Spectrometer System, Top View.....	10
0-3b	Spectrometer System, Side View.....	11
0-4	Gamma Ray Spectrometer	13
CHAPTER I		
I-1	Acceptance for the Spectrometer.....	22
I-2	Polar Angle Ranges of the Spectro- meter	23
I-3	Expected Cherenkov Amplitude.....	25
I-4	Block Diagram of the Data Acquisition System.....	39
CHAPTER II		
II-1	χ^2 Distribution of Particle Trajectories.....	47
II-2	Vertex Distribution of Events.....	48
CHAPTER III		
III-1	Direct Lepton Production from the Resonances.....	56
III-2	Electron's Momentum Spectrum.....	60
III-3	Hadron Filter Penetration Probability for Muons.....	62
III-4	Muon's Momentum Spectra.....	65
III-5	Shower Counter Amplitude for Muons....	71
III-6	Shower Counter Distribution for Electrons and Hadrons.....	73
III-7	Probability Distribution for the Shower Counter Amplitude	75
III-8	Probability Distribution for the Minimum Shower Counter Amplitude....	77
III-9	Correlation between the Shower Amplitude and Momentum.....	78

Figure	Page
III-10	Correlation between M and Momentum.....79
III-11	Probability Distribution of M.....81
III-12	Correlation between the RMS Shower Deviation and the Shower Amplitude.....82
III-13	Correlation between S and Momentum.....84
III-14	Probability Distribution for S.....85
III-15	Probability Distribution for Deposited Energy in the Side NaI Array.....86
III-16	Cherenkov Counter Amplitude for Hadrons and Electrons.....87
III-17	Cherenkov Counter Amplitude for Muons....90
III-18	Penetration Probability of Pions into the Hadron Filter.....93
III-19	Time of Flight Distribution for Muons....96
III-20	Time of Flight Distribution for Pions....97
III-21	The Velocity, β , of Hadrons from the TOF System.....99
III-22	Mass ² Distribution from the TOF System..101
III-23	Cherenkov Counter Amplitude for Hadrons.110
III-24	Momentum Distribution of Hadrons.....112
CHAPTER IV	
IV-1	Decay Probability of Pions and Kaons....122
IV-2	Correction Factors for Pion and Kaon Decay.....125
IV-3	Correction Factors for Pions.....132
IV-4	Correction Factors for Kaons.....133
IV-5	Correction Factors for Antiprotons.....134
IV-6	Correction Factors for Protons.....135
IV-7	Correction for Ionizational Energy Loss.136
CHAPTER V	
V-1	Inclusive Momentum Spectra for Ψ Decays.....149
V-2	Inclusive Momentum Spectra for Ψ' Decays.....151
V-3	Invariant Cross Sections for $\Psi \rightarrow$ Hadrons vs Momentum.....155
V-4	Invariant Cross Sections for $\Psi' \rightarrow$ Hadrons vs Momentum.....156

Figure	Page
V-5	Comparison of the Invariant Cross Sections for the ψ Decays and e^+e^- Annihilation at $\sqrt{s}=4.8$ GeV.....158
V-6	Invariant Cross Section for $\psi \rightarrow$ Hadron vs Energy.....161
V-7	Invariant Cross Section for $\psi' \rightarrow$ Hadron vs Energy.....163
V-8	A Comparison between the Invariant Cross Section for this Experiment and the DASP Experiment.....166
V-9	The Hadron Fractions for ψ and ψ' Decays..168
V-10	The Particle Ratios for ψ and ψ' Decays..170
V-11	A Comparison between the Hadronic Fractions for this Experiment and the DASP Experiment.....171
V-12	The Charge Multiplicity Distribution for ψ and ψ' Decays.....179
V-13a	The Observed Momentum Distribution Associated with Different Charge Multiplicities for ψ Decay.....181
V-13b	The Observed Momentum Distribution Associated with Different Charge Multiplicities for ψ' Decay.....182
V-14	The Momentum Distribution for the Corrected Multiplicities.....183
V-15	The Invariant Distributions for Corrected Multiplicities.....184
V-16	The Averaged Charged Multiplicity as a Function of the Spectrometer Hadron's Momentum.....186
V-17	The Missing Mass from the Spectrometer Hadrons.....192
V-18	The Observed Momentum Distribution for $n_{ch}=2$ Events from the ψ Decay.....197
V-19	The Observed Momentum Distribution for $n_{ch}=2$ Events from the ψ' Decay.....198
V-20	Velocity vs Observed Momentum for Fractional Charge Free Quark in the Spectrometer.....201
V-21	The inclusive gamma ray spectra for the ψ and ψ' decays.....211

Figure		Page
V-22	Mass from two neutral clusters in the NaI arrays.....	217
V-23	Photon spectra associated with spectrometer triggers from the ψ and ψ' decays.	218
V-24	Momentum distribution of hadrons associated with photons from the ψ' ...	221
V-25	Charged multiplicity distributions of hadrons associated with photons from the ψ' decays.....	222

APPENDIX C

C-1	Nuclear absorption corrections for pions.....	240
C-2	Nuclear absorption corrections for kaons.....	241
C-3	Nuclear absorption corrections for protons and antiprotons.....	242

LIST OF TABLES

Table		Page
III-1	Misidentification Probabilities of Hadrons and Leptons.....	107
III-2	Misidentification probabilities of pions and kaons.....	113
IV-1	Misidentification probability for pions and kaons within 2σ of the expected flight time.....	128
V-1	Momentum spectra for hadrons from the ψ decays.....	150
V-2	Momentum spectra for hadrons from the ψ' decays.....	152
V-3	Parameterization of the invariant cross sections as a function of momentum.	157
V-4	Invariant cross sections for the ψ hadrons.....	162
V-5	Invariant cross sections for the ψ' hadrons.....	164
V-6	Parameterization of the invariant cross sections as a function of energy for ψ and ψ' decays.....	165
V-7	Fractions of the hadronic species as a function of momentum.....	169
V-8	Parameterization of the invariant spectra of hadrons for different charge multiplicities.....	185

Table	Page
V-9	The fraction of the hadronic spectra above 0.25 GeV/c for different multiplicities.....188
V-10	The two-body decays of the ψ and ψ'193
V-11	The properties of the enhancements observed in the missing mass distributions.....194
V-12	Upper limits for free, fractionally- charged quarks from the ψ and ψ'206
V-13	Results of a fit to the inclusive gamma ray spectrum from the ψ'214
A-1	Properties of the $\psi(3095)$232
A-2	Properties of the $\psi'(3684)$233
A-3	Properties of $\chi(3410)$, $\chi(3510)$, and $\chi(3550)$234
B-1	Dimensions of the parts of the apparatus.....237

PREFACE

For the study of unstable particles, in particular, those that have properties similar to those of the photon ($J^{PC} = 1^{--}$), i.e. the ρ , the ϕ , the ω , and now the family of ψ mesons, it is highly desirable to produce these particles in an environment free from other distracting processes. Since these resonances share the same spin, parity and charge conjugation quantum numbers with the photon and therefore can couple directly to it, one of the natural places to study the properties of these particles is in electron-positron annihilation into a virtual photon. If this virtual photon has the same mass as these particles, the photon can materialize into them.

The primary focus of this work will be on the measurement of the momentum spectra of the various long-lived particles emitted from the decays of the ψ and ψ' hadrons, produced at the electron-positron storage ring, SPEAR, at the Stanford Linear Accelerator Center.

As the principal component of the decayed system consists of charged hadrons, the primary task will be to measure the inclusively produced spectra of these particles, via a single-arm magnetic spectrometer. Additionally, the spectrum of gamma rays produced in conjunction with the

charged hadrons will be analyzed and compared with the results of an experiment that measured the inclusively produced gamma ray spectrum. Some details of this other experiment will be presented.

In the Introduction, a short history of the discovery and the understanding of the ψ mesons is presented, along with a short description of the apparatus used in measuring the inclusive spectra. The details of the various pieces of equipment used in this experiment are presented in Chapter I, along with a description of the data acquisition system. Chapter II describes the way the data was accumulated and how events were selected and reconstructed. Chapter III contains the techniques of particle separation in the various devices. This includes a description of the response characteristics of these devices to the different charged particle species. Chapter IV contains the list of correction factors that must be applied to the observed data in order to extract the actual production rates. Finally, Chapter V contains the discussion of the results. Within this chapter, the inclusive spectra are displayed, the charged particle fractions are produced, the multiplicity of charged particles produced with the spectrometer particle is shown, the two-body and quasi two-body decays of the

resonances are analyzed and the spectrum of gamma rays produced along with the spectrometer particle is exhibited. -

INTRODUCTION

This work will present the results of an experiment performed at the electron-positron storage ring, SPEAR, at the Stanford Linear Accelerator Center (SLAC) from September, 1975 until January, 1976. Groups from the University of Maryland, the Istituto de Fisica Nucleare in Pavia, Italy, SLAC, and Princeton University participated in setting up and acquiring data with a magnetic spectrometer designed for observing the charged particle spectra from electron-positron collisions. At the same time, a group from the University of California at San Diego also set up an experiment around the same collision region to observe particles from photon-photon collisions. With the discovery of the J/ψ (3095) and ψ' (3684) and the states reached via radiative transitions from them, a joint effort was undertaken to measure the gamma ray spectra from the ψ and ψ' decays in addition to the originally proposed experiments. The chief goal of this special experiment was to confirm the existence of the associated states by measuring the monochromatic gamma rays emitted in the ψ or ψ' decays to these states. Using many of the sodium iodide crystals of the San Diego group, a gamma ray spectrometer with relatively high energy resolution, was

constructed.

A. The Recent History of the New Particles

1. The Discoveries.

The first member of the remarkable psion family to be uncovered was the J/ψ itself, simultaneously observed by the SLAC-LBL group, under the direction of B. Richter, in electron-positron collisions at SPEAR, and a MIT-BNL collaboration led by S.C.C Ting at the Brookhaven National Laboratory, in proton-beryllium collisions¹. Soon thereafter, many other important discoveries regarding these resonances were made at SPEAR and later at DORIS at the Deutsches Elektronen Synchotron in Hamburg².

Immediately, the narrow widths of these resonances, on the order of 100 keV and contrary to what would be expected for states formed by the strong interactions, suggested a plausible and now, seemingly the most likely explanation: the excitation of a new quantum number called "charm", that was introduced in the Glashow-Iliopoulos-Maiani scheme³ for fixing problems in the theory of the weak interactions. In this context, the ψ and ψ^0 are produced as a result of the excitation of the partially-conserved, charm quantity. The narrow width, and hence the long lifetime, results from the violation of charm conservation in the strong

interaction decays of these states.

In the quark model, one views the mesons as a bound state of two quarks. The psions are then composed of a charmed and an anti-charmed quark. Therefore, they have no net charm and can be produced directly from the virtual photon in electron-positron annihilation. However, one would expect the decay products of the psions to contain overtly charmed particles, due to the conservation law. It turns out that the lowest mass charmed meson, the D, has a mass greater than one-half the ψ or ψ' mass, therefore these psions can only decay into ordinary particles by violating the conservation principle.

This conservation law is expressed in the empirical Okubo-Zweig-Iizuka (OZI) rule⁴, which states that properties of the hadronic currents in the quarks must be preserved in the decay of particles containing these quarks. For psions, the charmed current must appear in the decay products, if this rule is obeyed. Due to mass conservation, the ψ and ψ' cannot decay into charmed meson, although the ϕ , which is thought to be composed of a strange quark-antiquark pair, does decay, preferentially, into kaons. The reason the ϕ is so narrow is due to the limited phase space available for this decay scheme.

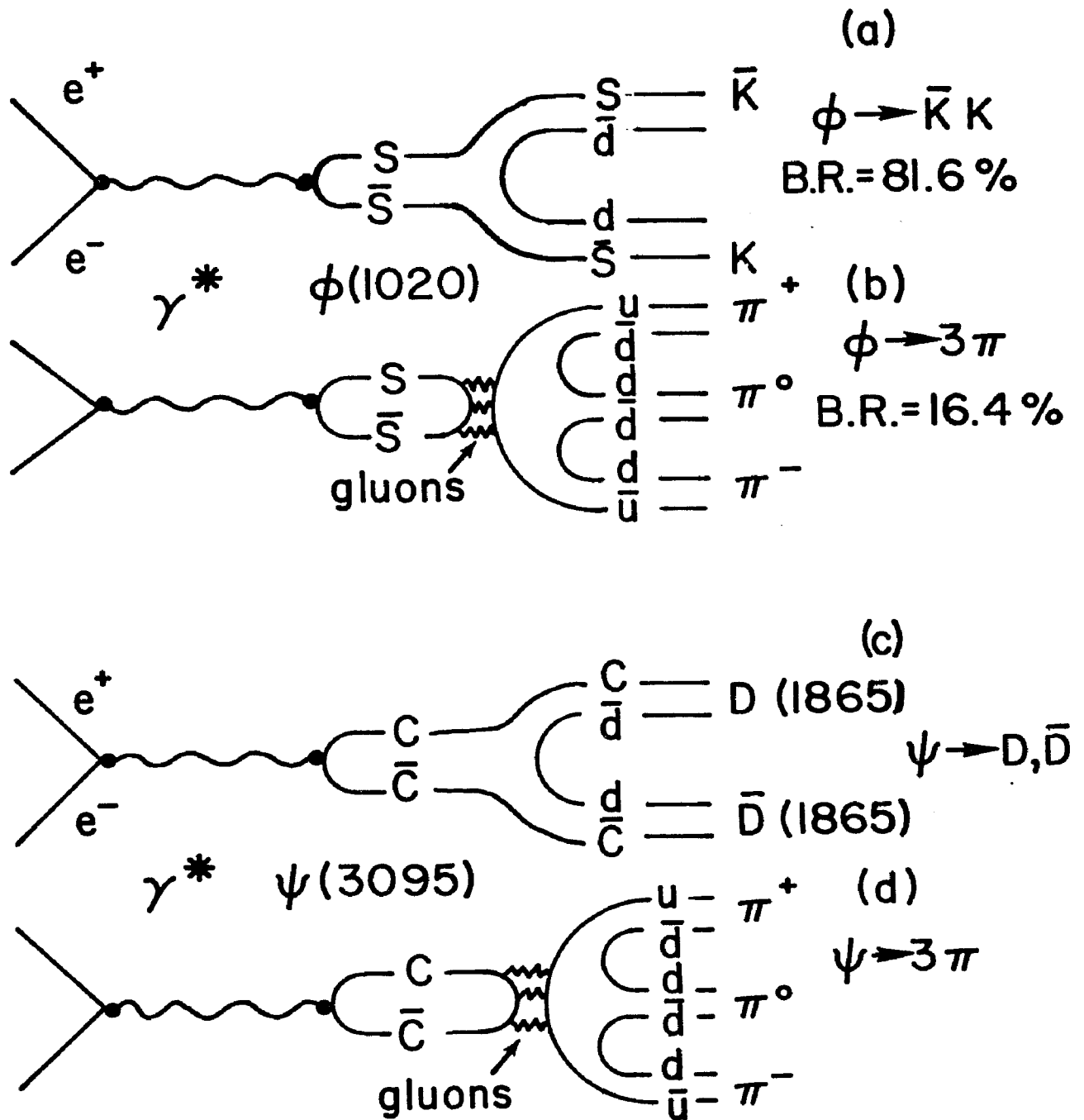


Fig. 0-1 The quark line diagrams illustrating the OZI allowed (a) and (c) and forbidden (b) and (d) decays of the ϕ and ψ , respectively. In the QCD approach, the forbidden decays proceed via the annihilation into colored, vector gluons. The known branching ratios (B.R.) of the ϕ indicate the validity of the OZI Rule, while the ψ is kinematically forbidden to follow this rule.

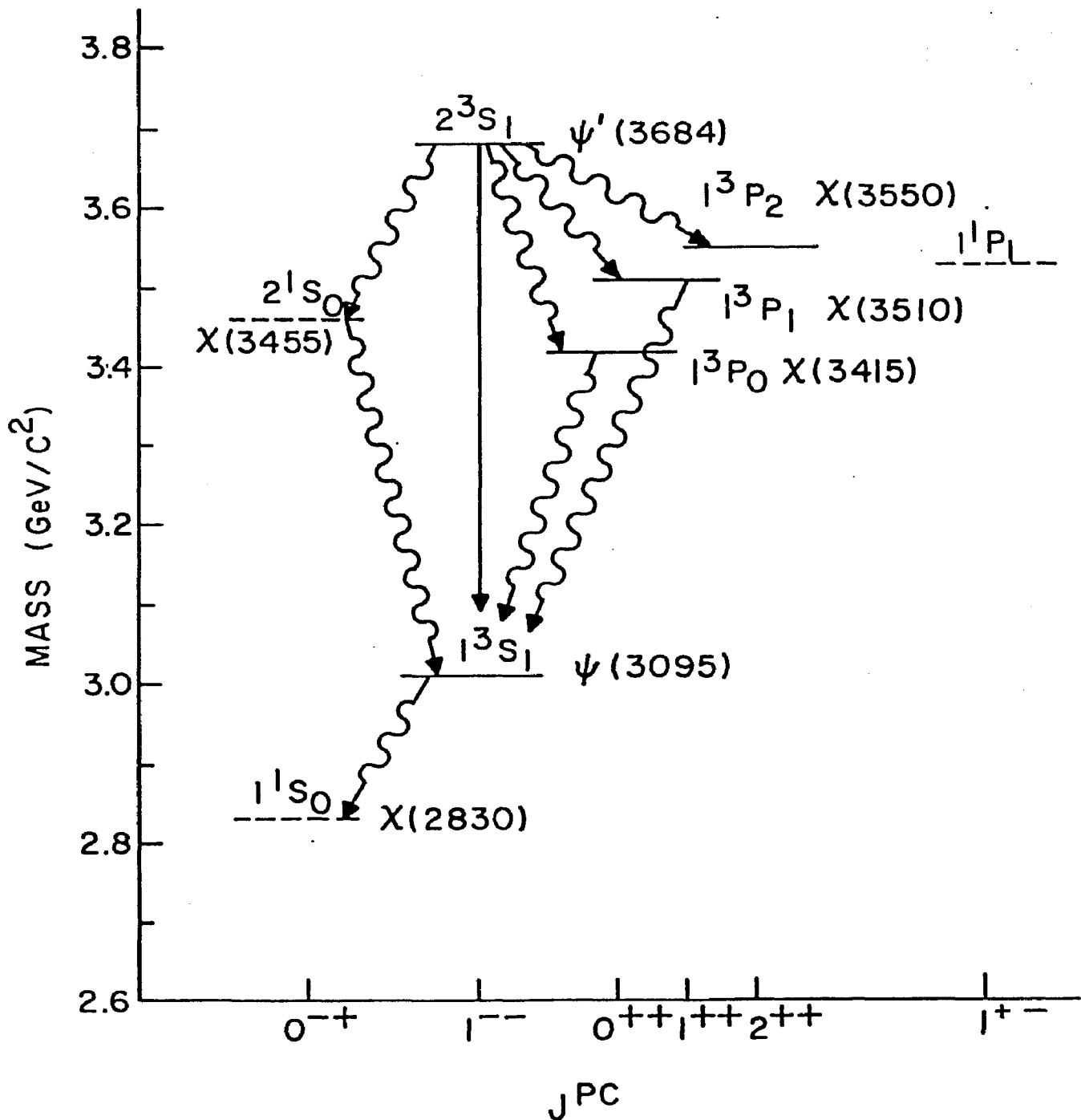


Fig. 0-2 The energy levels of the lowest mass charmonium states. The observed radiative transitions are indicated by \rightsquigarrow , while the hadronic transition is given by \longrightarrow . The dashed levels indicate states which have an uncertain assignment.

Fig. 0-1 shows the OZI allowed and forbidden decays of the ψ and the ϕ . If the ψ or ψ' could decay via the allowed channels, their lifetimes would have been considerably shorter, as is the case with ψ^{533} , which decays into charmed mesons.

One views the bound state of the charmed and anti-charmed quarks as an analog of the positronium system. The ψ is then thought to contain the quarks in a 1^3S_1 orbital wave function, with the ψ' in the 2^3S_1 state. With some assumptions about the potential confining the quarks, the energies of the other orbital wave functions can be predicted⁶. In particular, there is a group of states which lie below the ψ and ψ' in energy. These are the singlet 1^1S_0 and 2^1S_0 states ($J^{PC} = 0^{-+}$) and the triplet P states ($J^{PC} = 0, 1, 2^{++}$). Since these states have an even charge conjugation property, they can be reached by the radiative decays of the ψ and ψ' , which have an odd charge conjugation. The expected and observed energy levels of this family of states are shown in Fig. 0-2. These intermediate states have been studied at both SPEAR and DORIS⁷.

2. Properties of the New Resonances

Since the ψ and ψ' are produced directly in electron-positron annihilations, they are assumed to have the same quantum numbers as the photon, specifically, odd charge conjugation, a spin of 1, and odd parity. The SLAC-LBL group verified this hypothesis by observing the interference between the ψ and the photon in the muon and electron production channels⁸.

The G-parity was determined by looking at the dominate decay modes, in particular, the multipion modes. The SLAC-LBL group noticed that at the ψ , the partial production cross section for even numbers of pions was very similar to the off-resonance cross section, while the production of an odd number of pions was greatly enhanced⁹. This, along with other evidence, indicates that the ψ and ψ' have odd G-parity and are isoscalar states.

3. Properties of the Inclusive Particle Spectrum

Since there is an enormous number of decay schemes for the charmonium states to follow (see Appendix A), the inclusive momentum spectra of particles from these resonances contains the features of these final states. It is known that the inclusive production process for non-resonant e^+e^- annihilation into hadrons shows evidence

for "scaling" behaviour, presumably, due to the quark substructure of the hadron¹⁰. In this system, one measures the coupling of the virtual photon to the quarks. In the decay of the resonances, the features of the quark substructure may not be so evident. The decays can follow along the lines of a statistical or thermodynamical model, such as those proposed by Fermi¹¹ or Hagedorn¹², where the resonance is viewed as decaying into particles or fireballs at a temperature, T_f . If one then looks at the particle production rate in equal volumes of phase space, i.e. the Lorentz-invariant cross section, the expected behaviour is

$$E \frac{d^3\sigma}{dp^3} = C(s) \exp(-E/T_f),$$

where E and p are the energy and 3-momentum of a final particle, and $C(s)$ is a normalization factor, possibly depending on the total energy², s .

By comparing the spectra obtained from the resonances with that produced by the non-resonance annihilation, it may be possible to determine the quark-parton's contribution to the non-resonance decay mechanism¹³.

It may also be of some interest to compare the spectra from the resonances with similar inclusive spectra obtained in hadron-hadron collisions¹⁴. Here, the fireball model of

Hagedorn appears to be effective in describing the low transverse momentum spectra, over a wide range of total energy values¹⁵.

B. The Apparatus

To achieve the goals of this experiment, the equipment was designed with the following criteria in mind: the magnetic spectrometer should determine the momentum of the incoming particles with good resolution, and determine their species with a high probability. For the gamma ray spectrometer, there should be very good energy resolution over a fairly large solid angle with a method of clearly distinguishing gamma rays from charged particles, with the possibility of identifying particles which primarily decay into photons, e.g. π^0 and η .

The devices pictured in Fig. 0-3 were used to measure the charged particle spectra, with the detectors near the beam pipe used for gamma ray measurements. The charged particle spectrometer consisted of two major pieces: a single-arm, magnetic spectrometer with the ability of identifying charged particles that entered the approximately 0.095 ster. of solid angle located at 90° with respect to the beams' direction, and a crude particle identifier on the opposite side of the pipe. The single-arm spectrometer

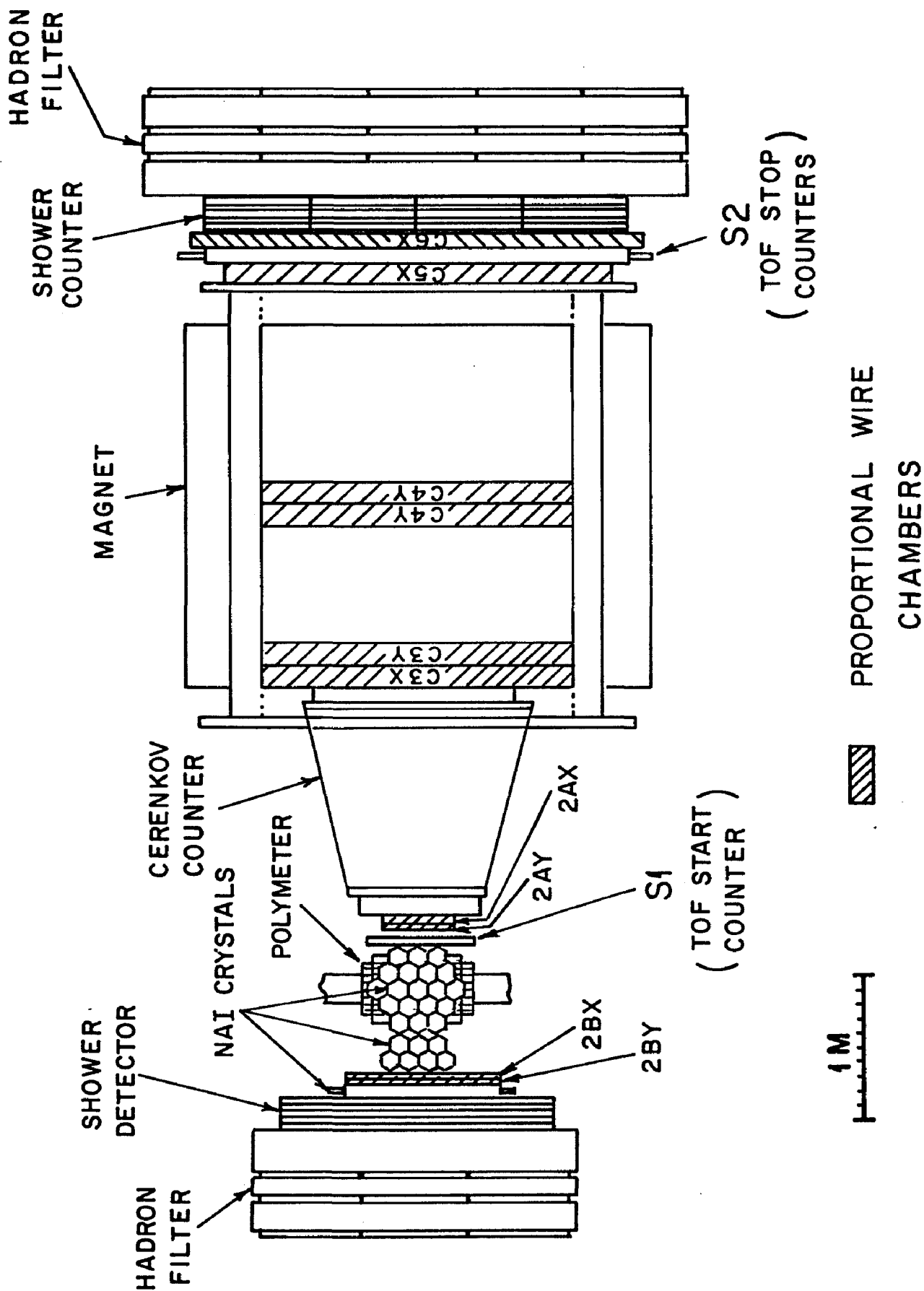


Fig. 0-3 a) The top view of the spectrometer used in this experiment. The intersection region is located at the center of the polymer.

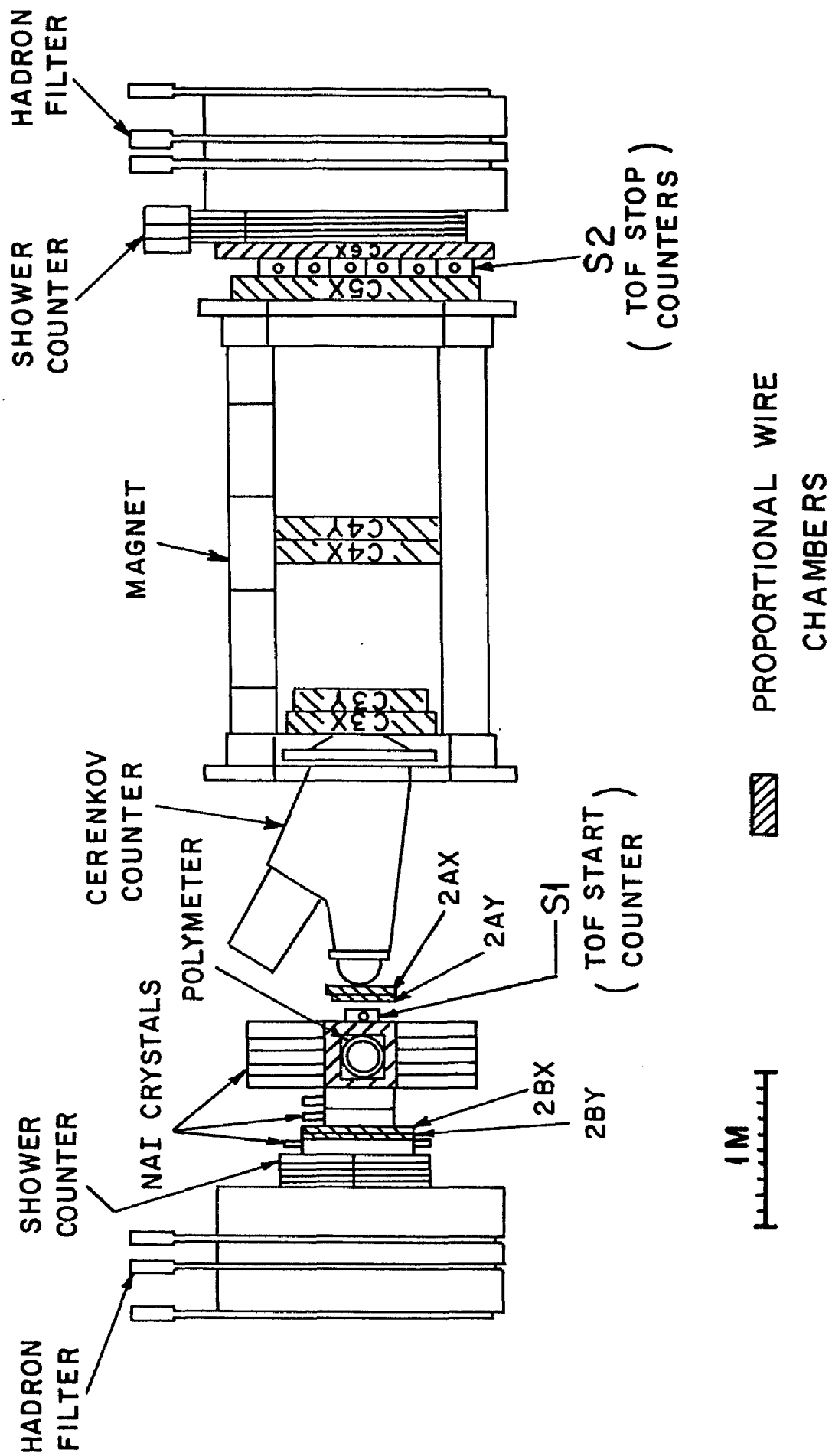


Fig. 0-3 b) The side view of the spectrometer system.

contained proportional-wire tracking chambers, a bending magnet with proportional chambers both in the middle and behind it for momentum measurement, a time-of-flight system for separating low momentum hadrons, a propane-filled threshold Cherenkov counter for hadron identification, a shower counter for electron identification, and a range counter for muon identification. A shower counter and range counter, similar to that on the spectrometer side, along with several planes of proportional chambers for tracking particles, faced the spectrometer arm. This so-called conjugate side system helped in the identification of muons and electrons, since they are generally pair produced and emerge from the reaction back-to-back.

The details of the gamma ray spectrometer are shown in Fig. 0-4. This device consisted of sodium iodide crystals for determining the energy of gamma rays via shower formation, a cylindrical array of proportional tube counters, and an array of proportional wire chambers surrounding the beam pipe, which served to measure the production angles of charged particles. They were also used to determine whether the deposited energy observed in the NaI crystals came from a charged or neutral particle.

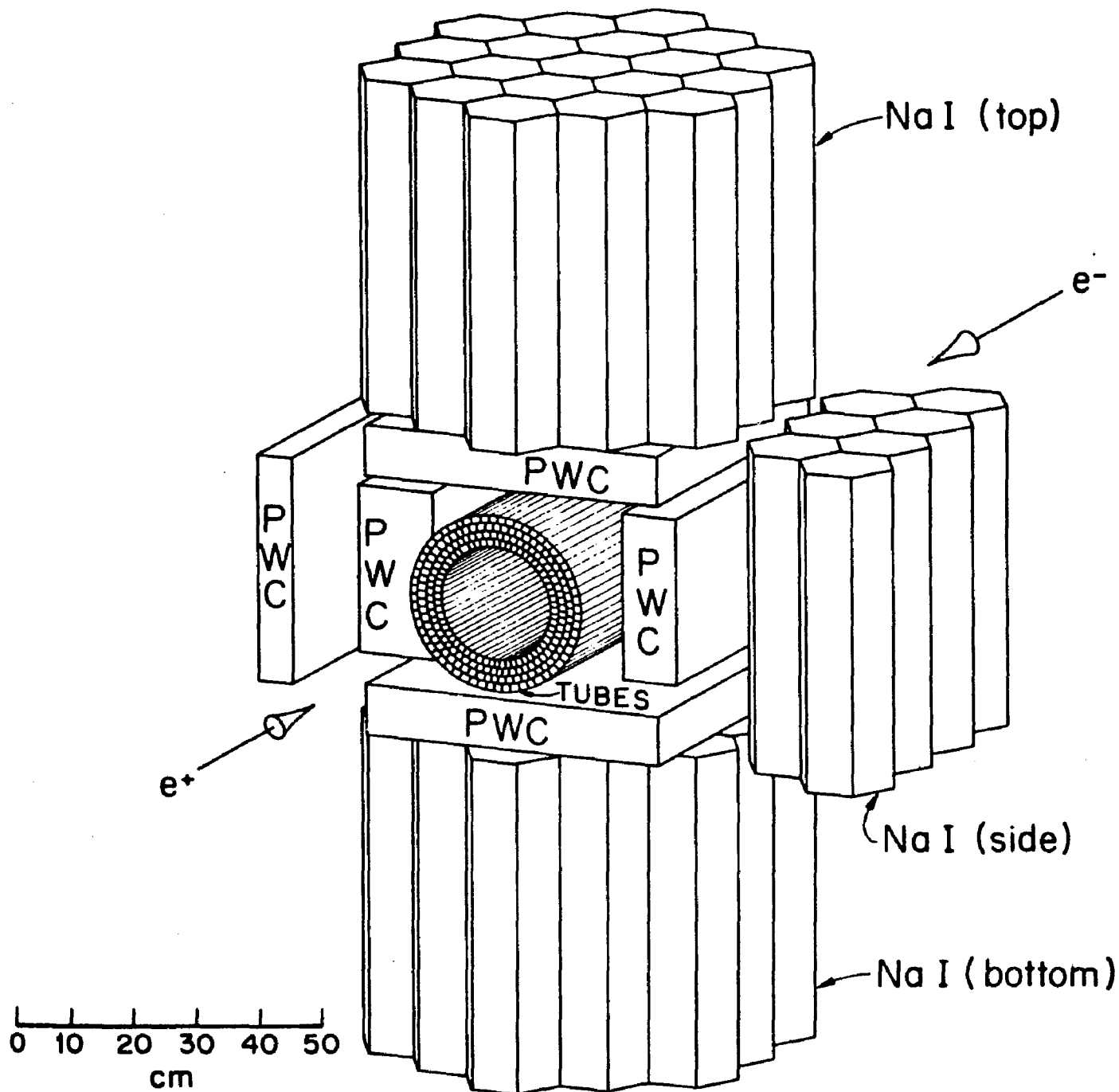


Fig. 0-4 The details of the gamma ray spectrometer shown in Fig. 0-3. The polymer(tubes) provides azimuthal coordinates, while the proportional wire chambers(PWC's) provide the polar coordinates of charged particles.

REFERENCES

INTRODUCTION

1. J.J. Aubert, et al., Phys. Rev. Lett. 33, 1404(1974);
J.E. Augustin, et al., Phys. Rev. Lett. 33, 1406(1974).
2. W. Braunschweig, et al., Phys. Lett. 57B, 407(1975);
B. Wiik, Proceedings of the 1975 International Symposium on Lepton and Photon Interactions at High Energy, Stanford, Calif., ed. by W.T. Kirk.
3. S. Glashow, J. Iliopoulos, and L. Maiani, Phys. Rev. D2, 1285(1970).
4. S. Okubo, Phys. Lett. 5, 165(1963); G. Zweig, CERN Preprints TH401 and TH412(1964), unpublished; J. Iizuka, Suppl. Prog. Theor. Phys. 37-38, 21(1966).
5. P. Rapidis, et al., Phys. Rev. Lett. 39, 526 (1977).
6. J. S. Whitaker, et al., Phys. Rev. Lett. 37, 1196(1976).
W. Bartel, et al., Proceedings of the XVIIIth International Conference on High Energy Physics, Tbilisi, USSR, (1976).
7. J. D. Jackson, Proceedings of the Summer Institute on Particle Physics, SLAC Report No. 198, p. 147, Stanford, Calif. (1976).
8. A.M. Boyarski, et al., Phys. Rev. Lett. 34, 1357(1975);
V. Lüth, et al., SLAC-PUB-1599 (1975).

9. B. Jean-Marie, et al., Phys. Rev. Lett. 36, 291(1976).
10. R.F. Schwitters, Proceedings of the 1975 International Symposium on Lepton and Photon Interactions at High Energy, Stanford, Calif., ed. by W.T. Kirk; F.J. Gilman, Proceedings of Summer Institute on Particle Physics, SLAC Report No. 191, p.1, Stanford, Calif. (1975).
11. E. Fermi, Prog. Theor. Phys. 5, 570(1950).
12. R. Hagedorn, Suppl. Nuovo Cimento 3, 147(1965).
13. G.J. Feldman and M.L. Perl, Phys. Repts. 19C, 233(1975).
14. B. Alper, et al., Nucl. Phys. B87, 19(1975).
15. H.J. Möhring, et al., Nucl. Phys. B85, 221(1975).

CHAPTER I

THE APPARATUS

The magnetic spectrometer was designed to study the inclusive spectra of charged particles emanating from electron-positron reactions near 90° with respect to the incident beams, and over the entire energy range of SPEAR ($S = 6$ to 64 GeV^2). Many details of this spectrometer have been previously discussed in the thesis of T.L. Atwood¹. The gamma ray spectrometer, on the other hand, was specifically designed to study the photons emitted from the resonance decays.

Appendix B lists some of the dimensions and characteristics of the chambers and counters used in these two devices.

A. The Storage Ring

The parameters of SPEAR have been exhaustively described elsewhere². There are, however, several properties of this device that are noteworthy for this experiment.

Each of the counter-rotating particles bunches contains approximately 5×10^{10} electrons or positrons. These bunches collide at the interaction region every 780 ns. This

produces an average current of 10 mA. Due to scattering and particle loss mechanisms, the currents decreased exponentially in time, allowing about two hours for taking data before the currents reached the point where it became necessary to refill the machine. The luminosity produced by the collision of the bunches was typically $5 \times 10^{29} \text{ cm}^{-2} \text{ sec}^{-1}$. The bunches were typically 0.2 mm high by 6 mm wide by 50 mm long at the ψ energy. The total spread in the center-of-mass energy was 0.55 MeV at the ψ energy, and the absolute energy of each bunch was known to 2 MeV.

B. Polymer and Central Detector

Central to both spectrometers was a cylindrical array of proportional tube counters immediately surrounding the storage ring's vacuum pipe. This counter, known as the polymer, detected charged particles emitted within a solid angle of 90% of 4π steradians, centered around the collision region. The polymer consisted of 219 square proportional tube counters, 60 cm. long by 1.27 cm. on a side, with 0.61 mm thick aluminium walls, and with a 20 μm gold-plated tungsten wire stretched through the middle. Since the sense wires were parallel to the beam direction, only the azimuthal angle of the emerging charged particles

could be measured. In order to measure the polar angle with respect to the colliding beams, a box of proportional wire chambers encircled the polymer.

The box of proportional planes girding the polymer consisted of three layers of proportional wire planes with 2 mm wire spacing. The wires were 35 cm. long in the top and bottom planes of the box, but only 11 cm. long on the side planes. The width of the planes on the top and bottom was 42 cm, while the side planes were 25 cm. wide. The angles subtended by these planes covered about 40% of 4π ster. The efficiency for detecting charged particles was near 100% for the angles from 45° to 135° for the top and bottom, with the sides covering from 60° to 120° in θ as measured from the electron direction and covering about 62% of 2π in the azimuthal direction.

C. Gamma Ray Spectrometer

The gamma ray spectrometer consisted of three arrays of sodium iodide crystals located above and below the proportional chamber box and on the side opposite the magnetic spectrometer. The top and bottom stacks consisted of 19 sodium iodide crystals, encased in stainless steel, with seven crystals in the side stack. Each stack had good energy resolution over about 7% of the full solid angle.

The crystals were hexagonal cylinders, 50 cm. long by 12 cm. on an edge. This length of NaI corresponds to 20 nuclear collision lengths and 20 radiation lengths. Each crystal was enclosed in a close-fitting, 0.025 cm. thick, stainless steel container. All crystals were mounted vertically, with a 2 in. photomultiplier at one end. The output signal was clipped to 100 ns. to avoid the problems of timing associated with the long ($\sim 1 \mu\text{s.}$) pulses that the sodium iodide produces. The signal from each photomultiplier was sent to an analog-to-digital converter (ADC) in a CAMAC crate, in addition to being sent to various circuits in the triggering logic.

The NaI energy calibration was determined in several ways: A detailed Monte Carlo program was prepared to simulate most of characteristics of the module; the results of this program showed the effect of the stainless steel walls and the leakage of showers from the sides and ends of the crystals on the energy resolution. The energy deposited by cosmic rays was constantly monitored and was used primarily for run-to-run calibration, i.e. to correct for the drifts in the phototubes and amplifiers attached to them. The pedestal values of each ADC was recorded during a fill of the storage ring and corrections were applied for

drifts in the final calibration. The absolute energy scale was fixed by monitoring the Bhabha scattering events and the electron-positron pairs produced directly from the resonant decays. After converting the digitized pulse heights back into voltage levels and correcting for the nonlinearities observed in the ADCs, the pulse height distributions in the 19 individual crystals for an electron-positron event were used as input for a 19 parameter fitting routine that optimized the energy resolution.

The Monte Carlo simulation showed that the shower loss from the sides of the stack was minimized if greater than 10% of the energy was deposited in the inner seven crystals. The resultant energy resolution ranged from 5% for a 200 MeV photon to 2.5% at 1500 MeV.

One of the advantages of segmenting the sodium iodide was to distinguish several gamma rays or charged particles entering the stack at the same time. In order to achieve this, the energy distribution in the stack was divided into clusters that had the distribution expected of a gamma ray or charged particle passing through the crystals. Typically one expects that the majority of the shower or ionization trail is contained in a small number of adjacent crystals. Generally, one or two crystals have a large pulse height,

with the surrounding crystals having somewhat smaller amplitudes. One can deduce the entrance position of the particle from the center-of-gravity of the cluster. If the particles or gamma rays enter the stack too closely together the cluster will appear to be wider than the cluster from a single particle, but, for the majority of cases, it cannot be distinguished from a single particle's distribution. Due to the rather large solid angle subtended by each crystal, this latter possibility is quite large, especially for high energy neutral pions which produce gamma rays that emerge preferentially in a narrow cone around the incident particle's direction.

D. Magnetic Spectrometer

This spectrometer determined the momentum and the species of a charged particle to a high level of precision. The momentum identification required the use of proportional chambers tracking the particle in front of the magnet, inside the magnet, and behind it. To identify the particle's species required the use of a threshold Cherenkov counter, a flight timing system, an electromagnetic shower counter, and a range counter. The conjugate side system of a range counter and shower counter, supplemented by the side array of sodium iodide, helped identify electrons and muons

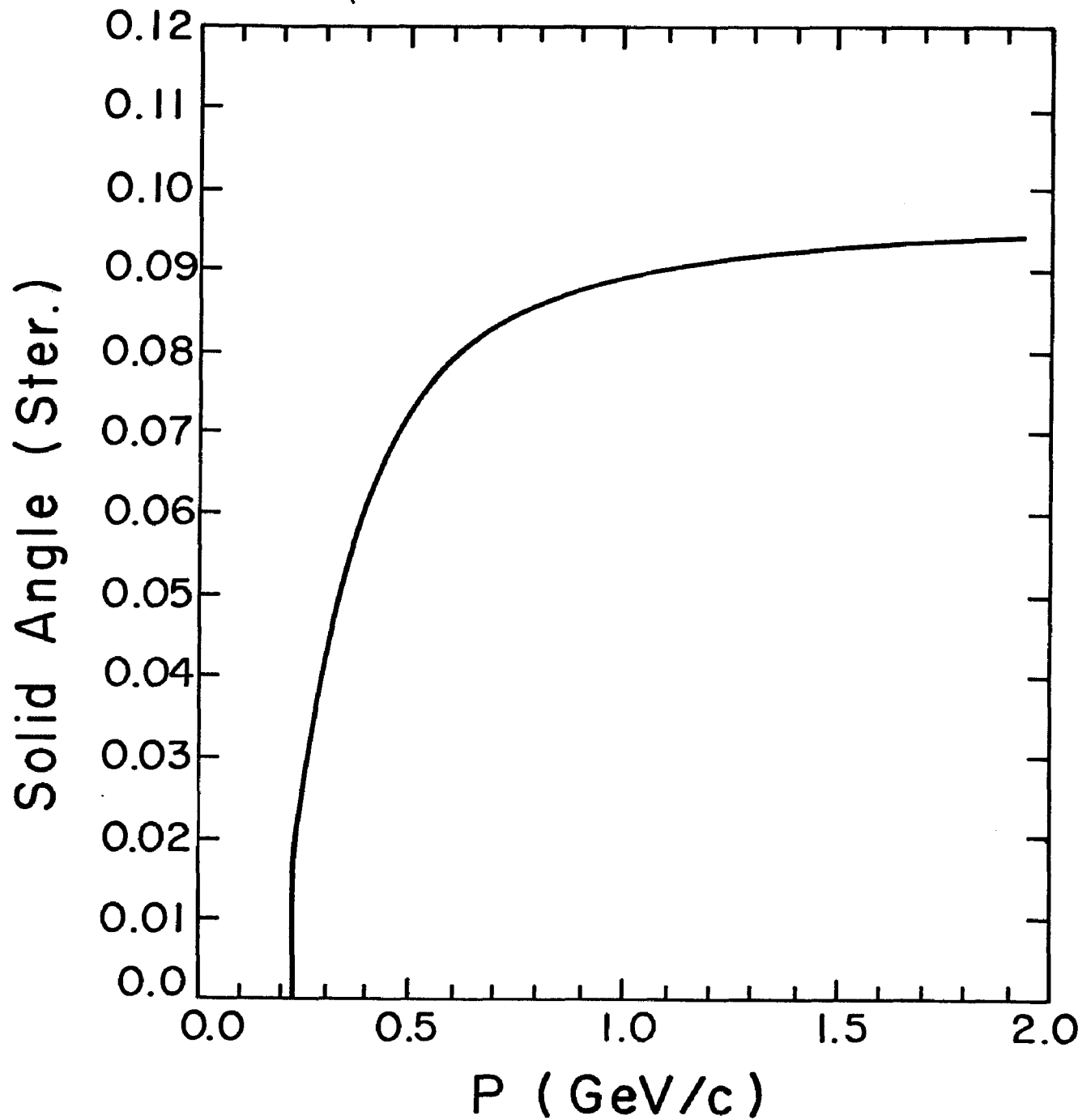


Fig. I-1 The effective solid angle of the magnetic spectrometer as a function of the incipient particle's momentum. The curve is generated by a Monte Carlo simulation of the data.

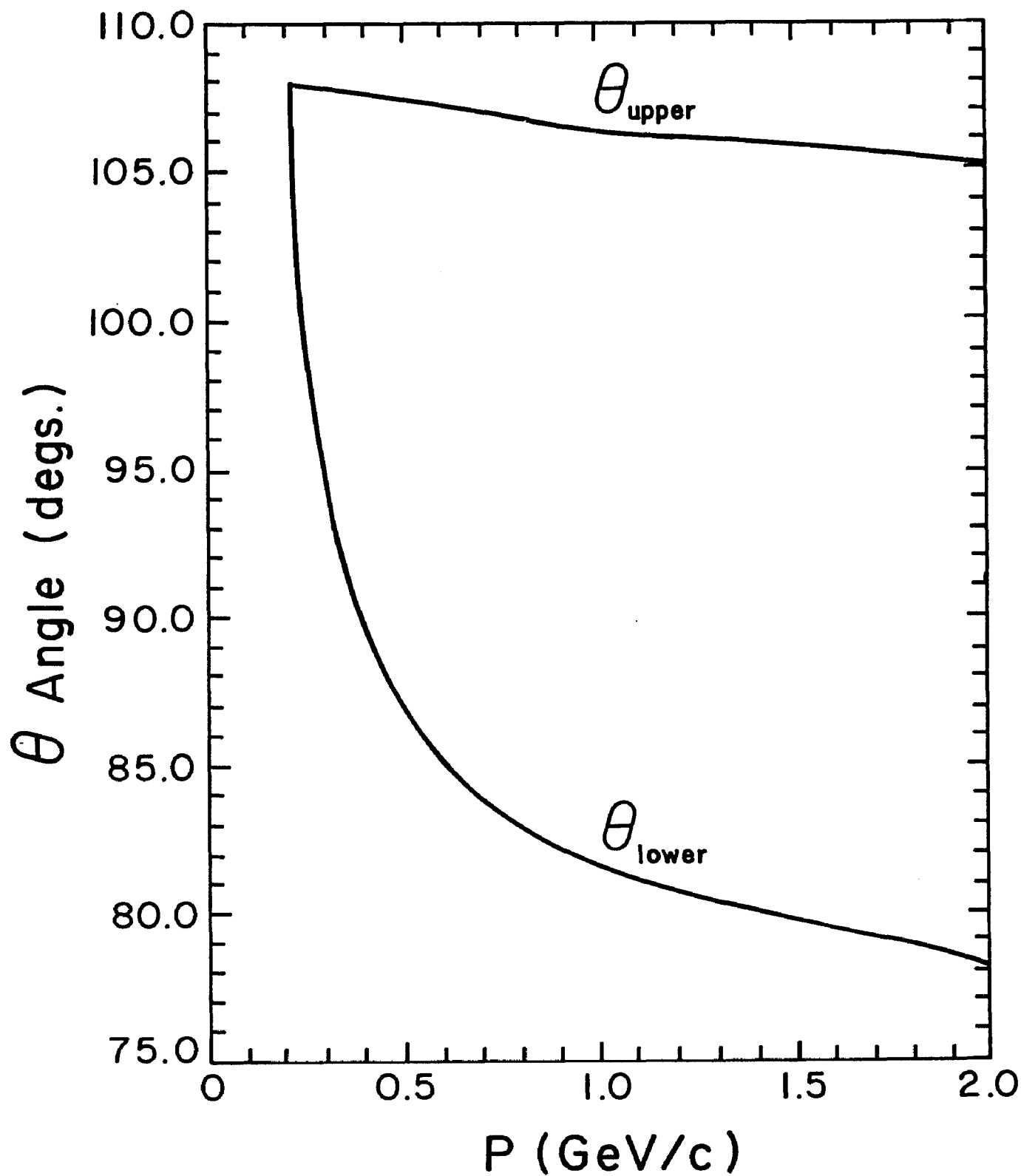


Fig. I-2 The effective polar angle limits of the magnetic spectrometer for positive particles. For negatively charged particles, the limiting lines are rotated about 90° . This angle is measured from the electron beam's direction.

in the spectrometer, since most of these particles are pair produced and emerge from the interaction region back-to-back.

The effective solid angle of the spectrometer as a function of the incident particle's momentum is shown in Fig. I-1, with the polar angle range as measured from the electron beam, shown in Fig. I-2 for positive particles. The azimuthal angle coverage ranged from $\pm 5.6^\circ$ from the plane of the ring, and was independent of momentum.

1. Tracking Chambers

The chambers that track the particles before they enter the magnet are shown in Fig. 0-3. In this assembly, there were 5 proportional planes that measured the X coordinate and 3 that measured the Y coordinate of the particles. These chambers also had a 2 mm wire spacing. The uncertainty in the vertex reconstruction of a particle was 0.1 mm from the wire spacing considerations.

2. Cherenkov Counter

The threshold Cherenkov radiation counter consisted of an aluminum pressure vessel, containing propane at 90 PSIG. The radiator length was 145 cm. A semicylindrical mirror focused the Cherenkov radiation onto a bank of 48, 56AVP

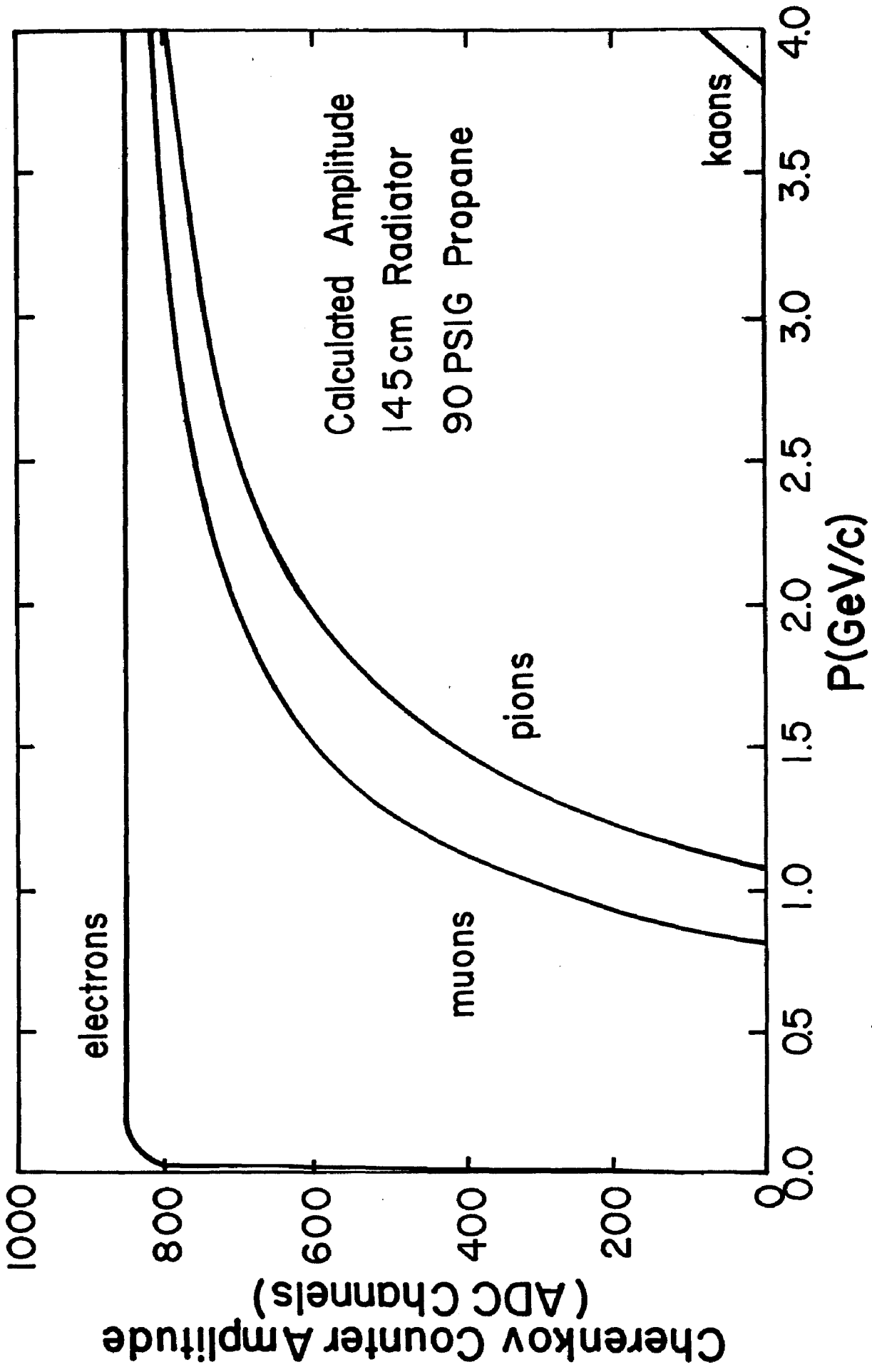


Fig. I-3 The expected pulse height from the Cherenkov counter as a function of the different particles' momentum. The curves are normalized to the observed pulse height for the electrons.

photomultipliers. The threshold for radiation from pions entering along the axis was 1.05 GeV/c, while for kaons it was 3.7 GeV/c. The output signals from the phototubes were added and passed to an ADC in a CAMAC crate for eventual collection by the computer. A detailed description of this counter can be found in Atwood's thesis³.

The performance of this counter was initially checked with a beam of protons to measure the efficiency and threshold characteristics, as a function of the particle's entrance position and angle with respect to the axis. Fig. I-3 shows the predicted mean amplitudes for various types of particles as a function of their momentum. The response of this counter to the data is described in Section III-B-4.

3. Magnet Proportional Chambers

Exiting from the Cherenkov counter, the particle entered four sets of proportional chambers (C3XY, C4XY, C5X, and C6X) placed inside and near the back end of the magnet. In the air gap of the magnet, which was 100 cm high by 204 cm wide by 244 cm long, the magnetic field reached a peak value of 2.85 kgauss and was uniform to within 1% across its width. The location of these chambers is shown in Fig. 0-3. All planes covered most of the cross section

of the magnet. These chambers also had 2 mm. wire spacing except for the last one, C6, which was made of square tube counters with an effective wire spacing of 0.95 cm.

The resolution in momentum is primarily limited by the uncertainty in the sagitta measurement which, in turn, is limited by the wire spacing, and the effects of multiple scattering in the material in the magnet. Other factors that can affect the resolution are the uncertainty of the chambers' positions, and the uncertainty in the magnetic field over the particle's path. The resolution from each of these sources is as follows:

$$\Delta p/p = 0.267 p \Delta s / Bz^2 = 0.012 p \Delta s,$$

from the uncertainty in the sagitta measurement.

$$\Delta p / p = \Delta z / z < 5 \times 10^{-4},$$

from the uncertainty in the distance between chambers.

$$\Delta p / p = \Delta B / B < 10^{-4},$$

from the uncertainty in the magnetic field measurement.

$$\Delta p / p = \frac{0.21}{B z} \sqrt{\frac{\bar{x}}{x_0}} = 0.003,$$

from multiple scattering.

Here, p is the particle's momentum in GeV/c, Δs is the uncertainty in the sagitta measurement which is dominated by the wire spacing, z is the distance, in meters, between

chambers measuring the momentum, Δz is the uncertainty in this measurement, B is the magnetic field in kilogauss, and x/x_0 is the number of radiation lengths between the chambers.

The only significant errors come from the multiple scattering and the determination of the particle's position, since the other sources were negligible.

For example, the magnetic field was parametrized to within 0.6% of the measured value over the entire air gap. The positions of the chambers were first carefully surveyed and then aligned precisely with respect to one another by fitting the chamber hits to cosmic ray tracks that passed through the magnet. The error on this alignment was estimated to be less than .3 mm for any chamber with respect to the others, in all three coordinates. The momentum resolution was determined from the RMS width of the muons' momentum distribution from the ψ decays. Including the effects of the initial and final state radiative effects and the natural energy spread of the beam energy, the intrinsic width of this distribution should be approximately 2.0 MeV. From the observed width (see Section III-A-5) and including the multiple scattering effects, the resolution is:

$$\Delta p / p = 0.012 p \oplus 0.003 \quad (p \text{ in GeV/c}).$$

where \oplus implies addition in quadrature. This implies that the uncertainty in the sagitta measurement is 1. mm., and consistent with the wire spacing.

4. Time-of-Flight (TOF) System

As the particle passed through the magnet, its flight time was clocked by a 1024 channel time-to-digital converter (TDC), with 0.1 ns per channel. For one set of TDC's, the start signal came from the S1 counter, shown in Fig. 0-3. This counter was 28 cm long, by 10 cm wide by 2.5 cm thick, and was viewed at both ends by a RCA-8575 photomultiplier. The stop signal came from a hodoscope, S2, behind the magnet, consisting of seven counters, each 275 cm. long by 20 cm wide by 2.5 cm thick. Again, these counters were viewed at both ends by RCA 8575 phototubes. For another set of TDC's, the start signal came from an capacitively coupled, pick-up plate, located within the vacuum pipe. This plate sensed the passage of the electron bunch, thus producing a signal whenever the beams crossed. The stop signals originated from the same hodoscope as the other set. There were actually four sets of TDC's for all combinations of start and stop signals from the two start, and two stop counter phototubes. On the average, the pathlength was 5 meters for a 1 GeV/c particle. In addition

to the timing information, the pulse height from each counter was recorded with an ADC, to correct the time slewing due to the signal level in the TDC's. The calibration of the TDCs and the counters was monitored every hour or so during a fill of the ring. The TDCs were calibrated by measuring their response to start and stop pulses of two different, but constant, temporal separations, while the gross features of the counters were monitored by pulsing light emitting diodes (LED) mounted in the light pipe of each photomultiplier tube. To get the best possible timing resolution, and hence, the best separation between hadrons, various corrections were applied to the signals in the analysis stages. These are discussed in Section III-B-6.

5. Shower Counter

One of the standard techniques to distinguish electrons from other particles is to observe their electromagnetic showering behavior as they pass heavy nuclei, such as lead. In our case, we used a counter composed of 5 layers of 1.91 cm. thick scintillator, interspersed with 0.64 cm. (1.14 radiation length) thick sheets of lead. An additional sheet of 0.64 cm. lead was attached to the front of the counter. Each layer of scintillator was divided into four

separate pieces, each viewed by a 56AVP photomultiplier. The sections were 137 cm high by 69 cm wide. A flat, triangular light pipe connected the scintillator to the photomultiplier. The signals were sent to a 16 bit ADC (Lecroy Model 2228). Light emitting diodes were attached to each counter to monitor the stability of the system.

On the conjugate side of the spectrometer, a shower counter of similar design was attached. This counter, however, had the scintillators subdivided horizontally with a photomultiplier mounted on the end. Some of the characteristics of this counter are described in Section III-B-2.

6. Range Counter or Hadron Filter

If the particle had managed to penetrate the shower counter, it entered a large sandwich of iron and scintillator that was designed to absorb hadrons by their ionizational energy loss and nuclear interactions, while allowing muons of sufficient energy to pass through it. This counter consisted of three layers of iron, 30.5 cm., 12.7 cm., and 25.4 cm. thick, with layers of 1.91 cm. scintillators placed between and behind them. Thus, a particle had to pass through 6.8 nuclear collision lengths in order to reach the final layer of scintillators.

As in the shower counters, these layers of scintillators were divided into 5 sections each 69 cm wide by 168 cm high, and viewed by a single 56AVP phototube placed on top of a 30 cm long triangular light guide. A similar counter was also incorporated on the conjugate side. Only an on-off signal from a discriminator was recorded for these counters. The properties of these counters are discussed in Section III-B-5, with the penetration probability for muons shown in Fig. III-3, and that for hadrons shown in Fig. III-18.

7. Triggering System

Essentially, the magnetic spectrometer's trigger fired whenever a charged particle passed through the chambers and counters in the spectrometer. Ideally, one would like to record only the annihilation and resonance decay events. However, there are other processes occurring at the same time that can also produce charged particles which may trigger the spectrometer. These processes include: beam-gas scattering, where the inelastic collisions with the residual gas in the machine can produce charged particles that enter the spectrometer; beam-wall scattering, where an electron either strikes the vacuum chamber, or undergoes beam-gas scattering releasing a bremsstrahlung photon which strikes the chamber, producing secondary charged particles; or cosmic rays. The first two processes occur near the time the beams^o intersect, making them, a priori, difficult to eliminate, but the cosmic rays are effectively eliminated by allowing the trigger to occur only in a short time interval around the beams' crossing.

Since the prime goal of the spectrometer was to measure the spectra of particles inclusively produced in e^+e^- interactions without regard to the final state, the triggering scheme reflected this desire. Essentially, as

long as the particle transversed the spectrometer, the counter and chamber information for it was recorded.

By using a combination of scintillation counters and proportional wire chambers in the triggering scheme, the possible biases, such as dead time for the chambers and momentum dependent scintillations for the counters, were reduced to a minimum.

In essence, the trigger was defined by: 1) A coincidence between both phototubes of the start counter for the time-of-flight system ($S1_{right}$ and $S1_{left}$). The thresholds of the discriminators attached to this counter were set such that 99% of the minimum ionizing particles that passed through this counter exceeded them. 2) A coincidence between 2 sets of magnet chambers; either X or Y coordinate plane in the first two magnet chambers (C3X, C3Y, or C4X, C4Y) had wires firing, 3) A coincidence between any of the seven right and seven left phototubes attached to the TOF stop hodoscope, S2 ($\Sigma S2_{left}$ and $\Sigma S2_{right}$). These signals must be in coincidence within a specific time interval, determined by their time jitter and by the beams' crossing (approximately 50 ns.). The coincidence with the beams' crossing removed unwanted triggers from cosmic rays and particles produced by the beams at other parts of the

ring, but which entered the spectrometer and could possibly have triggered it. The crossing signal originated from a capacitively coupled pick-up plate located several meters away from the intersection region, and was delayed and shaped appropriately.

Due to the very low trigger rate (0.1 triggers/sec) even in the presence of a modest luminosity of $5 \times 10^{29} \text{ cm}^{-2} \text{ sec}^{-1}$ and a production cross section on the order of 10^3 nb . on the resonances, the dead time associated with the counters and chambers produced a negligible effect on the triggering efficiency. The live time of the system was limited, principally, by the time necessary to transfer the data from the buffers in which they were stored, onto magnetic tape. During most of this time, any potential triggers were eliminated. The computer-generated dead time was reduced by having three data buffers available in the computer's core, each holding the information from one event, and were transferred to tape in one block once all three buffers were filled. Since all the counters and chambers status were recorded from both the magnetic and gamma ray spectrometers, even from the counters and chambers that neither produced pulses or fired wires, the transfer time was considerable, roughly 10 ms. per

event. Since the magnetic spectrometer data was taken in conjunction with data for the inclusive gamma ray measurement, which had a trigger rate of 10-15 Hz., the live time of both systems was reduced to 85%.

The reliability of the spectrometer's trigger was monitored in several stages: 1) The scintillation counters in the trigger had light emitting diodes attached to them which were pulsed during the times the beams were removed from the machine. The outputs from the phototubes were recorded on tape and the amplitudes were monitored on-line for possible drifts or discrepancies with previous measurements. 2) The status of the chambers and electronics attaching them to the data buffers was monitored both by pulsing one or more amplifiers on the planes with a signal at the same time the scintillators were pulsed, and by making wire-maps of the chambers to record the noise rate, thereby measuring their sensitivity.

8. Data Acquisition System

In order to transfer the information from the chambers or counters to the computers for on-line analysis and recording on magnetic tape, two different systems were used. The data from analog devices, such as the Cherenkov counter, the time-of-flight counters, the shower counters, and the

sodium iodide crystals, were collected in either ADC's or TDC's in CAMAC modules.

Due to the principle groups' original intentions, the data acquisition for this experiment, was divided along the following lines:

- a) The San Diego group recorded the sodium iodide information, along with information from the rest of their apparatus.
- b) The Maryland-Pavia-Princeton group recorded the magnetic spectrometer data, the polyimeter results, and the central proportional chamber information.

In order to analyze the gamma ray spectrometer data, information from both data tapes was necessary. Since each group accepted different triggers that were not jointly recorded, a synchronizing clock signal was also recorded with each event. Events from both data sets were then merged using this clock value, which was accurate to 1 msec.

Additional information was also recorded in CAMAC units. The strictly digital information coming from the wire chambers and from the hadron filter counters, was passed to a computer interface-buffer, known as SOBRL. This data acquisition system for the proportional chambers is described in Reference 3.

Two Hewlett-Packard minicomputers, Models 2114A and 2100, were used to perform the task of writing the data onto tape and of performing some on-line analysis. They were controlled by a disk operating system (DOS), with 8 kbytes of memory available in the 2114A and 32 kbytes in the 2100, and could share data via an interconnecting link. The primary goal of the 2114A was to read in the CAMAC units and the SORRL buffers and transfer the information to tape. The 2100 did all the on-line analysis and received data from the 2114A through the link.

Once the triggering requirement was met, either by the gamma ray or magnetic spectrometers, the following actions occurred. (Fig. I-4 shows a block diagram of this sequence.)

- 1) All subsequent triggers occurring before the data had been transferred to buffers were inhibited.
- 2) The reset for the proportional chamber wire latches was inhibited.
- 3) The ADC and TDC information from the Cherenkov counter, the shower counters, and the sodium iodide crystals was latched, along with other devices that resided in the CAMAC crates, such as scalars and voltmeters.

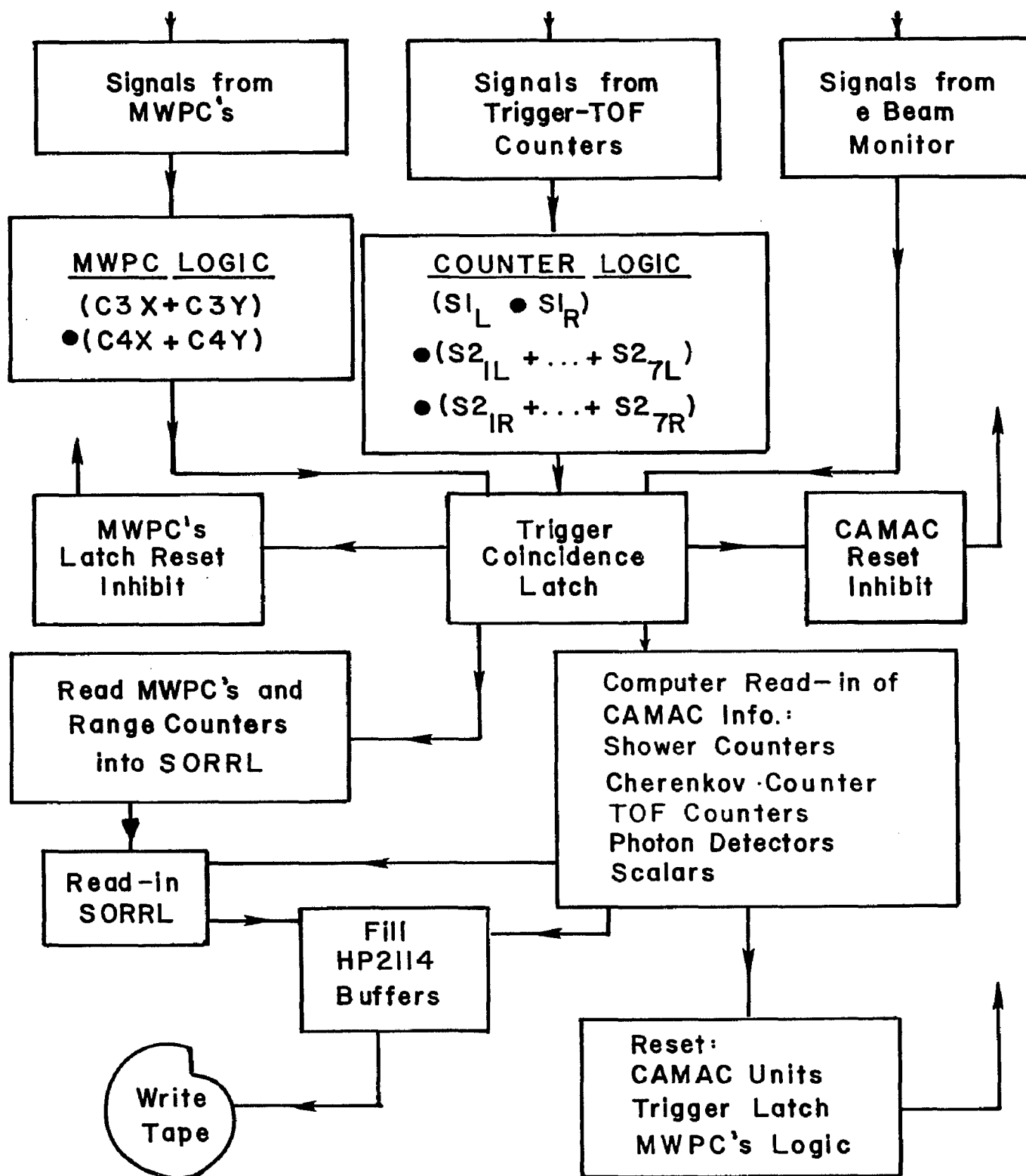


Fig. I-4 A block diagram of the triggering and data acquisition system. The various stages are described in the text.

4) The positions of the proportional wires that fired were encoded and passed to a shift register which subsequently sent the data to the interface-buffer, SORRL.

5) The data from the range counters, consisting only of an on-off bit, was placed into the SORRL buffers.

6) The data stored in the CAMAC units was transferred to the computer's buffers via a crate controller.

7) The SORRL data was transferred to the computer's buffers.

9) All latches were reset, placing the system in a ready state again.

10) Once the three buffers in the computer's memory were filled, the block of core was written onto tape. The buffers were arranged in a wrap-around fashion so that as soon as one of the buffers had been transferred to tape, it was available to accept an event, thereby reducing the dead time due to tape writing.

REFERENCES

CHAPTER I

1. T.L. Atwood, Ph.D. Thesis, Univ of Maryland Technical Report No. 77-040(1977), unpublished.
2. see e.g. Proceedings of the IX International Conference on High Energy Accelerators, (Stanford Linear Accelerator Center, Stanford, Calif., 1974).
3. M. Cavalli-Sforza, et.al., Nucl. Instr. and Meth. 113, 87(1973).

CHAPTER II

DATA ACQUISITION AND ANALYSIS

A. Data Accumulation

The data for this experiment was taken with the machine set at the peak of the resonance cross sections. The average drift in the center-of-mass energy was approximately ± 0.4 MeV. The data, therefore, may not have the peak cross section, but the cross section averaged over this spread in energy.

During the running time of this experiment, the luminosity was monitored by sodium iodide crystals placed within 3° of the beam. These crystals recorded the low angle Bhabha scattering events. From these monitors, we recorded 100 nb^{-1} of luminosity at the ψ and 600 nb^{-1} at the ψ' resonances. The total number of triggers in the spectrometer was 6800 at the ψ and 10525 at the ψ' .

B. Event Selection and Filtering

In the first stage of data preparation, the criteria for reconstructing and analyzing an event were established. The requirements that an accurate value for the momentum of the particle and that the particle could be clearly identified suggested the following criteria:

1) A particle's trajectory before the magnet must be established; this required hits in at least 3 out of the 5 X-coordinate tracking chambers, and 2 out of the 3 Y-coordinate chambers.

2) For the momentum-determining program to produce reliable results, hits must be present in at least 2 out of the 3 X-coordinate chambers in the magnetic field.

3) The ADC's and TDC's for the trigger counters must contain valid information. This criterion was necessary since occasional equipment malfunctions or less frequently, when a trigger occurred while the units were being reset, led to the recording of useless information from the CAMAC units.

Using the merged tapes as input, each event on them was checked for the above conditions. If it passed them all, it was written onto a tape. Only these tapes were used for further analysis.

Events that failed the above test were generally of two types: a) events produced by background processes, either by noise from the storage ring or in the detectors themselves, b) real events where decay or scattering processes made the event non-reconstructable, or c) real events where some

parts of the apparatus malfunctioned. Corrections can be calculated and applied to the latter two cases. These correction factors are discussed in Section IV.

C. Event Reconstruction in the Spectrometer

Once the data had been filtered, the next phase of the analysis began; that of reconstruction and momentum determination. This phase proceeded in the following fashion:

- 1) The least-squares method was applied to the hit positions in the X and Y tracking chambers to determine an incident track towards the magnet.
- 2) If a line was found in both the X and Y coordinates, a momentum analysis was attempted on the event.
- 3) If the program was successful in finding a momentum, the analyzed event was written onto a third generation tape.

1. Incident Track Finding

A linear, least-squares fit was made to combinations of points in the five X planes preceding the magnet and the four Y planes, including the chamber in the middle of the magnet. The program used the maximum number of chambers that contained hits, but would chose lines only if their

reduced χ^2 value was less than 5. The coordinates of the interactions' source were then determined.

2. Momentum Analysis

If both coordinates of the trajectory up to the front of the magnet were known, i.e. a track in both the X and Y directions was found, the analysis proceeded as follows:

1) An initial estimate was made by fitting the chamber hits to a circle, if the chambers at the beginning, the middle, and the end of the magnet contained hits. If this combination of hits did not occur, the estimate was made from the incoming trajectory and a parameterization of the hit locations with respect to this track. The expected trajectory for a particle with this incoming angle, source point, and momentum was extrapolated through the apparatus from the interaction region to the back of the muon identifier. The extrapolation through the magnetic field used the routine BFIELD^1 in which the actual field was parameterized to better than 0.6%.

3) The χ^2 was calculated for the extrapolated track, weighted by the width of the hit in each chamber, i.e. the number of adjacent wires firing times the wire

spacing.

4) A correction to the source point, the incident angle, and the initial momentum was calculated from a parameterization to the difference between the extrapolated and observed hit locations.

5) These last two steps were repeated until the χ^2 was minimized. If the χ^2 could not be reduced below a certain value by the iterative scheme, the program assumed that a scattering had taken place at the exit window of the Cherenkov counter, the most likely place for this to happen since it contained 0.14 radiation lengths of aluminum.

6) If a scattering was inserted, the above steps were again repeated until the χ^2 was minimized, changing the scattering angle if necessary.

7) Finally, either the chi square fell below the desired value, or the program stopped after ten extra iterations.

If the program successfully completed all stages of its analysis, the event was written onto tape for further data reduction. Fig. II-1 shows the final scattering angle and reduced χ^2 for the resulting events. Note that the reduced χ^2 distribution peaks at 1.0, as expected, and that the

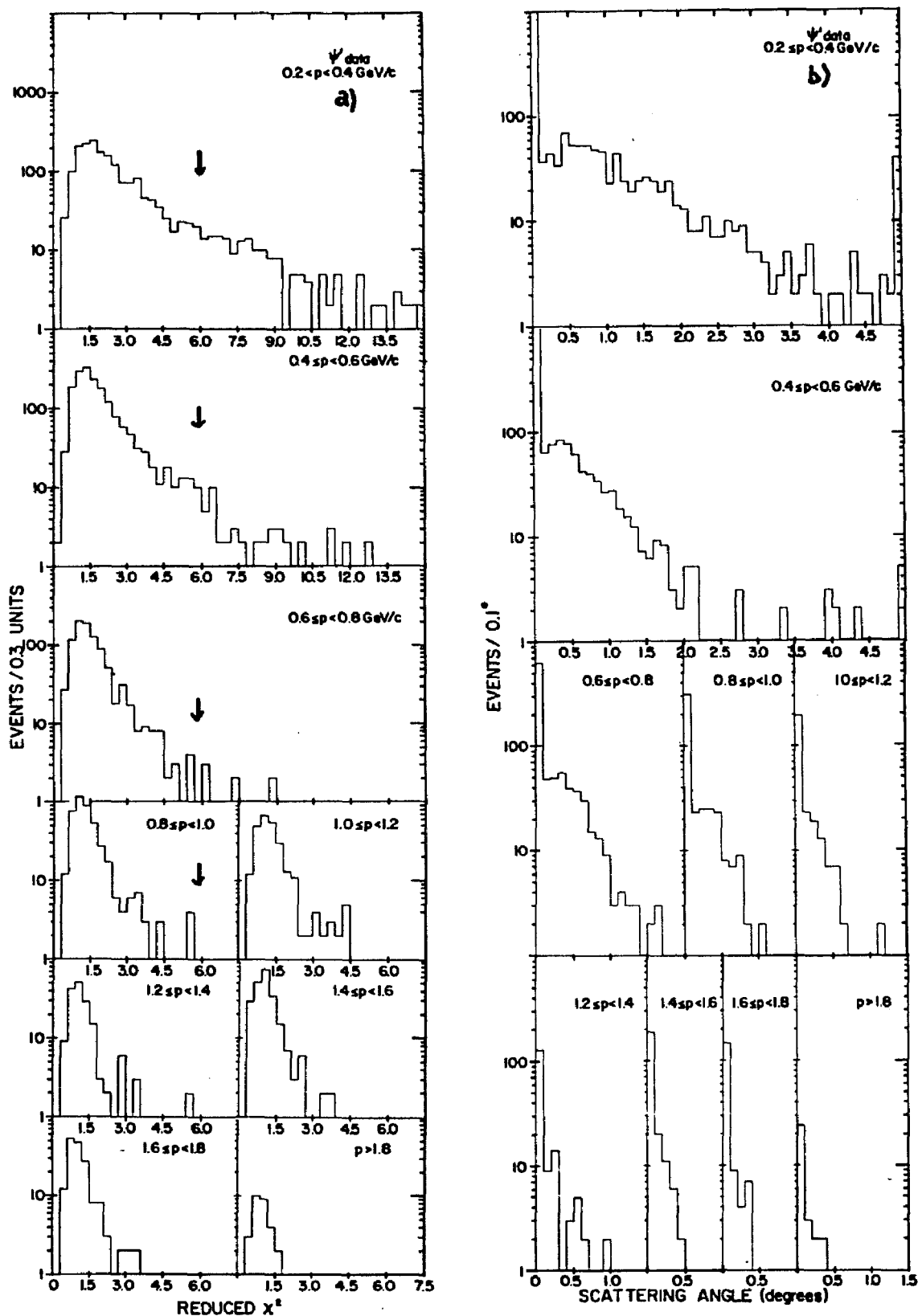


Fig. II-1 The reduced χ^2 of the particles' trajectories(a), and the scattering angle(b) as a function of the momentum. The arrows indicate the position of a cut in the reduced χ^2 to eliminate particles that decay in flight. The large spike at 0° of scattering is due to the way this quantity is calculated.

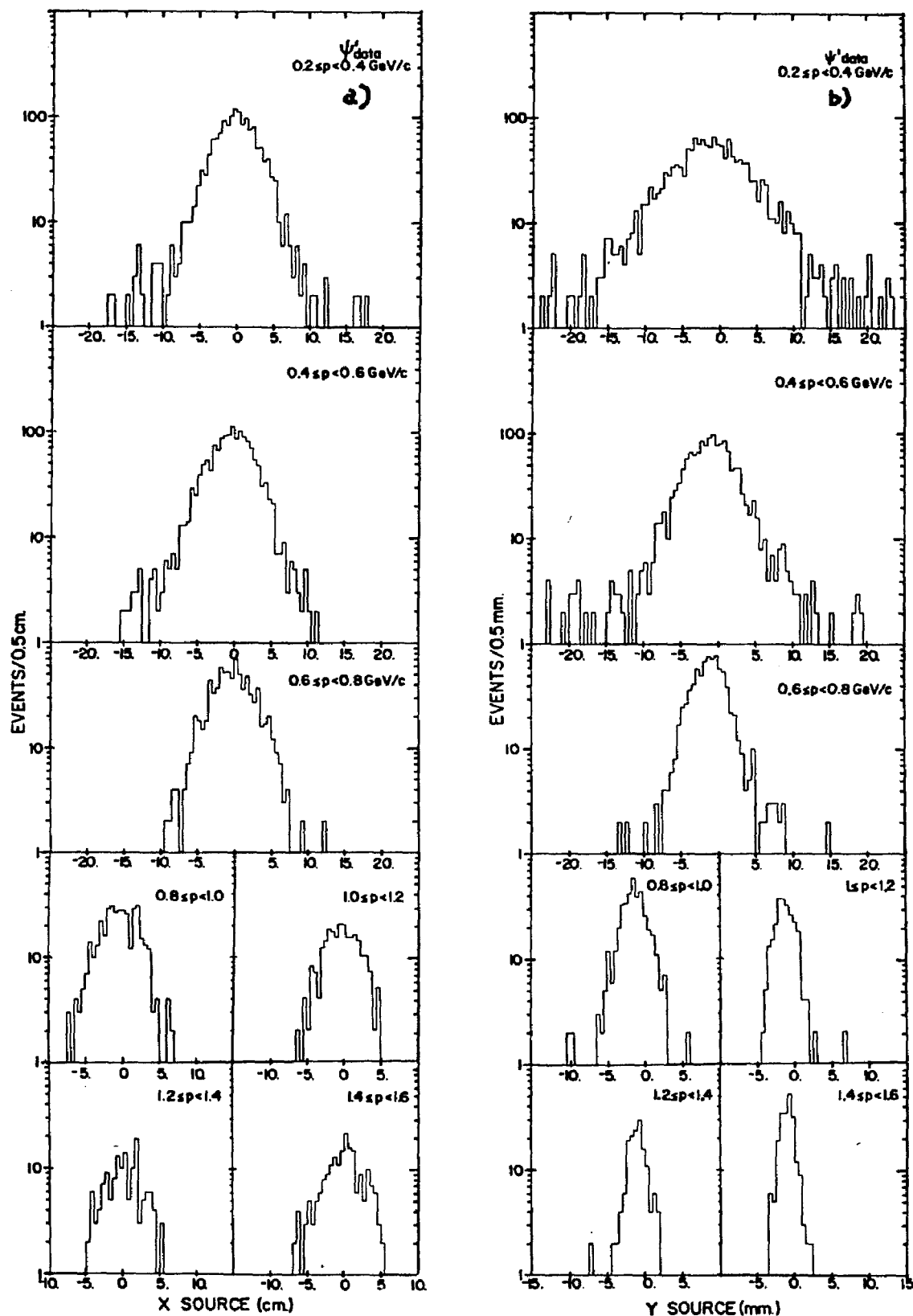


Fig. II-2 The vertex at the colliding beams' position for the X (a) and Y (b) coordinates for different momentum ranges. The X coordinate distribution is consistent with the length of the bunches, while the Y coordinate distribution is dominated by multiple scattering effects in the beam pipe.

scattering angle distribution is roughly consistent with that expected from multiple, Coloumb scattering and nuclear scattering. In Fig. II-2, the X and Y coordinate source points are shown for these events. The X distribution is roughly constant for different ranges of the spectrometer particle's momentum. The rms widths of the distributions are nearly 3 cm. The Y source, on the other hand, shows a marked variation with momentum. Since the expected height of the beams is approximately 0.4 mm, the observed height is presumably due to scattering effects in the beam pipe and in the rest of the apparatus. A detailed Monte Carlo (Section IV-B) simulation of the particle's passage through the apparatus and its reconstruction by the fitting programs, confirmed this hypothesis.

3. Further Event Selection

In order to reduce the background from beam-gas scattering and hadrons that are poorly reconstructed in the spectrometer, additional cuts were imposed on the data: 1) the X source point must be within 70 mm of the mean value; 2) the Y source point must be within 20 mm of the mean; 3) the reduced χ^2 of the trajectory must be less than 6; and 4) the extrapolated trajectory must lie within the active regions of all counters and chambers starting from the TOF

start counter until the third plane of the shower counter.

The first two requirements removed beam-gas and beam-vacuum pipe scattering events while removing less than 0.5% of the annihilation events. From the Monte Carlo results, one finds that less than 1% of those events that enter the spectrometer and do not decay or hit the walls of the magnet have a reduced χ^2 greater than 6. For events with larger values, the reconstructed momentum is totally unreliable. For the Monte Carlo events that decay, one encounters large χ^2 and a poor correspondence between the incident momentum and the reconstructed momentum. Thus, a large fraction of decayed events are eliminated. A correction factor is then applied to the data at a later stage. The fourth requirement also helps in eliminating decayed event and also events that strike the magnet's walls but which scatter back into the spectrometer and fire the triggering system.

For the ψ data, 4500 events survived the previous analysis stages, while 3570 passed these four cuts. For the ψ' data, the corresponding numbers of events are 6190 and 4125. The corrections that must be applied to the data to compensate for these cuts is outlined in Section IV, with details listed in Appendix C.

REFERENCE

CHAPTER II

1. T.L. Atwood, Ph.D. Thesis, Univ. of Maryland Technical Report No. 77-040(1977), unpublished, Appendix A.

CHAPTER III

PARTICLE IDENTIFICATION

A. Selection of Clean Particle Samples1. Introduction

Since the goal of this experiment is to measure the spectra of each particle species produced in e^+e^- reactions, a clear method of separating the various types must be found. In particular, this experiment attempted to measure the spectra of stable charged hadrons, i.e. pions, kaons, and protons, and to identify the charged leptons that are produced. One must first decide on what a priori characteristics can be used for identifying the different types. These characteristics are determined by the nature of the available detectors.

Ideally, one would like to have the response characteristics of each detector for the different species, as determined by an unambiguously-defined beam of each type. However, for our data, a self-consistent particle identification scheme was undertaken. The expected response for a given type of particle in a given device was used in order to initially separate the different species. This was done by producing the a priori probability functions,

$P(s, D_k(R_k))$, which is the expected probability that a particle of species, s , will have a response, R_k in the device, D_k . The various species' response functions are, in general, only roughly known for each detector. By using a limited range of the device's response which clearly identifies a certain species and excludes others with a high probability, a clean sample for testing the other devices is found. With these samples, which one believes to be representative of the total species' samples, one generates the corrected probability function, $P_c(s, D_k(R_k))$, for the other devices. Using these corrected probability functions to identify the types, the corrected probability functions for the devices used to generate the originally tagged sample can be obtained. Finally, the appropriate devices used in concert will form the joint probability function:

$$P_c(s, D_1(R_1), \dots, D_n(R_n)) = \prod_{j=1}^n P_c(s, D_j(R_j)).$$

This joint probability is then used to determine the identity of the individual particles by calculating its value assuming the particle falls under each of the different types, and by identifying the particle with the species that gives the maximum probability.

If the original probability functions are independent

of each other, in other words, if the various detectors' response span some n-dimensional space, then the misidentification probability for two different species is the integral of the overlap of their joint probability distributions.

2. Devices Used In Particle Identification

This analysis of the data will use the following responses to distinguish among the indicated particle types. The separation of electrons from hadrons and muons uses:

- 1) The number of charged tracks observed and the angles between them. The electrons, at least those produced at the ψ resonance, are expected to be pair-produced and emerge nearly back-to-back from the interaction region. Hadrons, on the other hand, are generally produced in large numbers, with an average multiplicity of 4.4 at these resonances¹.
 - 2) The energy deposited in the NaI crystal array opposite the spectrometer. From 1), the electron traveling away from the spectrometer should enter the NaI array and deposit most of its energy there.
 - 3) The amplitude from the Cherenkov counter.
 - 4) Various quantities derived from the shower counter.
- These are expected to be the strongest identifiers of

electrons.

5) The time-of-flight system for eliminating protons.

The separation of muons from hadrons and electrons uses:

1) The number of charged tracks and angle between them.

Again, since the major source of direct muons are pair-produced and, therefore, emerge back-to-back, restricting our attention to those events with two, collinear charged particles helps eliminate hadronic events.

2) The Cherenkov counter's amplitude.

3) The penetration of the spectrometer's range counter, i.e. the number of layers of scintillator that have pulses in them.

4) The penetration of the range counter on the conjugate side of the spectrometer. Since they are produced in pairs, the observation of a muon's characteristics in the conjugate side favor assigning the spectrometer particle as a muon.

The separation of the various hadronic species uses:

1) The Cherenkov counter's response.

2) The time-of-flight system's properties.

3. Selection of a Representative Electron Sample

In this experiment, the direct electrons are produced

Direct Muon, Electron Production

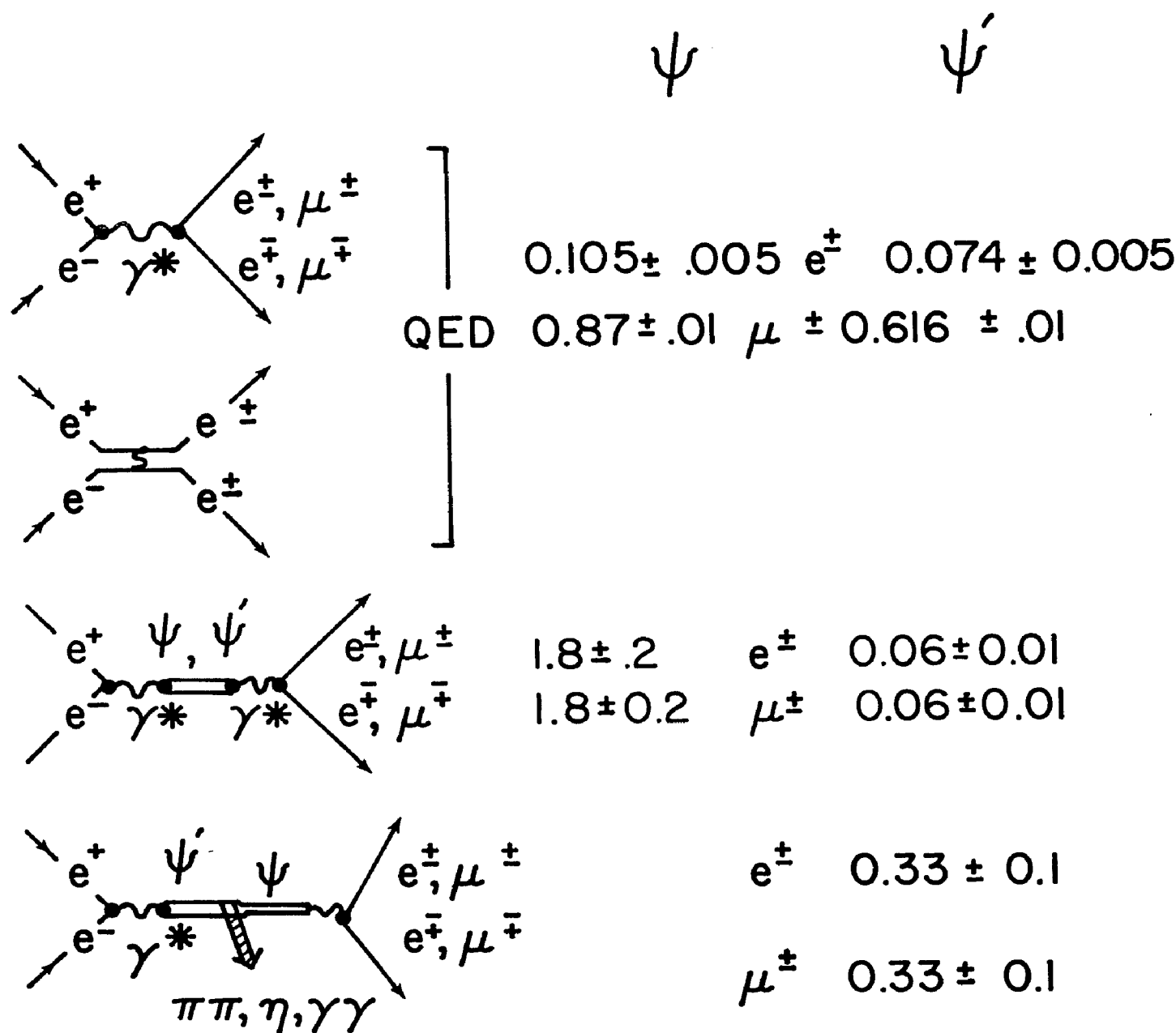
Contribution
at $\theta = 90^\circ$ (in nb)

Fig. III-1 The diagrams giving the major sources of direct leptons from the resonances. The contribution of each source is shown as a cross section into the solid angle of the magnetic spectrometer. The values are in nanobarns.

either from the decays of the ψ and ψ' resonances, or from quantum electrodynamical processes. In either case, they are produced in pairs (at least from the lowest order QED reactions) and carry most of the initial beam energy. In Fig. III-1, the main diagrams contributing to the direct electron production are shown, along with their relative contributions.

Since all these reactions are essentially two-body decays, one expects the electrons' momentum spectrum to be peaked at the beam momentum, with some low energy tail due to the contributions from higher order QED processes. Unfortunately, the path from the collision point through the magnet is filled with chambers and counters, comprising 0.5 radiation lengths. This material, of course, degrades the expected sharp peak in the electrons' momentum distribution, into a rather slowly-varying, exponential-like spectrum.

There exists a source of secondary electron, either produced indirectly from e^+e^- annihilations, such as particle decays or gamma ray conversions, or produced by the storage ring's operation, such as electrons scattering from residual gas nuclei. These sources, generally, do not produce electrons that have the characteristics of the directly produced ones. Thus, it is necessary to use somewhat looser

criteria for defining the total electron sample. An estimate of these secondary sources' contribution to the electrons in the data give a value of less than 5% of the total.

As described above, a clearly defined sample of electrons is necessary to test the response of the various identifiers, in particular, the shower counter. From an earlier experiment² employing this counter, we know that its energy resolution for 2.4 GeV electrons is approximately 25%. Since the pions can mimic electrons through nuclear interactions which produce a cascade of secondaries, as in charge exchange reactions, one must look at various aspects of the cascade's development in addition to the total deposited energy to establish the particle's identity. It is well known³ that the electromagnetic cascade builds up rapidly as a function of radiation lengths transversed, reaching a peak after

$$1.01 E/E_c [\log(E/E_c) - 0.37]^{-.5} \text{ radiation lengths (r.l.)}.$$

Here, E is the energy of the incident electron and E_c is the critical energy, where ionization losses dominate over radiation losses. For lead E_c is about 10 MeV. For electrons in our range of interest, the peak is reached after passing through about 2 - 3 r.l. Thereafter, the

shower dies out exponentially through collisional losses.

The hadrons, on the other hand, show a typical ionization loss in the counter, except when they interact. By looking at the minimum amplitude from the scintillators in the first three layers of the counter (the first 4.5 r.l.), one should be able to distinguish electrons from hadrons which do not interact in the first 2.2 r.l. before the first scintillator. The first three layers are chosen to minimize the effect of the Landau fluctuations in the hadron's energy loss.

In order to select the clean sample of electrons, we use the following criteria.

- 1) Two polymer tracks that are coplanar to within 10° . This is the expected QED and resonance electron production characteristic.
- 2) The deposition of at least 800 MeV in the conjugate side sodium iodide array. From the first criterion, an electron entering the spectrometer will usually be accompanied by an electron which enters the opposing sodium iodide stack. Since an electron will lose most of its energy in the 10 r.l. of NaI, the spectrometer particle can then be tagged as an electron.
- 3) The amplitude from the Cherenkov counter is at least

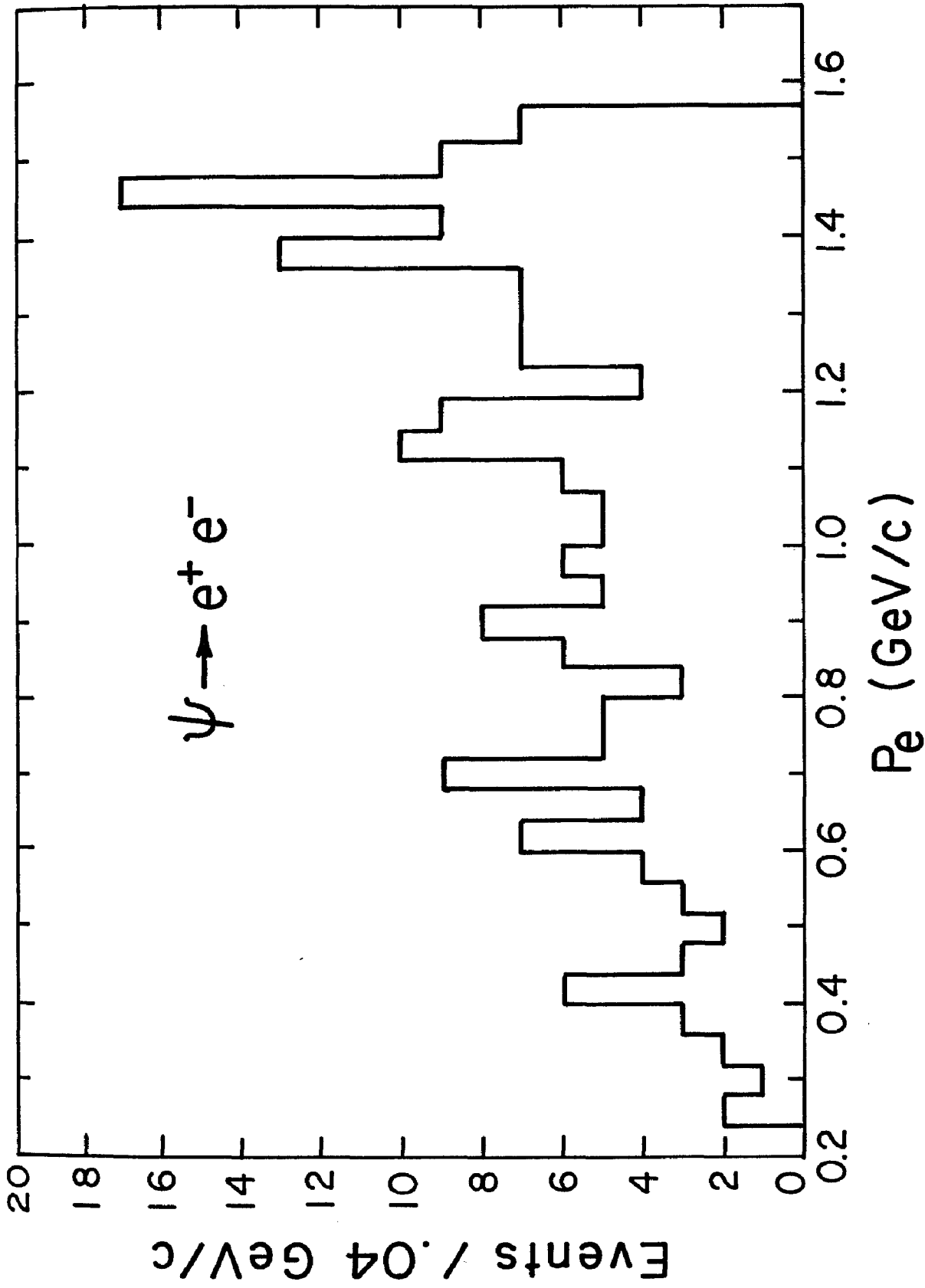


Fig. III-2 The spectrum of cleanly identified electrons from the ψ data sample. These events are not corrected for the acceptance.

600 out of a possible 1024 in the ADC. From the electron's expected response and the fluctuations of this value due to photoelectron statistics and the spread in the phototubes operating characteristics, the probability that an electron has a pulse height less than 600 is 1.0%.

4) No range counters are allowed to fire. This prevents contamination from muons, which have a similar topology, at the level of 0.2%.

The spectrum for this sample of electrons from ψ decays is shown in Fig. III-2.

4. Selection of a Representative Muon Sample

As with the electrons, the primary source of muons comes from the second order electromagnetic decays of the resonances and the direct QED contribution. The various production schemes are shown in Fig. III-1. A secondary source of muons comes from the decays of pions and kaons in flight, and also from cosmic rays.

The chief identifying feature of muons that have a momentum above about 1.2 GeV/c is that they have nearly a 100% chance of penetrating through the entire range counter. This penetration probability depends on the total amount of material in the muon's path, therefore on the angle with

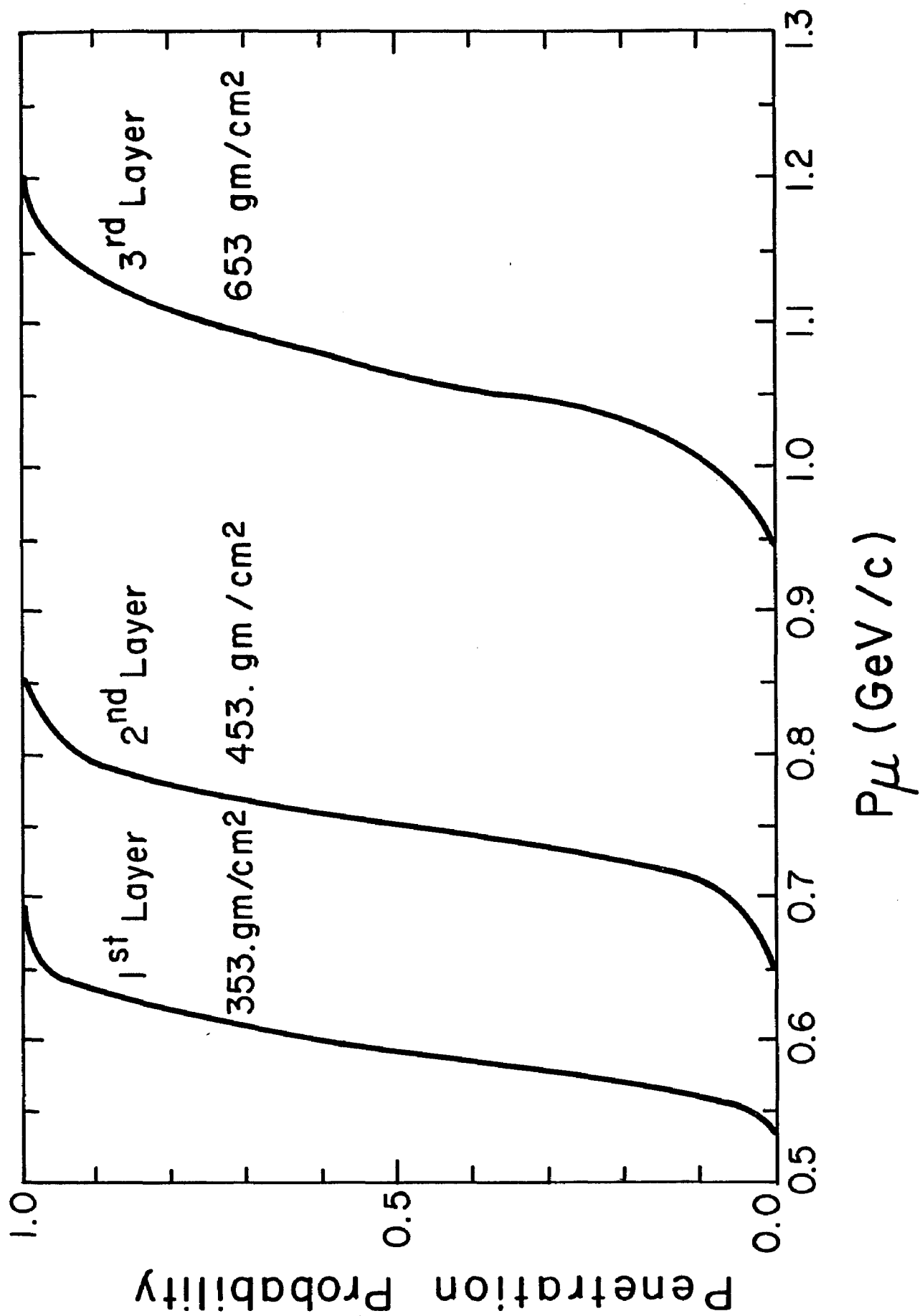


Fig. III-3 The penetration probability of a muon into the various layers of the hadron filter counter.

which it strikes the counter. The uncertainty in this probability is due to the straggling in the iron. Muons of lower momentum have a certain probability of penetrating the first and second layers of the counter, as Fig. III-3 shows. Muons between 0.8 and 1.1 GeV/c can be identified, to a limited extent, by using the additional information from the Cherenkov counter.

In selecting the representative sample of muons, the following criteria are applied:

- 1) There are two polymer tracks, coplanar to within 10° .
- 2) The Cherenkov counter's amplitude is greater than 25 out of 1024 ADC channels. From the expected response and the fluctuations about this value, less than 0.1% of the muons with momentum greater than 0.9 GeV/c could fail this test.
- 3) A scintillation counter in each of the three layers of the hadron filter must fire and the position of the particle, as extrapolated by the momentum-finding program, must lie within the fired counter. The probability that a muon above 1.15 GeV/c will not meet this requirement is less than 4%.
- 4) Since the muons are mostly produced in back-to-back

pairs, the muon in the spectrometer can be tagged by requiring the other muon to penetrate the range counter on the conjugate side. Since both range counters contain the same thickness of iron, the penetration probability for the conjugate side counter is the same as the spectrometer's counter. The penetration is met by having at least 2 out of the 3 layers of scintillator fire.

The probability that a hadron or an electron can pass these requirements is estimated to be less than 0.3% for electrons and 1.0% for hadrons.

5. Muons' Momentum Spectra

In Fig. III-4, the momentum spectrum of muons passing the above tests is shown. The width of the direct pair production peak ($\sigma \approx 30$ MeV/c) represents the overall momentum resolution, since the actual width is expected to be dominated by the spread in the energy of the beams ($\sigma \approx 2$ MeV/c) and higher order QED mechanisms. The observed spectrum has been corrected for the most likely energy loss in the material in front of the magnet. The momentum resolution, including the calculated multiple scattering effects, is

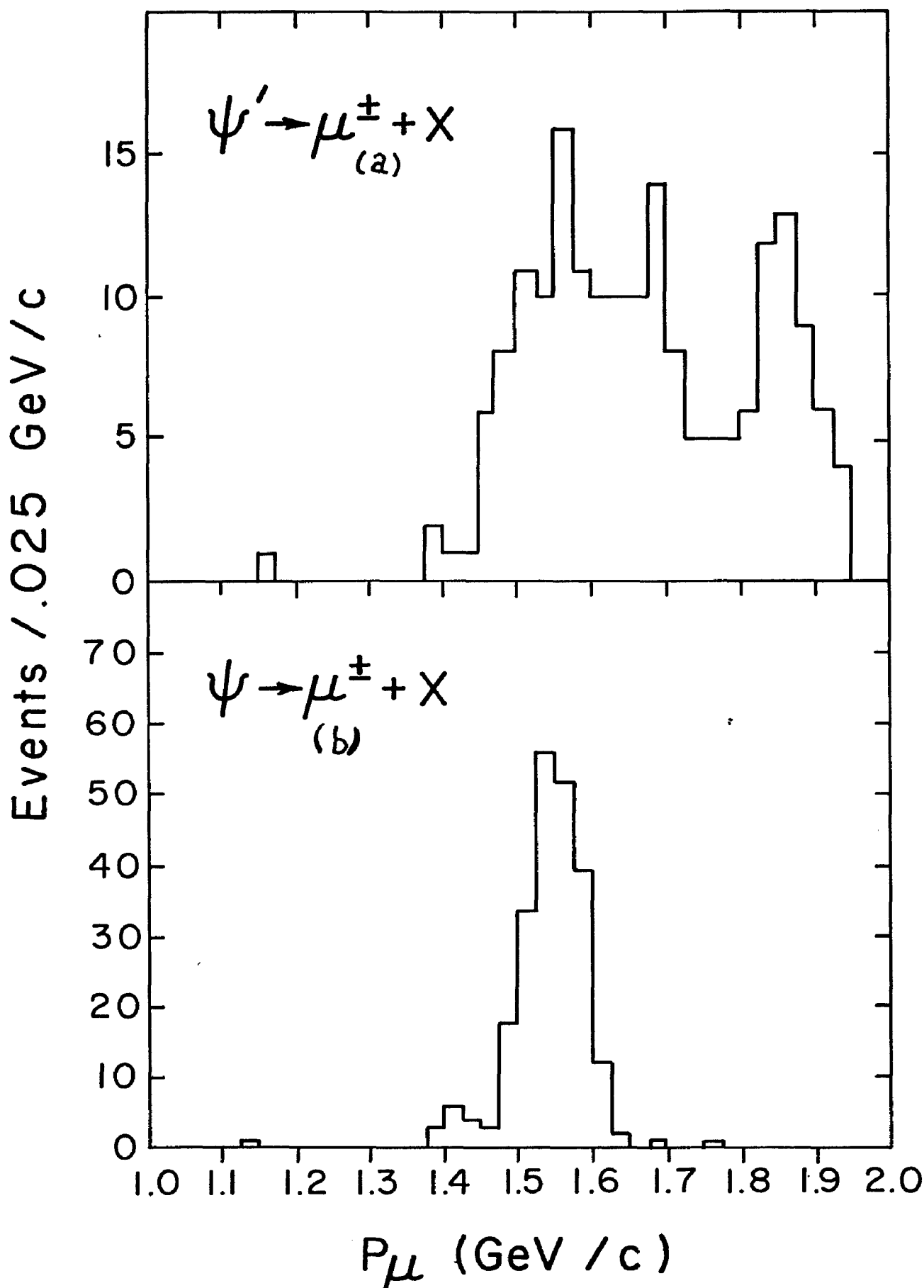


Fig. III-4 The momentum spectra for cleanly identified muons. Note that the "X" system has a high probability of containing another muon due to the conjugate-side range counter requirement.

$$\frac{\Delta P}{P} = .012 p \oplus .003,$$

where p is the momentum in GeV/c and \oplus implies addition in quadrature.

6. Selection of a Representative Sample of Hadrons

Since our primary focus will be on the spectrum of hadrons, the separation of electrons and muons from them is of a major concern. To initially check the response of the various counter, a clearly identified sample is needed. There are several distinguishing characteristics of hadrons that makes them rather easy to identify.

1) The average number of charge tracks produced in a hadronic decay is generally larger than two. For the clean sample, then, an event must have greater than two visible, charged prongs.

An important multiprong electron process is the cascade decay of the ψ^0 :

$$\psi^0 \rightarrow \psi + X \rightarrow e^+ e^- + X,$$

where X contains several charged particles. However, the electrons still emerge nearly back-to-back and can be identified by the conjugate side NaI array (see requirement 6).

2) The Cherenkov counter helps in the distinction of low momentum hadrons from electrons. Below 1.1 GeV/c, no hadron has a sufficient velocity to produce Cherenkov radiation directly, but there is a rather large probability that a gamma ray, produced along with the hadron, can convert, enter the Cherenkov counter, and produce a spurious signal. The probability for producing a spurious signal by this mechanism is estimated to be 14% (see Section III-B-4). To cleanly identify hadrons below 1.1 GeV/c, then, we require the Cherenkov counter to have an amplitude below 20 out of 1024 ADC channels.

3) For hadrons above 1.1 GeV/c, the Cherenkov counter can still be used to help in their identification. Referring to the Cherenkov counter's response curve, Fig. I-3, we see that there is a clear separation between the electrons' and pions' response in the momentum range of interest. In the presence of 20% fluctuations in the response, notice that for 1.5 GeV/c pions, the probability that they could produce an amplitude greater than 600 is less than 15%, while the probability that an electron will produce a pulse height less than 600 is less than 1%. Therefore, the

amplitude from the Cherenkov counter is required to be less than 600 for particles in the clean sample that have a momentum greater than 1.1 GeV/c.

4) The hadron filter allows a clean separation of high momentum hadrons from muons. Due to the large number of nuclear interaction lengths in the counter, hadrons above 1.1 GeV/c have a small probability to penetrate the filter. To identify an event as a hadron, no scintillation counters in the hadron filter must fire.

6) By requiring the deposited energy in the side NaI crystal array to be less than 800 MeV, multiprong electrons, such as from the ψ^* cascade decays, are effectively eliminated. The maximum non-collinearity between the electrons from this mode is 18° . Thus, if one electron enters the spectrometer, the probability that the other strikes the NaI package is greater than 90%.

7) Due to the fact that the antiprotons have a very large annihilation cross section, the probability that they will interact in the shower counter and produce a cascade similar to that from an electron is quite high (e.g. see Fig. III-6). Since the protons are easily identified by their flight time over their entire

momentum range in this experiment, they are eliminated from the hadron sample at the start. By definition, the initial hadron sample contains only pions and kaons.

B. Tests of the Particle Identifiers

1. Generation of the Complete Probability Distributions

With the selection of these representative samples of hadrons, electrons, and muons, it is now possible to determine the response functions of the various devices. Using these clean samples of events, the response functions were determined for those devices that were not used in defining the sample. Next, using the corrected response function for the tested devices, the corrected response functions for the defining devices were generated. The devices tested were the following.

1) The shower counter's response is measured with respect to the initial sample of electrons, muons, and hadrons. The quantity of interest will be the total energy deposited as measured by the sum of the amplitudes from the scintillation counters, the minimum amplitude from the first three layers, and the RMS deviation of the layers.

2) The conjugate side NaI array is tested with all the samples. This counter is used primarily for identification of electrons by their energy deposition in it. Since, in the hadronic reactions, high energy gamma rays or neutral particles that decay into photons are produced with some probability of entering the crystal array, the complete distribution of deposited energy for electrons and hadrons is necessary if it is to be useful for particle separation.

3) The Cherenkov counter is tested with samples defined without this device to assess its characteristics.

4) The range counter is tested with a sample of multiprong events to measure hadronic penetration probabilities.

5) The time-of-flight system can be tested with the initial sample to measure its ability to separate the various types of hadrons.

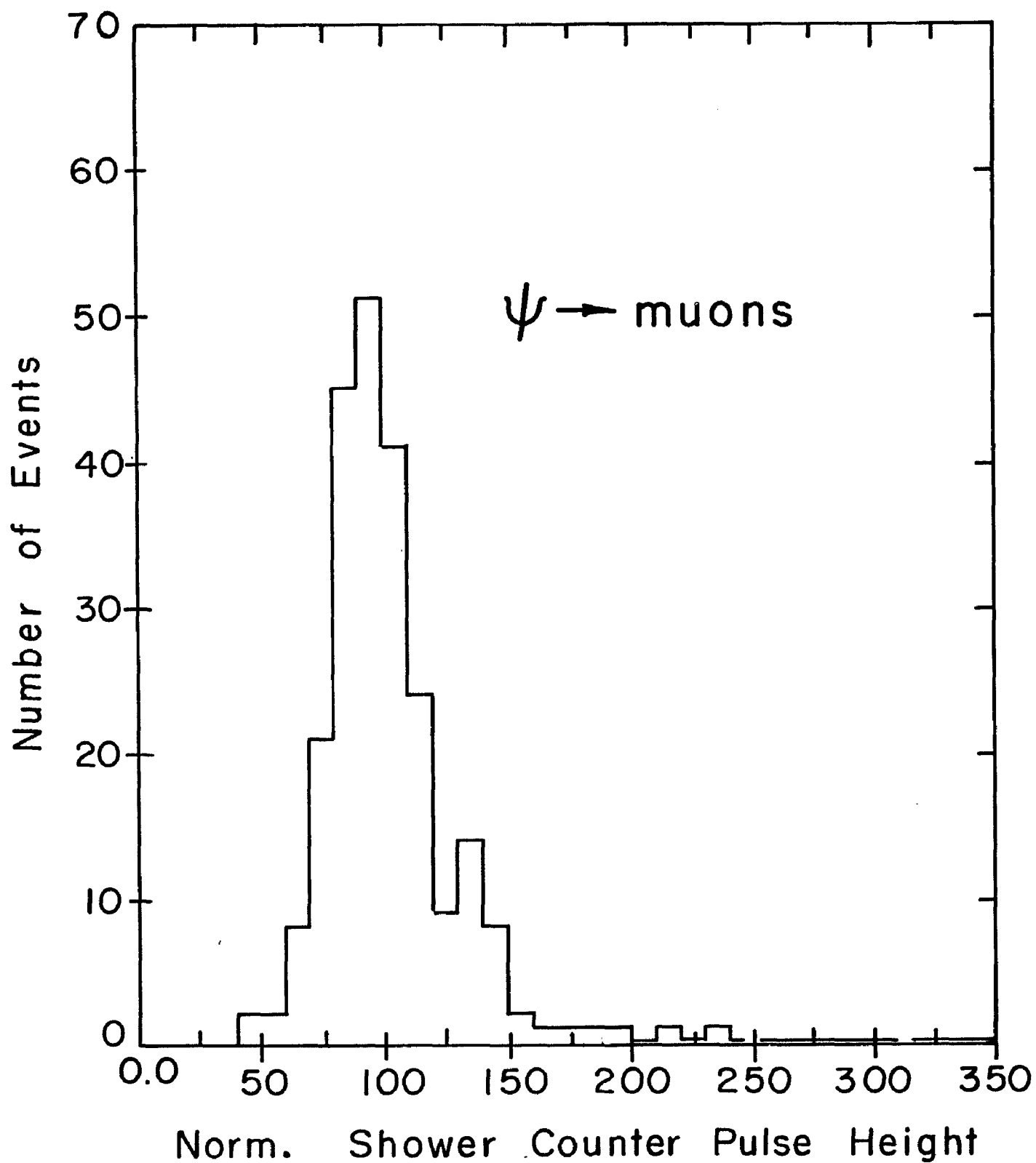


Fig. III-5 The total of the normalized shower counter amplitudes for the muon sample from the ψ decays. Note that each of the twenty-two counters was normalized to have a peak amplitude of 100 for muons. The total sum was divided by five, the number of planes in the shower counter.

2. Response of the Shower Counter

Response to Muons

Since the muons lose energy by ionization in the lead and scintillator of the shower counter, the expected energy loss distribution follows a Landau curve which is roughly Gaussian in shape. Neglecting the small effect of the angle of incidence on the counter, the individual counters were normalized to have the peak of their distributions at the same value, 100. Fig. III-5 shows the sum of the normalized amplitudes from all twenty-two shower counters arranged in five layers for muons from the ψ data sample.

Response to Electrons and Hadrons

For electrons, one expects the energy lost in the showering process to be proportional to the incident electrons energy. This energy shows up as the amplitude from the scintillators. Fig. III-6c) shows the sum of the shower counter amplitudes as a function of the electron's momentum. Note that in the absence of the electrons' radiating photons due to the material in the spectrometer, one would expect to see a momentum spectrum similar to the muons' spectrum (Fig. III-4). Even in the presence of large fluctuations, the average showering behavior seems to be independent of the measured momentum. This indicates that

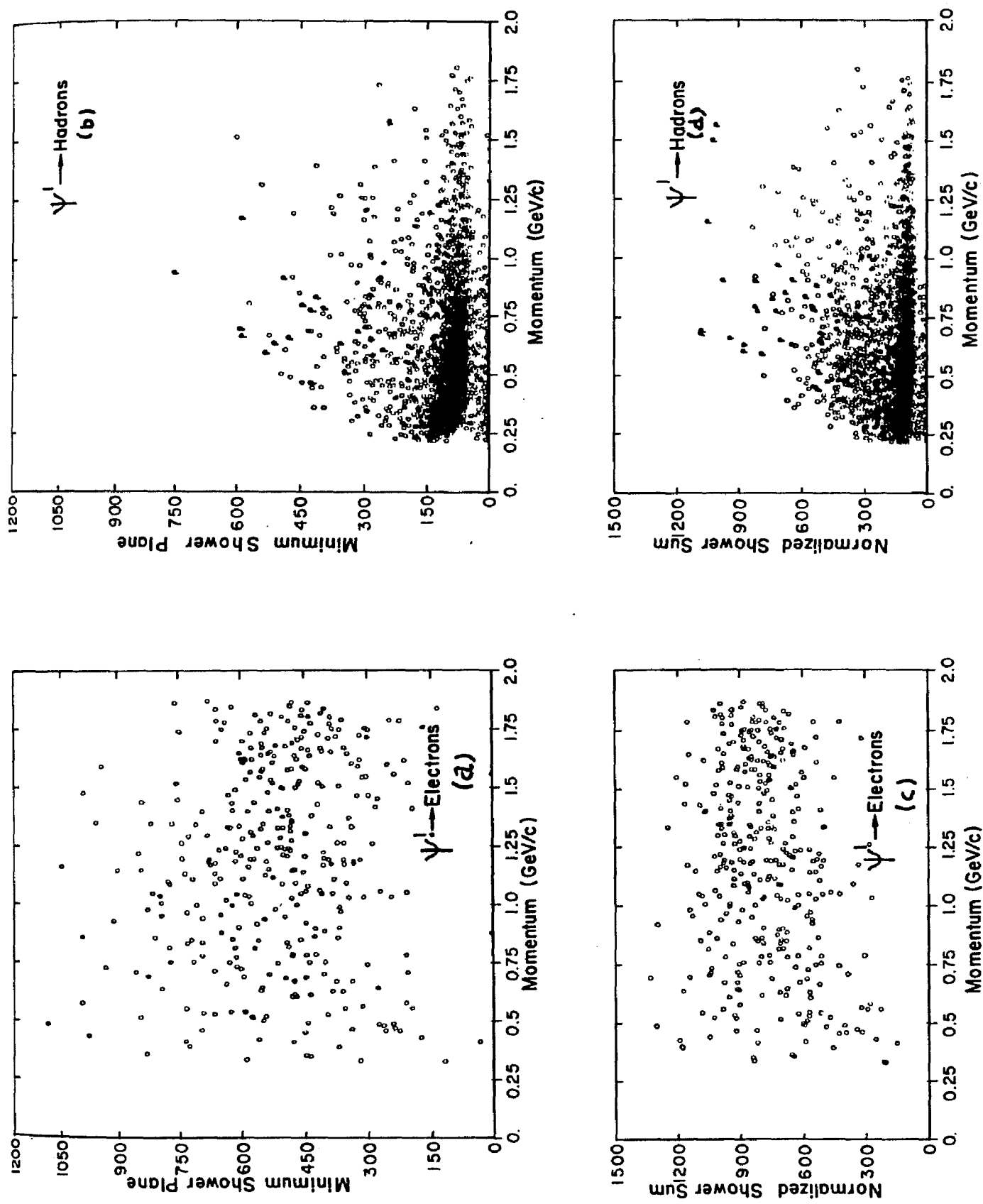


Fig. III-6 The correlation between the minimum of the amplitudes from the first three shower counter planes for the final sample of electrons(a), and hadrons(b), and the particles' momentum. The correlation between the normalized sum of the shower counter amplitudes and the momentum for the electron(c), and the hadron(d) samples. The "p" indicates events identified

the bremsstrahlung photons that cause the electrons' spectrum to be spread out in the first place, are actually caught by the counter in addition to the electron. Since the average angle between the electron and the photon it radiates is roughly $m_e c^2 / E$, where E is the incident electrons' energy, most of these photons will strike the shower counter. Thus, the shower counter measures the total energy of the emitted electron, rather than the electron's energy after passing through the spectrometer. Additionally, the average number of scintillation counters firing in the detector is 8.4 for electrons, but only 4.9 for hadrons or muons. For electrons, then, there appears to be at least two distinct showers developing, since the individual counter are much larger than the expected radial spread of a shower. The largest difference in the shower amplitude comes from the low momentum end. Here, either the high energy photon misses the counter, or these electron events are due to a gamma ray converting in the pre-magnet material or due to a beam-gas scatter.

Note that the correlation plots are derived from the final samples of electrons and hadrons. In this case, the hadron sample contains the antiprotons. Their response in the shower counter is indicated by a "P" on the correlation

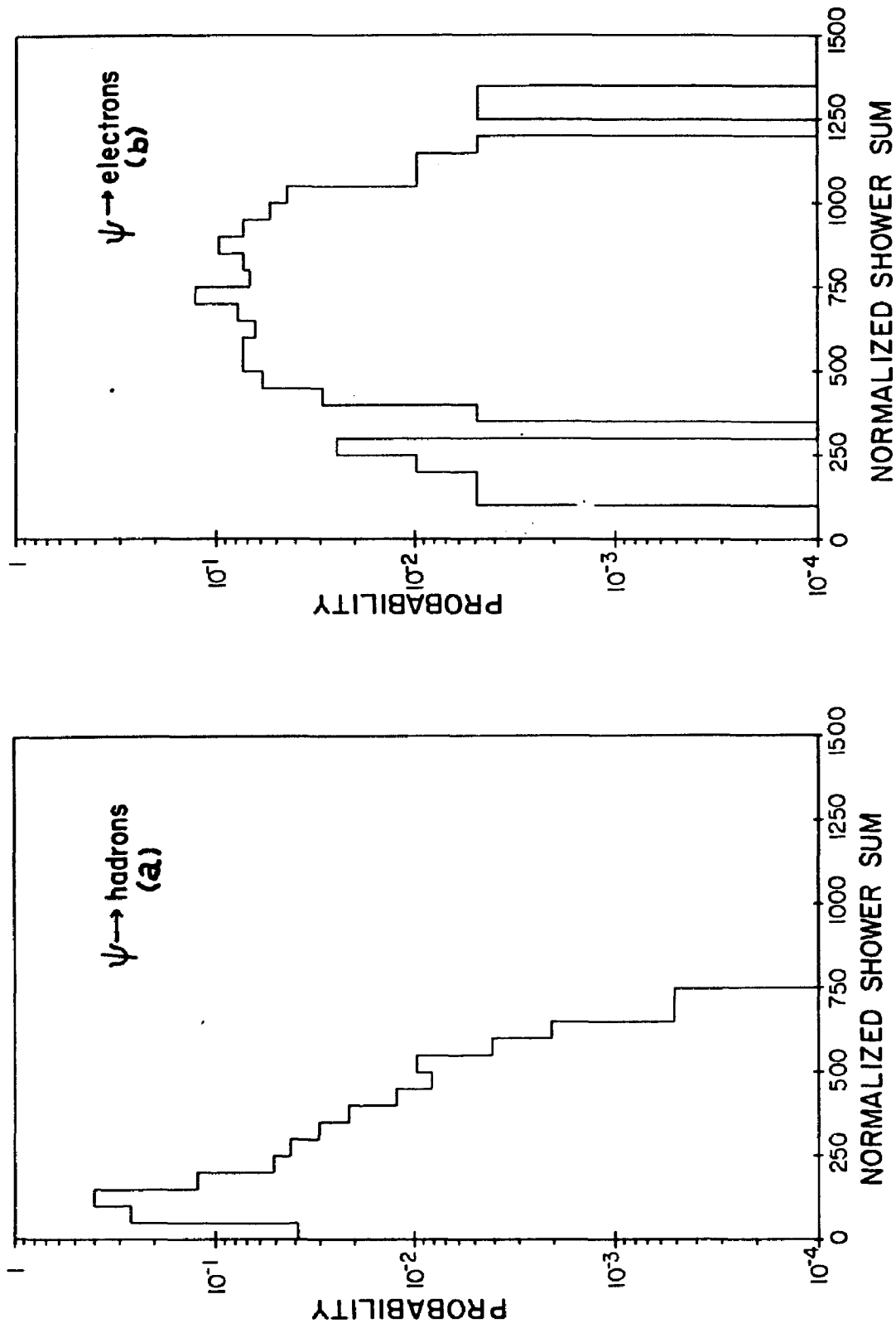


Fig. III-7 The probability distribution for the normalized shower counter sum for hadrons, (a), and electrons, (b), from the initial samples. These probability distributions come from 2000 pions and kaons, and 200 electrons.

graphs. One sees that a large fraction of the antiprotons mimic the electrons in terms of their response in the shower counter. Thus, they are removed at the start from the clean samples by their flight times to avoid a bias in the pions' and kaons' response when compared with the electrons' response.

In Fig. III-7, the probability distributions of the shower counter amplitude are shown for the clean samples of electrons and hadrons. Note that distribution for the hadrons comes from about 2000 events, while the distribution for the electrons contains nearly 200 events.

Another quantity of interest is the minimum amplitude from the first three layers. This is also relatively independent of the electron's momentum, as Fig. III-6a) shows. The probability distribution for this quantity is shown in Fig. III-8 for the clean electron and hadron samples. This quantity shows some correlation with the sum of the shower counter amplitudes, which can be seen in Fig. III-9. In comparison with the hadrons, a clear region of separation is evident. Rather than use the probability function for the total shower amplitude and the minimum separately, the fact that they are correlated leads one to use the quantity produced by projecting the minimum and the

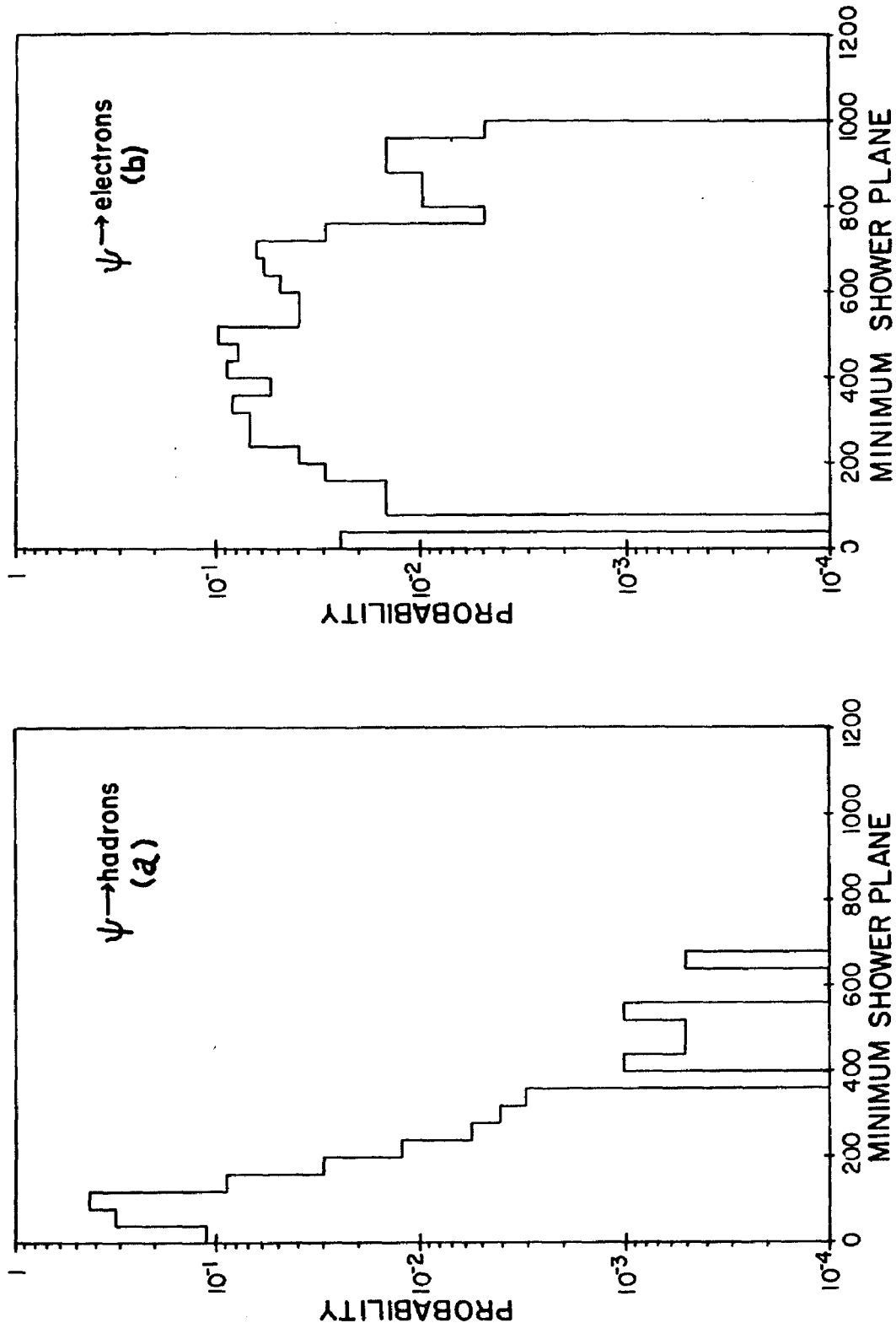


Fig. III-8 The probability distribution for the minimum of the amplitude from the first three shower counter layers for the initial sample of hadrons, (a), and electrons, (b).

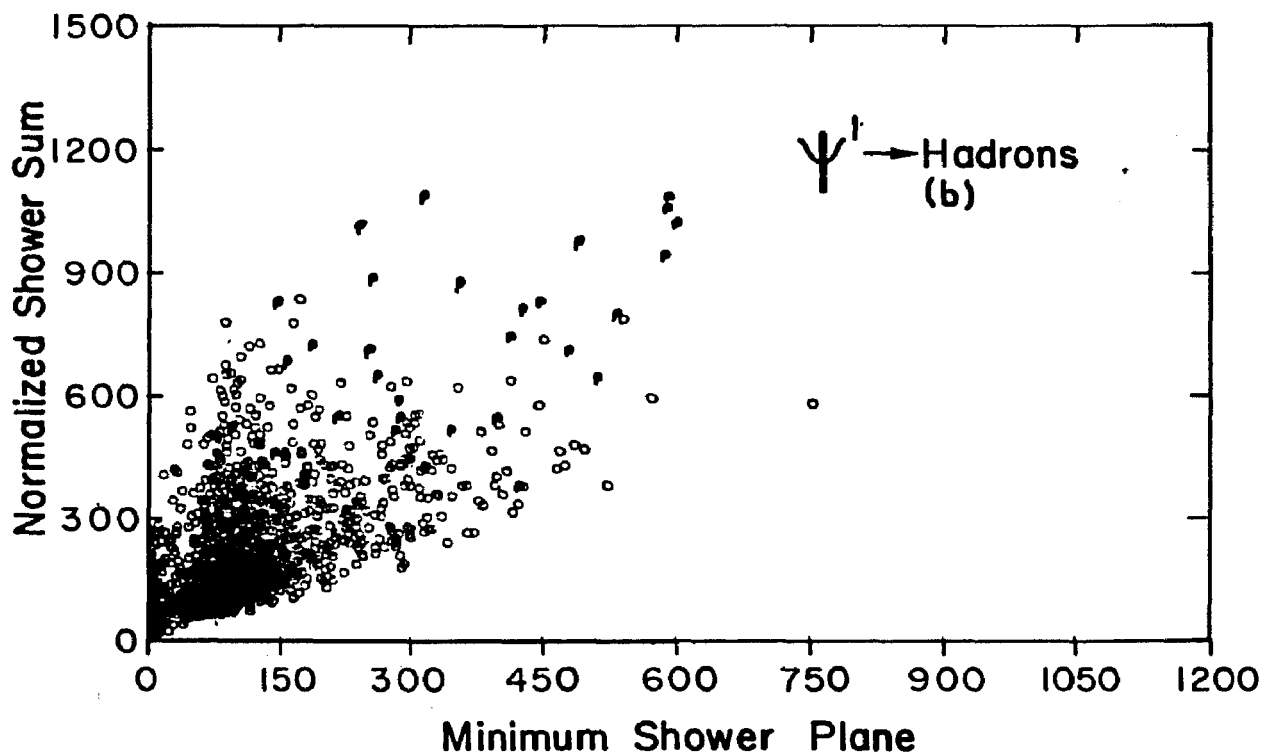
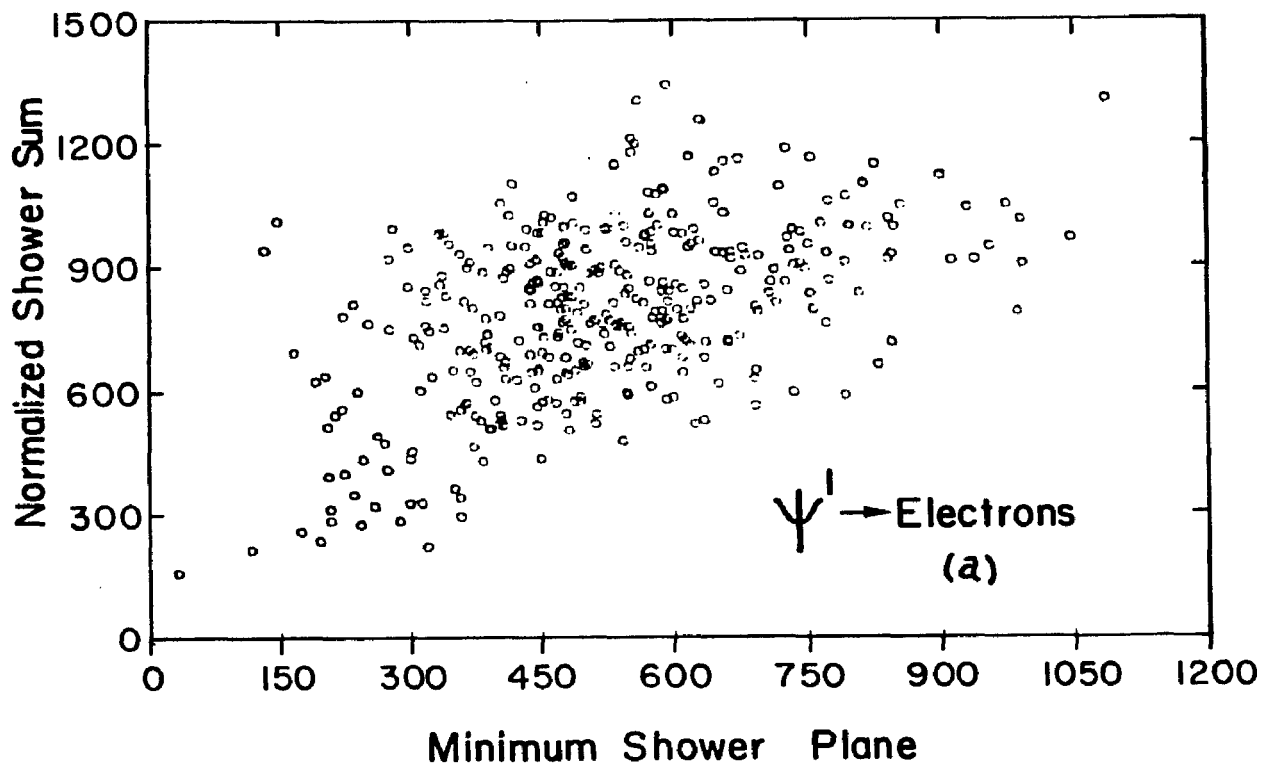


Fig. III-9 The correlation between the normalized shower counter sum and the minimum amplitude from the first three layers for the final electron, (a), and hadron, (b), samples.

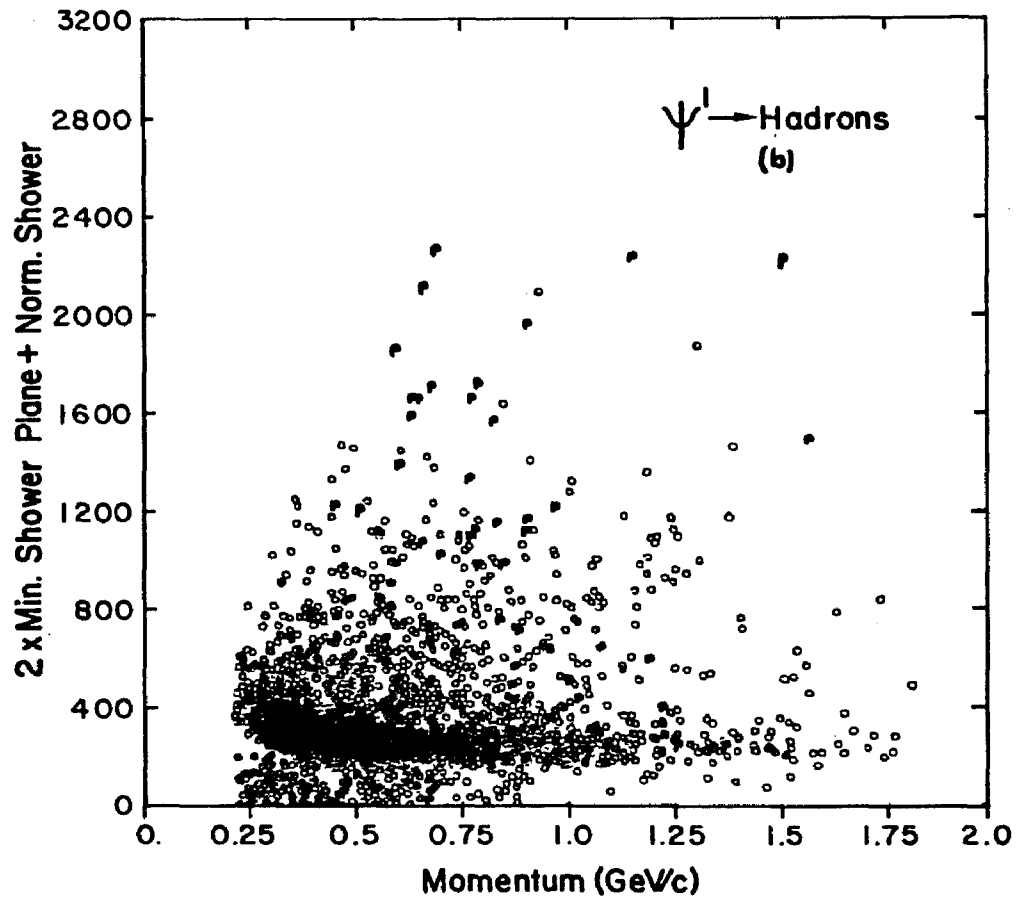
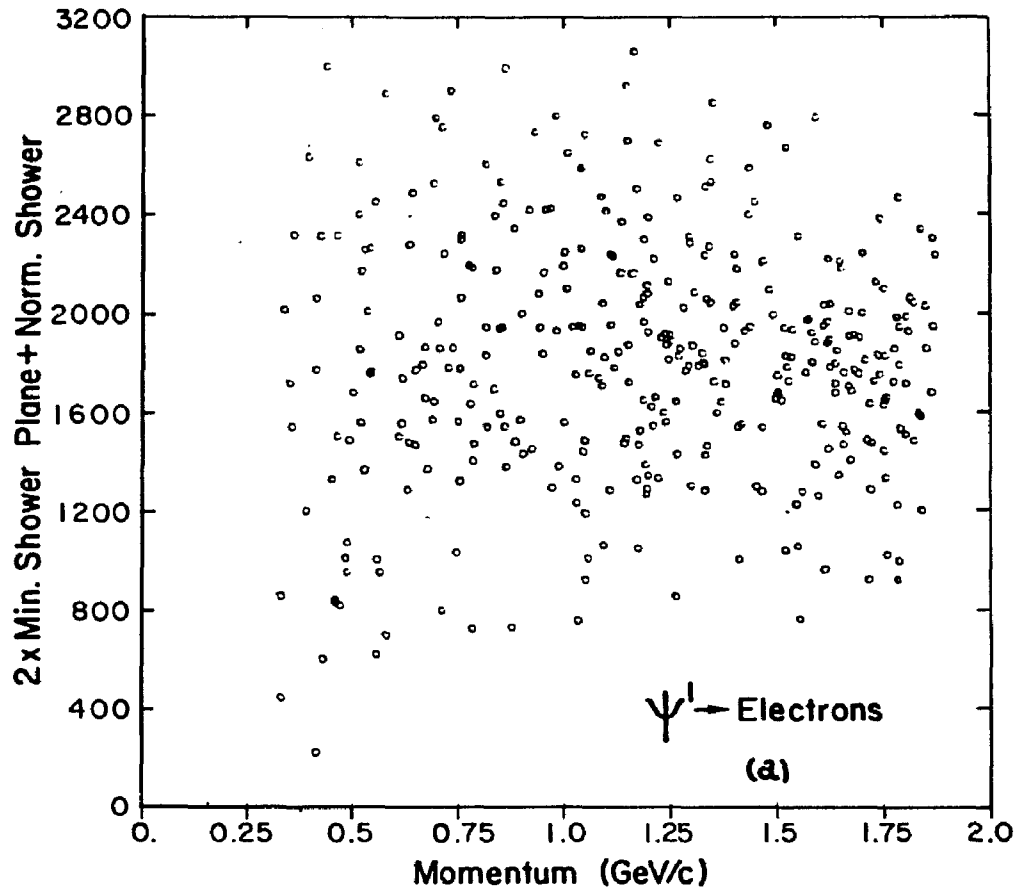


Fig. III-10 The correlation between the quantity, M , defined in the text and the momentum for the final electron, (a), and hadron, (b), samples from the ψ^1 data set.

shower amplitude onto a line passing along the axis of correlation. This is equivalent to defining a new quantity M , which in our units is:

$$M(A_m, A_T) = 2 A_m + A_T$$

where A_m is the minimum of the first three shower layers and A_T is the normalized total amplitude.

In Fig. III-10, the momentum dependence of M is displayed. Again, this quantity does not appear to be very momentum dependent, which may be attributed to the momentum independence of the quantities generating M . One can generate a simple probability function from it. Fig. III-11 shows the resulting probability distribution for this quantity for the clean electron and hadron samples from the ψ data.

Yet another interesting quantity is the RMS deviation of the shower counters layers from the average amplitude. This is defined as:

$$\sigma^2 = \frac{1}{5} \sum_i (A_i - \langle A \rangle)^2$$

where A_i is the amplitude from the i -th layer, and $\langle A \rangle$ is the average. As in the previous case, this quantity is also correlated with the total shower amplitude, as Fig. III-12

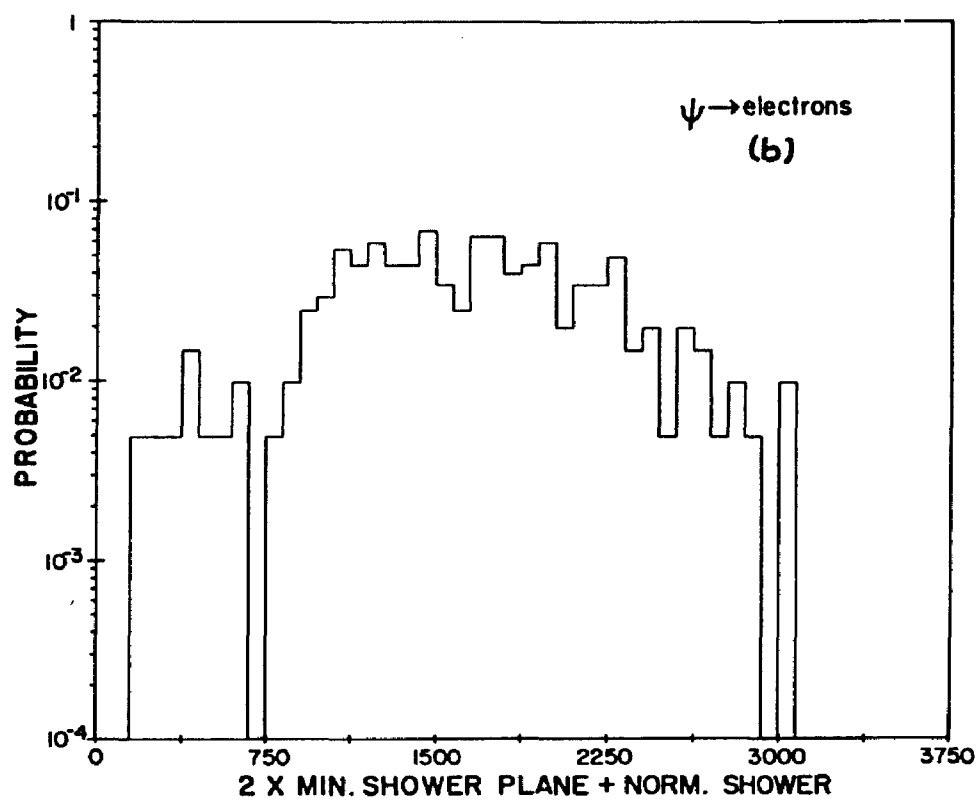
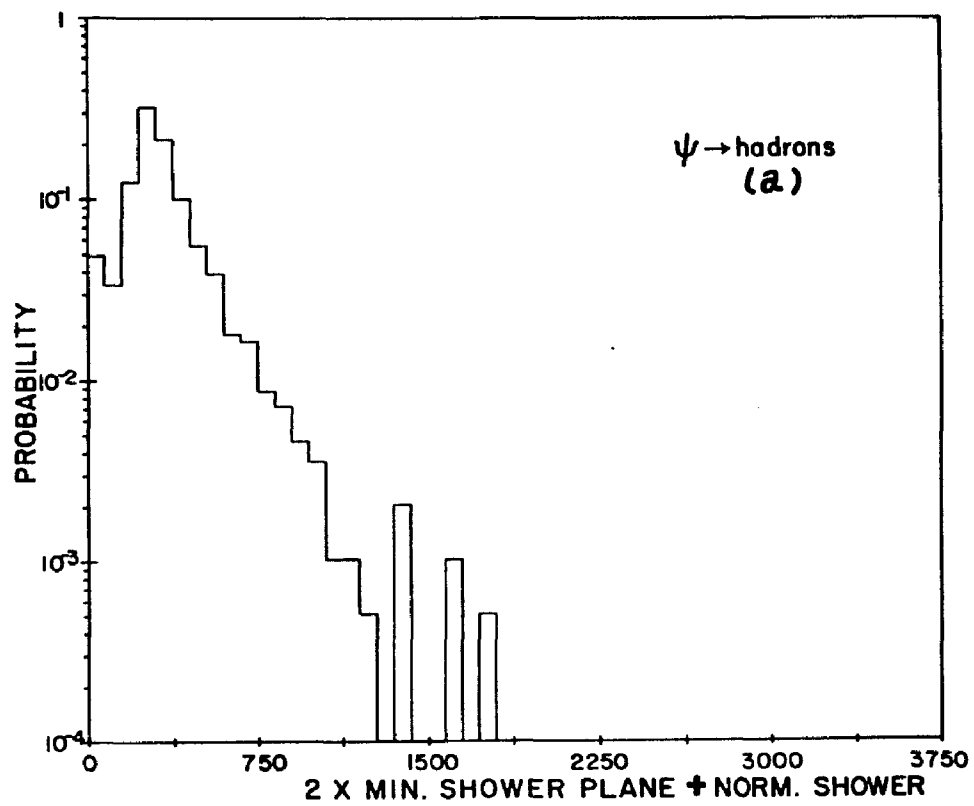


Fig. III-11 The probability distribution for the quantity, M , for the initial hadron, (a), and electron, (b) samples.

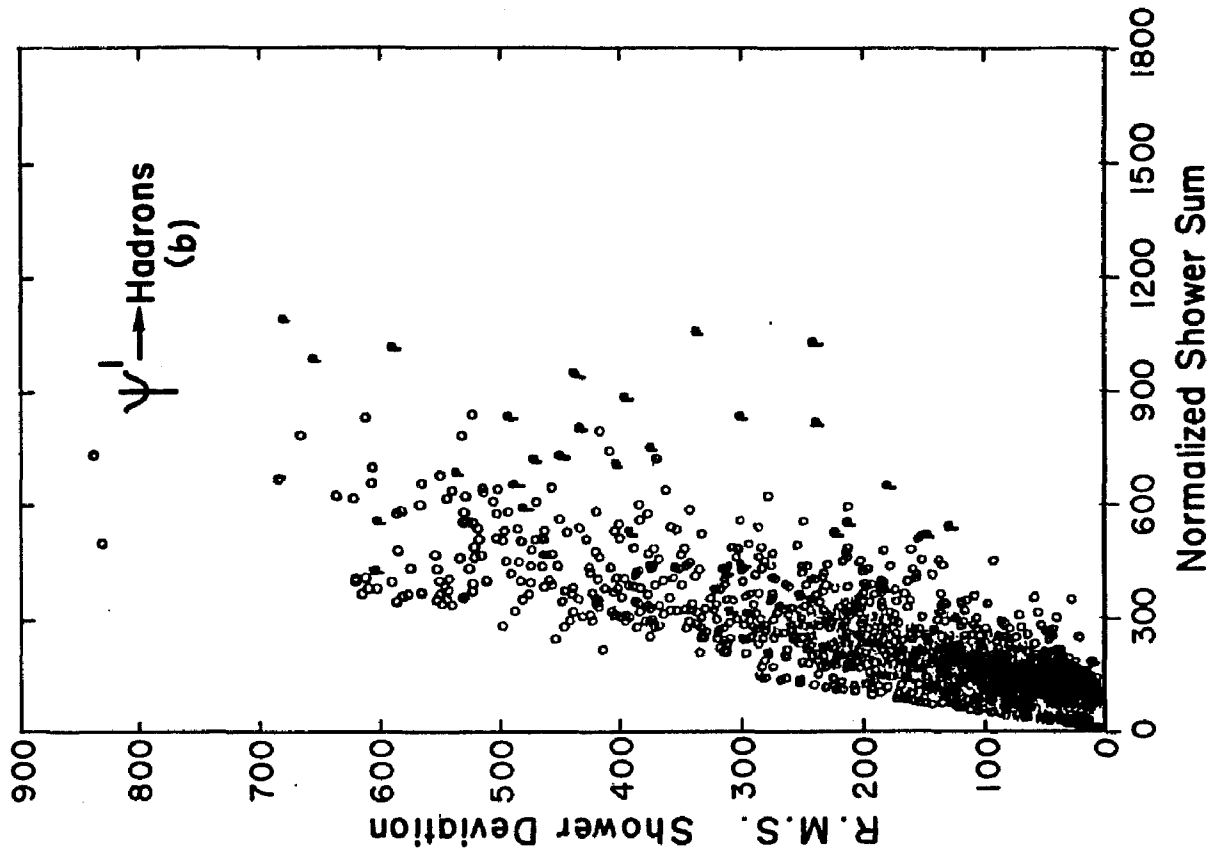
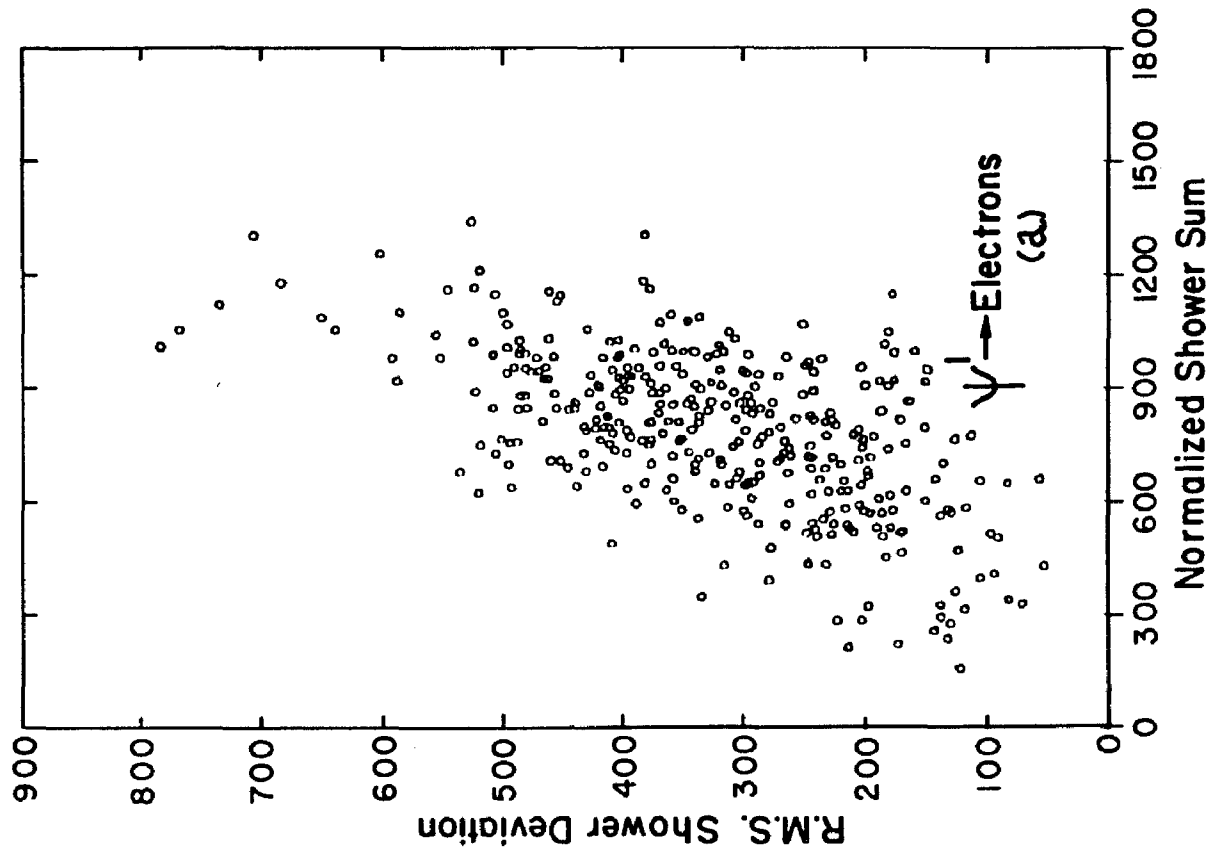


Fig. III-12 The correlation between the rms deviation of the shower planes and the total shower counter sum for electrons, (a), and hadrons, (b)

indicates. Vis-à-vis the hadron data, a clear separation between the two distributions is visible. This difference is best seen by projecting the data onto a line perpendicular to the distributions' axes. This is equivalent to producing the quantity S , defined in our units as:

$$S(\sigma, A_T) = 2 A_T - \sigma$$

This quantity is nearly independent of momentum as Fig. III-13 shows. In Fig. III-14, the resultant probability functions for the clean electron and hadron samples are shown.

3. Response of the Conjugate Side NaI Array

In Fig. III-15, the energy deposited in the array of sodium iodide is shown for the clean sample, with the dashed histogram showing the distribution for the final sample. Notice that the resolution for electrons is roughly 20%. The spectrum associated with hadrons peaks at very low energies since there is a small probability that a particle enters the NaI when one triggers the spectrometer, and when one does, it loses about 120 MeV of energy due to ionization.

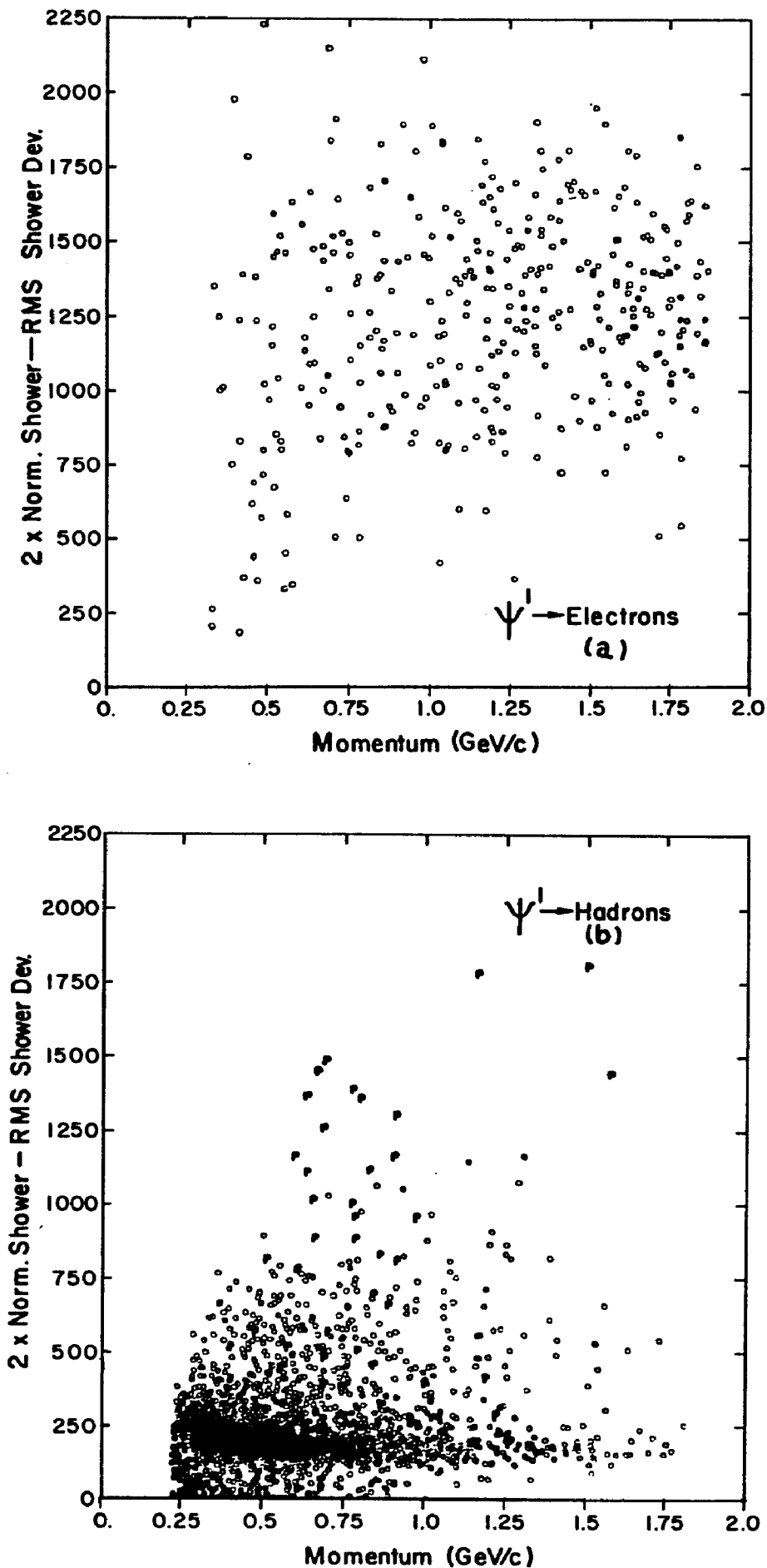


Fig. III-13 The correlation between the quantity, S , defined in the text, and the particle's momentum for the final electron, (a), and hadron, (b), samples.

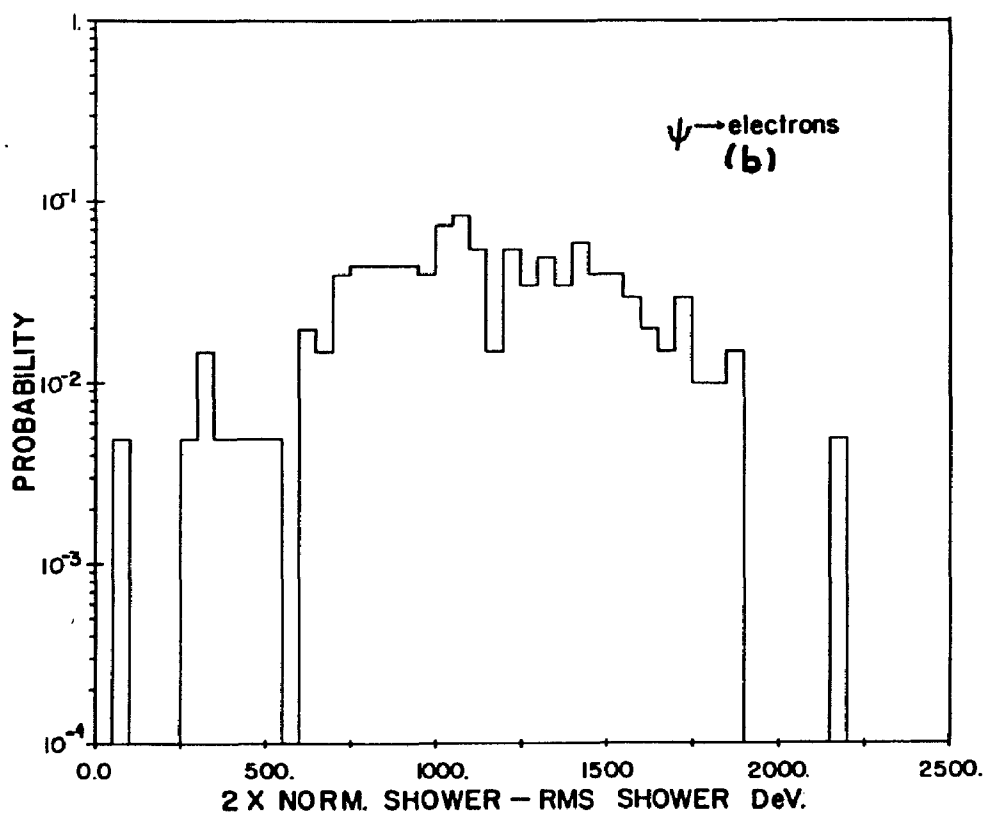
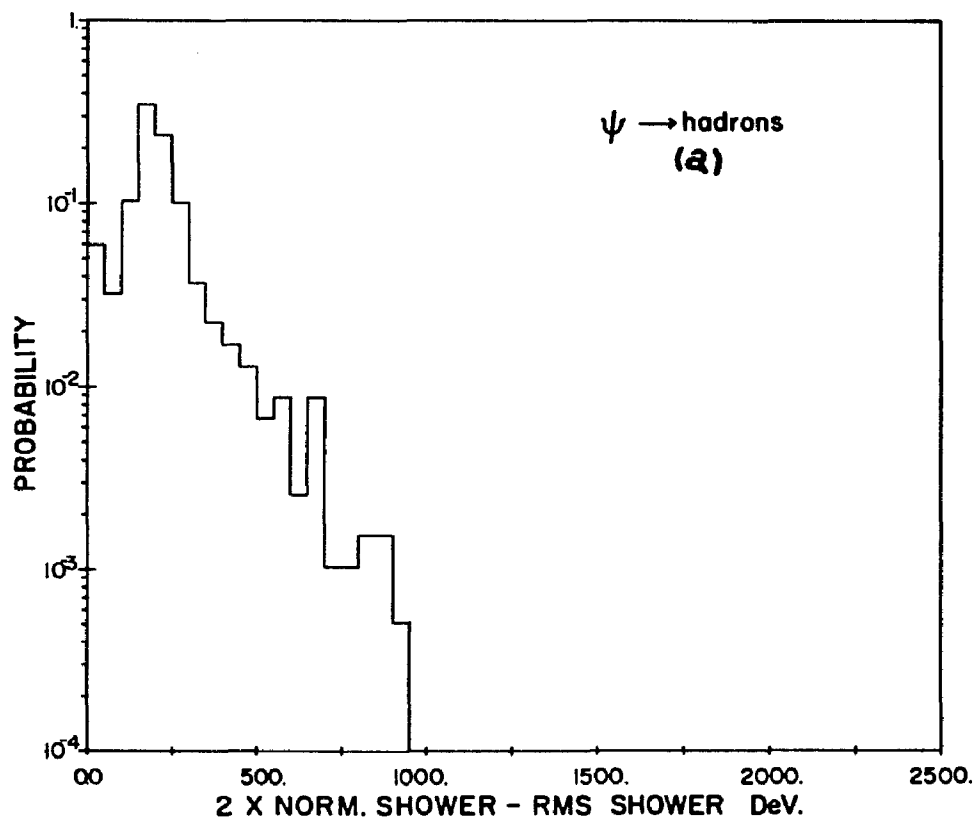


Fig. III-14 The probability distribution for the quantity, S , for the initial hadron, (a), and electron, (b), samples.

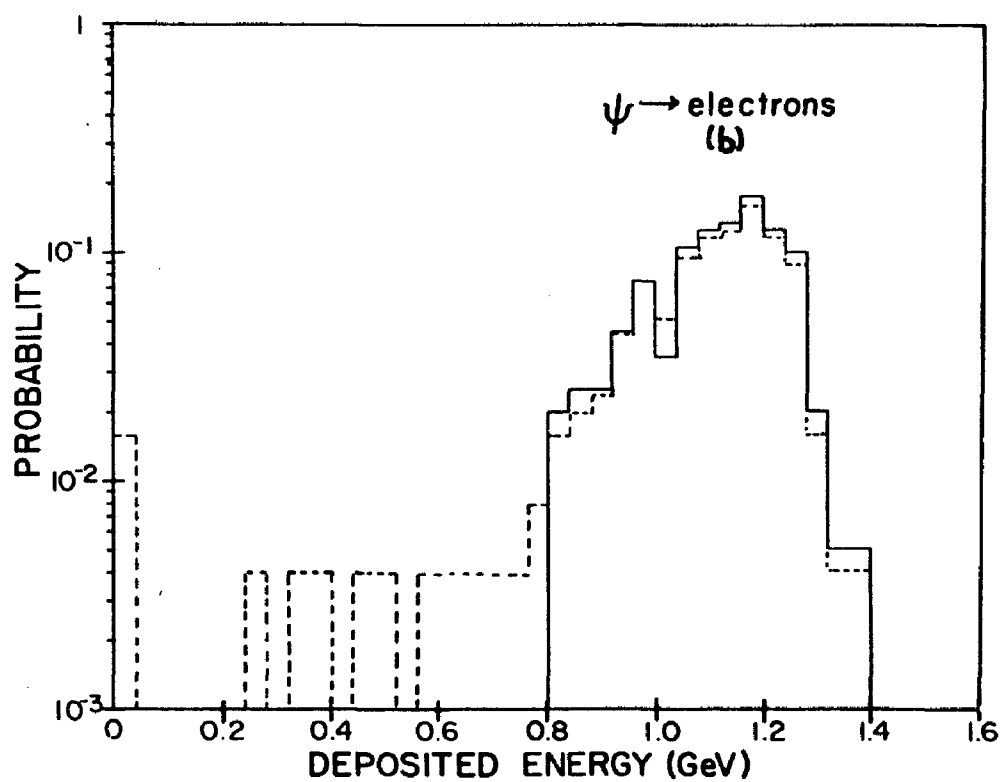
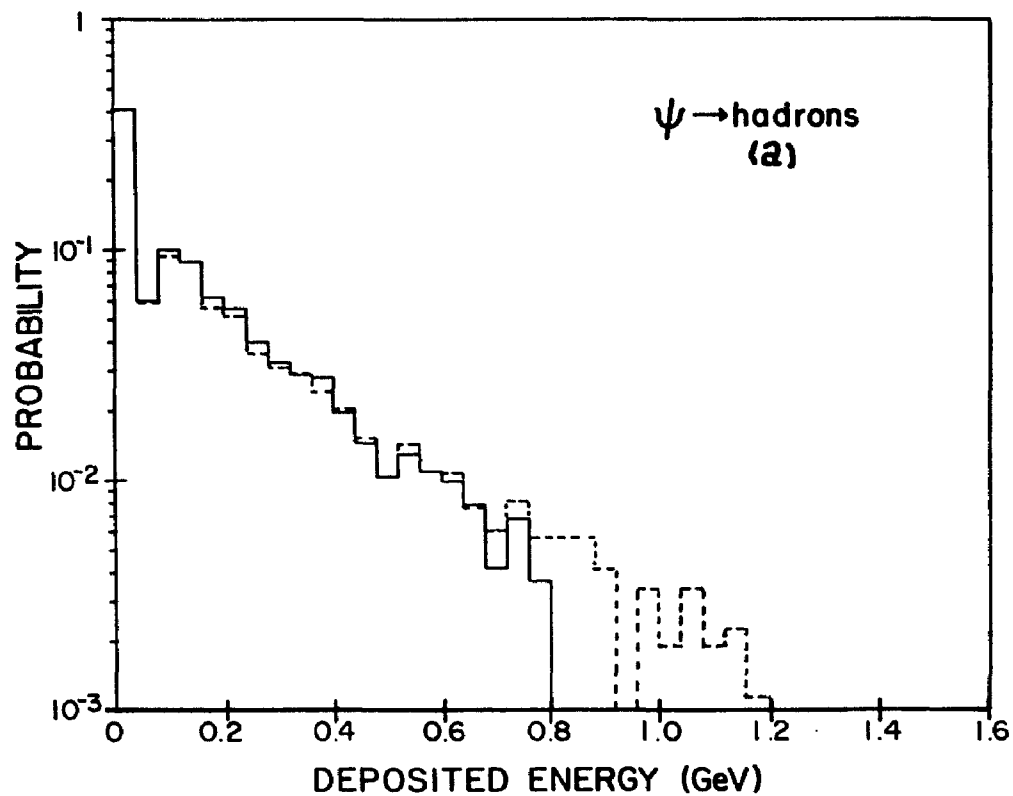


Fig. III-15 The probability distribution for the energy deposited in the conjugate side sodium iodide array for the initial (solid line) and final (dashed line) samples of hadrons, (a), and electrons, (b).

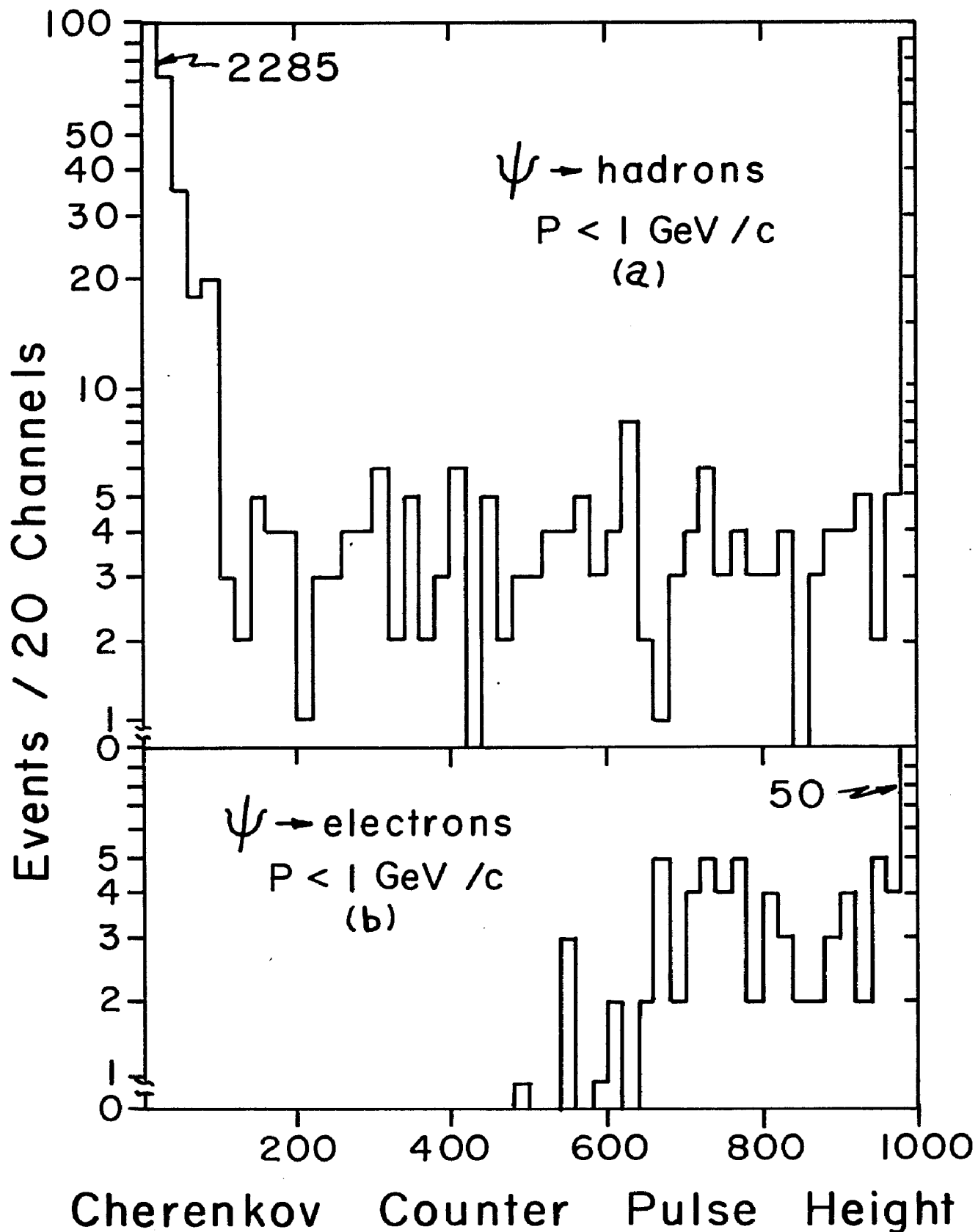


Fig. III-16 The distribution of Cherenkov counter amplitudes for the final sample of hadrons, (a) and electrons, (b), that have a momentum less than 1.0 GeV/c.

4. Response of the Cherenkov Counter

Fig. III-16 shows the response of the Cherenkov counter to the final sample of electrons and hadrons that have a momentum less than 1.0 GeV/c.

Notice that the velocity of all hadrons in this sample are below the Cherenkov radiation limit, but about 14% of them have signals which indicate the contrary. There are a number of possible effects that can give rise to spurious signals. One of the dominant mechanisms for producing the spurious pulse appears to come from converted gamma rays produced in the annihilation reaction along with the hadron. Since the active area of the Cherenkov counter subtends 0.33 ster. (Ω), the probability that a gamma enters the counter is then:

$$P(\gamma \text{ in C} \mid n \gamma\text{'s produced}) = \frac{n \Omega}{4 \pi} = 0.16$$

where the final value comes from assuming 6 gamma rays are produced, on the average.

Next, the probability that these photons can convert depends, of course, on the amount of material they transverse. In calculating the amount of interspersed material, contributions used come from:

- 1) The beam pipe. This has a wall thickness of 1.65 mm

of stainless steel, and contributes .097 r.l.

2) The polymer. Since this device is constructed of square aluminum tubes, the gamma ray can pass through the interior of each tube, or through the side walls. The walls are 0.71 mm thick by 12.5 mm long. Averaging over the solid angle of the Cherenkov counter, the polymer contributes 0.04 r.l.

3) The tracking chambers have two contributions; one from the interior and one from the frames. The interior, for each of the six chambers, contributes only 0.015 r.l., but the frames contain 0.1 r.l., mainly aluminum and G-10 (a fiberglass-epoxy material). Weighing these values by the fraction of the Cherenkov counter's solid angle they subtend, results in about 0.025 r.l.

4) The Cherenkov counter itself. From the aluminum surface and the propane filling, it is estimated that a gamma ray might pass through 0.14 r.l.

The total contribution is then 0.30 r.l. With the assumptions of the gamma ray multiplicity and directions that are independent of the hadron's direction, it is estimated that 6% of the hadrons should be accompanied by a above-threshold Cherenkov signal due to converted gamma

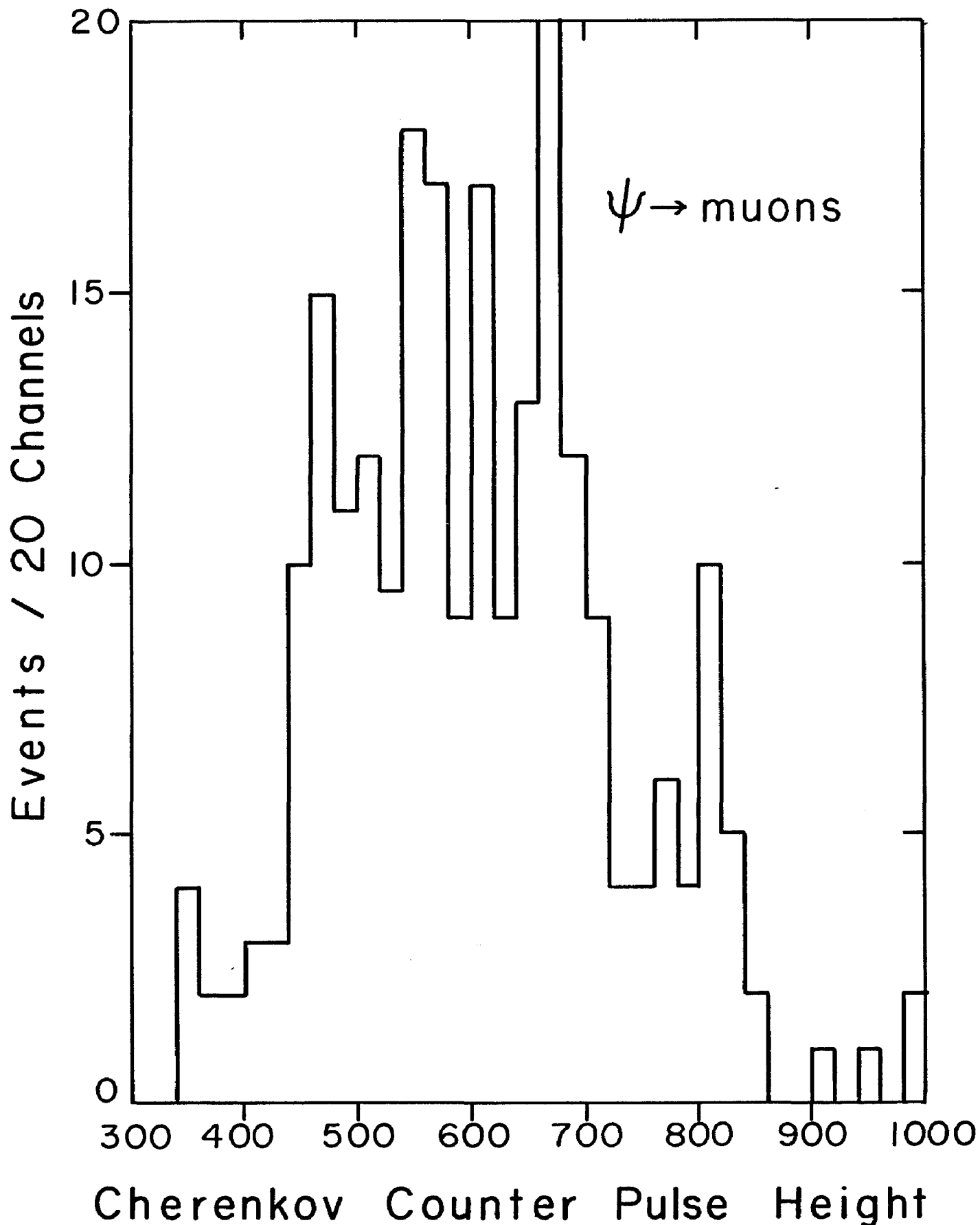


Fig. III-17 The Cherenkov counter amplitude distribution for the final sample of muons. Note that the distribution is centered at an amplitude of 575, with a rms spread of 119.

rays. Note that this is the contribution from gamma rays that enter the active solid angle of the Cherenkov counter. If one includes gammas that enter some other region of the solid angle, convert there, and then the electrons scatter into the Cherenkov counters active region, this contribution is then about 3%. Thus we can account for the observed contamination of the low momentum hadrons.

The Cherenkov counter's response to the muons from the γ data is shown in Fig. III-17. The spread of 21% comes from the fluctuations of the photoelectron statistics and the scatter in the operating characteristics of the phototubes.

5. Response of the Range Counter

Since this counter was used in the separation of muons from hadrons using a priori response functions, it is necessary to confirm these responses with the data. Using a sample of events which pass all the test of the clean hadron sample(see Section III-A-6), except for the cut on the hadron filter, the penetration probability of hadrons into this device can be measured. The probability for a particle to penetrate the filter depends on: a) The total amount of material in its path; this includes the incident angle; b)

the range of the particle, which is subsequently affected by the material and the particle's momentum, with the uncertainty in this quantity coming from straggling; c) the probability of nuclear interactions. This last case has a double-sided aspect since the secondary particles can be quickly absorbed if they are charged, or can penetrate even farther than the incident hadron, if they are neutral. This nuclear interaction probability, of course, depends on the material and the particle's momentum as well as its type and charge, and is modulated by the range probability for the incident hadron.

There are two ways to obtain the penetration probability for hadrons, one is to experimentally measure this probability with clearly identified particle types, and the other is to use a simulation program, using information about the apparatus and the reactions involved. The data from Sander⁴ on the penetration of pions and protons in iron appears to be reliable and is used in determining the penetration probability for our range counter. A simulation code HETC⁵ was prepared for this range counter and the results are in good agreement with Sander's data.

In testing the range counter, the sample of hadrons defined above was used. The various species were

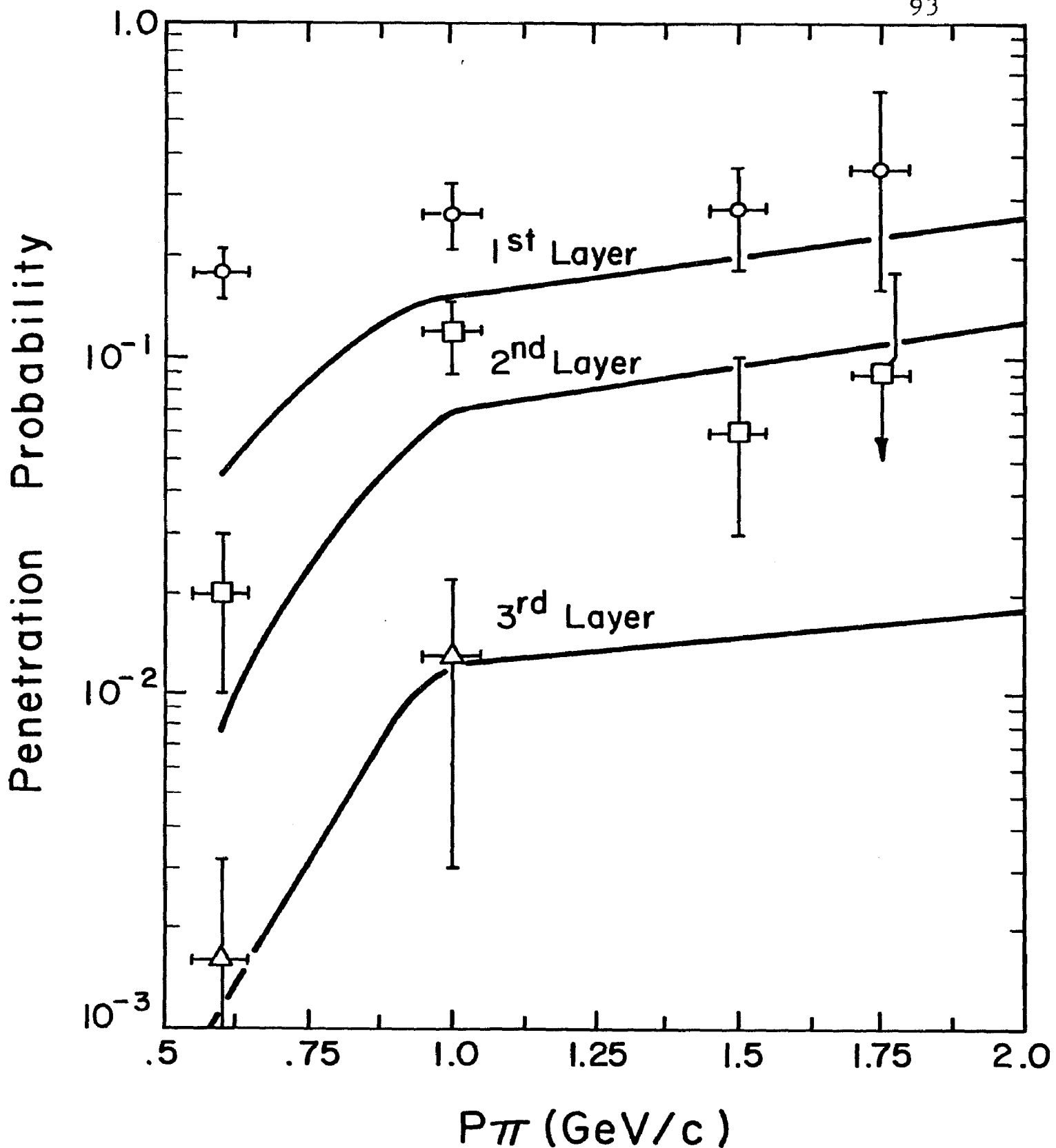


Fig. III-18 The penetration probability of pions into the range counter, as a function of momentum. The solid lines are extrapolations from the data of Sander, while the symbols, O, \square , and Δ correspond to measured penetration in the first, second, and third layers, respectively. For comparison, Fig. II-3 shows the penetration probability for muons.

identified (see Section III-C-3) and only pions were used since: a) kaons and protons represent only 10% of the total sample; b) K^+ and p, p have greater ionizational losses, and are therefore more limited in range; and c) the muons from K^+ decays in flight make a determination of the K^+ penetration probability very uncertain.

The number of pions observed to penetrate the various layers was corrected for the number of muons expected from decays in flight, which could penetrate the counter⁶. In Fig. III-18, the resulting penetration probabilities are compared with those of Sander's, interpolated to the thicknesses of iron in our range counter. The agreement is good for the highest momentum values and for the greater thicknesses of iron. One concludes that all the events that do not have the $\mu\mu$ signature probably result from either hadronic penetration or muons from decays. In particular, there is no evidence for an anomalous source of muons that is seen at higher center-of-mass energies⁷.

6. Response of the Time-of-Flight (TOF) System

Since the time-of-flight (TOF) system is used to separate the various hadronic species, it is desirable to have a clearly identified sample of the pions, kaons and

protons which can then determine the system's response. However, the TOF system is the only means of separating the hadrons with momentum below 1.1 GeV/c, the pion's Cherenkov radiation threshold. The separation properties of the TOF system dwindle rapidly as the momentum increases above this threshold, at least for the kaon-pion separation. In order to circumvent this problem, the system was normalized to the muons, since they represented a clearly identified sample with good statistics.

The time interval between the start and stop signals as recorded by the time-to-digital converters (TDC) was corrected for the position where the particle struck the counter, the amplitude of the signal as recorded in the ADC's, and the drifts in the TDC's themselves. The TDC channel-to-real time calibration was determined from test data recorded periodically among actual data. This test data contained the TDC values for two, fixed-interval, start-stop signal sequences.

In Fig. III-19, the observed flight time with the expected flight time subtracted from it is shown for the ψ muon data. This histogram was fitted with a Gaussian curve to measure the resolution. The width, σ , of the curve is 0.27 ± 0.02 ns, with a fit resulting in a χ^2 of 13.1 for 21

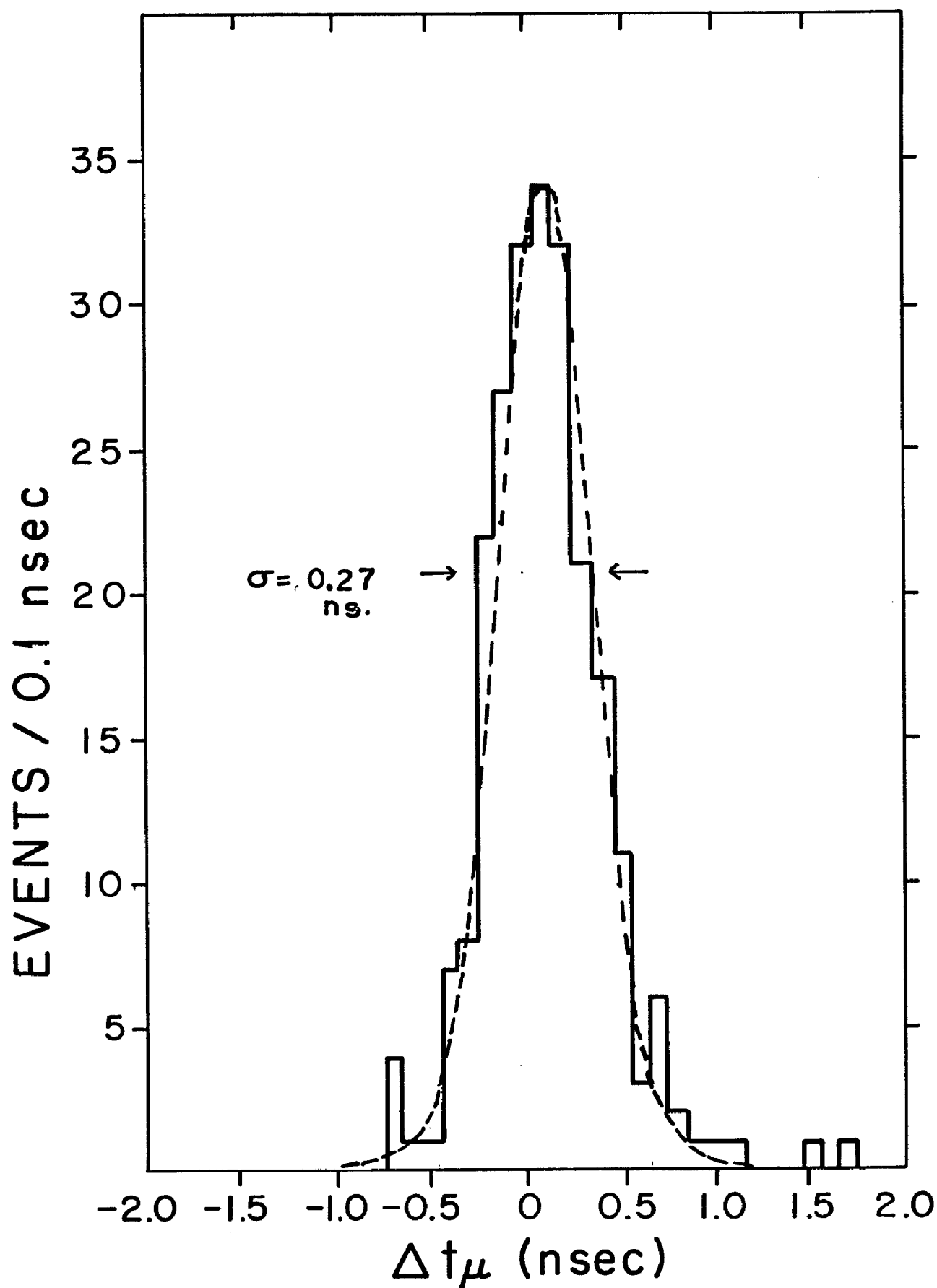


Fig. III-19 The quantity Δt for muons. This quantity is the difference between the expected and measured flight times. The dashed line is the Gaussian fit to the distribution, with a σ of $0.27 \pm .02$ ns.

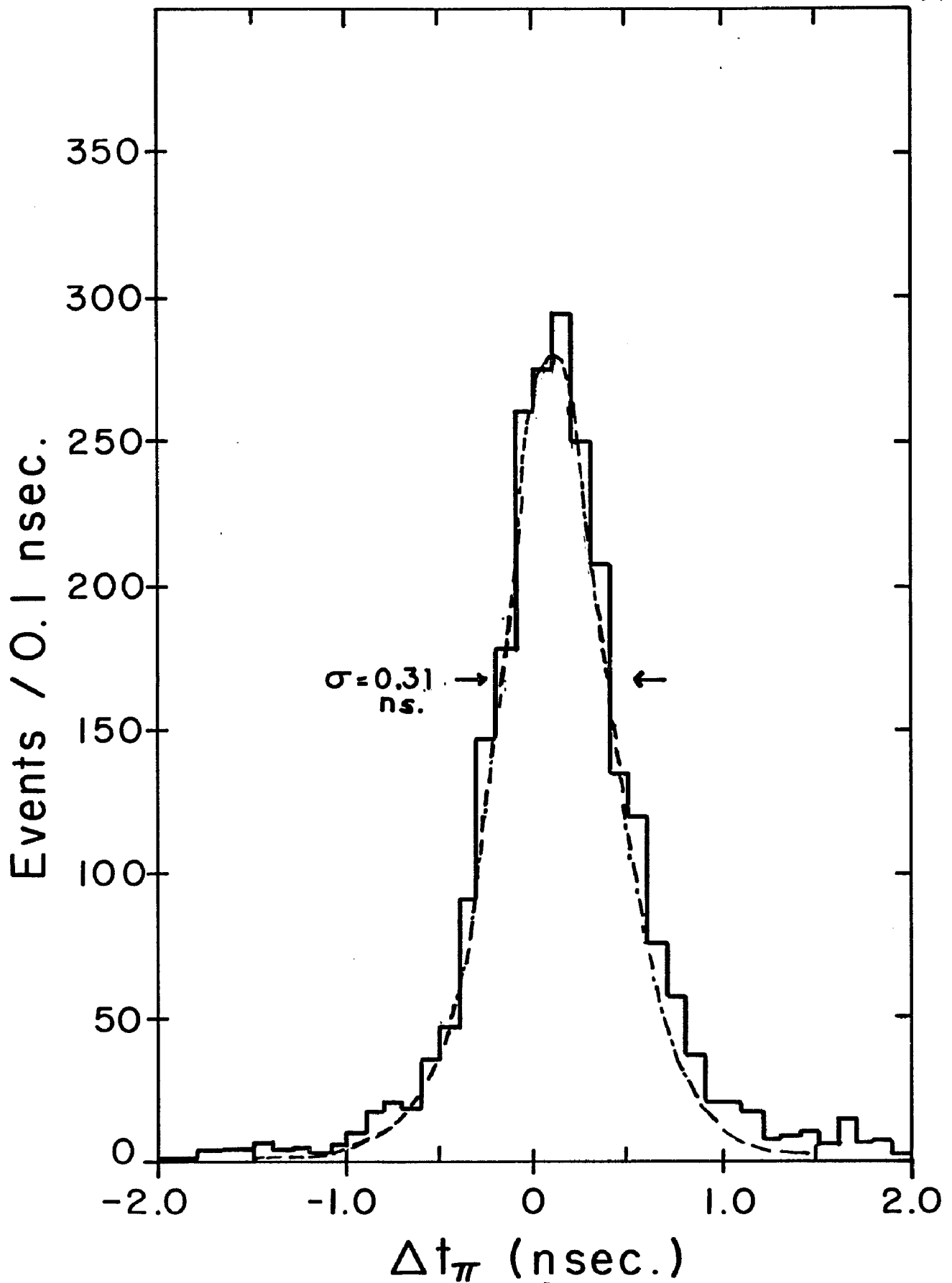


Fig. III-20 The difference between the expected and measured flight time for pions. The broken line is a Gaussian fit to the distribution with a σ of $0.31 \pm .02$ ns. The pion sample comes from the ψ' data set. Events in this sample have a momentum ≤ 1.0 GeV/c.

degrees of freedom. The resolution of this system can also be measured with the hadrons. In Fig. III-20, the difference in time between the observed and expected flight time for pions is displayed. The events selected all have a momentum less than 1.0 GeV/c. The width of this curve, when fit to a Gaussian was 0.31 ± 0.02 ns with a χ^2 of 30.3 for 23 degrees of freedom. The fact that this curve is wider than the same curve for the muons appears to be due to the differences in momentum resolution. The contribution to the uncertainty in the flight time arising from the uncertainty in the momentum measurement is;

$$\Delta t = \frac{l \cdot \Delta p}{c \cdot p} (1 - \beta^2) / \beta,$$

with l being the pathlength, c the velocity of light, and β is the particle's relative velocity. The value, $\Delta p/p$ is given in Section III-A-5. The quantity, β , of course, is l/ct , where t is the flight time.

In Fig. III-21, the value of β is shown as a function of the momentum of the hadron. One clearly sees the division between the various particle types, at least at momentum less than about 1.2 GeV/c. The three solid lines indicate the expected values for pions, kaons and protons, respectively. The "X" symbols indicate those hadrons that

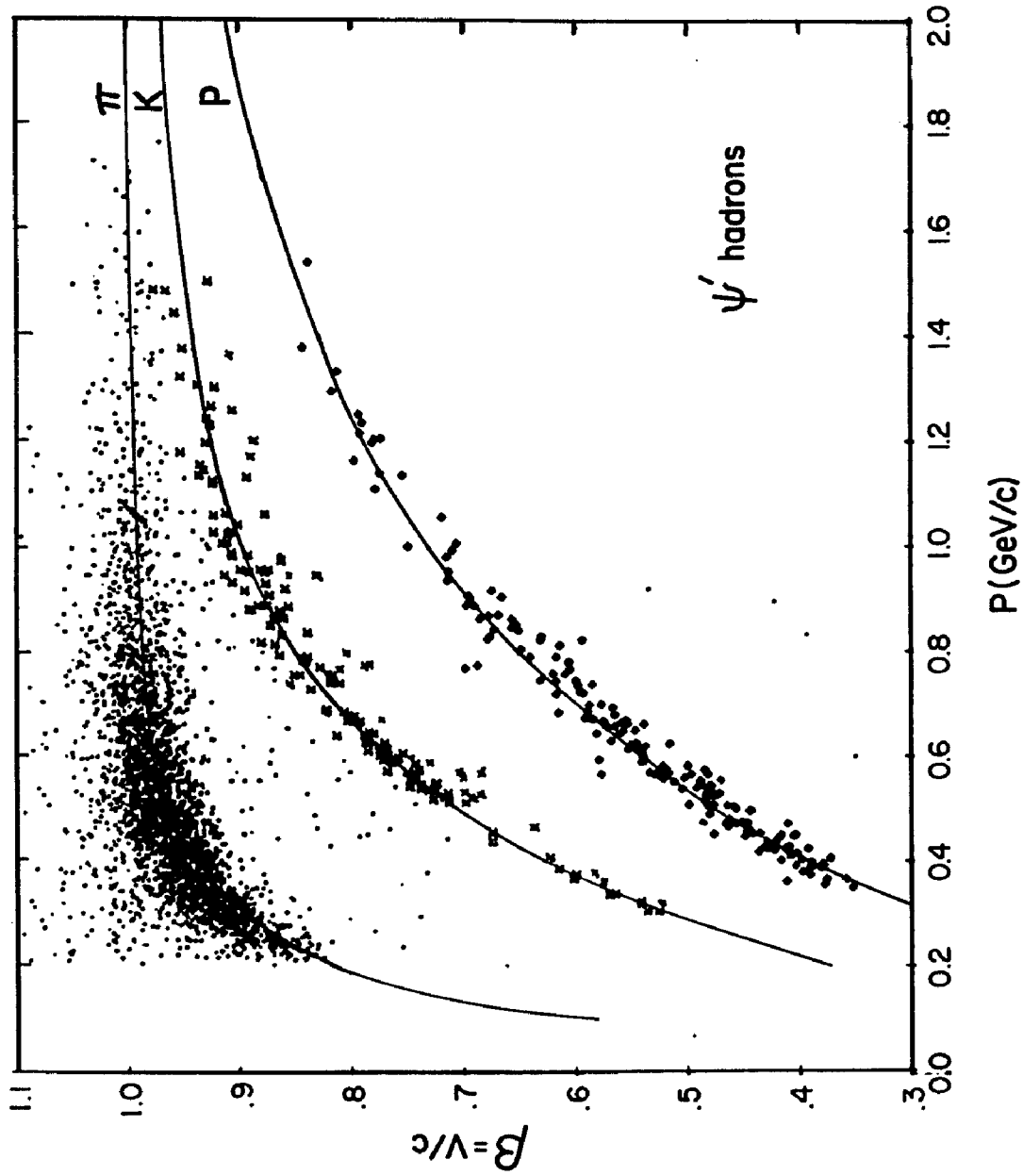


Fig. III-21 The distribution of the relative velocity, β , for hadrons from the ψ' data set. The symbol, x , indicates those events that are within 2σ of the kaons' expected flight time, while the symbol, \blacklozenge , indicates events within 2σ of the protons' flight time.

had a flight time within $\pm 2\sigma$ of that for K^+ , while the "<>" indicates the same thing, but for protons.

Another way of observing the TOF system's characteristics is to reconstruct the mass of the particle using the expression:

$$M_h^2 = p_h^2 (1/\beta^2 - 1)$$

where p_h is the hadrons's momentum and β is its velocity. In Fig. III-22, the mass squared is shown for the hadrons in various momentum ranges. Only those hadrons with mass² less than 0.5 GeV^2 are shown for the sake of clarity. There are two clear peaks, centered at the mass of the pion and kaon, respectively. The peaks begin to overlap substantially above $1.0 \text{ GeV}/c$.

The separation of the hadronic species is discussed further in Section III-C-3.

C. Separation of Electrons, Muons, and Hadrons

1. Identification of Muons

Since the directly produced muons are easily identified, at least those with momentum above $1.1 \text{ GeV}/c$, one notes that the tests placed on the clean sample are nearly sufficient to separate all the muons from the data

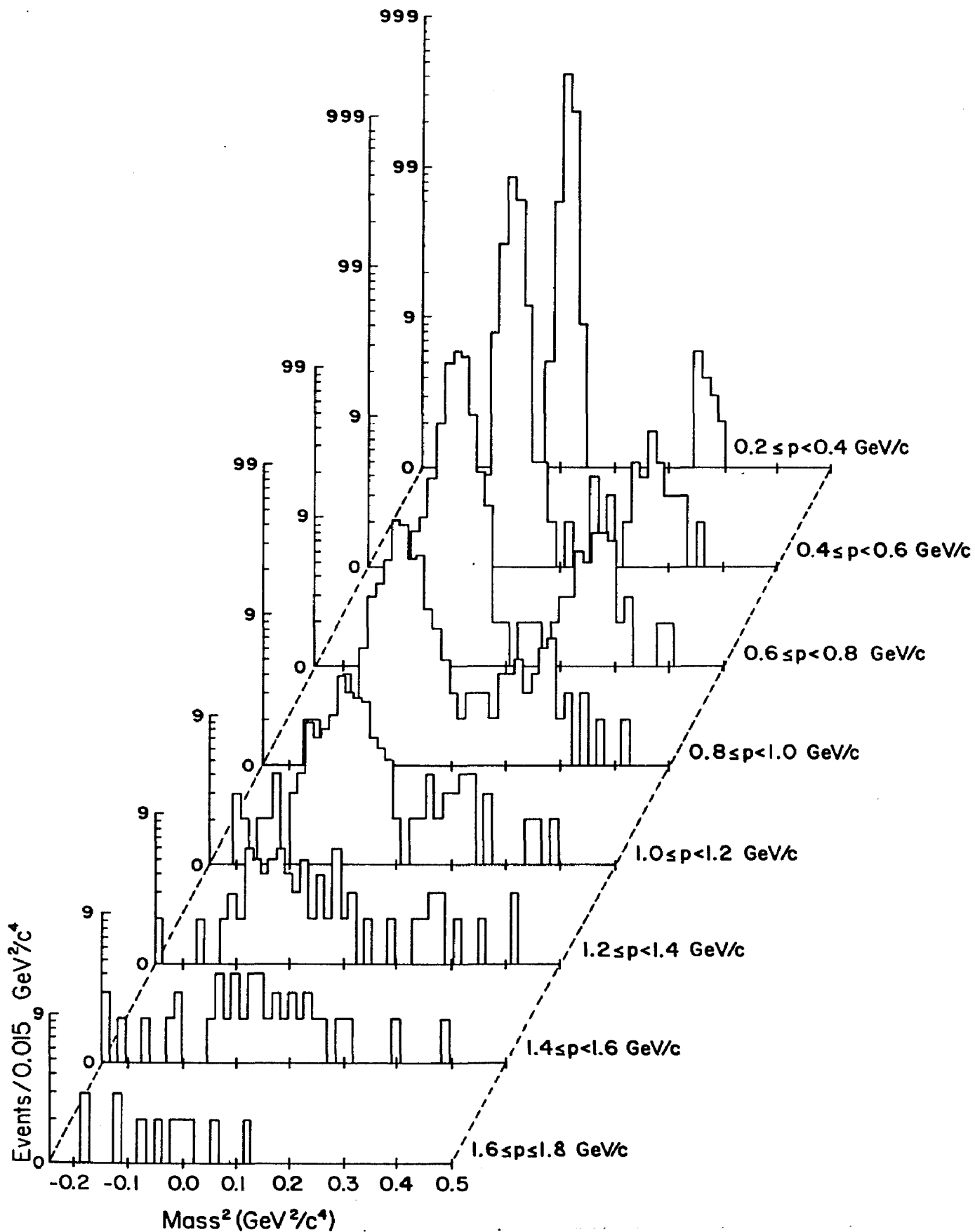


Fig. III-22 The distribution of the reconstructed mass² in GeV²/c⁴ for hadrons from the ψ' data set. Only those hadrons that have a mass² less than 0.5 GeV²/c⁴ are shown.

sets. It is seen that the probabilities for hadrons to mimic the characteristics of muons is small (on the order of 1% for this data sample), and that those events that appear as ambiguous muon-hadrons are consistent with the expected contamination from hadronic punch-through and decays into muons.

In summary, the tests an event must pass to be identified as a muon are:

- 1) At least two out of three layers of the hadron filter must have counters which fire, and the extrapolated position of the particle must lie within 50 cm of the counters that fired.
- 2) The Cherenkov counter must produce an above-threshold signal.
- 3) The hadron filter on the conjugate side must have two out of three layers of scintillator firing.

The probability for a hadron with a momentum above 1.1 GeV/c to mimic a muon is estimated to be $1.0 \pm 0.3\%$, while the chances that a muon above the same momentum will appear to be a hadron is about 0.7%. The probability that a muon appears to be a hadron is less than 0.8% in the momentum range of 0.8 to 1.1 GeV/c.

2. Separation of Hadrons and Electrons

It was stated before that there are two contributions to the electron sample; the QED and resonance decay contribution, and the converted photon and beam-gas scattering contribution. It is possible to isolate the QED and resonance decays fairly well by the tests placed on the initial sample. However, there still remain electrons that fail one or more of these tests. Since there is a large overlap in the different detectors' response to electrons and hadrons, it is necessary to use the joint probability functions to minimize the misidentification. The probability functions used are derived from: a) the Cherenkov counter, b) the shower counter, and c) the conjugate side NaI crystals. The variables of response are: a) the amplitude from the Cherenkov for momentum less than 1.1 GeV/c, the pion's threshold, b) the M and S quantities defined for the shower counter in Section III-B-2, and c) the energy deposited in the side NaI crystal array. As a final consistency check, the "clean" electron sample was passed through the probability tests to verify that this sample was, indeed, clean. Likewise, the purity of the initial hadron sample was checked.

The probability test consists of taking the product of these individual probability functions and forming their

product:

$$P_c(\{e, h\}, D_1(R_1), \dots, D_n(R_n)) = \prod_{j=1}^n P_c(\{e, h\}, D_k(R_k)).$$

The probability ratio is then formed:

$$R_{e/h} = \frac{P(e)}{P(h)}.$$

If the ratio is greater than 1., the particle is identified as an electron, if less than 1., it is called a hadron.

Note that protons (and antiprotons) are excluded from this test since they are easily identified by their flight time.

From the overlap of the probability functions, one can estimate the contamination probability of electrons in the hadron sample and vice versa. One problem, however, is the difference between the numbers of electrons and hadrons; there are roughly 10 times as many hadrons as electrons, but the momentum distributions are very different. Since the probability functions are the response functions normalized to the total number of electrons or hadrons in the test sample, the probability ratio, as defined above, assumes nothing about the relative number of each. By using this probability test, however, a good estimate can be made for the relative populations of each, which in turn, is used to renormalize the probability functions by the factor:

$$f_r(\{e,h\},p) = N(\{e,h\},p) / [N(e,p) + N(h,p)] ,$$

$$P_r(\{e,h\},p) = P_c(\{e,h\}) \cdot f_r(\{e,h\},p) ,$$

where $N(\{e,h\},p)$ is the number of electrons or hadrons of momentum p obtained from the first-order probability test. Due to the different momentum distributions, it is necessary to renormalize these functions with respect to momentum. From the renormalized probability functions, a better approximation to the true probability ratio can be obtained, and hence, a higher probability of identifying the particle correctly. This process can be carried out again to refine the functions, but in practice, it makes a negligible difference.

It is estimated that remnant electrons comprise less than 0.02% of the hadron sample and less than 0.3% of the hadrons are lost due to misidentification as electrons. These contamination probabilities are not totally independent of the particle's momentum and are shown in Table III-1 for various momentum ranges.

3. Separation of Pions, Kaons, and Protons

In order to identify the hadronic species, two devices must be used: the time-of-flight (TOF) system and the Cherenkov counter.

Each system has specific momentum ranges for particle separation:

- 1) The Cherenkov counter can only separate pions from kaons and protons that are above 1.1 GeV/c in momentum.
- 2) The TOF system separates pions from kaons and protons below 1.2 GeV/c.
- 3) This system separates protons from pions and kaons below 3 GeV/c.

Separation with the TOF System

Since the TOF distribution for the muons appears to have a Gaussian spread with a width of 0.27 ± 0.02 ns (see Section III-B-6), and assuming the hadrons have the same behavior, the probability distribution for hadron of type h to have a flight time t is:

$$P(h, t) = \frac{1}{\sqrt{2\pi} \sigma} \exp\left\{-\frac{1}{2} \left(\frac{\Delta t_h}{\sigma}\right)^2\right\}$$

where Δt_h is the difference between the observed flight time and the expected flight time for a hadron of momentum p_h travelling over a path of length ℓ , and σ is the expected resolution of the system, including both the intrinsic and momentum dependent uncertainties.

The hadron, then, is identified with the species

Momentum (GeV/c)	P_{eh}	P_{he}	$P_{\mathcal{H}h}$	$P_{h\mathcal{H}}$
0.2-0.7	$5 \pm 2 \times 10^{-3}$	$7 \pm 3 \times 10^{-4}$	--	--
0.7-1.2	$< 3 \times 10^{-3}$	$< 3 \times 10^{-4}$	$< 1.1 \times 10^{-2}$	$< 8 \times 10^{-3}$
1.2-1.8	$< 2 \times 10^{-3}$	$< 2 \times 10^{-4}$	$1.0 \pm .3 \times 10^{-2}$	$7 \pm 2 \times 10^{-3}$

Table III-1 The misidentification probability for hadrons and leptons. The notation, P_{eh} , for example, means the probability that the event was identified as an electron, but was a misidentified hadron. Note that by hadrons, we mean only pions and kaons, the protons and antiprotons having been eliminated by the time-of-flight cuts. These probabilities are calculated from the probability distributions listed in the text and are the renormalized values also described in the text.

producing the maximum probability. There are, however, some problems associated with this simple method. First, the assumption that the distributions in time of flight around the expected time is Gaussian is not completely true for the kaons. The decay probability for kaons is quite large, especially at lower momenta. In Section IV-E, this is discussed in more detail. The flight time of the decayed kaons, in general, will be somewhat different than the expected time. In order to quantify the difference between the expected Gaussian behavior for the intact kaons and the somewhat different behavior for the decayed ones, a computer code for simulating the passage of a particle through the spectrometer and its decay via certain modes was developed⁸. The results of this program were also used to determine the correction to the observed numbers of particles due to their decays. A second difficulty arises from the large differences between the various particle types. Without any a priori knowledge of the relative numbers of each species, the possibility of misidentifying a pion, for example, as a kaon increases. The same technique is used here as in the hadron-electron separation, namely to renormalize the probability functions by the relative populations of each species. This must be done as a function of momentum since

the relative numbers change rapidly, and the overlap of the probability functions depend on this quantity. One then forms the quantity:

$$F_r(h,p) = N_h(p) / \sum_{s=1}^3 N_s(p),$$

$$P_r(h,p,t) = P(h,p,t) \cdot F_r(h,p),$$

where N_h , N_s are the number of hadrons of species h or s, respectively, at a momentum p, with a flight time t.

Using this corrected probability function, the particles are then identified. Again, this correction can be repeated to obtain a better estimate for the actual numbers of each species, but in practice, the difference is slight and within the statistical and estimated systematic errors for this device.

Separation with the Cherenkov counter

The response of the Cherenkov counter is discussed in Section III-B-4 in the separation of the electron from the hadron sample. There it was seen that the hadrons with velocity below the Cherenkov limit still had a 14% chance of producing an above-threshold signal. This effect limits the identification of the pions above their Cherenkov threshold. The observed response for hadrons is shown in

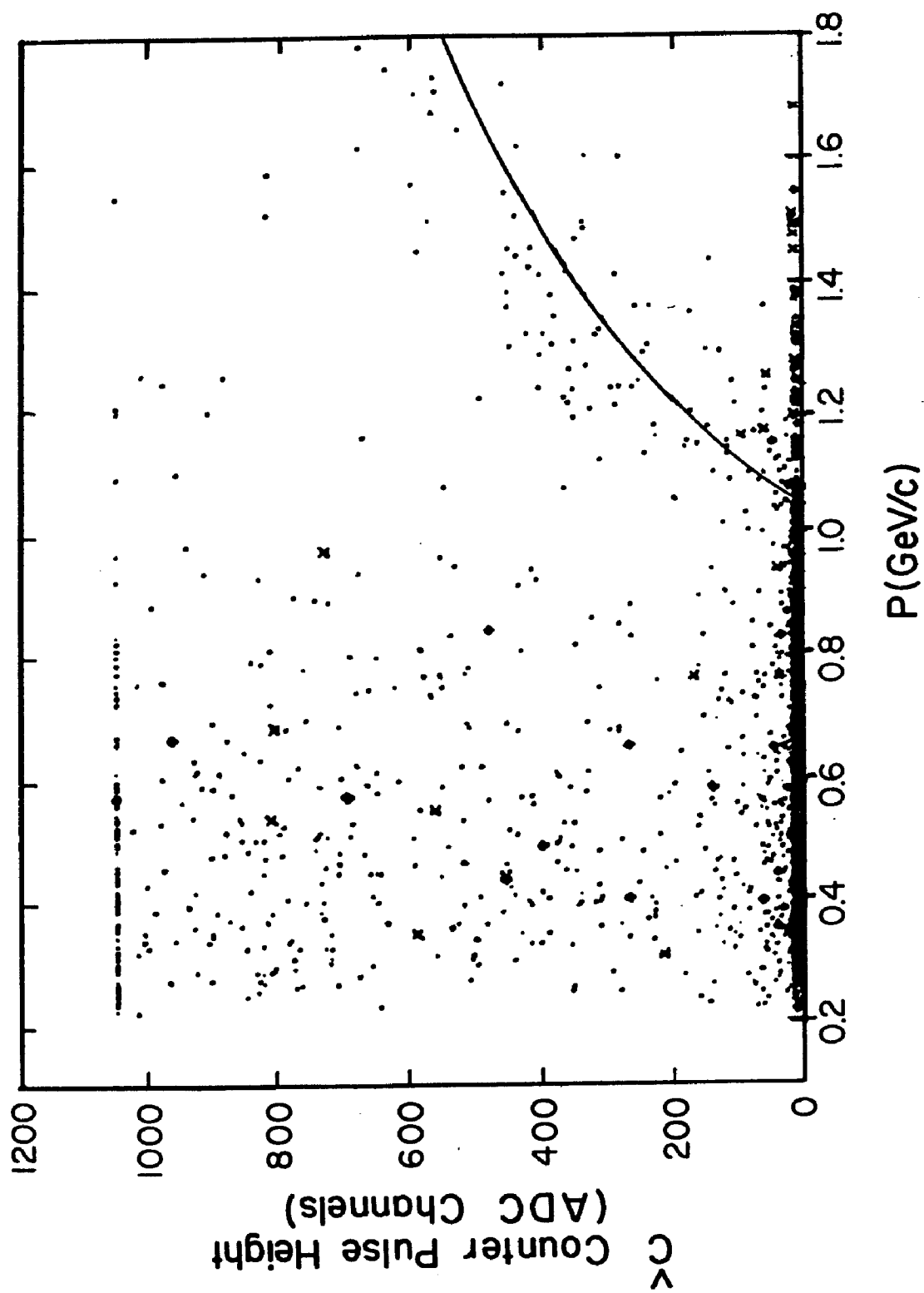


Fig. III-23 The amplitude in the Cherenkov counter for hadrons from the ψ' data set. The events with the symbol, \times , have a flight time within 2σ of the expected kaon flight time, while the events labeled with \blacklozenge have a flight time within 2σ of the expected proton flight time.

Fig. III-23. The solid line is the expected response of pions. Note that the symbol, x, identifies those events that have a flight time within 2σ of that expected for the kaons, while $\langle \rangle$ indicates those events that are within 2σ of the protons' flight time. The probability that an above-threshold particle would not produce a corresponding signal in the counter, was 10^{-3} . The place where most of the problems occur is near the pion's threshold since the fluctuation effects spread this threshold over a range of approximately 50 MeV/c. One can use the TOP information in addition to the Cherenkov signal to determine the probability of the particle's identity. The probability functions for particles above the pion's threshold are defined as such:

- 1) The probability that a pion has a below threshold signal is 10^{-3} .
- 2) The probability that a kaon or a proton has an above threshold signal is 0.14, assuming the behavior is momentum independent.
- 3) The probability that a particle has the contrary behavior is, of course, just the complement of the above values.
- 4) These probabilities are weighted by the probability

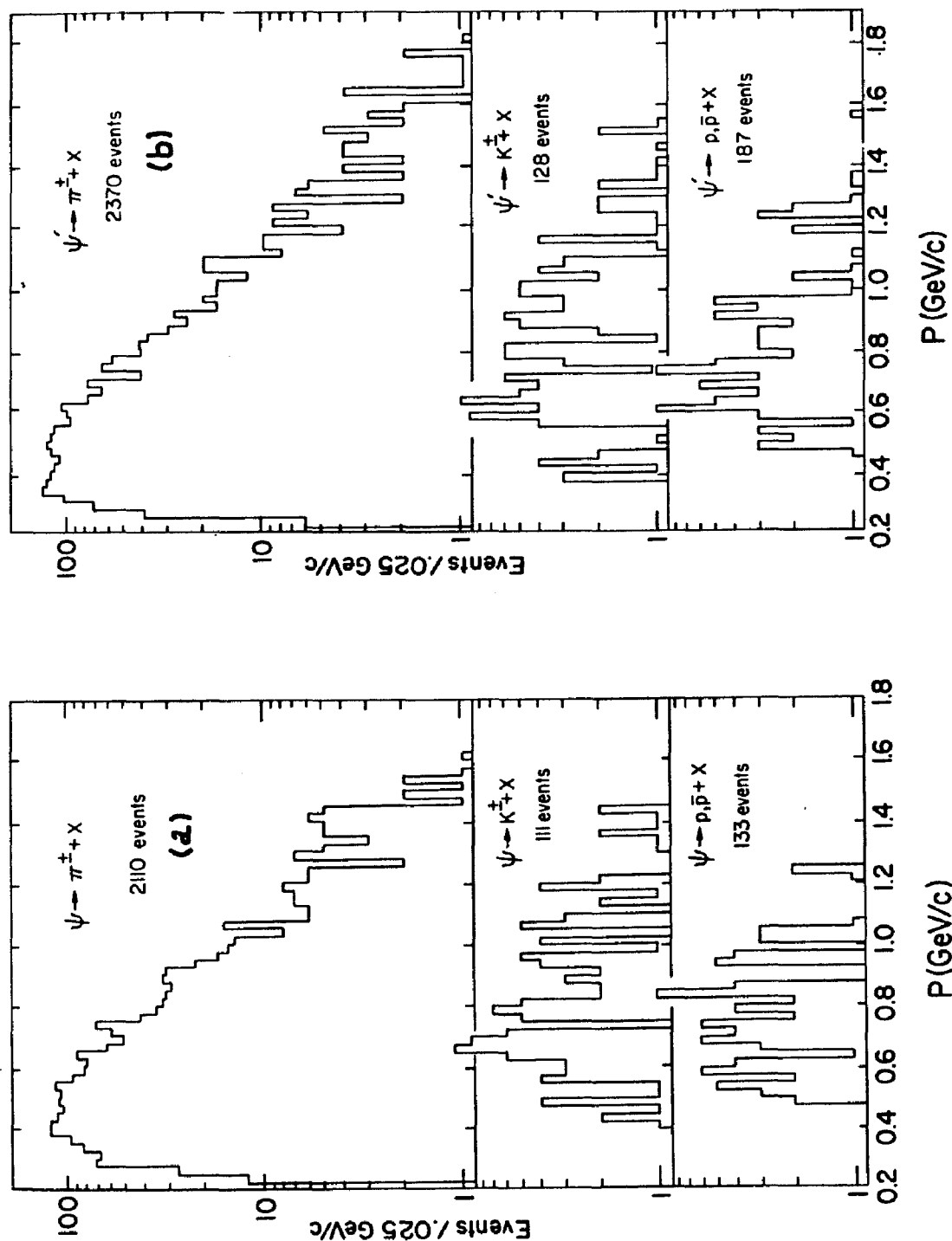


Fig. III-24 The momentum distribution of hadrons for the ψ' (a) and ψ' (b) data sets. These distributions are derived from the uncorrected data.

Momentum (GeV/c)	$P_{\pi K}$	$P_{K \pi}$
0.2-0.7	$< 5 \times 10^{-7}$	$< 10^{-7}$
0.7-1.2	$2 \pm 0.5 \times 10^{-2}$	$4 \pm 0.4 \times 10^{-3}$
1.2-1.8	$1.4 \pm .3 \times 10^{-2}$	$1. \pm 0.5 \times 10^{-3}$

Table III-2 The misidentification probabilities for pions and kaons. The notation, $P_{\pi K}$, means the probability that the event was identified as a pion, but was a misidentified kaon. These probabilities are calculated from the time-of-flight probability distributions and the Cherenkov amplitude probability distribution. They are the renormalized probabilities defined in the text.

from the TOF value, as described above.

5) The particle is identified with the particle type having the highest probability.

The misidentification probabilities are listed in Table III-2 as a function of the particle's momentum. Over the momentum range of this experiment, the probability for misidentifying a proton was estimated to be less than 10^{-4} .

In Fig. III-24, the raw distributions of the different hadronic species are shown. The number of events observed are 2210 pions, 111 kaons, and 113 protons and antiprotons from the ψ decays, while 2370 pions, 128 kaons, and 187 protons are observed from the ψ' decays.

In order to extract cross sections and other information from these raw distributions, various corrections must be applied to them for such effects as nuclear absorption and decays in flight. This is discussed in Chapter IV.

REFERENCES

CHAPTER III

1. R. Baldini-Celio et al., Phys. Lett. 58B, 471(1975), and see Section V-F, p. 121.
2. T. L. Atwood, et al., Phys. Rev. Lett. 35, 704(1975).
3. B. Rossi, "High-Energy Particles", Prentice-Hall, Inc., Englewood Cliffs, N.J., (1952), pp. 214-298
4. Heinz-Georg Sander, Diplomarbeit, Aachen University, 1974 (unpublished).
5. Neutron Physics Division, Oak Ridge National Laboratory, ORNL Report Number CCC-178. We thank A. Gabriel of ORNL for modifying and running the HETC for our range counter.
6. see Section IV-E and D.H. Badtke, Ph. D. Thesis, Univ. of Maryland, 1978 (unpublished).
7. see e.g. M. Cavalli-Sforza, et al., Phys. Rev. Lett. 36, 558(1976).
8. see Section IV-B and D.H. Badtke's Thesis, Appendix E.

CHAPTER IV

CORRECTIONS APPLIED TO THE DATA

A. General Considerations

Once the particle types are identified, it is then necessary to correct their numbers for various effects in order to generate cross sections from them.

The following corrections appear to be the dominant ones for this analysis:

- 1) Corrections for the limited and momentum-dependent angular acceptance of the apparatus (Section IV.C).
- 2) Corrections for nuclear absorption effects occurring in the material, dispersed along the particle's flight path (Section IV.D and Appendix C).
- 3) Corrections for the inability to reconstruct events that decay along their flight path (Section IV.E).
- 4) Corrections for the misidentification and, consequently, the impurity of the particles' samples (Section IV.F).
- 5) Corrections for background events, either from machine-induced processes, or natural causes (mainly cosmic rays) (Section IV.G).
- 6) Corrections for ionizational energy losses from the

material in the particles' flight path (Section IV.H).
programs (Section IV.H).

7) Although this is not in the same category as the corrections listed above, the luminosity is needed to produce the cross sections from the final, corrected numbers of particles (Section IV.I).

These various factors and the method of obtaining and of applying them will be discussed in the appropriate sections.

The nature of many of the above effects was gauged by a detailed Monte Carlo simulation program¹.

B. The Monte Carlo Simulation of the Data

This program produced test particles which interacted with the apparatus in nearly the same fashion as the real particles did. Some of similarities between the program's conditions and the actual data are:

a) Both multiple-Coulomb scattering and nuclear scattering were taken into account, as a function of the material in the flight path, the momentum, and the species of the test particle. From these factors, one deduced the probability that a particle will enter the apparatus and scatter out of it.

b) The wire spacing of the chambers was included to estimate the momentum resolution and the performance of the momentum-determining software.

c) The parametrized magnetic field was used to bend the test particles from their incident trajectory. One could obtain the solid angle for accepting particles, as a function of their momenta, but, in an effort to conserve computer time, a simpler program was used which lacked many features. The full program, then, only generated events which were ab initio in the spectrometer's acceptance. Within this solid angle, however, the particle's direction was chosen at random.

d) The nuclear absorption effects were included to estimate the loss of particles.

e) The lifetimes and the principal decay modes of the particles were inserted. The program would then follow the trajectories of all the decay products.

Essentially, this program generated the spatial position where the particle passed through a chamber or counter, with a random smearing to mimic the effect of the actual wire spacing. The analysis programs then treated the events as they would treat the real data. From the results of these programs, several of the correction factors were

obtained.

C. Corrections for the Angular Acceptance

It is clear that the active solid angle subtended by the spectrometer is limited for very high momentum particles by the proportional chambers' dimensions, while at the lower momenta it is limited by the curvature in the magnetic field. Thus, below some momentum, no particle can traverse the spectrometer without striking the walls. Obviously, a certain fraction of the particles that strike the magnet's walls scatter back into the magnet's gap and possibly traverse the rest of the spectrometer, thus starting the data acquisition sequence. In the reconstruction stage, these events are eliminated by the inability of the momentum-determining program to define a reasonable trajectory for them. The residual contamination from this type of an event is estimated to be less than 10^{-3} of the total sample.

The angular acceptance was determined in the following manner. The trajectories of test particles produced isotropically were followed, and limits were found on the angles that the test particles could have while still passing through the active areas of all the chambers and

counters. Specifically, the test particles must pass through the incident tracking chambers, the TOP-start counter, the magnet chambers, the TOP-stop counters, and the first three layers of the shower counter. Additionally, the particle was required not to pass through any part of the magnet's frame.

In order to determine the trajectory, the spatially-parameterized magnetic field was used. In Fig. I -1, the resulting solid angle for accepting particles is shown as a function of their momenta. Note that the acceptance is nearly zero for particles with less than 225 MeV/c, and it rises rapidly to a limiting value of 0.094 ster. The uncertainty associated with this acceptance is assumed to be less than 3%, arising from the uncertainty of the chambers' active area, the magnet's position, and the effects of scattering along the particle's path. In Fig. I -2, the limits on the θ angles, i.e., the angle from the beams' direction in the horizontal plane, are shown as a function of the particles' momentum.

Note that this acceptance is purely geometrical, and does not include the effects of scattering in the apparatus. However, from the Monte Carlo program, the probability that a particle would enter the acceptance of the magnet and

scatter out of it was found to be compensated for by the particles that were traveling outside the acceptance but which scattered into it.

D. Corrections for Nuclear Interaction Effects

Due to the large amount of material between the luminous region and the chambers inside the magnet's gap (0.45 collision lengths or 0.30 absorption lengths), there is a certain probability for a hadron to be inelastically scattered or absorbed in the nuclei of these materials. The measured nuclear absorption cross sections² for aluminum, iron, carbon and hydrogen were used to predict the loss of hadrons in the materials composed from these substances. The obstructing materials were reduced to the equivalents of these elements and the appropriate densities of each element composing the materials were used to obtain the absorption corrections.

Details of the results of these calculations are listed in Appendix C.

E. Corrections for Reconstruction Failure due to Decay

To ascertain the magnitude of this correction, the Monte Carlo simulation program followed the expected

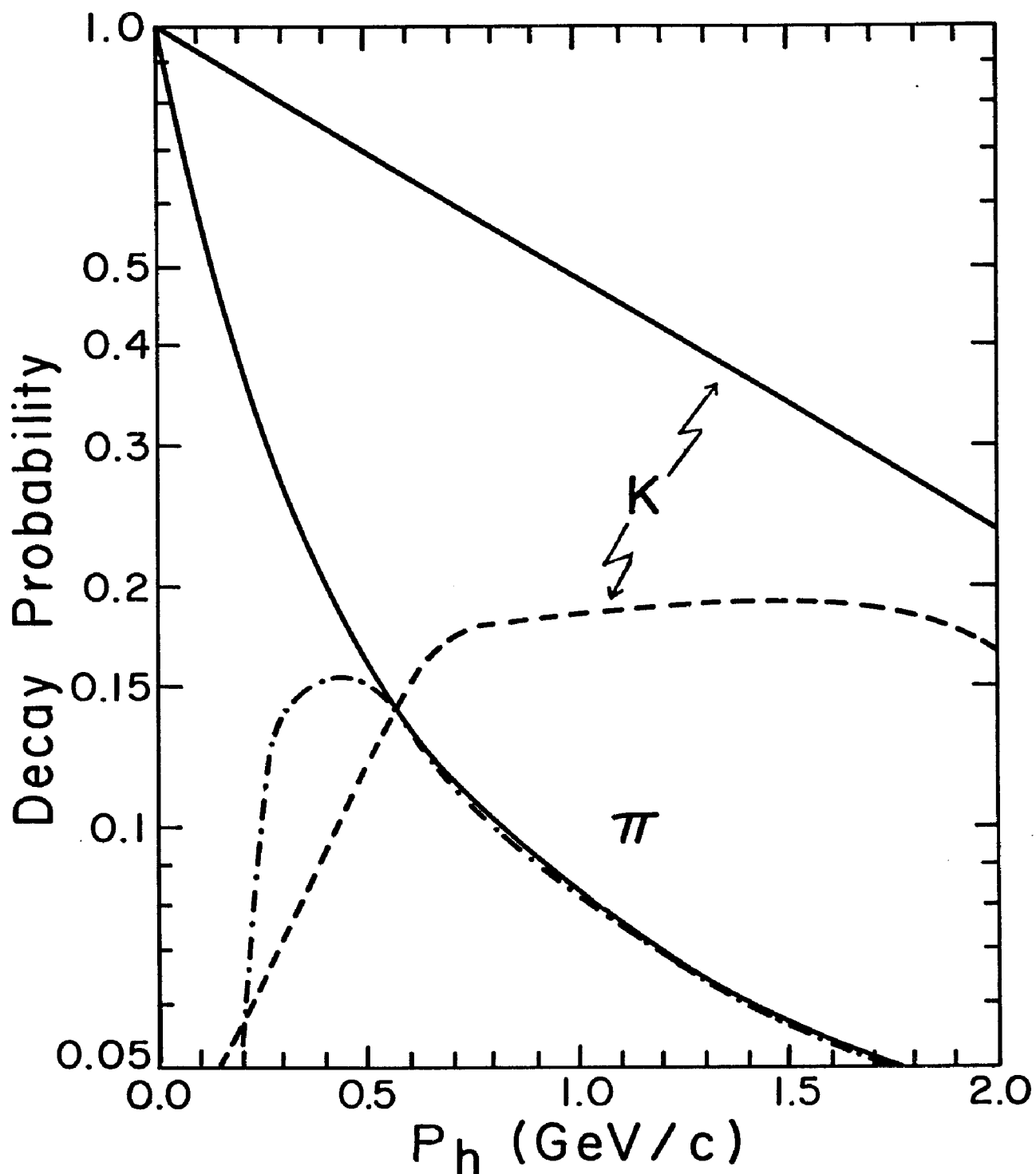


Fig. IV-1 The probability that a pion or kaon will enter the spectrometer and decay in flight (solid line), and, additionally, that the charged secondary(ies) from the decay will traverse the spectrometer magnet up to the proportional chamber, C5X (dashed line), as a function of momentum.

trajectory of the decay products through the spectrometer. For decayed events, several quantities were examined, such as the flight time of the decayed particle, the χ^2 of the trajectory, the momentum, and the Cherenkov counter's expected pulse height. In Fig. IV-1, we show, for instance, the probability that a pion or kaon emitted from the collision region will decay before reaching the proportional chamber, C5X, at the back of the magnet, as a function of the incident particle's momentum. The dashed line, however, shows the probability that the particle will decay and that the decay products will arrive at C5X. One sees that the muon from the pion decays almost always makes it through the spectrometer, but particles from the kaon decays traverse the spectrometer only about 50% of the time.

By comparing these quantities from the decayed kaons or pions with the same quantities from the non-decaying particles generated by the Monte Carlo program, the following results were obtained.

- 1) The probability that a particle would decay and would be reconstructed by the analysis programs.

This depended strongly on the incident particle's momentum.

- 2) The probability that the secondary particle from the

decays would be identified a muon via the Cherenkov counter, and the penetration into the range counter. This probability distribution reflected the muons' penetration probability and the probability that either the incident particle produced a signal in the Cherenkov counter, or that the particle decayed before the Cherenkov counter and the muon produced the signal.

3) The χ^2 distribution for the decayed trajectories, produced by the momentum-determining program, appeared to be flat vis-à-vis the distribution for the non-decayed particles.

4) The generated flight time for decayed particles agreed well with the result produced by the momentum analysis program. However, the decayed particles generally produced a flight time that was lower than that expected for the intact particle, and followed an exponential curve, modulated by the intrinsic resolution of the TOF system.

The correction factors applied to the pion and kaon data are shown in Fig. IV-2. These factors are computed from the probability that the hadron will decay in flight and that the secondary(ies) traverse the spectrometer to chamber C5X, and the probability that the χ^2 of the

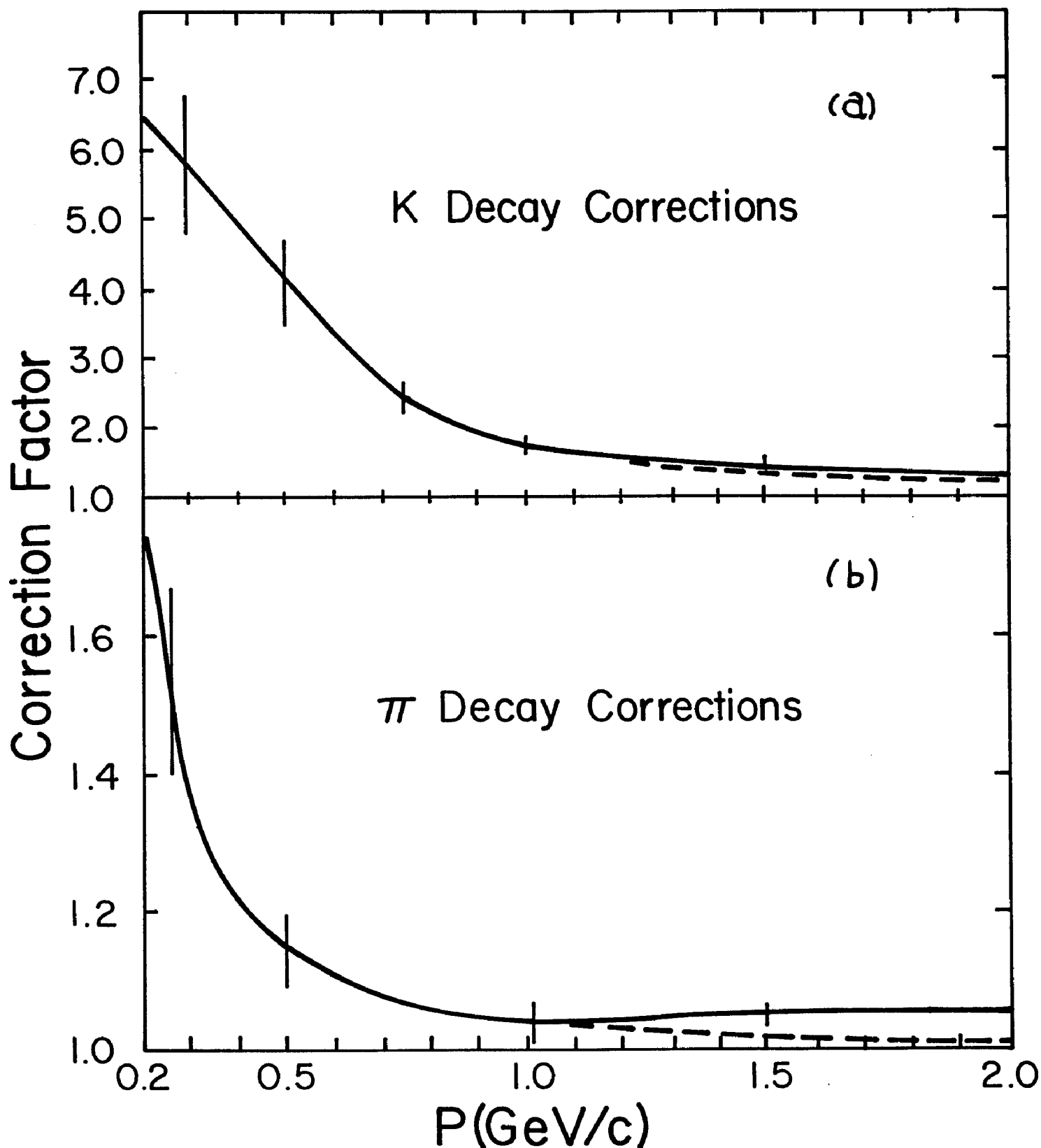


Fig. IV-2 The multiplicative correction factor to account for kaons (a) or pions (b) that decay in flight in the spectrometer, and whose secondary particles fail the various cuts imposed on the observed trajectory (solid line). If one does not use the information from the hadron filter to identify muons, then the dashed line is the resultant factor. The error bars indicate the uncertainty in these factors due to the statistics of the Monte Carlo simulation.

resulting trajectory is less than 6.0 (see Section II-C-3), and that the flight time of the entire event was within 2σ of the time expected for that type of hadron of that momentum (see Section III-C-3). Thus this correction is applied to those hadrons that fall within 2σ of the expected flight time. Those hadrons outside these limits are discarded and, assuming a Gaussian behavior, the number of events inside the limits is increased by $1./0.95$ to correct for the loss of events.

If the decay product is identified as a muon by the Cherenkov counter and the hadron filter, and thus rejected from the hadron sample, the solid curve results. If the muon is left in the hadron sample, the dashed curve is the result. The error bars represent the uncertainties in these decay corrections, primarily from the statistics of the Monte Carlo data.

F. Corrections for Particle Misidentification

The misidentification of an electron or muon as a hadron was estimated in Section III-C-2, and is momentum dependent. The data is corrected then for the percentage of hadrons that are misidentified as electrons or muons, and the percentage of muons or electrons that are misidentified as hadrons. The overall correction factor for hadron-lepton

misidentification that is applied to the hadron data is 1.003 with a slight momentum dependence.

The misidentification of the various hadronic species can be estimated in the following fashion:

a) If the momentum is less than 1.2 GeV/c, meaning that the time-of-flight system separates the types, then the overlap of the renormalized probability functions determines the misidentification probability. Assuming a Gaussian shape to this distribution and truncating the distributions at 2σ from the expected flight time, one gets the misidentification probabilities listed in Table IV-1. Note that these probabilities are generally smaller than the statistical error on the observed number of events. The data are corrected with the appropriate factor for the misidentification.

b) For momenta greater than 1.2 GeV/c, the misidentification probability is determined by the Cherenkov counter's probability distribution for the various types and the TOF probability distributions.

From the low momentum sample, we know that 14% have a spurious Cherenkov signal, nearly independent of momentum. Assuming this contamination probability can be extended to higher momenta and including the TOF's probability distribution, we estimate that about 1.4%

Momentum (GeV/c)	$P_{K\pi}$	$P_{\pi K}$
0.2-0.9	$< 10^{-6}$	$< 10^{-9}$
0.9-1.0	$1.6 \pm 0.5 \times 10^{-4}$	$3.2 \pm 1.2 \times 10^{-5}$
1.0-1.1	$2.0 \pm 0.9 \times 10^{-3}$	$3.6 \pm 0.8 \times 10^{-4}$
1.1-1.2	$1.4 \pm 0.6 \times 10^{-2}$	$3.0 \pm 0.8 \times 10^{-3}$

Table IV-1 The misidentification probability for pions and kaons that are within 2σ of the expected flight time for pions and kaons, respectively. The notation $P_{K\pi}$ means the probability that the event was identified as a kaon but was a misidentified pion. These probabilities are the renormalized ones defined in the text.

of the non-decayed kaons will be misidentified. The kaon sample is then corrected accordingly. The pion misidentification as a kaon is expected to be less than 0.1% from the efficiency of the Cherenkov counter.

The misidentification of the protons and antiprotons can occur only if they interact and form low mass secondaries, such as pions or electrons, since their TOF probability distribution is well separated from that of the kaons and pions. However, for protons produced from the resonances, the secondaries will not have sufficient energy to traverse the spectrometer. Therefore, the misidentification for protons is expected to be negligible.

G. Corrections for Background Events in the Data

The principal corrections for backgrounds come from beam-gas scattering. By examining the events outside the interaction region, i.e. events that arise from greater than ± 10 cm from the center of the interaction region along the beams' direction, one can extract this contribution from inside the region. From Fig. II-2, one sees that the distribution of events along the beams' direction is nearly Gaussian with a

width of 3 cm. In the final analysis, the source point of the events was restricted to come from ± 7.0 cm. from the centroid of the distribution. A similar cut was placed on the source point in the direction transverse to the beams to eliminate beam-vacuum pipe scattering events. However, due to multiple scattering in the vacuum pipe and the polymer, the distribution in this Y coordinate source point was very momentum dependent. This distribution is shown in Fig. II-2b). One sees that the high momentum events have a distribution with a width of 0.8 mm., which is consistent with the beams' dimension and the chambers' resolution. At low momenta, the source size expands 30-fold, presumably the result of multiple scattering. This same feature is also noted in the Monte Carlo program. Thus, to reduce the background from beam-gas and beam-wall scattering, the source point was restricted to ± 20 mm. for the data.

Interestingly, the background to the pion and kaon data was found to be much less than 0.5% and was neglected. The background from the antiprotons was, likewise, found to be negligible. However, the background in the protons sample was very large at low momentum. This was mainly due to the beam-gas

scattering process, where the protons from the source dominated those produced by e^+e^- collisions. The correction factor for the protons fits the exponential distributions:

$$1.0 - A \exp\{-B p\}, \quad (p \text{ in GeV}/c)$$

where A and B take on the values of 6.68 and 5.22 for the protons from the ψ decays, and 4.33 and 3.80 for the protons from the ψ' decays.

Cosmic rays were also eliminated by the cuts on the source point. Though a few fell within the source point window, they were effectively eliminated by the maximum momentum cut.

The results of the momentum-dependent corrections to the number of observed events are summarized in Figs. IV-3, 4, 5, and 6 for the pion, kaon, and proton-antiproton data, respectively. The various curves represent the multiplicative correction factor for such processes as nuclear absorption, decay in flight, beam-gas scattering background, and for the ratio of the solid angle accepted by the spectrometer over the full solid angle. Thus the curve labeled TOTAL reflects the number of particles produced in the

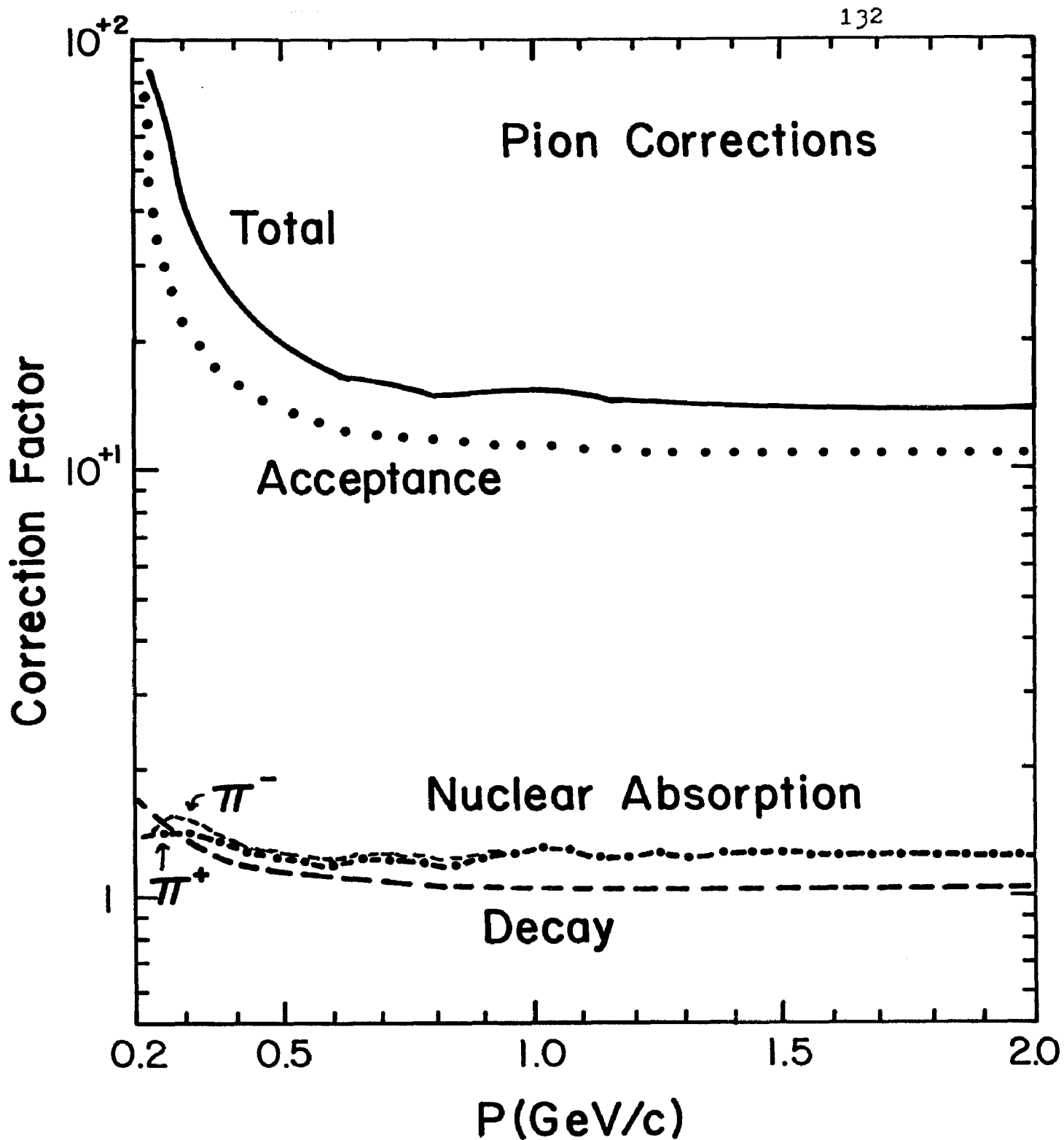


Fig. IV-3 A summary of the multiplicative corrections that are applied to the pion data as a function of the pions' momentum. The curve labeled "Acceptance" accounts for the solid angle of the spectrometer, thus producing the number of pions per steradian. The curve labeled "Nuclear Absorption" accounts for pions which enter the spectrometer's acceptance, but undergo an inelastic nuclear collision and are lost. The curve labeled "Decay" accounts for the pions which enter the spectrometer, decay, and are lost. The curve "Total" is the product of these.

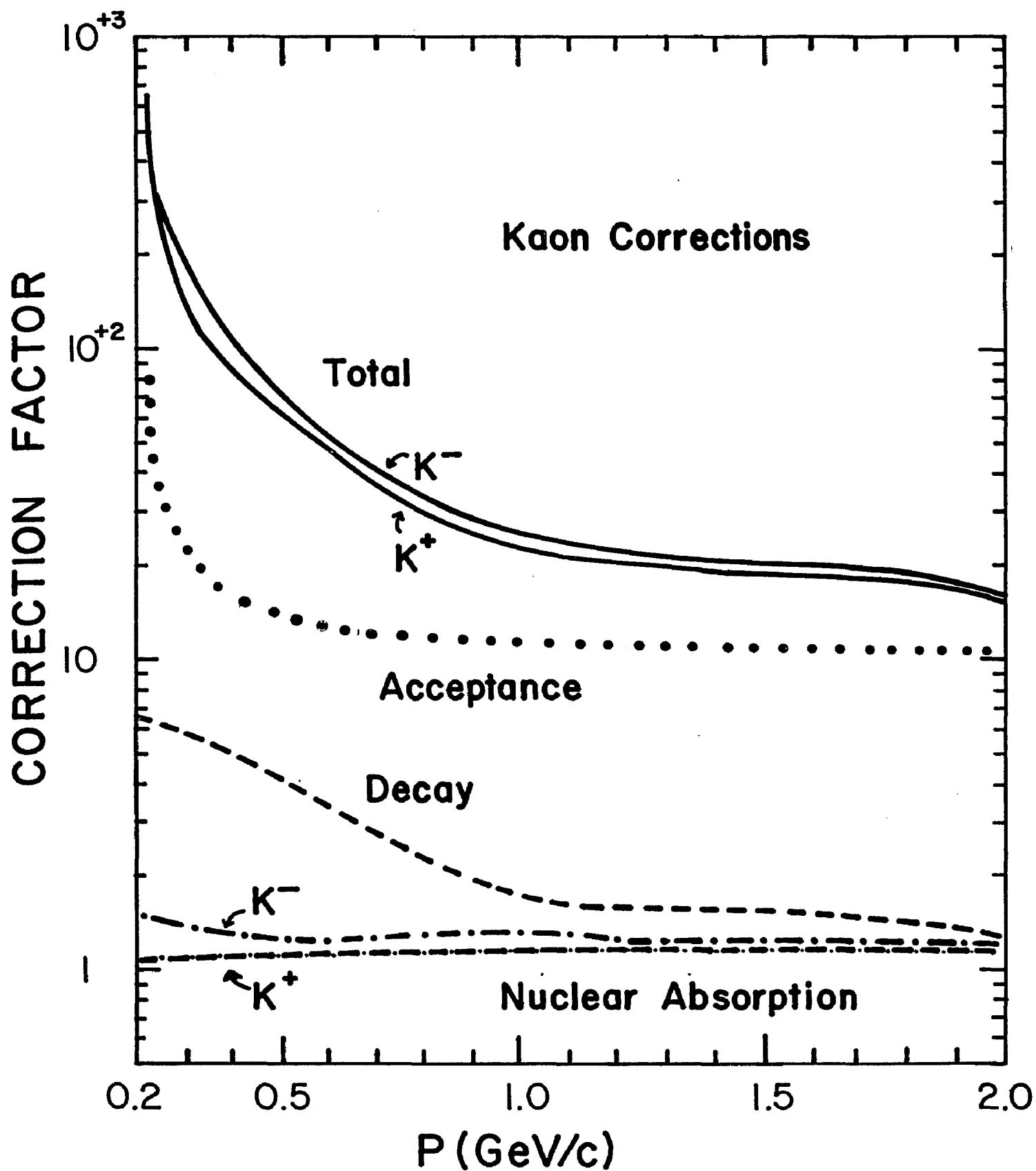


Fig. IV-4 A summary of the multiplicative correction factors that are applied to the observed number of kaons. The curves are labeled in accord with Fig. IV-3.

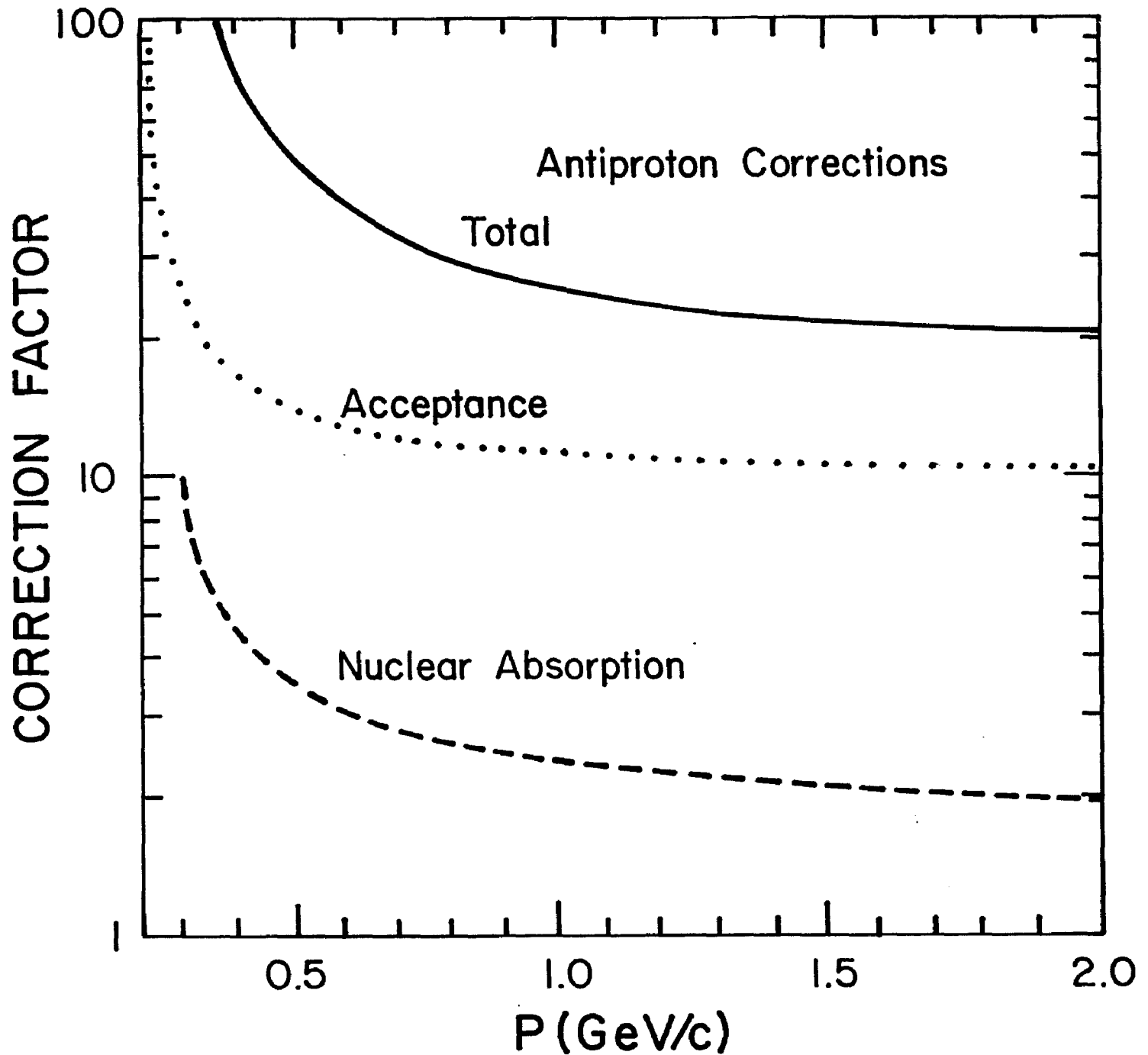


Fig. IV-5 A summary of the multiplicative correction factors applied to the observed number of antiprotons. The curves are labeled in accord with Fig. IV-3.

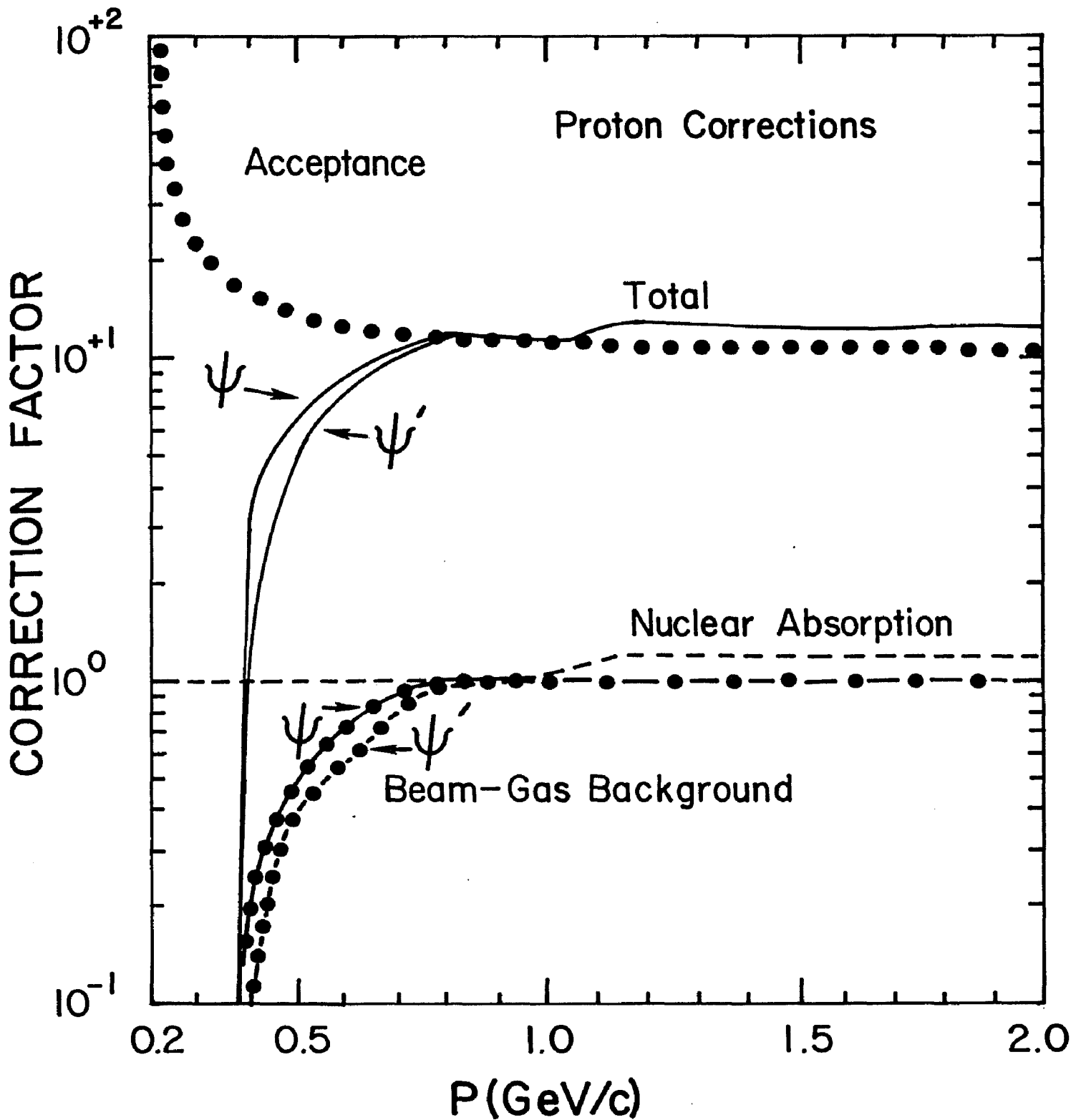


Fig. IV-6 A summary of the multiplicative correction factors applied to the proton data. The curves are labeled as in Fig. IV-3. The curve labeled "Beam-Gas Background" accounts for the contribution of beam-gas scattering to the proton data. These factors are different for the ψ and ψ' data sets.

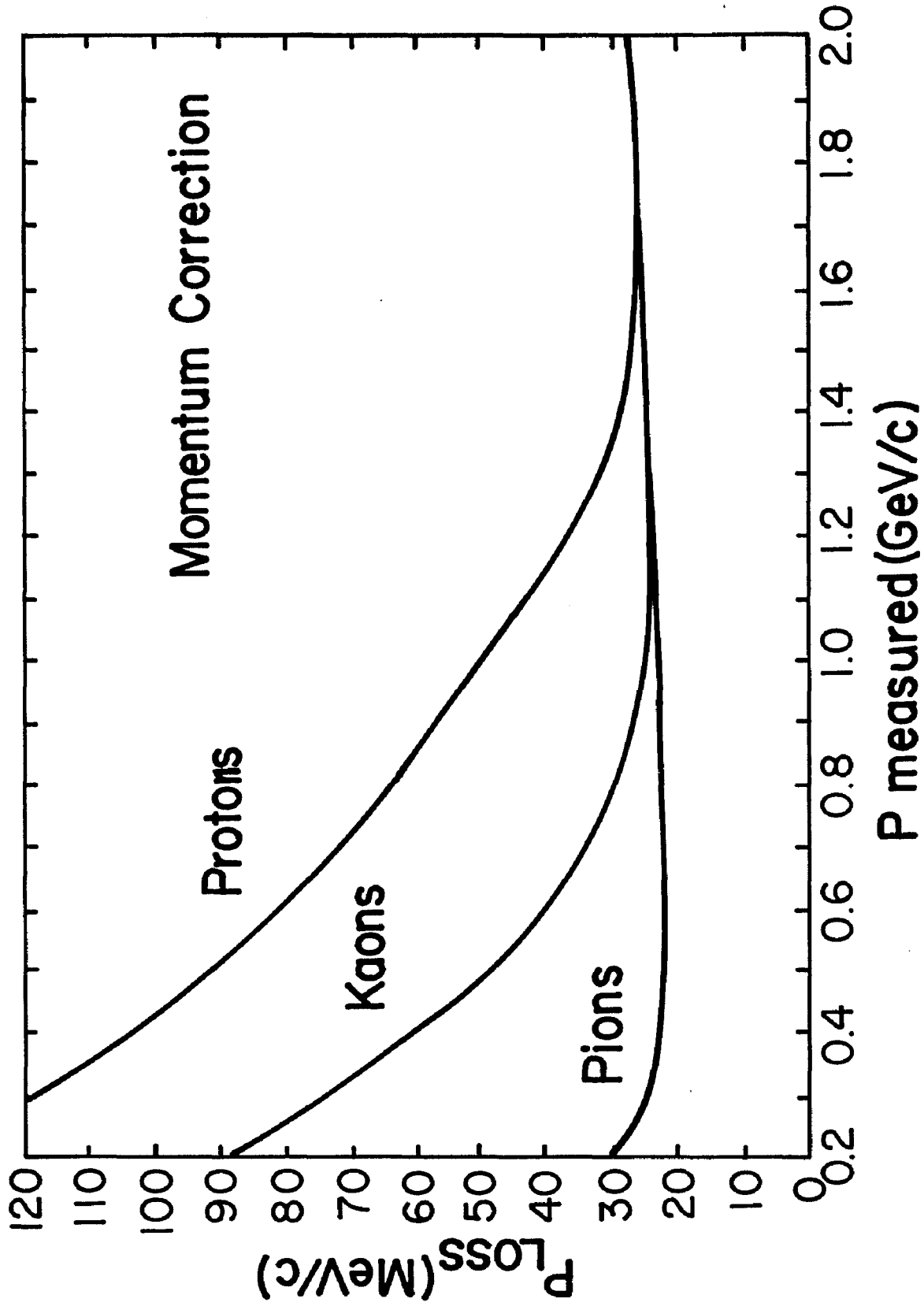


Fig. IV-7 The additive correction to the measured momentum of the hadrons to account for the ionizational energy loss in the material between the interaction region and the magnetic field.

full solid angle for each particle observed in the spectrometer.

The uncertainties on all these corrections range from 4 to 15% depending on the momentum, and are included when the correction factors are applied to the data.

H. Corrections to the Momentum for Energy Losses

While the hadrons traverse the various counters and detectors, they will lose some energy due to ionizational collisions. The most probable loss can be computed for each species and is shown in Fig. IV-7. The lost momentum is added to the observed momentum from the analysis programs since the majority of the materials are before the chambers in the spectrometer's magnet.

I. Normalization of the Data Via the Luminosity

To produce a cross section from the observed and corrected number of particles, one must know the luminosity of the source, in our case, the colliding bunches of electrons and positrons. It is easy to see³ that for colliding bunches with n_e electrons and n_p

positrons, rotating with a frequency, f , and having the rms radii for these Gaussian particle distributions, σ_x, σ_y , then the number of events produced by some mechanism with a cross section, σ , is:

$$N = \frac{n_e n_p f}{4\pi \sigma_x \sigma_y} \cdot \sigma = \mathcal{L} \cdot \sigma .$$

The luminosity function, \mathcal{L} , can then be expressed in terms of the average current in each bunches, $i = n \cdot e \cdot f$, as:

$$\mathcal{L} = \frac{1}{4\pi e^2} \frac{i_e i_p}{\sigma_x \sigma_y f} .$$

For the typical operating conditions at SPEAR, the luminosity at the ψ energy was $5 \times 10^{29} \text{ cm}^{-2} \text{ sec}^{-1}$. This value decays exponentially with time due to particle-losses from the bunches. Thus, the luminosity integrated over the active time of the experiment, when divided into the observed event numbers, produced the cross sections. Since our spectrometer measured a small fraction of the solid angle, the correct expression is:

$$\frac{dn}{d\Omega} \Delta\Omega = \frac{d\sigma}{d\Omega} \Delta\Omega \cdot \mathcal{L}_I .$$

where $\Delta\Omega$ is the acceptance of the spectrometer, which, as noted above, depends on the particle's

momentum. There are, however, some subtleties in deriving the total cross section from the differential one. If the final state consists of N charged particles with a possible angular distribution around the beam's direction of $f(\theta)$, but emitted at random directions and with an equal probability of entering some solid angle $\Delta \Omega$ located at θ_d , then the total cross section is:

$$\sigma = \frac{1}{N} \frac{dn}{d\Omega} \frac{\Delta\Omega}{\mathcal{L}_I} \frac{1}{f(\theta_d)} \int_{4\pi} f(\theta) d\Omega,$$

where the factor, N , is required since anyone of the charged products can enter the acceptance. However, the acceptance is not the same for all the particles, as has been assumed, and the situation becomes more complicated. The actual momentum spectrum must be known beforehand, and the correlation among the particles' kinematics must be accounted for.

In order to calculate the luminosity, the observed muon signal is used, since the cross section for their production is, presumably, already well known from QED and the resonances decays. The other advantage of the muon signal is that it is very clean; the contamination and uncertainty in the correction factors applied to this sample are very small; both are less than 0.5%.

In calculating the luminosity, the multiplicity factor is now included, since the process of interest contains only two particles in the final state, both of which have the beam energy, and hence, have the same acceptance. The integrated luminosity is then:

$$\mathcal{L}_I = \Delta \Omega \frac{2 \sigma(\mu\mu)}{\frac{dn}{d\Omega}} \int_{4\pi} f(\theta) d\Omega \cdot \frac{1}{f(\theta_d)}$$

For muons from both the QED and resonant decays, the angular distribution function, $f(\theta)$, is $1 + \cos^2(\theta)$. Then, for the spectrometer at 90° to the beams, the luminosity is:

$$\mathcal{L}_I = \Delta \Omega \frac{2 \sigma(\mu\mu)}{\frac{dn}{d\Omega} \frac{16}{3} \pi}$$

The Feynman diagrams giving α^3 contributions to the muon production can also be included in the calculating the cross section, σ . Note, though, that these radiative processes are limited, in the case of the resonant production, by the energy at which the machine is operating, and by the natural energy fluctuation in the beams. This is because the resonances are much narrower than the beams' energy spread. Thus, the radiative effects serve to decrease the cross section at the peak of the resonance. For

our calculation of the luminosity, we used the muon production cross section as measured by the SLAC-LBL group⁴ at the 90° angle.

From the observation of 220 muon events (100 of which are μ^-), the luminosity for the ψ data is $106.5 \pm 4.0 \text{ nb}^{-1}$.

A similar analysis is used in the ψ' data. However, the partial cross section into muon pairs is overwhelmed by the cascade decay to the ψ . Since the branching ratio to the ψ is fairly well known with a value of $57 \pm 8\%$, the observed momentum distribution of muons can be fit for both the directly produced muons from the ψ' and QED, and the cascade decays. This give a value of $360 \pm 30 \text{ nb}^{-1}$. The uncertainty in this number comes from the errors on the known ψ' branching ratio into the ψ as well as the statistical, acceptance solid angle, and production cross section uncertainties.

REFERENCES

CHAPTER IV

1. D.H. Badtke, Ph.D.. Thesis, Univ. of Maryland, 1978, Appendix E, (unpublished).
2. E. Bracci, et al., CERN/High Energy Reactions Analysis Group #72-1 (1972), and #72-2 (1972; U. Casadei, et al., CERN/High Energy Reactions Analysis Group #75-1(1975); J.W. Cronin, R. Cool, and A. Abashian, Phys. Rev. 107, 1121(1958).
3. see e.g. M. Sands, "The Physics of Electron Storage Rings, An Introduction" in Physics with Intersecting Storage Rings, ed. by B. Touschek, Academic Press, N.Y., (1971).
4. V. Luth, et al., Phys. Rev. Lett. 35, 1124(1975).

CHAPTER V

RESULTS AND DISCUSSION

A. Introduction

The results of the preceding sections are now presented. They will include discussions of the inclusive momentum spectrum, the invariant cross section, the ratios of the various hadronic types, the multiplicity distributions and their derivation, and a comparison of these data with other experiment and models. In particular, a comparison with the non-resonant e^+e^- inclusive hadronic spectra will be attempted.

To begin, we will discuss some of the physics underlying the production mechanisms of hadrons from e^+e^- collisions.

B. Models for Hadron Production from e^+e^- Collisions

A vast amount of data from hadron-hadron collisions and e^+e^- annihilations can be described with statistical¹ or thermodynamical² models, where the collisions are thought to produce a cloud of excited, hadronic matter which then emits particles according to either a statistical or Boltzmann-like distribution. In the latter case, one can define a hadronic "temperature" of the cloud which will then

describe the energy spectrum of the emitted particles.

In hadron-hadron collisions, the particles that are produced in the peripheral process tend to obscure the details of the fireball's decay. However, in e^+e^- collisions, the incident particles have a large chance of annihilating into a single virtual photon, which can then decay as a single fireball.

In general, the cross section for the reaction

$$e^+e^- \rightarrow N \text{ particles,}$$

can be written as³,

$$\sigma_N = \frac{(2\pi)^6 \alpha^2}{s^2} \sum_{\text{spin}} \int \prod_{n=1}^N \left(\frac{d^3 p_n}{(2\pi)^3} \frac{1}{2E_n} \right) J^\mu J_\mu \delta^4(p_f - p_i),$$

where J_μ is the transition current between the vacuum and the final particles. In the Fermi statistical model, one assumes that the annihilation occurs in a volume, Ω , and that the quantity, $J^\mu J_\mu$, is proportional to the density of states in momentum space:

$$J^\mu J_\mu = A \prod_{n=1}^N \frac{\Omega}{2E_n},$$

where A is a proportionality constant and E_n is the energy of the n -th particle. The N -particle cross section is then:

$$\sigma_N = \frac{(2\pi)^6 \alpha^2 A}{s^2} \int \prod_{n=1}^N \left(\frac{E_n \Omega}{(2\pi)^3} \frac{d^3 p_n}{E_n} \right) \delta^4(p_f - p_i).$$

The total cross section is then the sum over the N-particle results.

At some point, the underlying dynamics of the high energy collisions may involve the interaction of the constituents of the hadrons. Thus, the simple statistical models will not adequately describe the phenomena.

In order to describe the inclusive production process,

$$e^+ e^- \rightarrow \text{one hadron} + \text{anything else,}$$

the current-current interaction form⁴ is used:

$$\frac{d\sigma}{dx d\Omega} = \frac{2\pi \alpha^2}{s} x\beta \left(m_h W_1(\nu, s) + 1/4 \beta^2 x \nu W_2(\nu, s) \sin^2\theta \right)$$

where $W_1(\nu, s)$ and $W_2(\nu, s)$ are the structure functions of the hadronic interaction, x is the fraction of the total energy taken by the hadron, i.e. $x = 2E_h / \sqrt{s}$, β is the hadron's velocity, ν is the energy of the virtual photon in the hadron's rest frame and equal to $\frac{E}{m} \cdot \sqrt{s}$.

For sufficiently high energies, one expects the form of the current-current interaction to be dominated by the light cone behavior⁵, giving rise to production cross sections that are independent of the total energy, but depend only on x . In the parton model⁶, one expects to see a scaling

behavior of the cross sections, since, at high enough energies, the quarks inside a hadron are thought to act independent of the other constituents. This leads to production mechanisms which then depend only on the fraction of the total energy in the individual constituents. One, therefore, expects to observe

$$-m_h W_1(\psi, s) \rightarrow F_1(x), \text{ and}$$

$$\nu W_2(\psi, s) \rightarrow F_2(x)$$

for sufficiently high s -values. This is known as Bjorken scaling⁷.

At energies where the inter-constituent interactions are strong enough so that the quarks do not act independently of each other, one might expect a two-component picture⁸ of the interaction. In this view, one observes the statistical process of the photon fragmenting into hadrons, and of the photon materializing as partons which then, acting individually, decay into observable hadrons. This phenomenological picture appears to explain the non-scaling behavior of the low- x region, where the statistical process dominates, and also the observed scaling in the high- x region for the existing e^+e^- data⁹. Furthermore, one sees that these data as a function of momentum exhibit thermodynamic

or Feynman scaling, at least for momentum below about 1.5 GeV/c. In addition, the data from the ISR on the inclusive production at $\theta_{cm} = 90^\circ$, appear to behave similarly¹⁰. The invariant cross sections for both processes empirically behave as¹⁰:

$$E \frac{d^3\sigma}{dp^3} = C(s) e^{-2rp} + f(x) / (p^2 + m^2)^N.$$

Here, the first term describes the statistical emission process, and the second term describes the parton production process. Fitting this function to the pp collision case, one sees that $C(s)$ is a slowly varying function of s , r is a hadronic production radius, approximately 3 GeV^{-1} , p is the transverse momentum, m is a phenomenological mass parameter on the order of 1.2 GeV., $f(x)$ is about e^{-12x} , as given by the constituent interchange models¹¹, and N is about 4.

In e^+e^- annihilation, $C(s)$ is found to depend on the total cross section, N is 2 if Bjorken scaling is obeyed, and $f(x)$ is proportional to $x^2 e^{-6x}$. Interestingly, the production radius for the statistical term is approximately the same in both pp and e^+e^- cases.

In the direct decays of the s-channel resonances, such as the ψ , the thermodynamic models may adequately describe the spectra. Since the lifetimes of the resonances are much

longer than the collision time, the chances for "thermal equalization" is enhanced. The "thermal equilibrium" may be the result of the interactions of the constituents, mediated through colored, vector gluon fields. One then expects the spectra from these resonances to be very much like the fireball decays. In the quantum chromodynamics (QCD) picture, one of the main decay modes of the resonances is through the annihilation of the quarks into three gluons, which then decay statistically (e.g. Fig.0-1).

C. Inclusive Momentum Spectra for Hadrons

With the data and corrections obtained from the preceding analysis, the final results are shown in Figs. V-1 and 2, and Tables V-1 and 2: the momentum spectra for hadrons from ψ and ψ' decays. Each event was weighed by the correction factors in Chapter IV. These cross sections have been normalized according to the luminosity determined in Section IV-1. The errors shown include the errors from the various correction factors in addition to the statistical errors, but do not include the normalization uncertainty of about 10% from the $\mu\mu$ pair statistics and the uncertainties of the branching ratio of the resonances into this mode. The cross sections are actually the differential cross sections into the

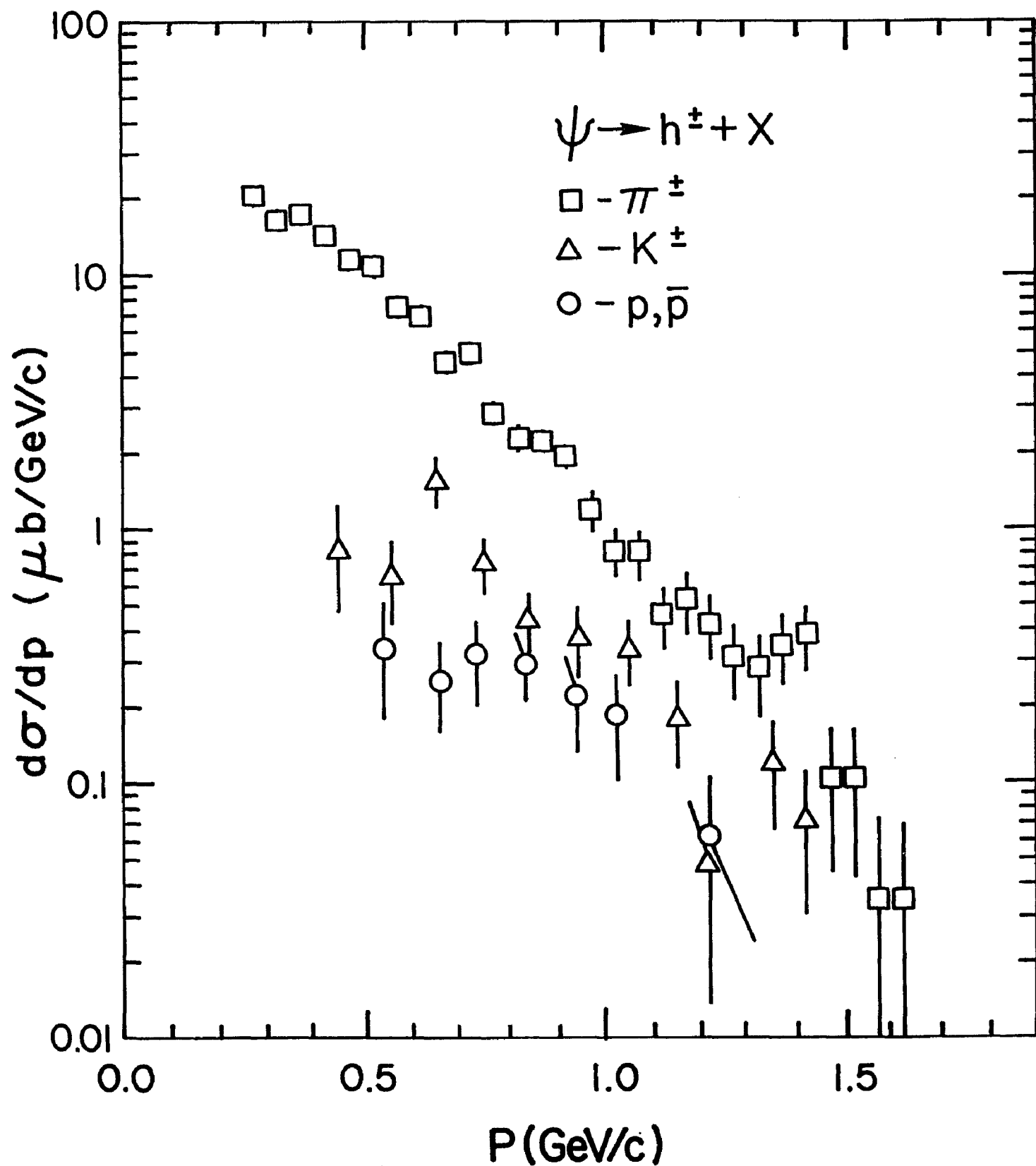


Fig. V-1 The inclusive momentum spectra of π^\pm , K^\pm , and p, \bar{p} for the ψ decays. The errors reflect both the statistical and systematic uncertainties in the correction factors, but do not include an overall 10% uncertainty due to normalization with the luminosity.

P	π^\pm	P	K^\pm
(GeV/c)	($\mu\text{b}/\text{GeV}/\text{c}$)	(GeV/c)	($\mu\text{b}/\text{GeV}/\text{c}$)
.275	20.5 ± 2.3	.45	$0.85 \pm .37$
.325	16.5 ± 1.4	.55	$0.66 \pm .24$
.375	16.8 ± 1.1	.65	$1.56 \pm .30$
.425	14.5 ± 1.0	.75	$0.75 \pm .18$
.475	11.5 ± 0.8	.85	$0.44 \pm .13$
.525	10.5 ± 0.7	.95	$0.38 \pm .11$
.575	$7.67 \pm .58$	1.05	$0.35 \pm .10$
.625	$6.96 \pm .54$	1.15	$0.18 \pm .07$
.675	$4.55 \pm .43$	1.25	$.050 \pm .035$
.725	$5.04 \pm .44$	1.35	$0.12 \pm .06$
.775	$2.90 \pm .33$	1.45	$.072 \pm .04$
.825	$2.30 \pm .29$	p, \bar{p}	
.875	$2.23 \pm .29$		
.925	$1.95 \pm .27$.45	$.019 \pm .015$
.975	$1.19 \pm .21$.55	$0.34 \pm .16$
1.025	$0.83 \pm .18$.65	$0.26 \pm .10$
1.075	$0.81 \pm .17$.75	$0.32 \pm .11$
1.125	$0.47 \pm .13$.85	$0.30 \pm .09$
1.175	$0.53 \pm .14$.95	$0.23 \pm .09$
1.225	$0.43 \pm .12$	1.05	$0.19 \pm .09$
1.275	$0.32 \pm .11$	1.15	$0 \pm .05$
1.325	$0.28 \pm .10$	1.25	$.064 \pm .043$
1.375	$0.36 \pm .11$		
1.425	$0.39 \pm .12$		
1.475	$0.11 \pm .06$		
1.525	$0.11 \pm .06$		
1.575	$.035 \pm .035$		
1.625	$.034 \pm .034$		

Table V-1 The differential production cross section, $\frac{d\sigma}{dp}$, as a function of the particles' momentum, for the ψ data set. The notation, $0 + \dots$, indicates a 1 standard deviation upper limit.

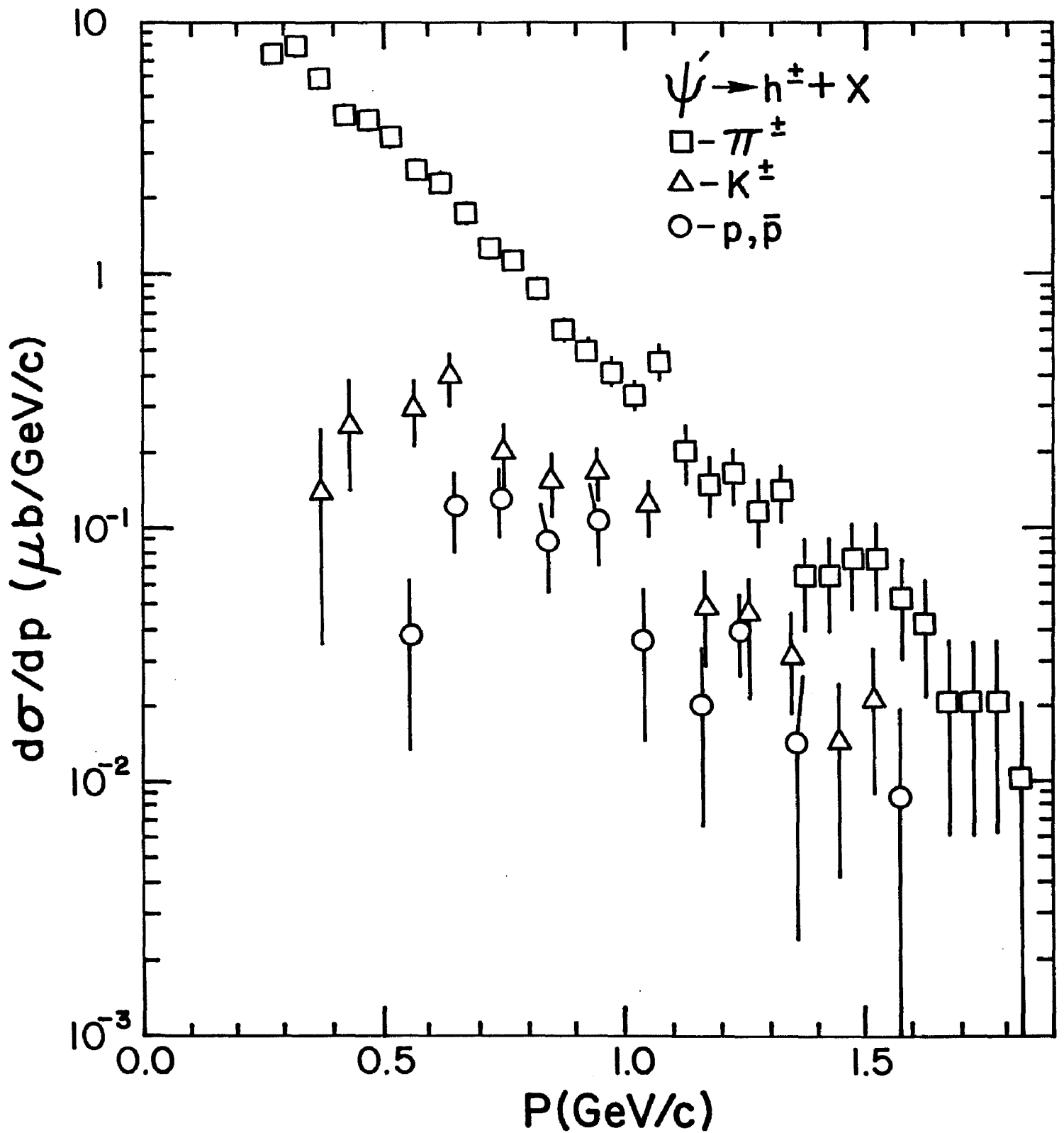


Fig. V-2 The inclusive momentum spectra for π^\pm , K^\pm , and p , \bar{p} from the ψ' decays. The errors include both statistical and systematic uncertainties, except for the 10% normalization uncertainty.

P	π^\pm	P	K^\pm
(GeV/c)	($\mu\text{b}/\text{GeV}/\text{c}$)	(GeV/c)	($\mu\text{b}/\text{GeV}/\text{c}$)
.275	7.39 \pm .79	.45	0.26 \pm .12
.325	7.84 \pm .52	.55	0.29 \pm .09
.375	5.77 \pm .37	.65	0.38 \pm .08
.425	4.18 \pm .28	.75	0.19 \pm .05
.475	3.96 \pm .25	.85	0.15 \pm .04
.525	3.45 \pm .22	.95	0.16 \pm .04
.575	2.56 \pm .18	1.05	0.12 \pm .03
.625	2.29 \pm .17	1.15	.048 \pm .020
.675	1.73 \pm .14	1.25	.045 \pm .018
.725	1.25 \pm .12	1.35	.030 \pm .015
.775	1.12 \pm .11	1.45	.014 \pm .010
.825	0.88 \pm .10	1.55	.021 \pm .012
.875	0.59 \pm .08		
.925	0.50 \pm .07		p, \bar{p}
.975	0.41 \pm .07		
1.025	0.33 \pm .06	.45	.008 \pm .004
1.075	0.44 \pm .07	.55	.037 \pm .024
1.125	0.19 \pm .05	.65	0.12 \pm .04
1.175	0.15 \pm .04	.75	0.13 \pm .04
1.225	0.16 \pm .04	.85	.087 \pm .035
1.275	0.12 \pm .035	.95	.105 \pm .035
1.325	0.14 \pm .04	1.05	.035 \pm .022
1.375	.064 \pm .026	1.15	.020 \pm .013
1.425	.064 \pm .026	1.25	.038 \pm .018
1.475	.075 \pm .028	1.35	.014 \pm .011
1.525	.074 \pm .028	1.45	0 \pm .01
1.575	.052 \pm .023	1.55	.009 \pm .010
1.625	.042 \pm .021		
1.675	.021 \pm .015		
1.725	.021 \pm .015		
1.775	.021 \pm .015		
1.825	.010 \pm .010		

Table V-2 The differential cross section, $\frac{d\sigma}{dp}$, as a function of the particles' momentum, for the ψ' data set.

spectrometer's angular acceptance, multiplied by 4π to account for the assumed isotropic production distribution. These cross sections, of course, include hadrons from the decays of the various short-lived resonances produced in the ψ decays, and which contaminate the measurement of the directly produced pions, kaons, and protons. In particular, the ψ' has a $57 \pm 8\%$ branching ratio into ψ . Thus, a determination of the direct decays of the ψ' are difficult. Note that the h^+ and h^- spectra are nearly the same.

One notices that the π^\pm spectra in both the ψ and ψ' decays falls off exponentially and smoothly, except near $1.4 \text{ GeV}/c$ where π^\pm 's from the $\rho\pi$ decay of the ψ enhance the cross section. In the ψ spectrum, an additional enhancement may be present at $0.775 \text{ GeV}/c$, which could be due to the pion recoiling from a meson of mass $2.15 \pm 0.05 \text{ GeV}/c^2$. Additionally, the ψ' spectrum has a slight enhancement at $1.075 \text{ GeV}/c$, again possibly due to a recoiling from a meson of mass $2.32 \pm 0.08 \text{ GeV}/c^2$. However the statistical significance of both these structures is marginal. The significance of these possible two-body decays and others is discussed in Section V-G.

In the K^\pm spectrum from the ψ decays, an enhancement at $0.65 \text{ GeV}/c$ is present, which may indicated a two-body

decay, K^+K^* , where the K^* has a mass of $2.18 \pm 0.08 \text{ GeV}/c^2$. The enhancement at 1.3-1.4 GeV/c in the K^+ spectrum from the ψ decays is due to the KK^* (892) mode. In the proton's spectrum from the ψ decays, the broad structure at 0.8 GeV/c may correspond to the pN^* (1470) decay mode. A similar structure is seen in the ψ' decays, possibly corresponding to a pN^* (1688) mode. The enhancement at 1.2 GeV/c in the ψ decays corresponds to the $p\bar{p}$ decay, while the enhancement at 1.55 GeV/c in the ψ' case corresponds to this mode.

D. Invariant Cross Sections

In Figs. V-3 and 4, the invariant cross sections are shown as a function of the particle's momentum. This cross section

$$E \frac{d^3\sigma}{dp^3} = \frac{E}{4\pi p^2} \frac{d\sigma}{dp}$$

displays the production rate into equal phase space volumes. A simple exponential curve fit to these spectra yield the parameters shown in Table V-3.

Note that the ψ' π^+ spectrum below 0.4 GeV/c. tends to break away from the simple exponential line. The DASP

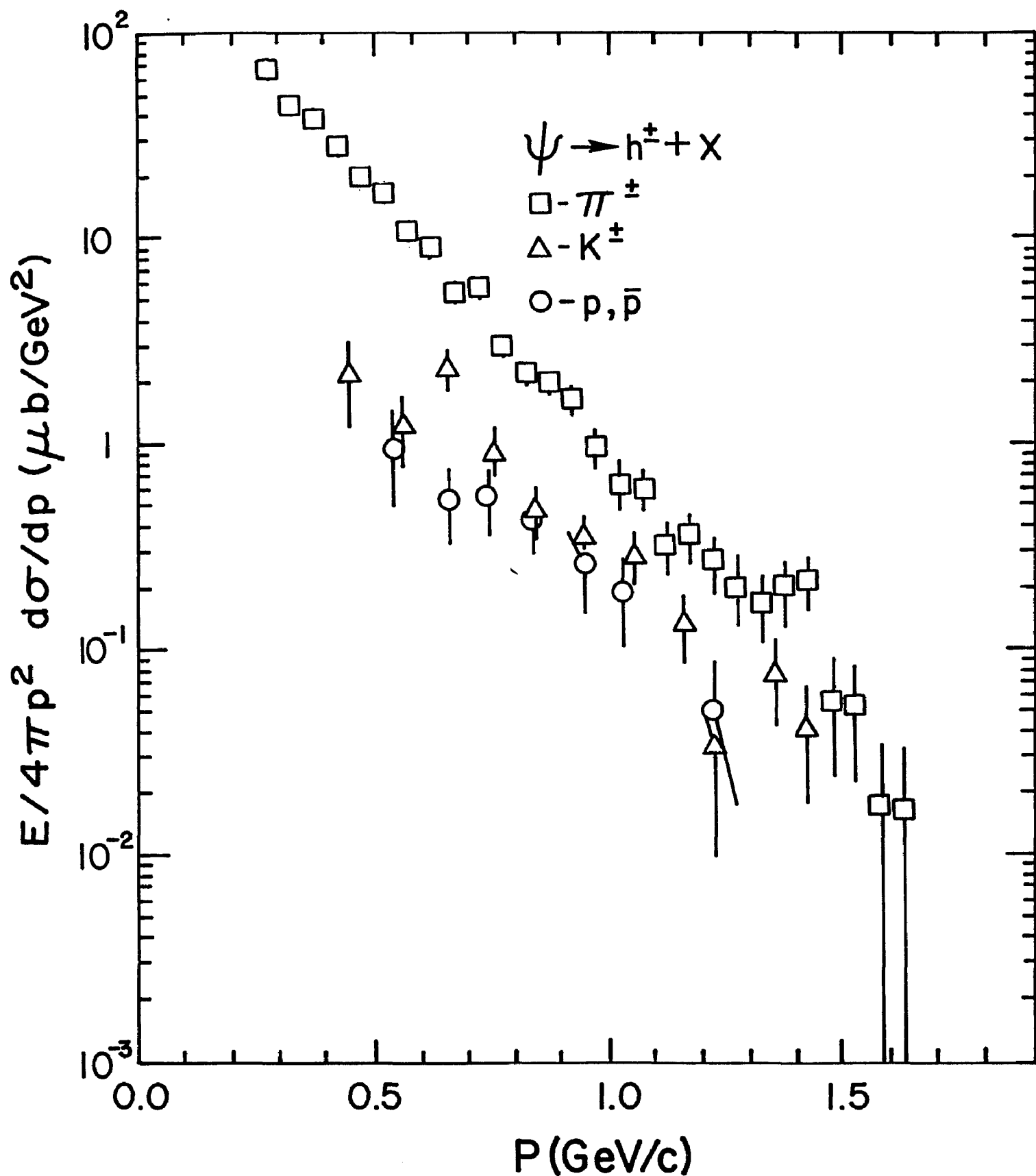


Fig. V-3 The invariant cross section for π^{\pm} , K^{\pm} , and p, \bar{p} from the ψ decays, as a function of the hadron's momentum.

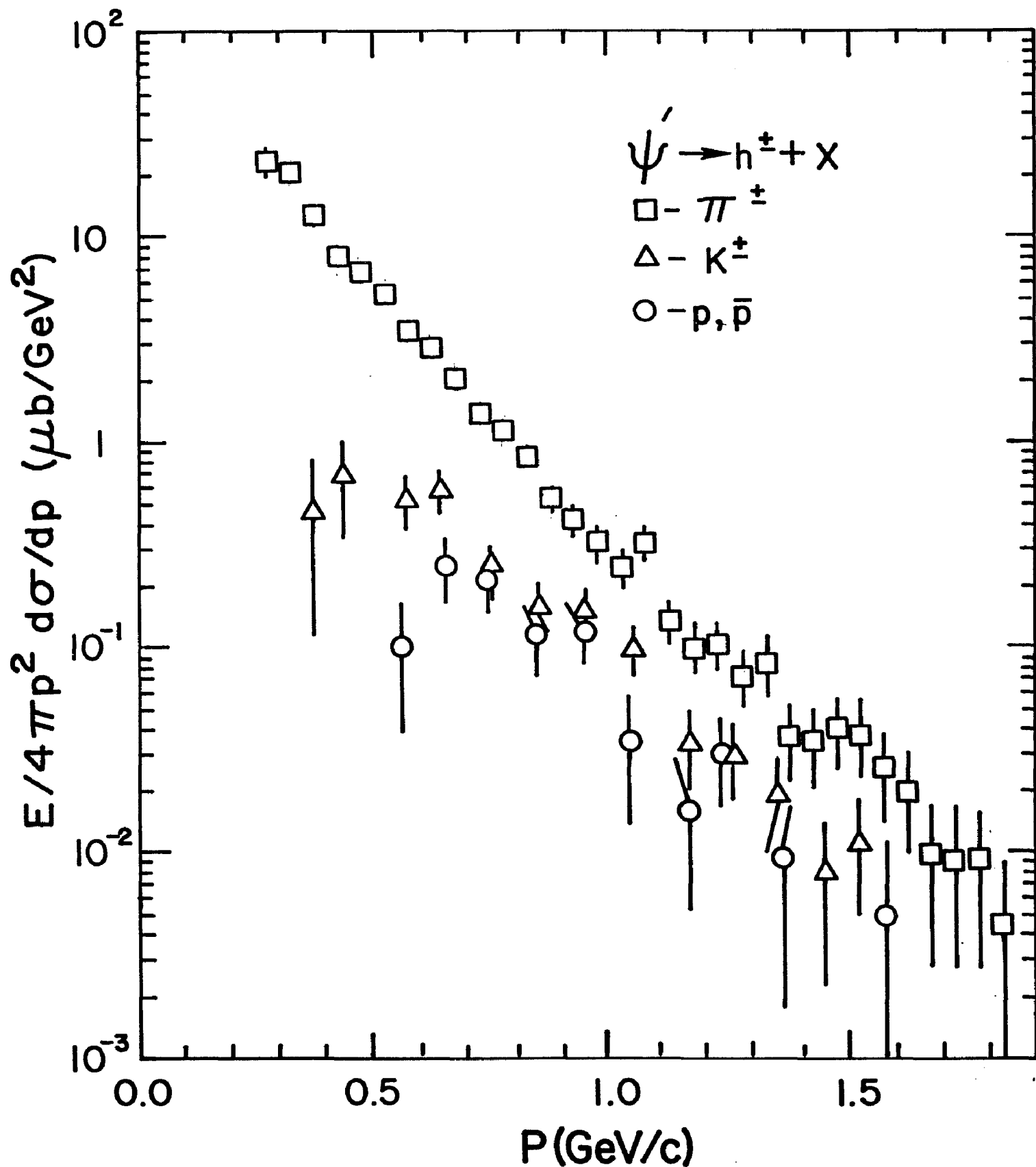


Fig. V-4 The invariant cross section for π^\pm , K^\pm , and p, \bar{p} from the ψ' decays.

Invariant Cross Section Parameterization

$$\frac{E}{4\pi p^2} \frac{d\sigma}{dp} = A e^{-bp}$$

Particle	A ($\mu\text{b}/\text{GeV}^2$)	b (c/GeV)	$\chi^2/\text{D.o.F.}$
ψ decays			
π^\pm	37.56 ± 0.15	6.02 ± 0.18	16.9/14
K^\pm	4.52 ± 0.11	5.03 ± 0.06	14.5/6
p, \bar{p}	0.52 ± 0.01	3.11 ± 0.20	0.56/5
ψ' decays	p > 0.4 GeV/c		
π^\pm	10.8 ± 0.1	5.83 ± 0.17	14.1/14
K^\pm	0.78 ± 0.06	4.34 ± 0.42	4.64/6
p, \bar{p}	0.23 ± 0.02	3.50 ± 0.84	19.1/6

Table V-3 Exponential fits to the invariant cross sections from the ψ and ψ' data sets. Note that the ψ' cross sections are only fit for p > 0.4 GeV/c

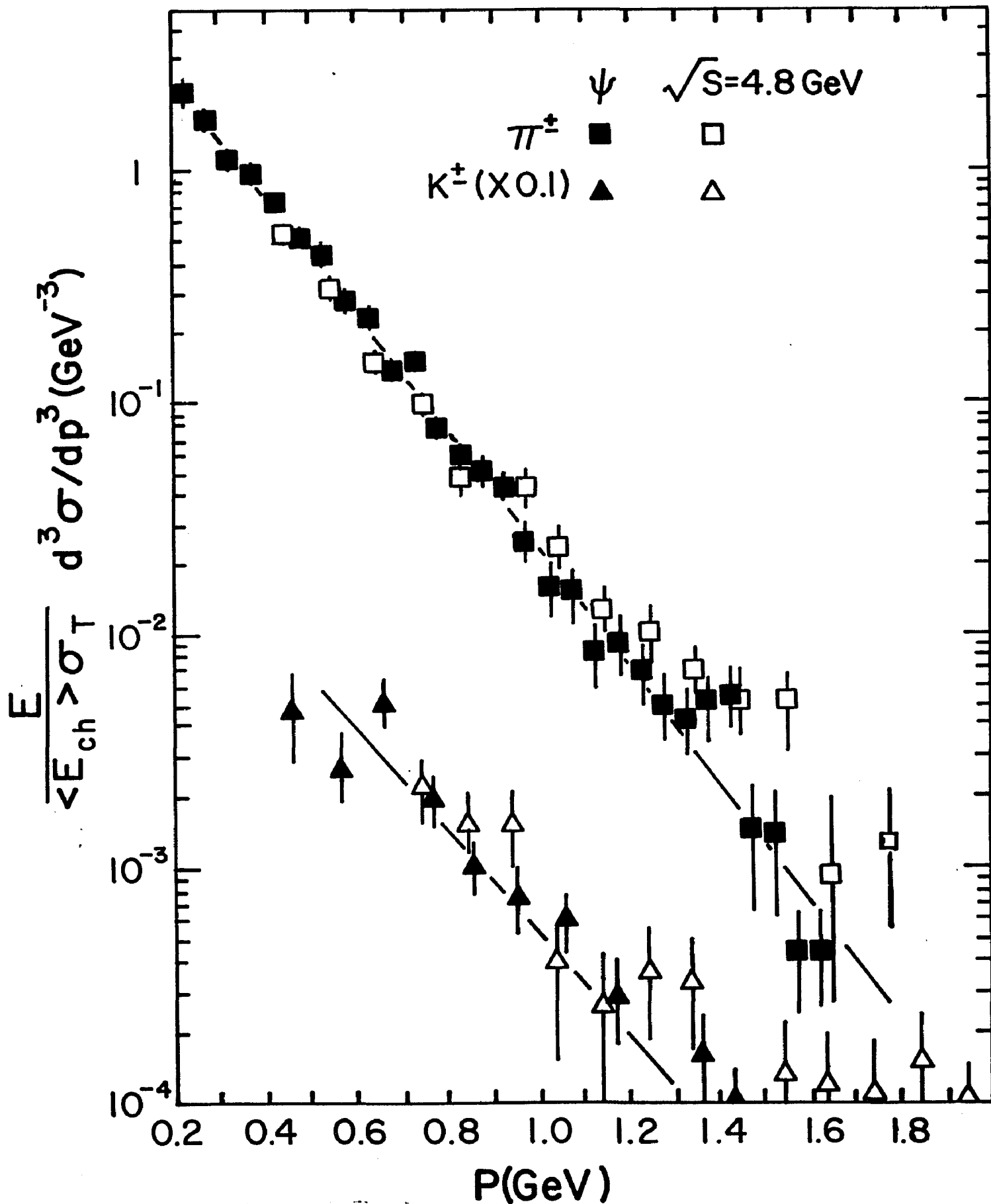


Fig. V-5 The invariant cross sections for π^\pm and K^\pm from the ψ decays and the e^+e^- annihilation data at $\sqrt{s} = 4.8 \text{ GeV}$, normalized by the integral of each cross section over momentum.

group¹² attributes this to the decay,

$$\psi' \rightarrow \psi \pi^+ \pi^{-+}.$$

The slope parameters for the ψ and ψ' are nearly the same. Interestingly, the slope parameters for the inclusive hadron spectra at $\sqrt{s} = 4.8$ GeV, obtained with the same spectrometer¹³, are nearly the same. Note that the integral of the invariant cross section gives $\langle E_{ch} \rangle \sigma_{tot}$, where $\langle E_{ch} \rangle$ is the average energy into charged hadrons and σ_{tot} is the total hadronic cross section. If the ψ and 4.8 GeV cross sections are normalized by their appropriate integrals¹⁴, the Fig. V-5 is the result. The line through the points is the fitted curve for the ψ results. The shape of both the 4.8 GeV and ψ , π^+ and K^+ curves are nearly identical below 1.0 GeV/c and begin to diverge thereafter. One notices that the ψ and 4.8 GeV π^+ cross sections have the same behavior around 1.4 GeV/c. In the ψ case, it is due to the two-body decay, $\rho \pi$, while in the 4.8 GeV case, it appears to be due to the contributions from the scaling interactions coming into play. Recalling the two-component hypothesis, we see that the low momentum part of the spectrum appears to follow the exponential behavior of the statistical models, while above about 1.0 GeV/c, the scaling component of the

cross section begins to show up.

From the pp data by Alper, et al.⁸ on the inclusive production of hadron near 90° in the center of mass, the slope parameters they obtain are suprisingly close to those from the ψ and ψ^* decays. Over a wide s range, and nearly the same momentum range, their slopes are:

$$B_{\pi^\pm} = 6.0 \text{ GeV}^{-1}, \quad B_{K^\pm} = 5.0 \text{ GeV}^{-1}, \quad \text{and} \quad B_p = 4.0 \text{ GeV}^{-1}.$$

It seems unlikely that the slopes agree with those of the ψ decays due to chance alone. The fact that the non-resonant e^+e^- data exhibit similar slopes may indicate the validity of the statistical models in explaining the low momentum part of the spectrum.

If the invariant cross sections are plotted as a function of the particle's energy, Fig. V-6 and V-7 result. Tables V-4 and 5 list the values of these cross sections. Fitting the data with a simple exponential, $A \exp(-B E)$, gives the results in Table V-6. The slope parameters, in this case, correspond to an effective hadronic temperature of about 160 MeV. Again, this is nearly the same as is found in hadron-hadron collisions¹⁵.

In Fig. V-8, the cross sections are compared with those from the DASP collaboration¹². However, their cross sections

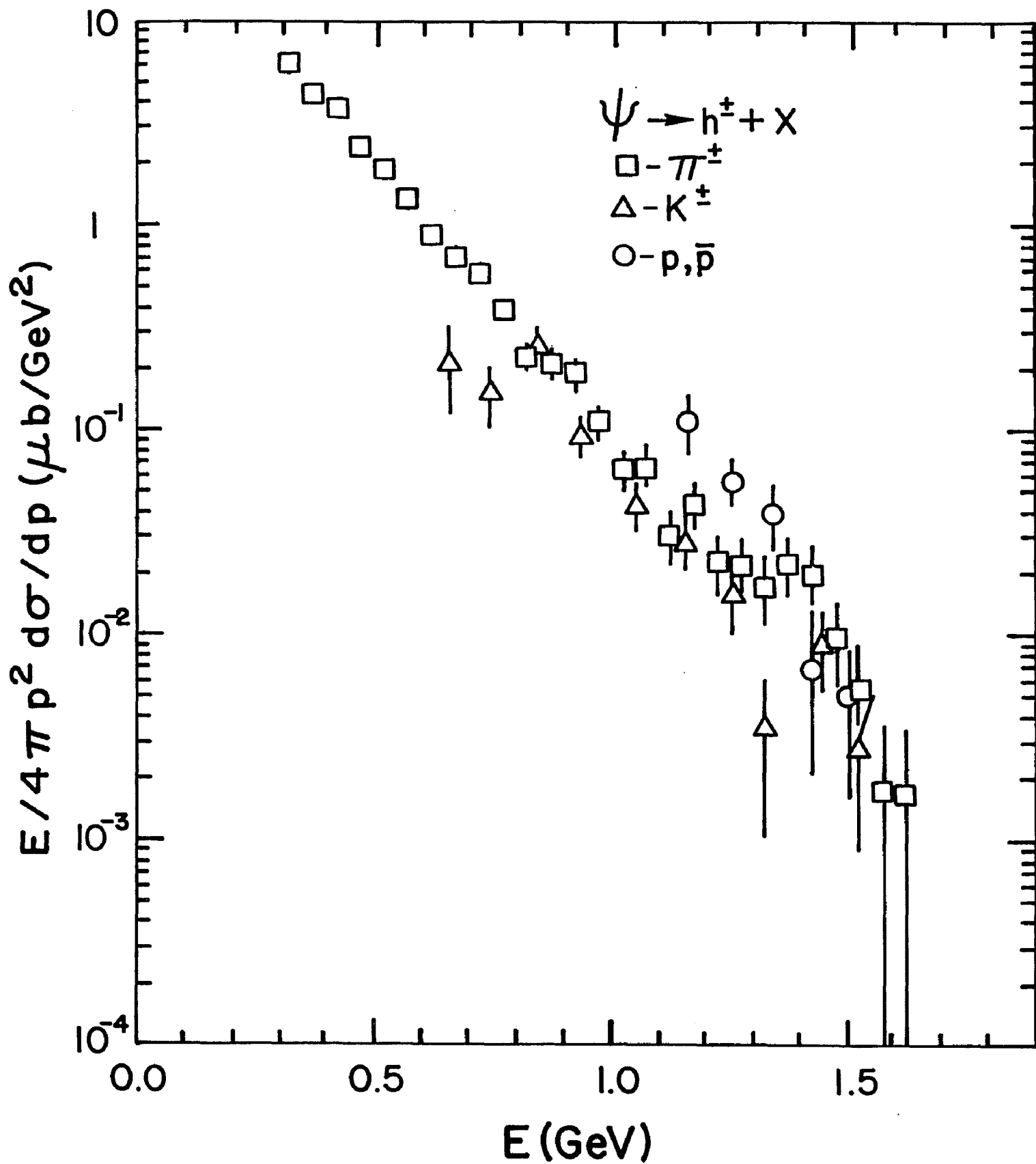


Fig. V-6 The invariant cross section for π^{\pm} , K^{\pm} , and p, \bar{p} from the ψ decays as a function of the hadron's energy.

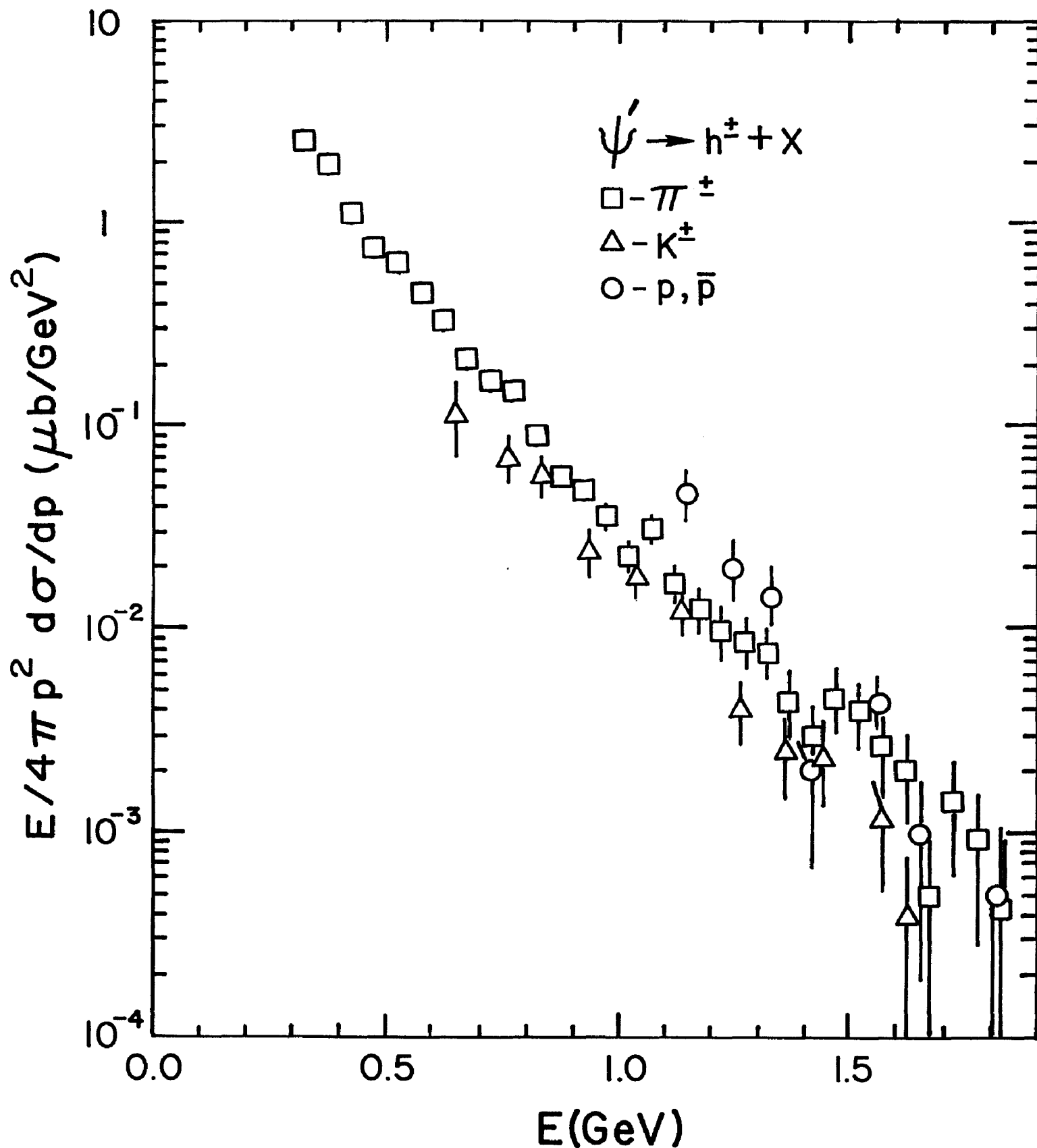


Fig. V-7 The invariant cross section for π^\pm , K^\pm , and p, \bar{p} as a function of the hadron's energy from the ψ' decays.

E (GeV)	π^{\pm} (nb/GeV ²)	E (GeV)	K^{\pm} (nb/GeV ²)
.325	2472 \pm 194	.65	116. \pm 48.
.375	1911 \pm 116	.75	68.3 \pm 17.3
.425	1082 \pm 69.	.85	56.5 \pm 12.1
.475	746. \pm 49.	.95	24.2 \pm 5.8
.525	636. \pm 40.	1.05	18.5 \pm 4.3
.575	442. \pm 30.	1.15	12.6 \pm 3.1
.625	324. \pm 23.	1.25	4.1 \pm 1.5
.675	211. \pm 18.	1.35	2.5 \pm 1.1
.725	166. \pm 15.	1.45	2.3 \pm 1.0
.775	147. \pm 13.	1.55	2.3 \pm 0.7
.825	91.2 \pm 10.	1.65	0.76 \pm 0.38
.875	56.1 \pm 7.6	1.75	0 \pm 0.2
.925	47.6 \pm 6.8	1.85	0 \pm 0.1
.975	37.1 \pm 5.9		
1.025	23.2 \pm 4.6		p, \bar{p}
1.075	31.9 \pm 5.2	1.15	45.6 \pm 11.9
1.125	17.2 \pm 3.7	1.25	20.1 \pm 6.5
1.175	12.5 \pm 3.0	1.35	14.7 \pm 4.7
1.225	9.8 \pm 2.6	1.45	4.0 \pm 1.4
1.275	8.8 \pm 2.4	1.55	4.3 \pm 1.8
1.325	7.8 \pm 2.2	1.65	1.0 \pm 0.8
1.375	4.4 \pm 1.6	1.75	0 \pm 0.5
1.425	3.0 \pm 1.3	1.85	1.0 \pm 0.6
1.475	4.6 \pm 1.6		
1.525	3.9 \pm 1.5		
1.575	2.7 \pm 1.2		
1.625	2.0 \pm 1.0		
1.675	0.50 \pm .50		
1.725	1.4 \pm .8		
1.775	0.93 \pm .66		
1.825	0.45 \pm .45		

Table V- 5 The invariant cross section for the different hadrons from the ψ' data set, as a function of the particles' energy.

Invariant Cross Section Parameterization

$$\frac{E}{4\pi} p^2 \frac{d\sigma}{dp} = A e^{-bE}$$

Particle	A ($\mu\text{b}/\text{GeV}^2$)	b (GeV^{-1})	$\chi^2/\text{D.o.F.}$
ψ decays			
π^\pm	45.1 ± 0.1	6.13 ± 0.17	16.1/14
K^\pm	13.8 ± 0.2	5.29 ± 0.89	12.3/5
p, \bar{p}	95.2 ± 3.5	5.92 ± 0.95	1.28/4
ψ' decays $E > 0.4 \text{ GeV}$			
π^\pm	13.8 ± 0.2	6.00 ± 0.17	18.4/14
K^\pm	3.45 ± 0.05	5.06 ± 0.4	2.69/5
p, \bar{p}	57.1 ± 10.5	6.3 ± 1.2	7.7/6

Table V-6 Exponential fits to the invariant cross sections as a function of energy. Note that the ψ' data are fitted only above 0.4 GeV.

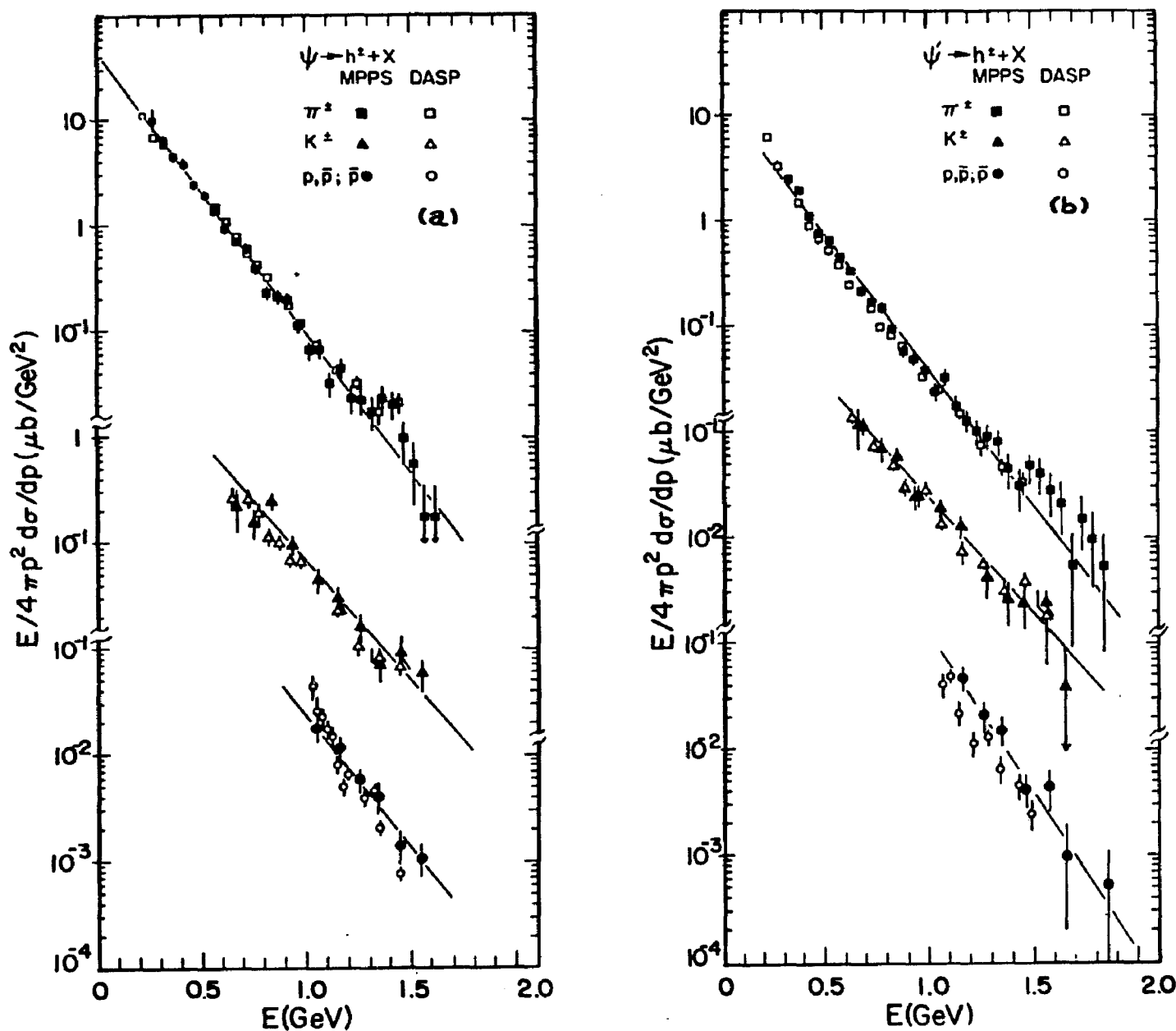


Fig. V-8 A comparison between the invariant cross sections obtained in this experiment and those from the DASP experiment (Ref. 18) for hadrons from ψ (a) and ψ' (b) decays. Note that the DASP data has been scaled by factors of 4.7 and 6.1 for the ψ and ψ' data, respectively, to account for the fact that they integrate their cross sections over the full width of the resonances.

are produced by integrating over the entire resonance, while our data is taken near the resonance's peak. A scale factor is applied to their data which is equal to the ratio of the area of the peak measured in our experiment, to the total area. Using the SLAC-LBL values, the scale factor is 4.7 at the ψ and 6.1 at the ψ' . The agreement is very good.

E. Particle Fractions

In Fig. V-9, as well as in Table V-7, the fractions of each charged species in the total cross section is shown as a function of the particle's momentum. Both the ψ and ψ' fractions show a similar behavior; the K^+ fraction approaches 0.2 and the p, p fraction approaches 0.1. The fact that the two fraction distributions are so similar is not surprising since over half of the ψ' decays include ψ decays. On this same figure, the 4.8 GeV data particle fractions are also shown. One sees that they have nearly the same magnitude and behaviour as the resonance decay fractions. Data taken at $\sqrt{s} = 7$ GeV with this spectrometer ¹⁶ appear to have surprisingly similar particle fractions as the resonances.

Fig. V-10 shows the ratio of the particles as a function of their momentum. Note that the K^+/π^+ ratio

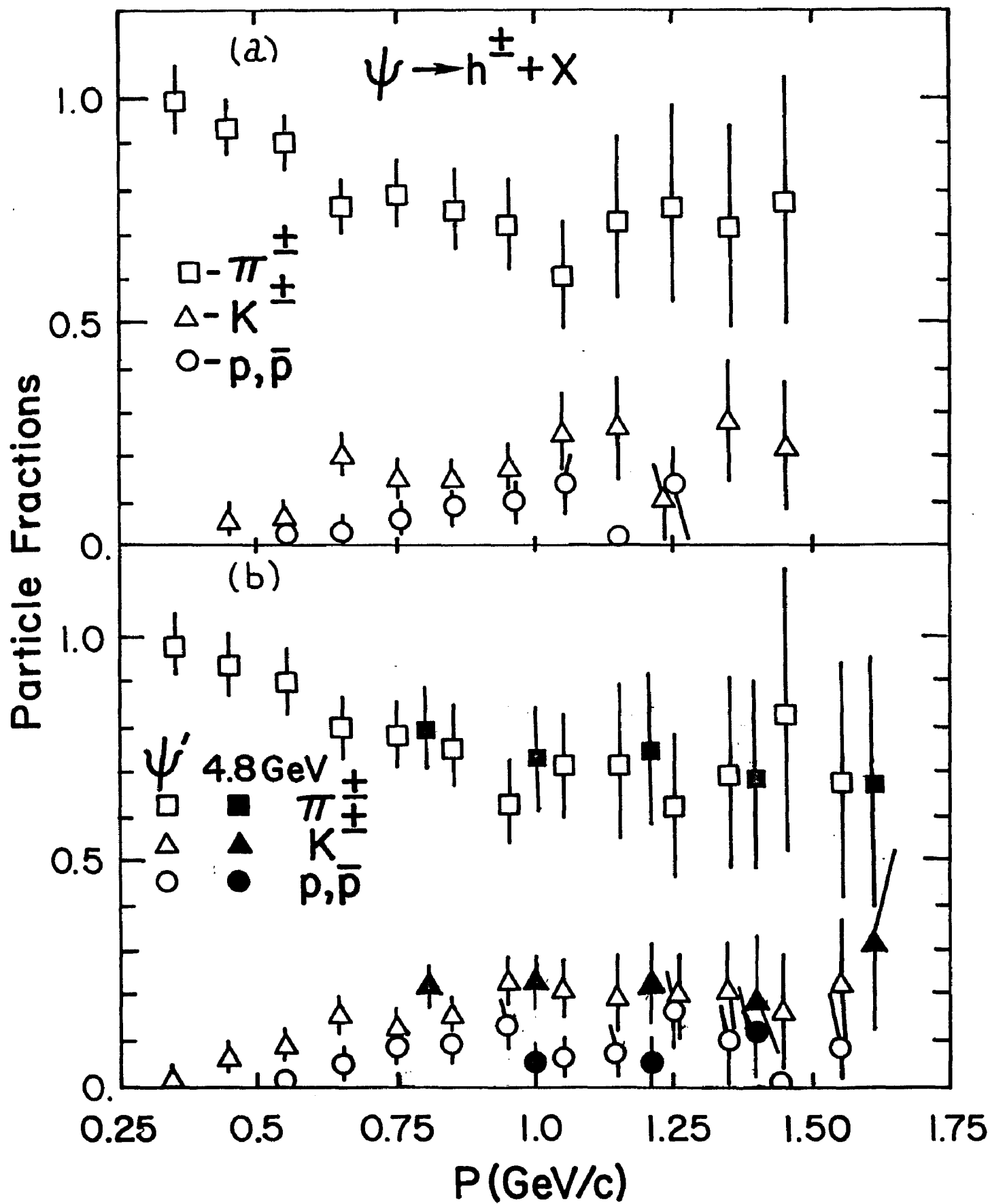


Fig. V-9 The fraction of π^\pm , K^\pm , and p, \bar{p} in the hadron samples from the ψ , (a), and ψ' , (b), decays, as a function of the hadron's momentum. In (b), the particle fractions from the e^+e^- data at $\sqrt{s} = 4.8$ GeV are compared with those from the ψ' decays.

Ψ (a)	P (GeV/c)	π^{\pm}/All	K^{\pm}/All	$p, \bar{p} / \text{All}$
	.45	.937 \pm .076	.061 \pm .027	.002 \pm .002
	.55	.902 \pm .066	.064 \pm .024	.033 \pm .016
	.65	.760 \pm .065	.206 \pm .042	.034 \pm .014
	.75	.787 \pm .077	.149 \pm .037	.064 \pm .022
	.85	.755 \pm .094	.146 \pm .045	.099 \pm .031
	.95	.721 \pm .108	.175 \pm .054	.104 \pm .045
	1.05	.607 \pm .122	.256 \pm .082	.138 \pm .067
	1.15	.732 \pm .187	.268 \pm .112	0.0 \pm .1
	1.25	.766 \pm .228	.102 \pm .076	.132 \pm .093
	1.35	.721 \pm .228	.279 \pm .138	---
	1.45	.775 \pm .280	.225 \pm .140	---

Ψ' (b)	P (GeV/c)	π^{\pm}/All	K^{\pm}/All	$p, \bar{p} / \text{All}$
	.45	.939 \pm .066	.059 \pm .015	.002 \pm .001
	.55	.901 \pm .063	.088 \pm .026	.011 \pm .007
	.65	.800 \pm .064	.153 \pm .035	.048 \pm .016
	.75	.786 \pm .078	.129 \pm .035	.085 \pm .028
	.85	.756 \pm .092	.155 \pm .044	.089 \pm .036
	.95	.628 \pm .094	.227 \pm .060	.145 \pm .051
	1.05	.712 \pm .117	.223 \pm .065	.060 \pm .041
	1.15	.719 \pm .162	.200 \pm .088	.082 \pm .057
	1.25	.624 \pm .162	.203 \pm .090	.173 \pm .087
	1.35	.696 \pm .215	.209 \pm .113	.095 \pm .081
	1.45	.830 \pm .316	.170 \pm .128	0.0 \pm .10
	1.55	.681 \pm .265	.226 \pm .144	.092 \pm .110

Table V- 7 The particle fractions as a function of their momentum, for the Ψ ,(a) and the Ψ' ,(b) data sets. The errors are derived from the statistical and systematic uncertainties.

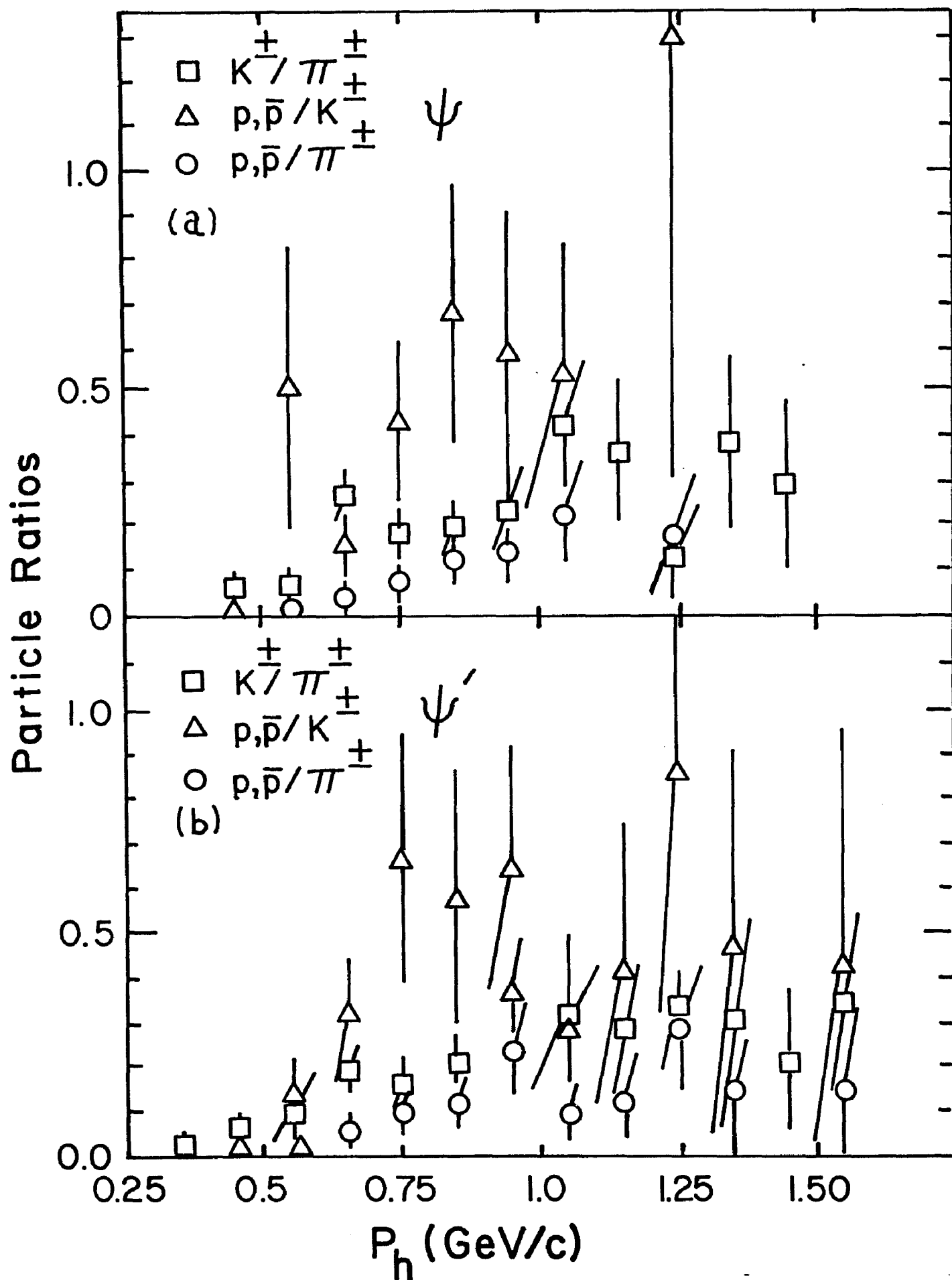


Fig. V-10 The ratios, K^\pm/π^\pm , $p, \bar{p}/K^\pm$, and $p, \bar{p}/\pi^\pm$ as a function of the hadrons' momentum for the ψ , (a), and ψ' , (b), decays.

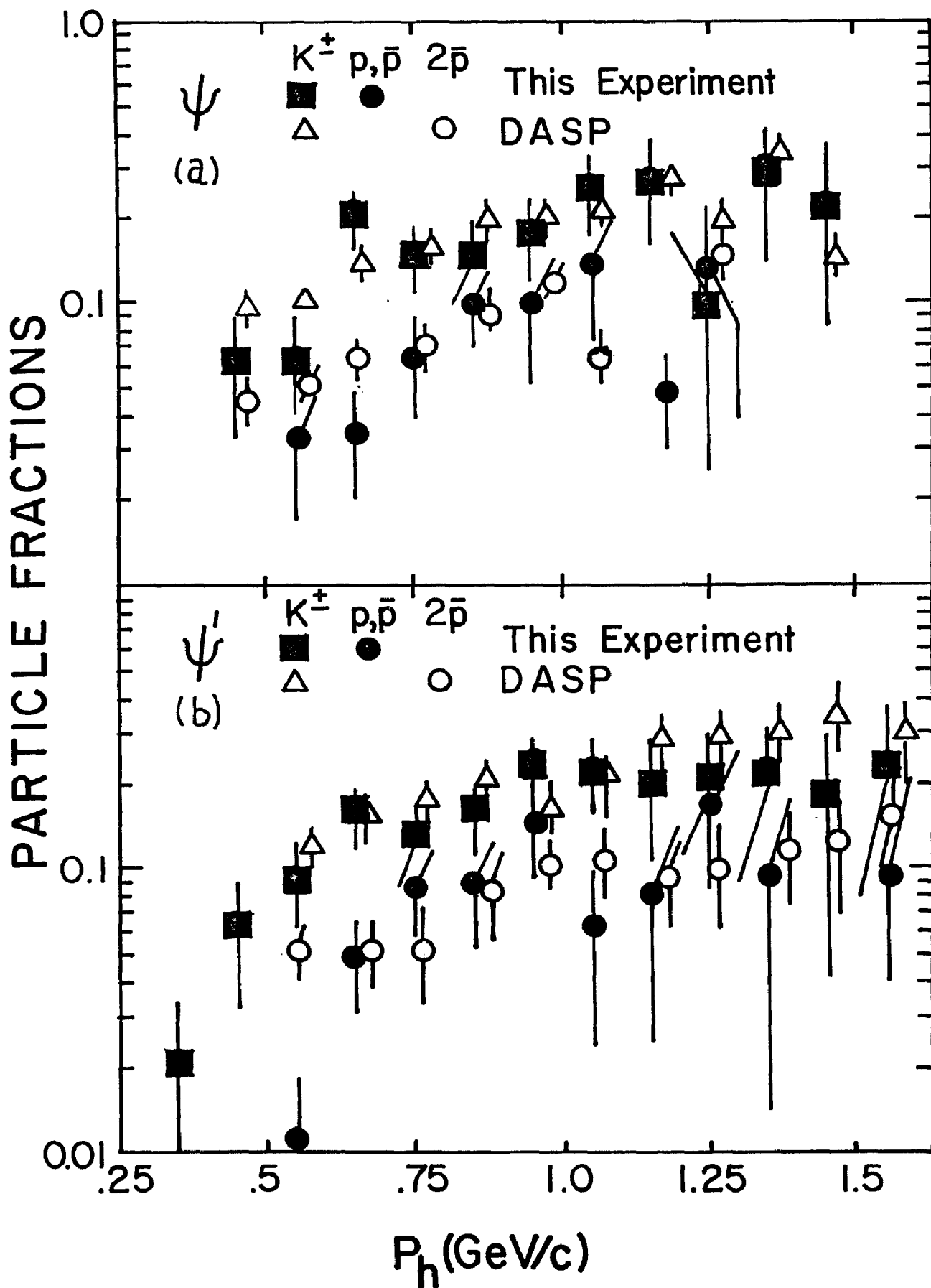


Fig. V-11 A comparison of the hadronic fractions from the ψ , (a), and ψ' , (b), decays as measured by this experiment with those from the DASP experiment.

approaches 0.3, while the p/K^+ ratio rises to 0.5. It may be amusing to note that these ratios are nearly the same as the inverse of the particles' mass ratio.

The particle fractions at the high momentum end are slightly different than the DASP results. In Fig. V-11, the K^+ and proton fractions from the two experiments are compared. One notices that the DASP K^+ fraction is rising above 1.0 GeV/c, while our K^+ fractions appear to stabilize at this momentum. However, within the errors of both experiments, the fractions agree. It should be remarked that the DASP group relies solely on a time of flight system for hadron separation, while our spectrometer uses both a time of flight and a threshold Cherenkov counter system.

The total fraction of each species comes from the integral of the momentum distribution. Although the data are truncated below 200 MeV/c due to the magnetic field, one can extrapolate the data to zero momentum by noting the relationship between the momentum spectrum and the invariant cross section, and the fact that the invariant cross section follows a simple exponential. Assuming the exponential behavior in $E d^3\sigma/dp^3$ continues to zero momentum, the following are the total inclusive cross sections for the ψ decays:

$$\sigma_{\pi^{\pm}} = 10.45 \pm 0.2 \mu\text{b.}, \quad \sigma_{K^{\pm}} = 1.19 \pm 0.07 \mu\text{b.},$$

$$\sigma_{p, \bar{p}} = 0.25 \pm 0.03 \mu\text{b.}$$

This gives branching fractions of:

$$b_{\pi^{\pm}} = 0.878 \pm .008, \quad b_{K^{\pm}} = 0.100 \pm .006, \quad b_{p, \bar{p}} = 0.022 \pm .002.$$

For the ψ^0 decays the results are:

$$\sigma_{\pi^{\pm}} = 3.63 \pm 0.10 \mu\text{b.}, \quad \sigma_{K^{\pm}} = 0.43 \pm 0.03 \mu\text{b.},$$

$$\sigma_{p, \bar{p}} = 0.09 \pm 0.01 \mu\text{b.}$$

with branching fractions of:

$$b_{\pi^{\pm}} = 0.874 \pm .017, \quad b_{K^{\pm}} = 0.103 \pm .007, \quad b_{p, \bar{p}} = 0.023 \pm .002.$$

Since many of the decay modes of the ψ^0 involve the decays of the ψ , and the intermediate χ states, we can subtract the appropriate branching fractions into these states from the measured totals. In lieu of a measurement, the χ states are assumed to have the same branching fractions into the stable hadrons as the ψ . The necessary subtraction from the total cross sections are then:

$$\sigma_{\pi^{\pm}} = 2.47 \pm 0.52 \mu\text{b.}, \quad \sigma_{K^{\pm}} = 0.29 \pm 0.08 \mu\text{b.},$$

$$\sigma_{p, \bar{p}} = 0.06 \pm 0.02 \mu\text{b.}$$

This gives the branching fractions for the direct ψ' decays as:

$$b_{\pi^{\pm}} = 0.87 \pm 0.035, \quad b_{K^{\pm}} = 0.11 \pm 0.04, \quad b_{p, \bar{p}} = 0.02 \pm 0.01.$$

Thus, there appears to be little difference between the direct decays of the ψ and ψ' . Further, we note that the branching fractions in the 4.8 GeV data are:

$$b_{\pi^{\pm}} = 0.92 \pm 0.11, \quad b_{K^{\pm}} = 0.073 \pm 0.009, \quad b_{2\bar{p}} = 0.009 \pm 0.007.$$

Even above the charm threshold, the total kaon fraction is not much different than the psions' decays.

F. Multiplicity Distributions

Since we find that the statistical model accurately describes the hadronic momentum spectra, it is of some interest to see if further predictions of this model hold. In particular, the model makes specific predictions about the multiplicity of the particles emitted from the collisions. For example, the thermodynamic analysis¹⁷ of Engels, Schilling, and Satz predicts a total particle multiplicity of

$$\langle N_{\text{tot}} \rangle \propto M$$

where M is the mass of the fireball. For most experiments only the charged fraction of the multiplicity is usually measured, thus comparing the statistical predictions with data can be somewhat misleading if the neutral particle multiplicity is totally unknown. For example, if only pions are produced in the final state, one might expect from isospin invariance that

$$\langle N_{\pi^+} \rangle = \langle N_{\pi^-} \rangle = \langle N_{\pi^0} \rangle .$$

Thus the charged multiplicity is two-thirds of the total. However, the inclusion of other hadrons such as η , K and nucleons, along with the various resonances, may change the charged fraction significantly.

In the simple case, one might expect that the energy into the charged hadrons is two-thirds of the total energy. The data from the SLAC-LBL group find¹⁸ the charged energy fraction to decrease significantly with total energy, and lower than the simple picture predicts. At $\sqrt{s} = 3.1$ GeV, they find a charged fraction of about 54%.

In hadron-hadron collisions, the charged multiplicity as a function of

$$M = \sqrt{s} - M_a - M_b$$

where M_a, M_b are the masses of the initial particles, fits ¹⁹ the empirical relation:

$$\langle N_{ch} \rangle = 2.45 + 0.32 \ln(M) + 0.53 \ln^2(M).$$

One sees that the statistical model falls short of fully describing the results. However, returning to the two component picture, we see that by including both the statistical and constituent contributions, the multiplicity is predicted to be

$$\langle N_{ch} \rangle = \frac{1}{\langle E_{ch} \rangle \sigma_{tot}} \sum_{\text{hadron types}} \int d^3p [C(M)e^{-2r_h p} + \frac{x^2 e^{-6x}}{(p^2 + m^2)^2}].$$

In defining the multiplicity in our data, we use the polymer to measure the charged tracks. Since this device has several non-ideal properties, such as a limited solid angular coverage, a large photon conversion probability and limited angular resolution, a Monte Carlo simulation was made to determine the detection efficiency as a function of the number of charged particles produced. This program generated events where one particle entered the solid angle of the spectrometer, and the other particles were distributed isotropically. The input parameters were: the solid angle of the polymer (0.905 of 4π ster), the track

detection efficiency (0.982), and the minimum angle for which two tracks can be separated (4.0°), along with the observed angular resolution (1.5°). The result is then a matrix, O , which gives the probability of observing N tracks if $M-1$ tracks were isotropically produced and one enters spectrometer, i.e.:

$$O_{NM} = P(N \text{ observed} \mid M \text{ produced}).$$

One then needs the inverse probability to obtain the true multiplicity from the observed one. It should be noted that the problem of photon conversion is particularly troublesome in deciphering the true probability. From the known amounts of material in the beam pipe (.097 radiation lengths) and in the inner part of the polymer (.021 r.l.) the probability of a photon to convert and mimic a charged particle is 10.9%. Thus if 4 photons are produced, the chance that one converts is 43.%, while the probability that two convert is about 6%. The charged multiplicity is then dependent on the model one expects the final state to have, particularly on the number of photons in the final state. Due to the non-negligible photon conversion, the system of equations for the unfolding of the multiplicity is no longer constrained. To compensate for this dilemma, one finds the

expected multiplicity for all charge numbers, and then assumes that the ratio of odd to even reflects the number of photons. Thus the expected three prong distribution compared to the expected two prong distribution gives the number of events having one photon convert to those that have no photon conversion. From this procedure, we find that the average number of photons ranges from 10 ± 3 to 6.0 ± 1.5 as the charged multiplicity ranges from 2 to 10 from the ψ decays. The corresponding photon multiplicities from the ψ' decays range from 10.0 ± 2.5 to 7.0 ± 2.0 for 2 to 10 charged-track events. The average photon multiplicities over all events are 6.6 ± 1.0 and 8.2 ± 1.5 for the ψ and ψ' data, respectively.

In Fig. V-12, the results of unfolding the multiplicity are shown. This figure shows both the expected even multiplicity and the observed multiplicities for events that have a hadron entering the spectrometer. The number in each multiplicity bin has been corrected according to the nature and momentum of the spectrometer particles associated with them. The observed distributions do not show any large difference between odd and even multiplicities. This is what one expects from particle losses from the ends of the polymer and from photon conversion.

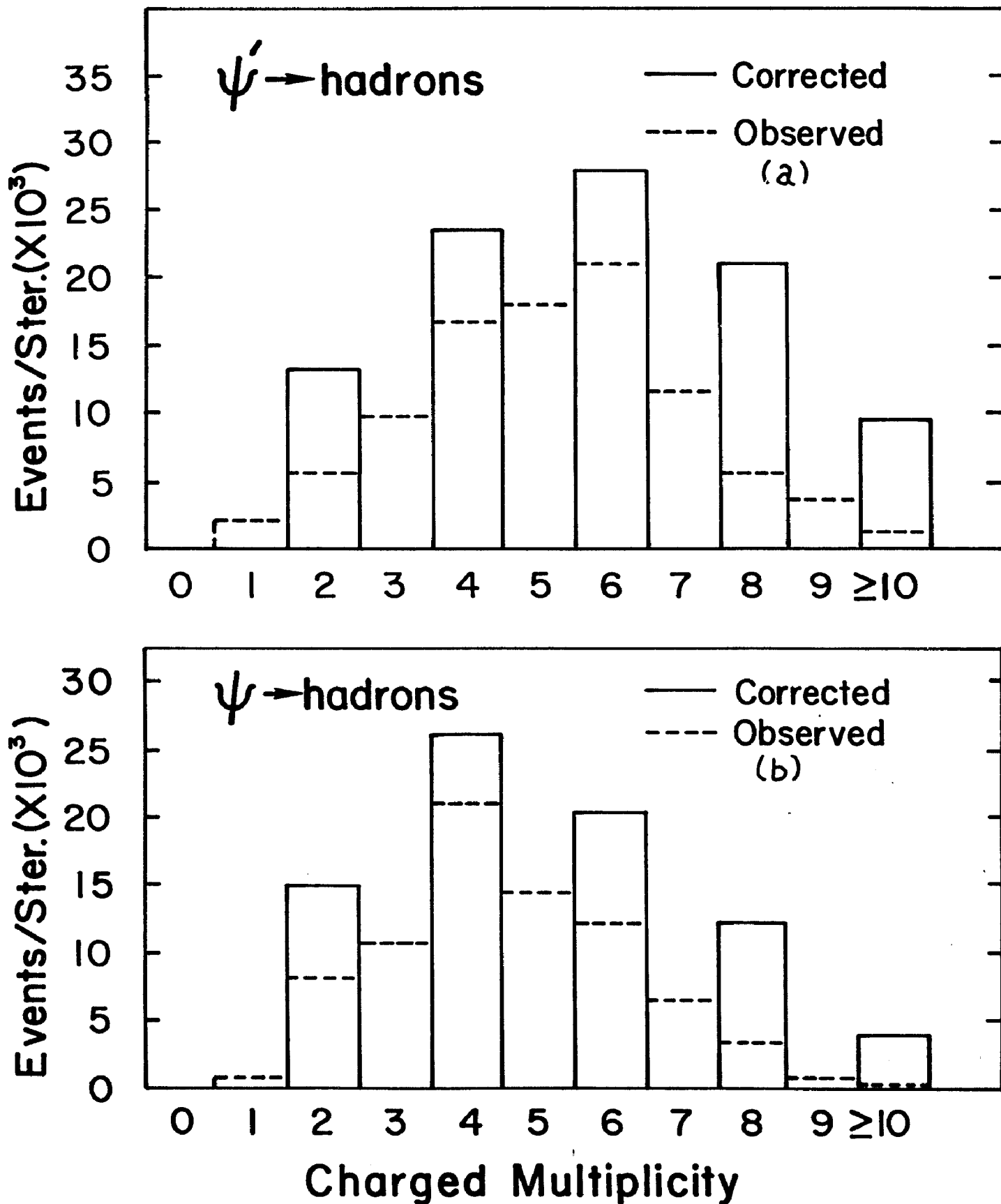


Fig. V-12 The observed (dashed line) and corrected (solid line) charged multiplicity distributions associated with a hadron in the spectrometer, for the ψ' , (a), and ψ , (b), decays. The corrected multiplicities are constrained to be even.

Figs. V-13 and V-14 show the spectrometer particle's momentum distributions as a function of the observed and expected multiplicity. Note that these distributions have been corrected with the inclusive distribution's factors, but are not normalized to the luminosity. One notes that the slope of the spectra increases with increasing multiplicity. In order to observe the production into equal phase space volumes, the invariant spectra are shown in Fig. V-15. One notes the generally exponential nature of the distributions. The lines drawn through the data are exponential fits, with the parameters given in Table V-8. In the ψ^0 data, the data seem to break away from the curve below 0.4 GeV/c, reflecting the pattern seen in the inclusive distribution. Again, this indicates the cascade decay of the ψ^0 to the ψ emitting two charged pions.

In order to produce the average multiplicity associated with the hadron in the spectrometer, one must account for the intrinsic multiplicity bias in the triggering of the apparatus. For instance, if the spectrometer had a triggering acceptance extending to zero momentum, the chances that a four prong event would trigger it would be twice that of a two prong event. However, the momentum cutoff and the fact that the momentum spectra of different

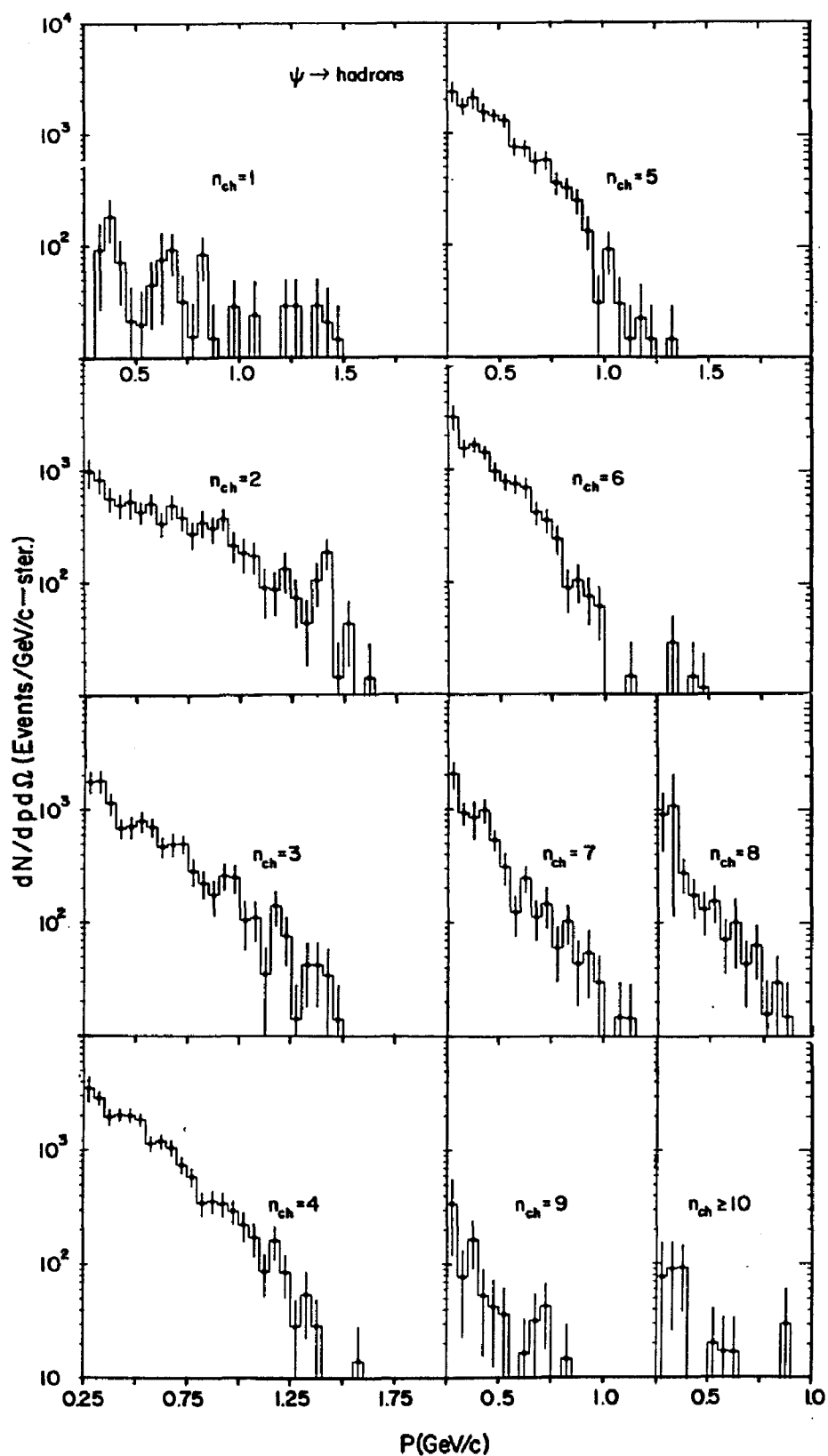


Fig. V-13 a) The observed momentum distributions associated with from 1 to ≥ 10 charged tracks in the polymer. The number of spectrometer particles has been corrected in accordance with the results of Chapter IV. The observed multiplicities, however, have no corrections applied to them. The hadrons are from the ψ decays.

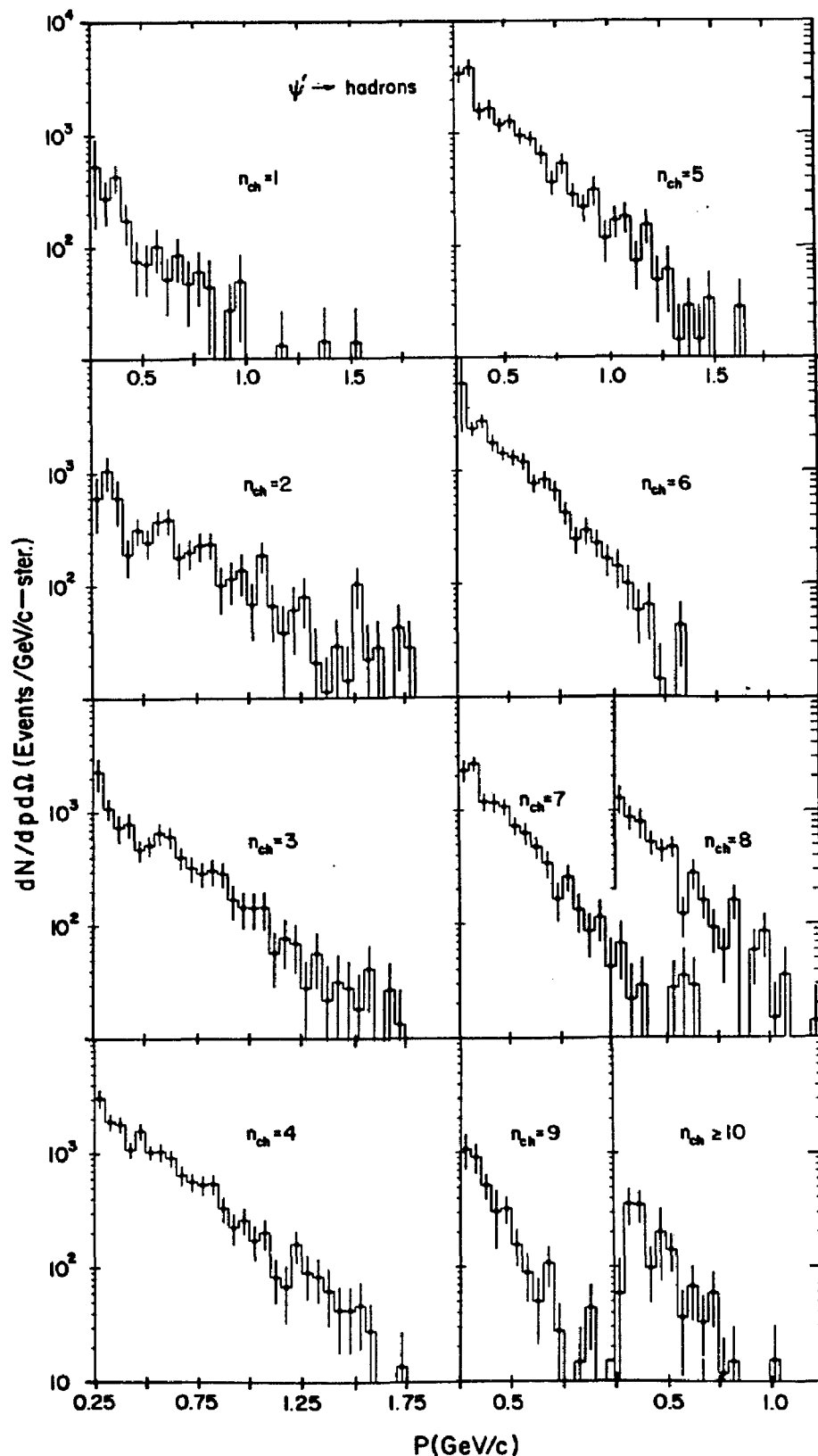


Fig. V-13 b) The observed momentum distributions associated with from 1 to ≥ 10 charged particles in the polymer. The multiplicities have not been corrected but the momentum distribution of hadrons have the appropriate corrections applied to them. The hadrons are from the ψ^+ decays.

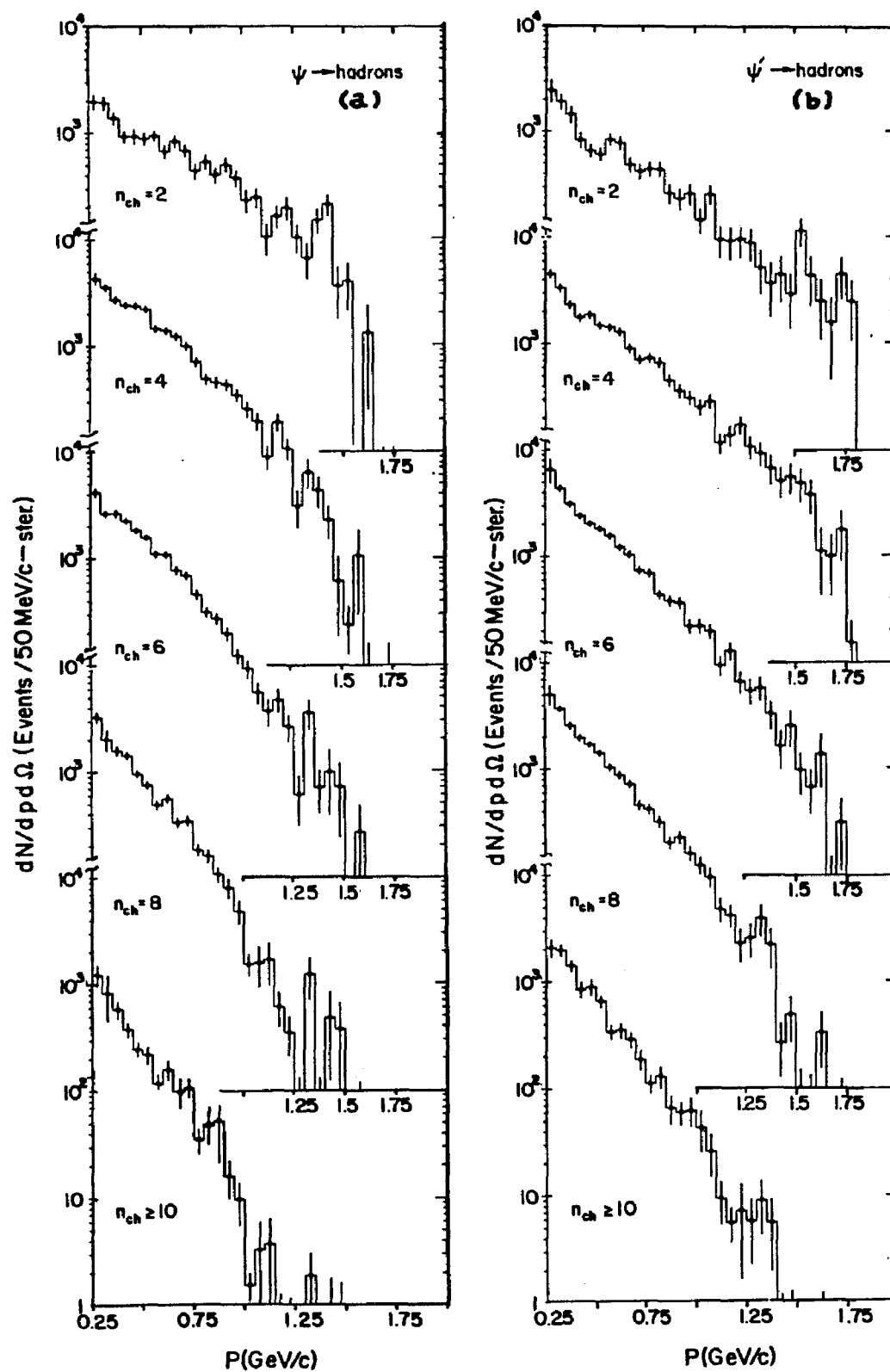


Fig. V-14 The momentum distribution associated with the corrected multiplicities for the ψ (a) and ψ' (b) hadrons.

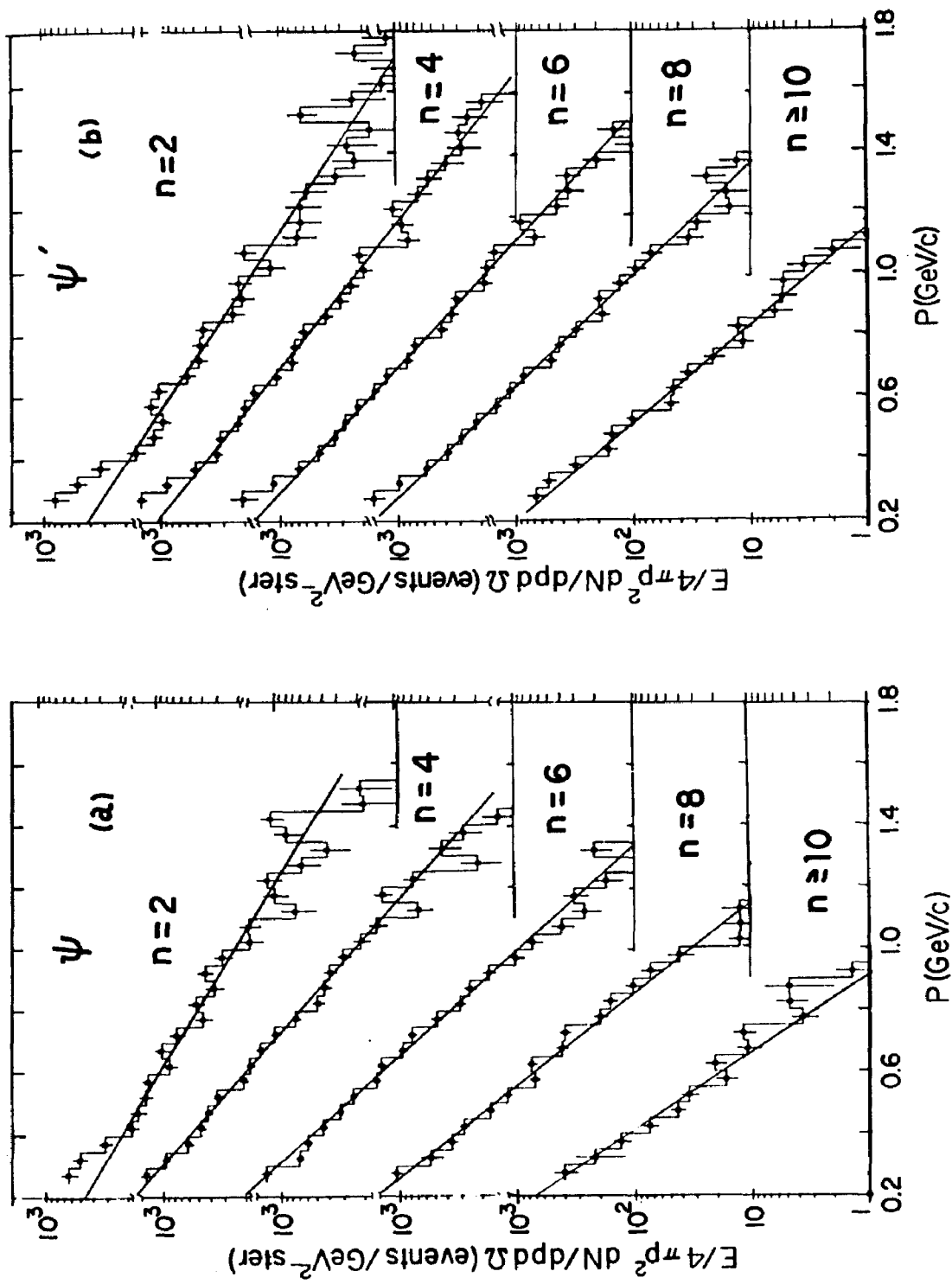


Fig. V-15 The invariant distributions associated with the corrected multiplicities. The lines drawn through the curves are fits to an exponential. The parameters of the fits are listed in Table V-8. The correct mass of each hadron is assumed. The hadrons come from the ψ (a) and ψ' (b) decays.

Parameterization of the Invariant Spectra

$$\frac{E}{4\pi p^2} \frac{dN}{dpd\Omega} = A e^{-bp}$$

Charged Multiplicity	A ($\text{GeV}^{-2} \text{ster}^{-1}$)	b (GeV^{-1})	$\chi^2/\text{D.o.F}$
ψ data			
2	1005 ± 10	-3.69 ± 0.18	25.1/18
4	5451 ± 40	-5.47 ± 0.15	33.4/18
6	7919 ± 82	-6.64 ± 0.16	28.8/16
8	6441 ± 54	-7.49 ± 0.34	42.3/13
≥ 10	1141 ± 35	-7.11 ± 0.55	13.0/9
ψ' data			
2	956 ± 22	-4.02 ± 0.22	26.2/18
4	2903 ± 33	-4.76 ± 0.13	24.4/18
6	5379 ± 25	-5.65 ± 0.10	18.8/18
8	5914 ± 26	-6.34 ± 0.12	17.9/18
≥ 10	3633 ± 43	-7.04 ± 0.30	11.9/12

Table V-8 The parameterization of the invariant hadronic spectra associated with different charged multiplicities. All corrections have been applied to the data, except for the normalization via the luminosity.

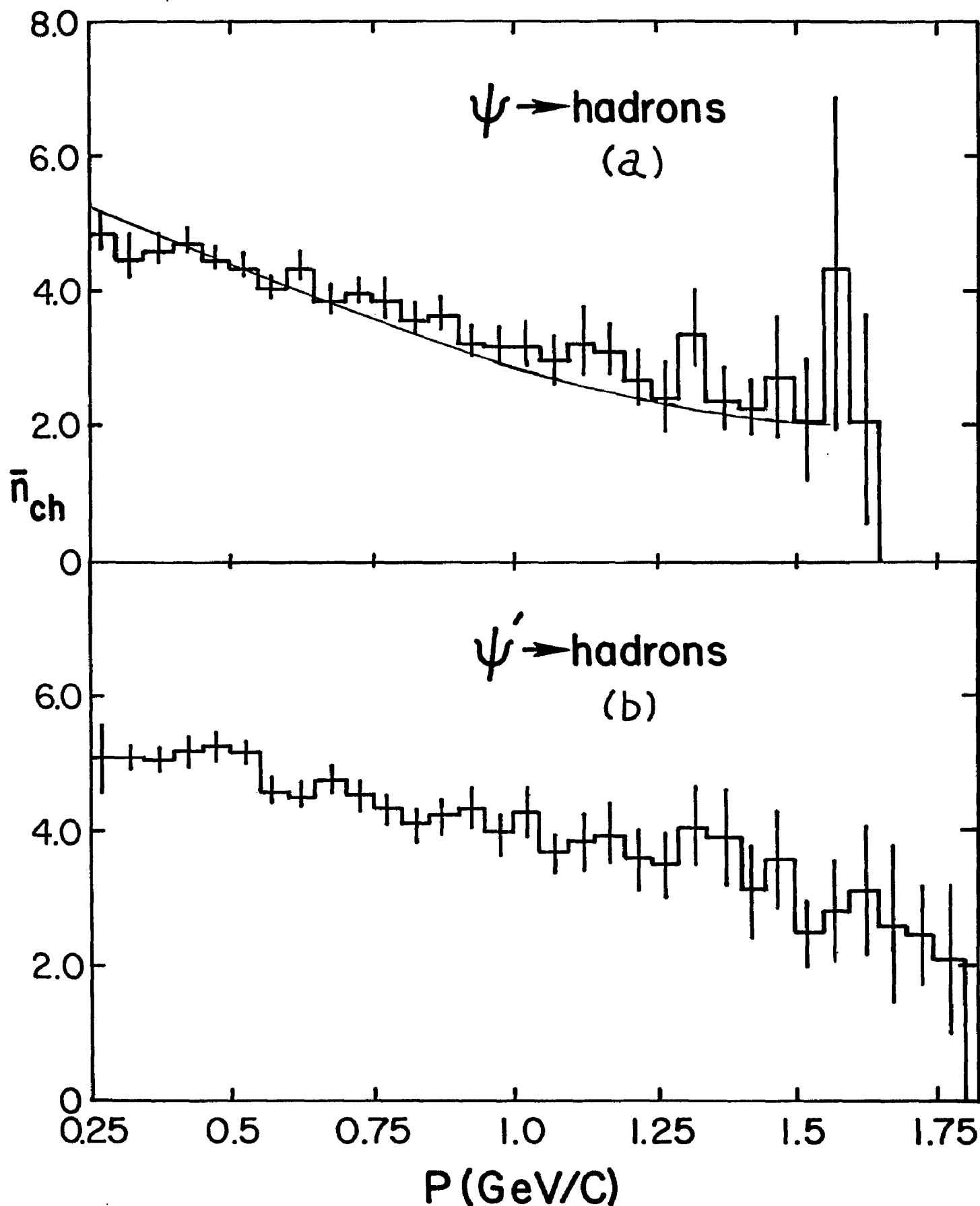


Fig V-16 The averaged charged multiplicity as a function of the spectrometer hadron's momentum for ψ (a) and ψ' (b) decays. The line through the ψ distribution comes from a Monte Carlo simulation of the ψ decays according to phase space.

multiplicities are different, changes the relative triggering weight, $P(1 \text{ triggers} | N \text{ produced})$. In order to calculate this probability, we use the observed exponential behavior of the invariant distributions for different multiplicities to extrapolate the momentum spectrum down to zero momentum. The fraction of the integrated spectrum above 250 MeV/c is then compared to the complete integral. The probability that a N prong event will trigger the spectrometer is then

$$P(1 \text{ triggers} | N \text{ produced}) = N \cdot F_{>}(N) \cdot \Omega .$$

Here, $F_{>}(N)$ is the fraction of the N prong spectrum above 250 MeV/c and Ω is the solid angle of triggering acceptance. In Table V-9, the values of $F_{>}(N)$ are shown.

The average charged multiplicity is then defined as:

$$\langle N_{\text{ch}} \rangle = \frac{\sum \{E_N / P(1|N)\} \cdot N}{\sum_N E_N / P(1|N)}$$

where E_N is the observed number of events of charged multiplicity N and $P(1|N)$ is the probability defined above.

The average charge multiplicity is shown in Fig. V-16 as a function of the momentum of the hadron in the spectrometer. One sees that the multiplicity falls smoothly from about 5 at the lowest momentum to 2 at the highest.

Charged Multiplicity	$F_{>0.25 \text{ GeV/c}}$
ψ data	
2	0.81
4	0.67
6	0.56
8	0.49
≥ 10	0.35
ψ^- data	
2	0.81
4	0.76
6	0.69
8	0.64
≥ 10	0.55

Table V-9 The fraction of the momentum spectrum above 0.25 GeV/c of hadrons associated with the different charged multiplicities. These values are derived from the invariant spectra's parameterizations listed in Table V-8.

In order to assess the significance of this result, the decays of the ψ were simulated with a Monte Carlo event generator²⁰ in which the final hadrons were produced according to phase space. The fraction of kaon and nucleons in the final state were taken from our data and given to the program, as well as the average total and neutral multiplicity. These values were 7.0 and 3.2, respectively. The total multiplicity for a given event was chosen according to a Poisson distribution, with the charged and neutral multiplicity picked from a binomial distribution. The resultant charged particles were then weighed by the spectrometer's acceptance with this weight accumulated into histograms. The average charge multiplicity as a function of momentum was then calculated as per the actual data, with the result compared in Fig. V-16 with the ψ data. The agreement between the two results is quite fair. This again indicates that the statistical description of the resonance decays is valid.

The average charged multiplicity over the observed momentum range turns out to be 4.06 ± 0.50 at the ψ and 4.62 ± 0.4 at the ψ' . If we use the spectra extrapolated to zero momentum, the corresponding charged multiplicities are 4.53 ± 0.73 and 4.96 ± 0.85 . From the multiplicity

relation for hadron-hadron collisions, the predicted values would be 3.49 and 3.77 for invariant masses as large as the ψ and ψ' , respectively. From the data of the SLAC-LBL magnetic detector¹⁸, one would expect mean charged multiplicities of 3.51 and 3.95 at the ψ and ψ' energies, respectively. The $\Upsilon\Upsilon 2$ group at ADONE has measured²¹ the mean charged and the photon multiplicity at the ψ to be 3.8 ± 0.3 and 6.2 ± 1.6 , respectively. Thus our data indicate a mean charged multiplicity that is slightly larger than expected from either the hadronic collision data or other existing e^+e^- data.

It is possible that the method of extracting the mean charged multiplicity from the observed distribution may not totally correctly account for the problems of photon conversion, and could produce a slightly higher multiplicity.

G. Two-Body Decays

In order to assess the SU(3) character of the psion family, the various decay modes need to be studied in detail. With a small-solid angle spectrometer, the only decay modes that can be identified are the $h^{\dagger} + M$, two-body decays. Here, h^{\dagger} is an observed, stable hadron, and M represents

represents another particle. For instance, M can represent the radial recurrences of the normal mesons, e.g., the ρ and K^* , since there may be a large amount of phase space available for these decays²².

The presence of the M particle can be seen in a missing mass plot as a peak, provided the width of the particle is large compared to the spectrometer's resolution.

In Fig. V-17, the mass recoiling from the spectrometer particles is shown. Note that these spectra are obtained from the uncorrected events, though the corrections themselves would not produce peaks, except for a possible broad structure associated with the increase of the acceptance with momentum.

In the ψ case, one sees evidence for the SU(3) allowed $\pi^+\rho$ decay around a missing mass of $1 \text{ GeV}/c^2$. The position of this peak is determined by the momentum resolution of the recoiling pion. There may exist an enhancement at a missing mass of $2.15 \text{ GeV}/c^2$, though it is of very marginal significance on this plot. In the antiproton recoil spectrum, one sees evidence for the $p\bar{p}$ and pN^* (1470) mode. In the recoil spectrum from the K , one sees the SU(3) allowed K^+K^* (892). One also sees a peak near $2.18 \text{ GeV}/c^2$. Although the acceptance of the spectrometer is increasing slowly in

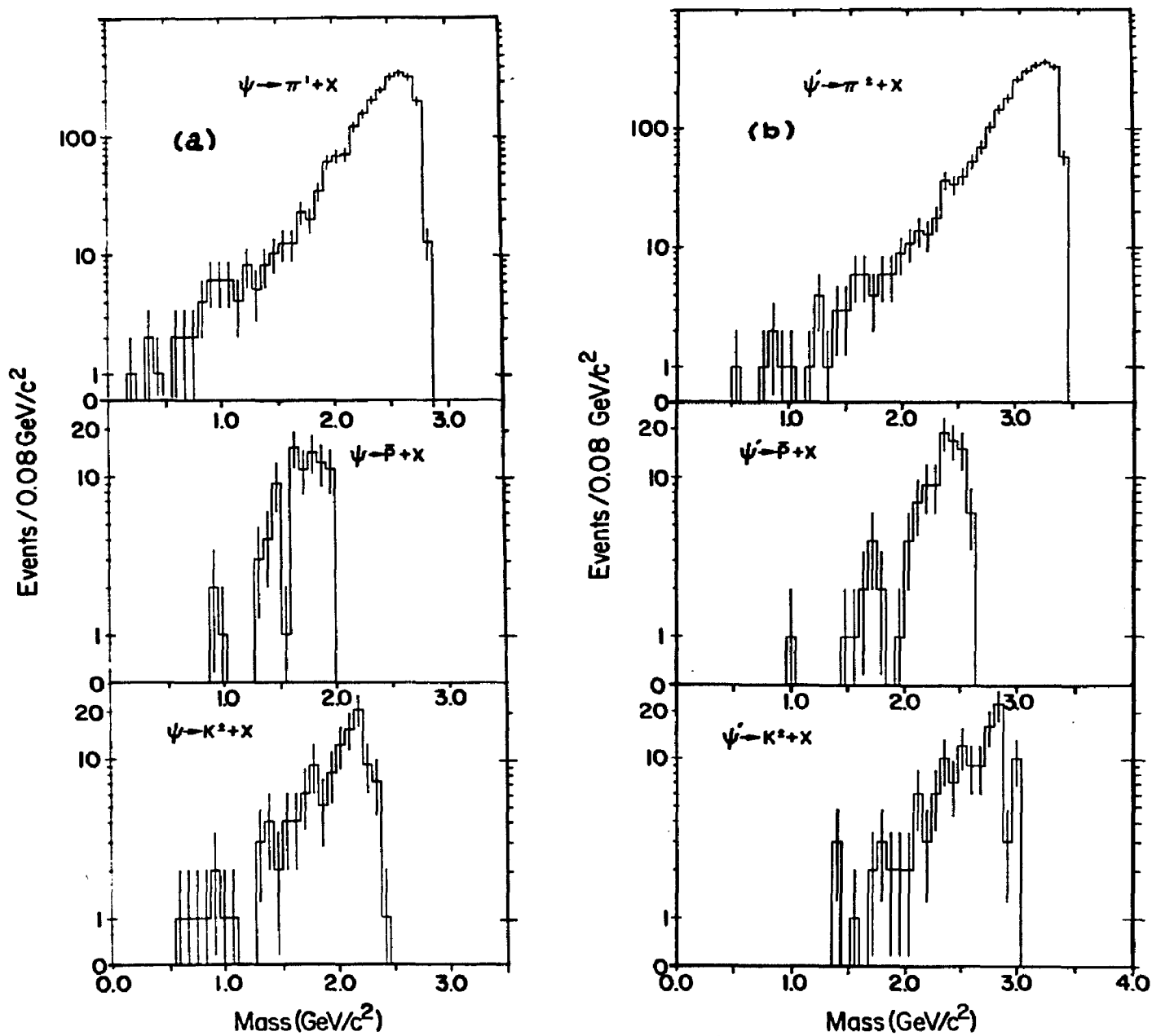


Fig V-17 The missing mass from the spectrometer particle for the ψ (a) and ψ' (b) hadrons. The number of events is uncorrected.

ψ Decays				ψ' Decays		
Mode	Events	Background	$\frac{\sigma_M}{\sigma_{tot}}$ (%)	Events	Background	$\frac{\sigma_M}{\sigma_{tot}}$ (%)
$\pi^+ \pi^- @$	2 ± 1.7	1 ± 1	$0.06 \pm .04$ ($.011 \pm .007$)	1 ± 1	~ 1	< 0.033 (< 0.005)
$\pi^\pm \rho$	12 ± 4	10 ± 4.7	$0.74 \pm .25$ ($0.84 \pm .20$)	1 ± 1	1 ± 1	$0.066 \pm .066$ (< 0.1)
$\pi^\pm B(1235)$	4 ± 4	20 ± 4.5	$0.25 \pm .25$ ($0.28 \pm .07$)	< 4	7 ± 3	< 0.26
$\pi^\pm \rho'(1600)^\dagger$	< 5	40 ± 6.3	< 0.6			
$\pi^\pm M(2150)^\dagger$	< 35	238 ± 16	< 2.5			
$\pi^\pm M(1960)^\dagger$	< 29	85 ± 9	< 2.0			
$\pi^\pm M(2350)^\dagger$				< 20	60 ± 8	< 1.5
$K^+ K^- \#$	1 ± 1	< 1	$0.023 \pm .023$ ($0.020 \pm .016$)	0	0	< 0.05 (< 0.005)
$K^+ K^* (892)$	4 ± 2	< 1	$0.4 \pm .2$ ($0.34 \pm .06$)	0	0	< 0.1
$K^+ K^{**} (1420)$	< 4	5 ± 4	< 0.4 (< 0.15)	< 1	1 ± 1	< 0.1
$K^\pm K^* (1800)^\dagger$	< 5	12 ± 4	< 0.5			
$K^\pm K^* (2200)^\dagger$	< 8	26 ± 5	< 1.6			
$K^\pm K^* (2850)^\dagger$				< 16	32 ± 6	< 3.5
$p \bar{p}$	3 ± 1.7	< 1	$0.22 \pm .12$ ($0.22 \pm .02$)	1 ± 1	< 1	$0.11 \pm .11$ ($0.023 \pm .007$)
$p N^* (1400)$	11 ± 4	4 ± 4	$0.85 \pm .31$	0	0	$< .1$
$p N^* (1780)$	6 ± 4	10 ± 4	$0.62 \pm .41$	2 ± 2	4 ± 2	$< .22$

Table V-10 The two body decays of the ψ and ψ' observed in the recoil spectra of the hadrons. The values listed in parentheses are the currently accepted values for these decays from SPEAR and DORIS.

@) Forbidden by isospin, assumed to proceed via second-order electromagnetic decays. Implies $|F_\pi(\psi)|^2 = 9.1 \pm 7.3 \times 10^{-3}$

#) Forbidden for an SU(3) singlet state. Implies $|F_K^\pm(\psi)|^2 = 4.6 \pm 4.6 \times 10^{-3}$

†) The existence of these states is questionable.

Reaction	Recoil Mass (MeV/c ²)	Width (MeV/c ²)
$\psi \rightarrow \pi^{\pm} + X$	800 \pm 100	200 \pm 100
	[$\rho(770)$]	
	1250 \pm 75	150 \pm 75
	[B(1235)]	
	1960 \pm 50	150 \pm 80
	2150 \pm 50	170 \pm 100
$\psi' \rightarrow \pi^{\pm} + X$	800 \pm 100	160 \pm 80
	[$\rho(770)$]	
	2320 \pm 80	100 \pm 60
$\psi \rightarrow K^{\pm} + X$	880 \pm 80	160 \pm 75
	[K [*] (892)]	
	1780 \pm 60	230 \pm 100
	2180 \pm 80	320 \pm 120
$\psi' \rightarrow K^{\pm} + X$	2850 \pm 50	180 \pm 100
$\psi \rightarrow p, \bar{p} + X$	1450 \pm 50	120 \pm 40
	[N [*] (1470)]	
	1650 \pm 60	150 \pm 60
	[N [*] (1688)]	
$\psi' \rightarrow p, \bar{p} + X$	1700 \pm 75	110 \pm 40
	[N [*] (1688)]	

Table V-11 The parameters of mass and width inferred from the the enhancements in the missing mass plots. The states listed in brackets are the closest known resonances to the observed mass.

the corresponding recoiling momentum range, it does not explain the narrowly peaked structure. This may be the $K^*(2200)$ that is seen from time to time.²³

In the ψ' case, there exists enhancements at 1.7 GeV corresponding to the cascade to the ψ which then decays to $\pi^{\pm}\rho$. The enhancement at 2.35 GeV may either correspond to a direct or cascade decay: $\psi' \rightarrow \psi \rightarrow \pi^{\pm} M(2150)$.

In the kaons' spectrum, the enhancement at about 2.85 GeV may be due to the cascade decay with the ψ decaying into $K^+ K^*$ (2180). The cascade decay with the ψ decaying into $K^+ K^*$ (892) appears as an enhancement at around 1.4 GeV.

In the protons' spectrum, the enhancement at 1.68 GeV may also be due to a cascade where the ψ decays into $p\bar{p}$.

The various branching ratios into different two-body channels are summarized in Table V-10, with a comparison with existing DORIS and SPEAR data.²⁴

In Table V-11, the parameters of the enhancements observed in the missing mass spectra are listed.

Since the $\pi\pi$ decay of the ψ is forbidden by G-parity, and if the ψ is an SU(3) singlet state, then the decay into $K\bar{K}$ is also forbidden. However, if the ψ is an SU(3) octet state, the $K\bar{K}$ is allowed. The fact that both modes are observed indicates that G-parity is violated, i.e. the

decays proceed via second order electromagnetic processes. However, the fact that these modes are highly suppressed with respect to the $p\bar{p}$ mode favors an SU(3) singlet assignment for the ψ and ψ' and since the expected ratio for these two decay amplitudes is 1.0 for a singlet state. When the observed branching ratios are corrected for the difference in phase space (the KK^* branching ratio is increased by $1/0.85$) the ratio $A(\psi \rightarrow \pi^{\pm}\rho) / A(\psi \rightarrow K^{\pm}K^*(892)) = 1.57 \pm 1.08$. This indicates that SU(3) may be broken in these decay modes.

Additionally, a few of the properties of the M particle can be extracted from observing its decay modes. For example, one can require that the M decay into only one charged particle with some number of neutrals. In Figs. V-18 and 19, the momentum spectra of the recoiling hadron from such a system are shown. One clearly sees the SU(3) allowed decays, $\pi^{\pm}\rho$ and $K^{\pm}K^*(892)$ in the ψ decay, in addition to the $p\bar{p}$ decay. Also, the G-parity violating $\pi^{\pm}\pi$ and the SU(3) singlet violating $K^{\pm}K$ decays are also observed.

In the ψ' decays, one sees evidence for a state recoiling from a pion of 1.1 ± 0.05 GeV/c with a mass of 2.32 ± 0.08 GeV/c², and also for the decay mode $p\bar{p}$.

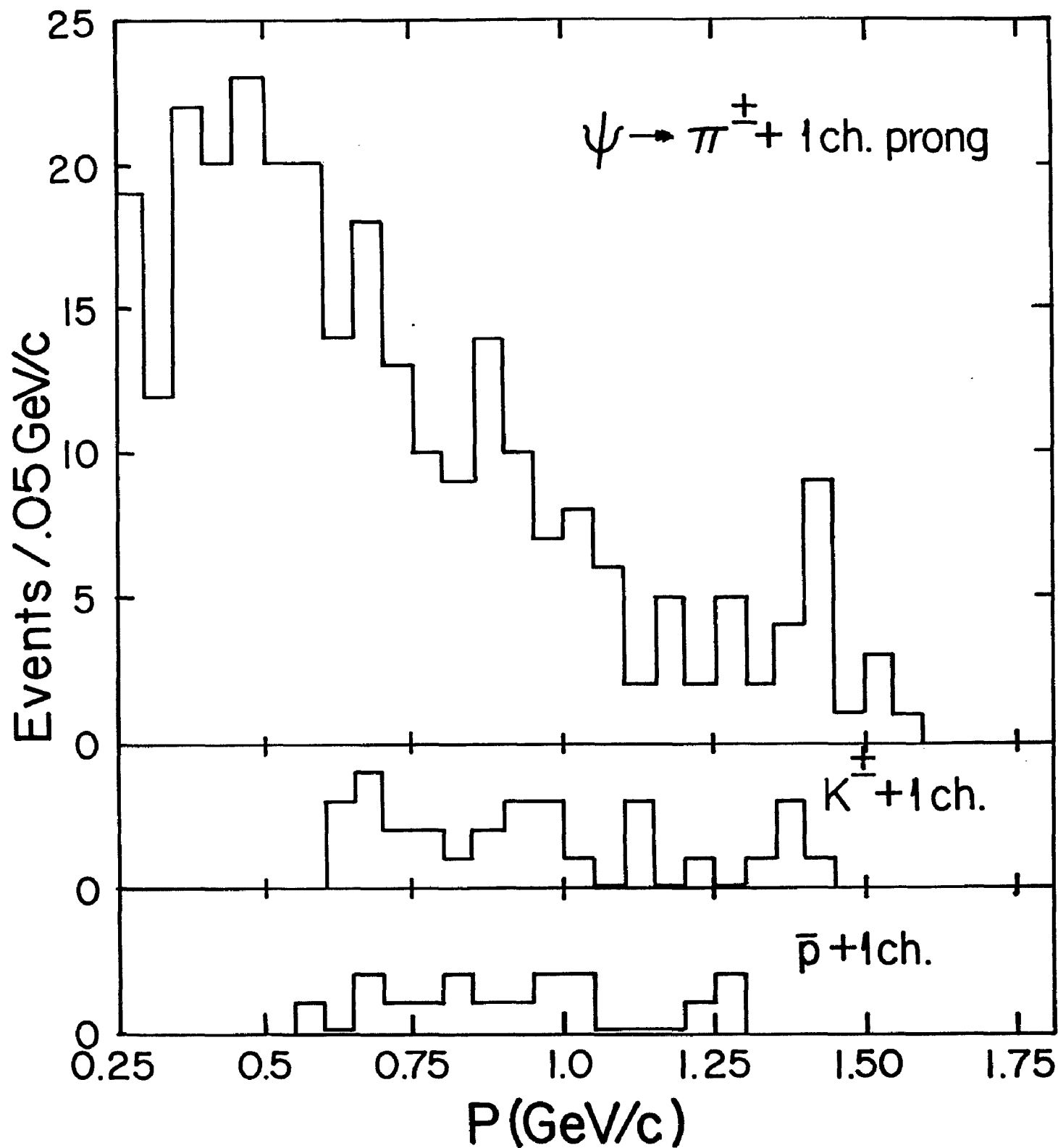


Fig. V-18 The observed momentum distribution of hadrons from the ψ decays in which there is only one other charged particle detected in the polymer.

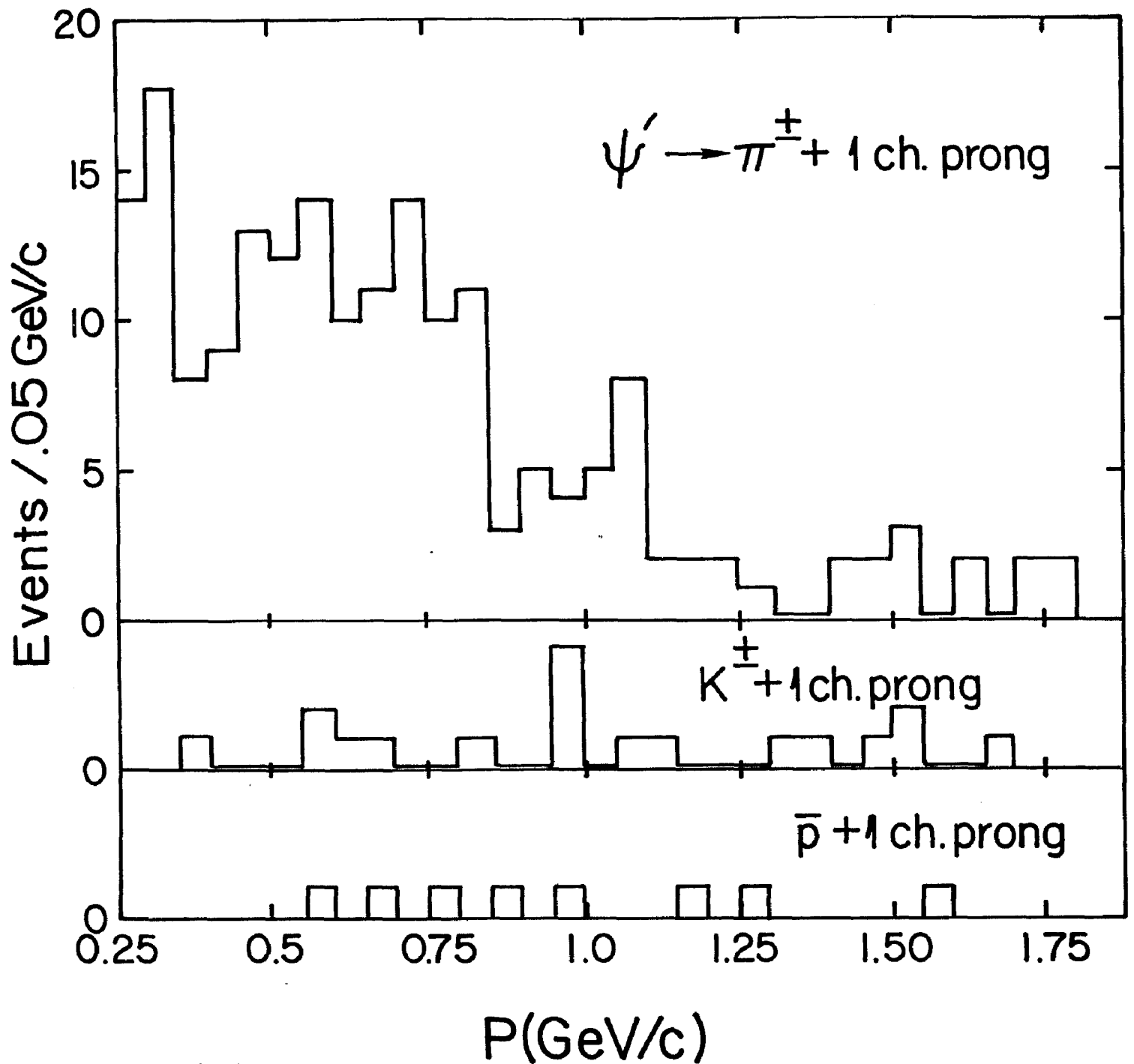


Fig. V-19 The observed momentum distribution of hadrons from the ψ' decays in which there is only one other charged particle detected in the polymer.

In summary, many of the previously unseen excited states of the normal mesons may be present in the psion decays. However, with the statistical level and the resolution of the present experiment, no valid claims can be made concerning their existence.

H. A Search for Quarks²⁵

As a subset of the two-body decays, we consider the process

$$\psi \rightarrow \text{quark} + \text{antiquark},$$

where at least one quark "breaks free" and travels into the spectrometer.

For simplicity, the quarks are assumed to arise from the second order electromagnetic decays of the psions in the same fashion as the electrons and muons. Then, though QED, the production cross section for quark-antiquark pairs is²⁶

$$\sigma(\psi \rightarrow Q\bar{Q}) = e_Q^2 \left(\frac{3\beta - \beta^3}{2} \right) \cdot \sigma(\psi \rightarrow \mu\mu)$$

where β is the velocity of the quark and e_Q is the quark's charge, in units of the electron's charge.

In this experiment, the only signature that can be clearly recognized is from stable, fractionally-charged

particles. The required characteristics of a fractionally charged object in our spectrometer are:

a) An anomalous flight time. If the free quarks have a mass in the 0.4 to 1.5 GeV/c² range, then their observed velocity versus their observed momentum will have a characteristic response far different from the usual stable particles. Fig. V-20 shows the range of velocity vs observed momentum for 1/3 and 2/3 charged quarks ranging from 0.4 to 1.5 GeV/c² in mass. By observed momentum we mean the momentum derived from the analysis programs which assume a charge of one.

b) An anomalous momentum. If the 1/3 charged quarks are lighter than 1.3 GeV/c² or the 2/3 charged ones are lighter than 0.7 GeV/c², then their observed momentum will appear to be greater than 2.0 GeV/c. This is clearly above the kinematic limit for normal particles, and provides a clean signature.

c) An anomalously low energy loss in the shower counter. Since the ionization losses in the scintillators will be one-ninth and four-ninths that of singly charged particles of the same velocity for 1/3 and 2/3 charged quarks, the pulse height in the shower counter could be used to identify the quarks. However,

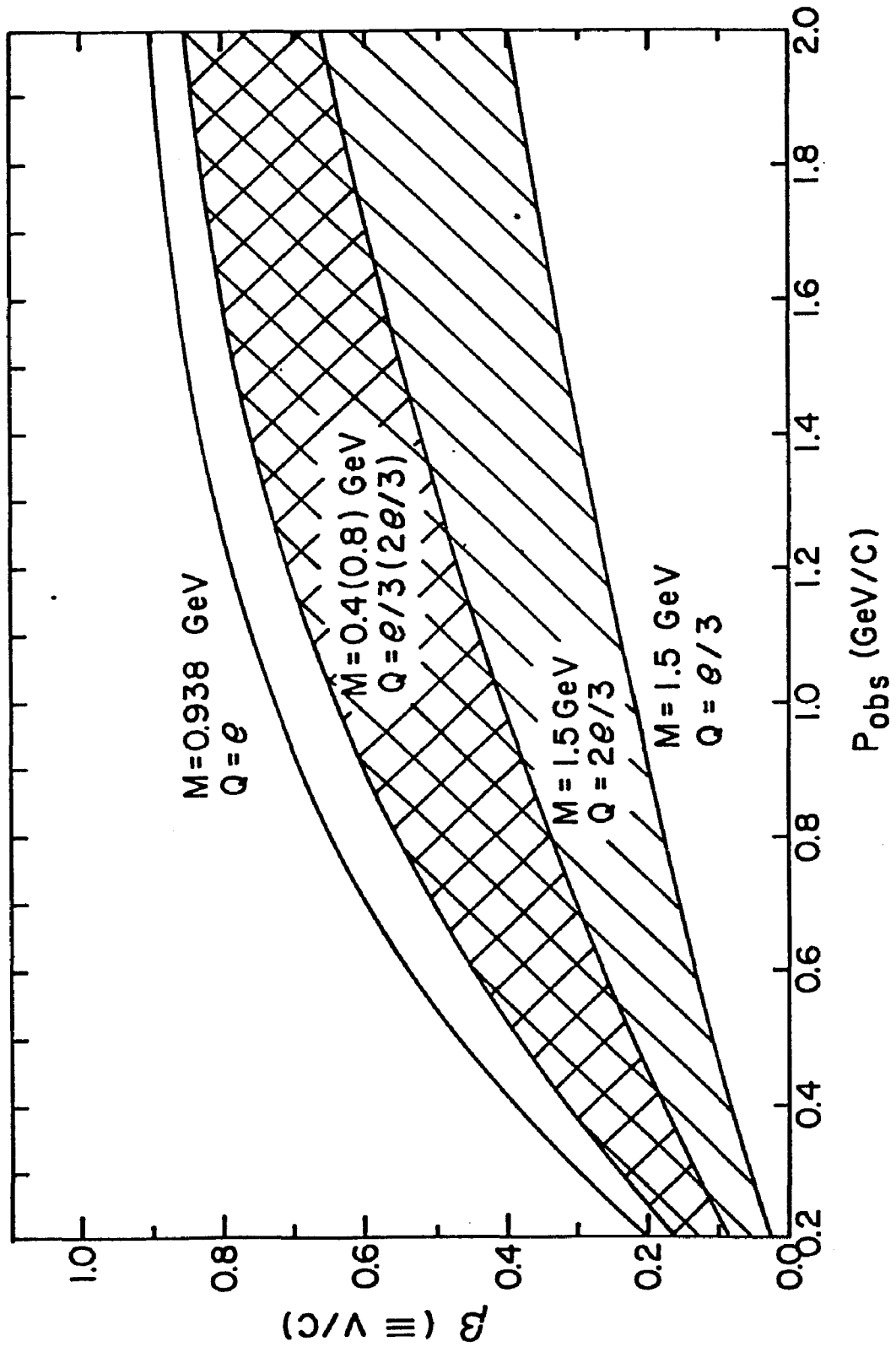


Fig. V-20 The velocity vs observed momentum for particles of the indicated mass and charge. The top curve is for protons, while the cross-hatched region indicates the range of mass which are kinematically allowed for our data sets and can be resolved by our spectrometer.

the large Landau fluctuations in the energy losses of normal particles can allow them to overlap substantially with the energy losses from fractionally charged objects. A low shower counter pulse amplitude, therefore, will not be a substantive test, but when the time-of-flight and momentum information is combined with it, will be a powerful discriminant.

For each one of these test, there is, of course, a certain background from mundane processes. This leads to the upper limit on the sensitivity of these tests.

For the anomalous time-of-flight test, the principal backgrounds come from particles that enter the spectrometer and decay or strike the magnet's walls and scatter back into the spectrometer. The reconstructed momentum for such events can be anything. Imposing constraints on the χ^2 of the trajectory reduce these possibilities considerably.

The principal background to measuring the momentum also comes from poorly reconstructed events due to decays in flight or scatterings. Cosmic ray muons will also give very large momentum values. These are effectively eliminated by the restrictions imposed on the location of the event's source point, and on the disagreement between the time of flight as measured from the beam crossing and as measured

from the S1 start counter.

The triggering efficiency for fractionally charged particles depends strongly on the energy loss in the counters and chambers, since the threshold settings on the discriminators attached to each device were optimized for singly charged particles. Since the energy loss is roughly proportional to $(e_Q/\beta)^2$, the counter's single particle efficiency is highly dependent on β once the energy loss is within one or two standard deviations from the electronics' threshold.

For $e_Q = 2/3$, the triggering-scintillation counters efficiencies are estimated to be 0.90 for $\beta > 0.7$ and 0.95 for $\beta < 0.7$. For $e_Q = 1/3$, the estimated efficiencies are 0.60 for $\beta > 0.5$ and 0.90 for $\beta < 0.5$. For the proportional chambers, the estimated efficiencies are 0.85 for $\beta > 0.7$ and 0.95 for $\beta < 0.7$, with $e_Q = 2/3$, and 0.35 for $\beta > 0.5$ and 0.90 for $\beta < 0.5$, with $e_Q = 1/3$.

The overall reconstruction efficiencies are 0.37 and 0.71 for $\beta > 0.7$ and $\beta < 0.7$, $e_Q = 2/3$, and 4×10^{-4} and 0.48 for $\beta > 0.5$ and $\beta < 0.5$, $e_Q = 1/3$.

In the ψ data set, there are 7 events that have an observed momentum greater than 2.0 GeV/c, and that satisfy all the other conditions for being an acceptable event, i.e. a χ^2 less than 6.0, a good source point, a minimum of 3 momentum defining chambers fired, and the extrapolated track was inside the active area of the spectrometer. However,

all of these events appeared to have amplitudes in the shower counter that are consistent with a singly charged particle. Furthermore, it appeared that they were consistent with either scattering from the magnets walls or decays in flight. For these events, the analysis programs appeared to fail to get the right momentum. The observed flight times imply that $\beta > 0.8$. Thus, there appears to be no evidence for light quark production in the ψ decays. The 90% confidence level for the branching fraction of ψ to quarks with mass less than $0.7 \text{ GeV}/c^2$ is 0.26% for $e_Q = 2/3$.

For heavier quarks, the time of flight distributions indicate one event within the expected bands in Fig. V-20. However, further examination of this event indicates it has the characteristics of a deuteron coming from a beam-gas scattering interaction. Thus the 90% confidence level for the ψ branching fraction to quarks with mass between 0.8 and $1.5 \text{ GeV}/c^2$ is 0.09% for $e_Q = 2/3$, and 0.13% for $e_Q = 1/3$.

In the ψ^0 data set, 14 events are found which have a momentum greater than $2.0 \text{ GeV}/c$. All these events have a normal pulse amplitude in the shower counter, and, on further examination, appear to be due to decays and scattering in the magnet. The time of flight of these events does not appear to be anomalous. Thus, the conclusion is that the 90%

confidence level for the branching fraction into quarks from the ψ' is 0.30% for quark with $m_q < 0.7 \text{ GeV}/c^2$ and $e_q = 2/3$.

From the time of flight distribution, 4 events are found which fall within the expected velocity vs momentum bands for fractionally charged quarks. However, these events are also consistent with being deuterons coming from beam-gas scattering, since they are all positively charged. Also, the amplitude in the shower counter is about three times larger than expected for a singly charged minimum ionizing particle. Hence, the 90% confidence level for the branching fraction of the ψ' to quarks in the mass range of 0.8 to 1.5 GeV/c^2 is 0.08% for $e_q = 2/3$, and 0.12% for $e_q = 1/3$.

Adding together all the data, the upper limits for the branching fractions for quarks from the psions is 0.11% assuming the quarks behave like antiprotons in terms of their nuclear interaction strength, or is 0.05% assuming the quarks do not have any strong interactions with matter. These upper limits are summarized in Table V-12.

Mass Range: (GeV/c ²)	< 0.7	0.8 - 1.5	
Charge:	$\frac{2e}{3}$	$\frac{e}{3}$	$\frac{2e}{3}$
ψ data			
weak	0.14%	0.08%	0.05%
strong	0.36%	0.13%	0.09%
ψ' data			
weak	0.16%	0.07%	0.04%
strong	0.30%	0.12%	0.08%
Total			
weak	0.11%	0.05%	0.03%
strong	0.20%	0.09%	0.07%

Table V-12 The 90% C.L. upper limits for the decay of the ψ or ψ' into fractionally-charged, free quarks. The limits are quoted for both light and heavy quarks separately due to the difference in the analysis procedure. The terms weak and strong refer to the nuclear interaction strength. In the weak case, the free quarks are assumed to have little or no nuclear interactions with the material in the spectrometer, while in the strong case, they are assumed to have the same nuclear interaction strength as antiprotons.

I. The Gamma Ray Distributions

1. Introduction

One of the major predictions of the charm model is the existence of positronium-like energy levels of the charm-anticharm quark system²⁷. Thus, there should exist a series of states that can be reached from the higher energy states through radiative deexcitation. In particular, the 1^{--} states that are formed in e^+e^- annihilation, e.g., the ψ and ψ' , can radiate a photon in their decays to the even-charge conjugation states.

Recalling Fig. 0-1, the 3S states can decay to the lower energy 1S states while the 2^3S state can decay to the 1^3P states. Also, the 1^3P states can decay to the 1^3S state.

One should be able to observe the emitted monochromatic photons in the radiative decay processes. The cascade decay from the 1^3P to the 1^3S level will not appear to be monochromatic due to the motion of the 3P states.

The existing evidence for the 1S and 3P states comes from a study of their decay modes and the photon spectra from the ψ and ψ' decays²⁸.

2. Inclusive Photon Spectra

Using the gamma ray spectrometer described in Section I-C, the inclusively produced photon spectra from the ψ and ψ' decays were measured. These results were published by the MPPSSSD collaboration²⁹ and are summarized here.

The apparatus was triggered where the following conditions were satisfied.

- a) There were at least two charged particles in the polymer as defined by the coincidence between two of thirty-two distinct azimuthal sectors.
- b) There was at least 110 MeV of energy deposited in any one of the three NaI stacks.
- c) No signal came from the veto counters that were located close to the beam pipe and about 1 m from the interaction region. These counters were used to eliminate backgrounds from beam-gas and beam-vacuum pipe interactions and appeared to have a negligible effect on the triggering rate from annihilation events.
- d) Less than two layers of the polymer had 8 adjacent tubes firing. This requirement also vetoed background processes while having a negligible effect on the annihilation events.
- e) A magnetic spectrometer trigger occurred as defined

in Section I-D-7. In this case, only requirement b) was additionally necessary to produce a trigger for the photon spectrometer.

A total of 10^7 and 4.5×10^6 triggers were obtained in this fashion from the ψ' and ψ running conditions, respectively. The total luminosity for each data set was 600 nb^{-1} at the ψ' and 100 nb^{-1} at the ψ .

In the analysis of the events, the following conditions were imposed.

a) There were at least two tracks that could be reconstructed from the polymer and the surrounding proportional chambers that came from the interaction region.

b) There was at least greater than 140 MeV of energy deposited somewhere else in the NaI arrays besides the shower of interest.

c) At least 70% of the energy of the shower was contained in a single crystal.

d) At least 10% of the total energy deposited in the NaI stack was contained within the central seven crystals. (See Section I-C for an explanation.)

e) The extrapolated trajectories of charged particles did not overlap within $\pm 5 \text{ cm}$ of the center of a

shower.

f) There was only a single neutral shower in an array. This requirement reduced the background from π^0 decays.

g) The shower was produced within ± 10 ns of the beams' intersection time. This eliminated backgrounds from cosmic rays.

h) The topology of the event must not have looked like a cosmic ray event. A cosmic ray event is easily identified by the line-up of proportional wires and with the reconstructed track's vertex outside the interaction volume. Specifically, if a straight line of fired tubes and proportional wires was found such that the distance between the line and the center of the intersection region was greater than 7 cm, the entire event was rejected.

The total number of events surviving these requirements were 24000 and 18000 for the ψ' and ψ data sets. With these restrictions on the data, the resulting spectra are shown in Fig. V-21 for the ψ and ψ' runs. Note that with the above restrictions, there can be up to two photons entered into the histograms from each event.

For the ψ decays the spectrum of the photons was

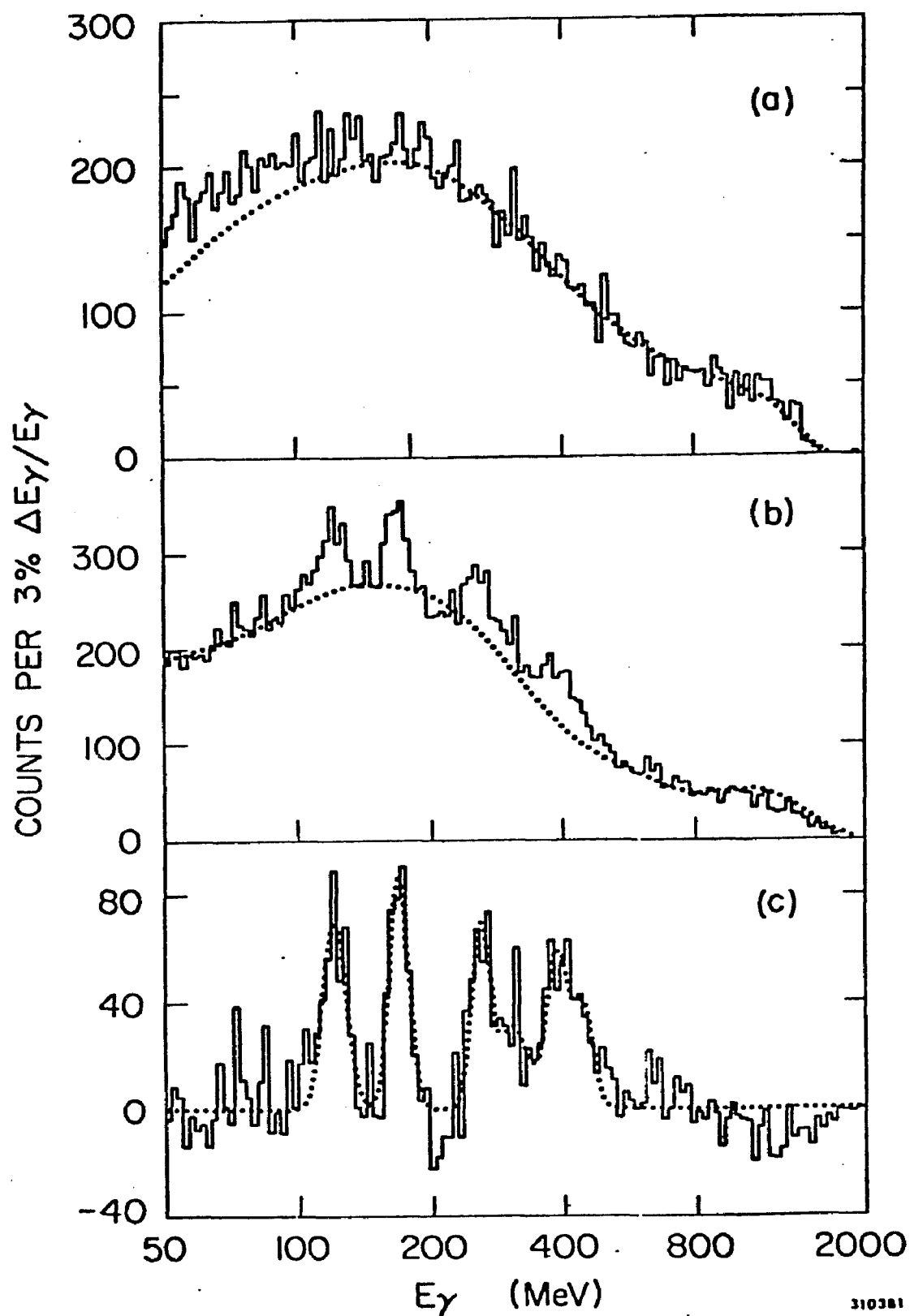


Fig. V-21 The inclusive gamma ray spectra for the ψ (a) and ψ' (b) data. The data are displayed in bins that are $3\% \times E_\gamma$ wide to suppress the effects of the NaI's energy resolution-dependence. The dotted lines in (a) and (b) are the Monte Carlo simulation of the ψ and ψ' decays, the latter without photons from the cascade decays. In (c) the Monte Carlo curve has been subtracted from the ψ' data and the dotted curve is the fit described in the text and Table V-13. (from Ref, 29)

simulated with an all-pion invariant phase space model³⁰. This is shown as a dotted line in Fig. V-21(a). The simulated spectrum was normalized to the data above 150 MeV. Note that there is some discrepancy between the data and the Monte Carlo's results below this energy. The reason for this discrepancy is unclear, but it may be due to background related processes, such as beam-gas scatterings, which are not completely eliminated from the data and would tend to populate the lower energy range of the gamma ray spectrum.

The ψ' decays are treated similarly, with all the known hadronic decays included, but with the radiative decays associated with the χ states eliminated. To account for the discrepancy between the ψ data and the Monte Carlo for $E_\gamma < 150$ MeV, the ψ' result is scaled by the ratio of the ψ data to the ψ Monte Carlo results. This corrected ψ' Monte Carlo result is shown as a dotted line in Fig. V-21(b). The spectra were then fitted by

$$a_0 F(\ln(E_\gamma)) + \sum_i \frac{a_i}{2\pi\sigma_i} \exp\left\{-\frac{1}{2} \left(\frac{\Delta E_{\gamma i}}{\sigma_i}\right)^2\right\}$$

where $F(\ln(E_\gamma))$ is the Monte Carlo's spectrum, σ_i are the widths of the peaks determined from the known energy resolution of the NaI arrays and the necessary Doppler shifts in the lines, and $\Delta E_{\gamma i}$ is equal to $\ln(E_\gamma) - \ln(E_i)$.

The normalization for the continuum, a_0 , and the peaks, a_i , as well as the energy of the peaks, E_i , were fitted over the region of 50 to 1000 MeV. The sum of the Gaussian terms is shown as a dotted line in Fig. V-21(c), where the histogram comes from subtracting the Monte Carlo's continuum from the data. In Table V-13, the results of the fit are shown. The branching fractions are computed by taking the ratios between the number of entries in each peak to the number in the continuum, using the detection efficiencies appropriated to the different energies. The results in Table V-13 contain a systematic error of 20% from the uncertainty in the average gamma ray multiplicity from the hadronic decays of the ψ .

Thus, there is clear evidence for gamma ray transitions between the ψ' and what appear to be the 3P states, and also between these 3P states and the ψ . The branching ratios for the initial transitions to the 3P states are about the same, namely 7.0%. The branching fractions for the 3P states to the ψ via radiative decay appear to be on the order of 50% or larger, since the branching fractions listed are actually $B(\psi' \rightarrow \gamma \chi) \cdot B(\chi \rightarrow \gamma \psi)$.

There appears to be no structure in the ψ spectrum at the level of 2.0% for a 90% C.L. The upper limits (90% C.L.)

a_i (Events)	E_i (MeV)	σ_i ($\Delta E_\gamma/E_\gamma$)	Mass χ (MeV/c ²)	Branching Fractions (%)
360 ± 50	120.9 ± 1.3	0.06	3561 ± 7	7.0 ± 2.0
367 ± 47	169.2 ± 1.4	0.05	3511 ± 7	7.1 ± 1.9
290 ± 44	260.6 ± 2.9	0.05	3413 ± 9	5.5 ± 1.8 (7.2 ± 2.3)*
180 ± 45	309.5 ± 8.0	0.07	3420 ± 14	3.3 ± 1.7
297 ± 38	390.7 ± 4.7	0.06	3511 ± 13	5.0 ± 1.5
137 ± 31	449.9 ± 6.3	0.045	3577 ± 14	2.2 ± 1.0

Table V-13 The results of a fit to the ψ' gamma ray spectrum shown in Fig. V-21(c). The resulting masses are calculated by assuming the three lowest energy photon lines arise from the decay $\psi' \rightarrow \gamma\chi$, while the three highest energy lines come from the decays $\chi \rightarrow \gamma\psi$. The branching fractions are calculated from the ratio of the total number of events in a particular line times the detection efficiency for photons of that energy to the total number of events in the Monte Carlo continuum curve. The listed errors for the mass and branching fraction of the χ states contain both statistical and systematic uncertainties, while the errors for the fitted parameters come from the statistical uncertainties of the fit. (from Ref. 29)

* This branching fraction for the $\chi(3413)$ results if a $1 + \cos^2 \theta$ angular distribution is assumed for the photon rather than an isotropic one.

for the decays into the apparent 1S states are:

$$\psi \rightarrow \gamma \chi(2850), 1.7\%;$$

$$\psi' \rightarrow \gamma \chi(3455), 2.5\%;$$

$$\psi' \rightarrow \gamma \chi(2850), 1.0\%.$$

3. Photon Spectra for Spectrometer Triggers

In this section, the photon spectra associated with a magnetic spectrometer trigger will be analyzed. In general, one expects the contamination of the photon spectra from non-annihilation events to be smaller than in the inclusive case where almost no information is present about the nature of the charged particles. If the discrepancy between the Monte Carlo results and the data for the photon spectrum from the ψ decays can be attributed to background contamination, then the low photon energy range can be explored with greater confidence if additional constraints are imposed on the charged particles that emerge from the luminous region. Specifically, we identify the particle's species and determine its momentum.

The following requirements were then imposed on photon candidates.

- a) There must be a cleanly identified spectrometer particle which passes the qualifications listed in Section II-C. This category includes charged pions,

kaons, and antiprotons, as well as electrons and muons. Protons have been excluded since a large fraction of them with momentum below 0.8 GeV/c come from beam-gas scatterings.

b) At least 10% of the total energy deposited in the NaI Stack was contained within the central seven crystals.

c) The extrapolated trajectories of charged particles did not overlap within ± 5 cm of the center of the shower.

d) The majority of the energy in the shower was deposited in one or two adjacent crystals, with the remaining energy deposited in the surrounding, adjacent crystals. This serves to eliminate π^0 photons which enter the NaI arrays too close together to produce two distinguishable showers, but produce an elliptical energy distribution in the array, rather than a circular one expected from a single photon or particle.

e) There was only one neutral shower in an array. This eliminates π^0 background. For instance, Fig. V-22 shows the reconstructed mass from two neutral showers in a single array. A clear π^0 peak is seen, with little background.

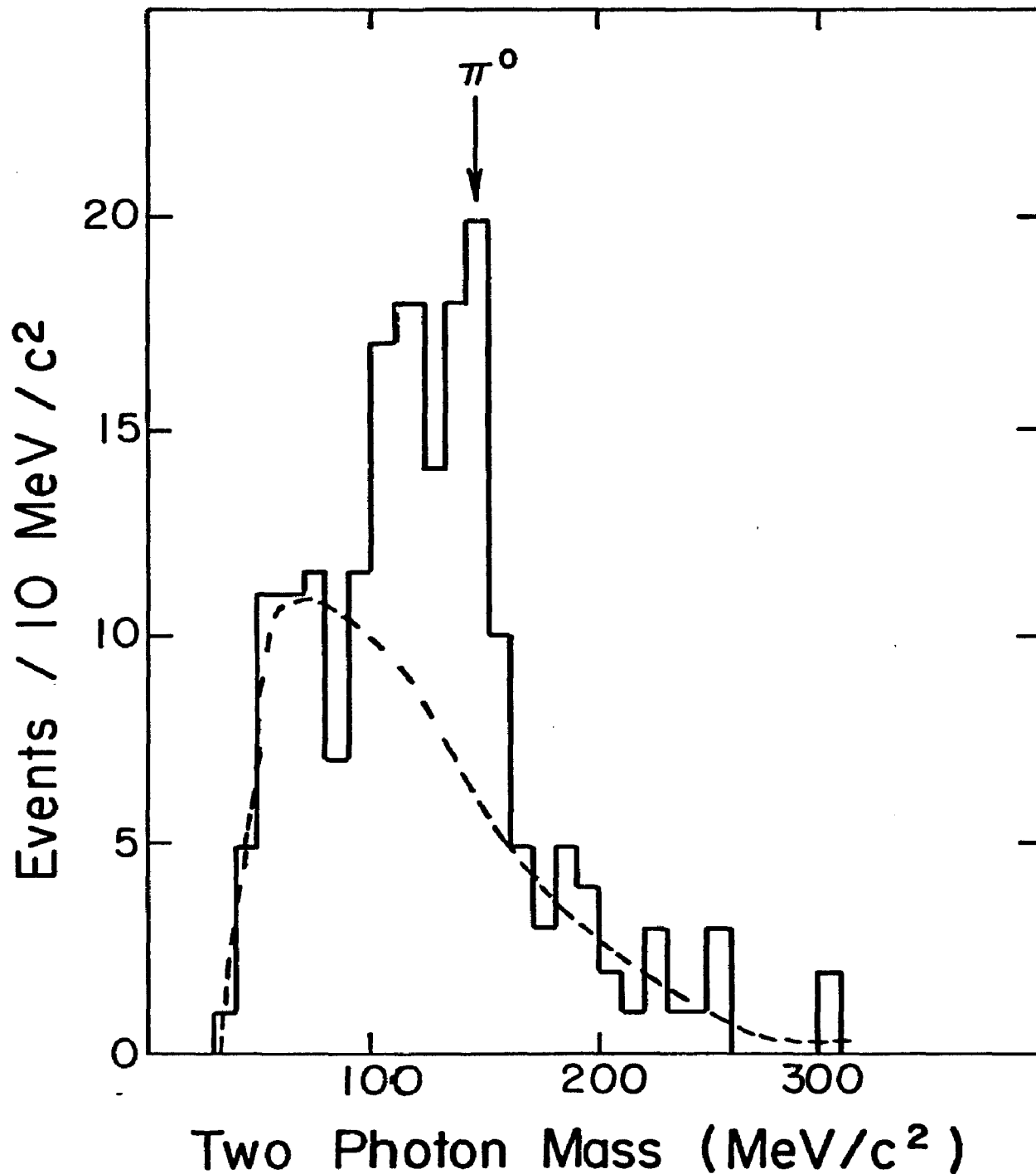


Fig. V-22 The reconstructed mass from two neutral showers in a single NaI stack from the ψ data. A clear π^0 peak is evident with the width expected from energy and angular resolution. The arrow indicates the true π^0 mass. The dashed line is the expected background from random photon pairings.

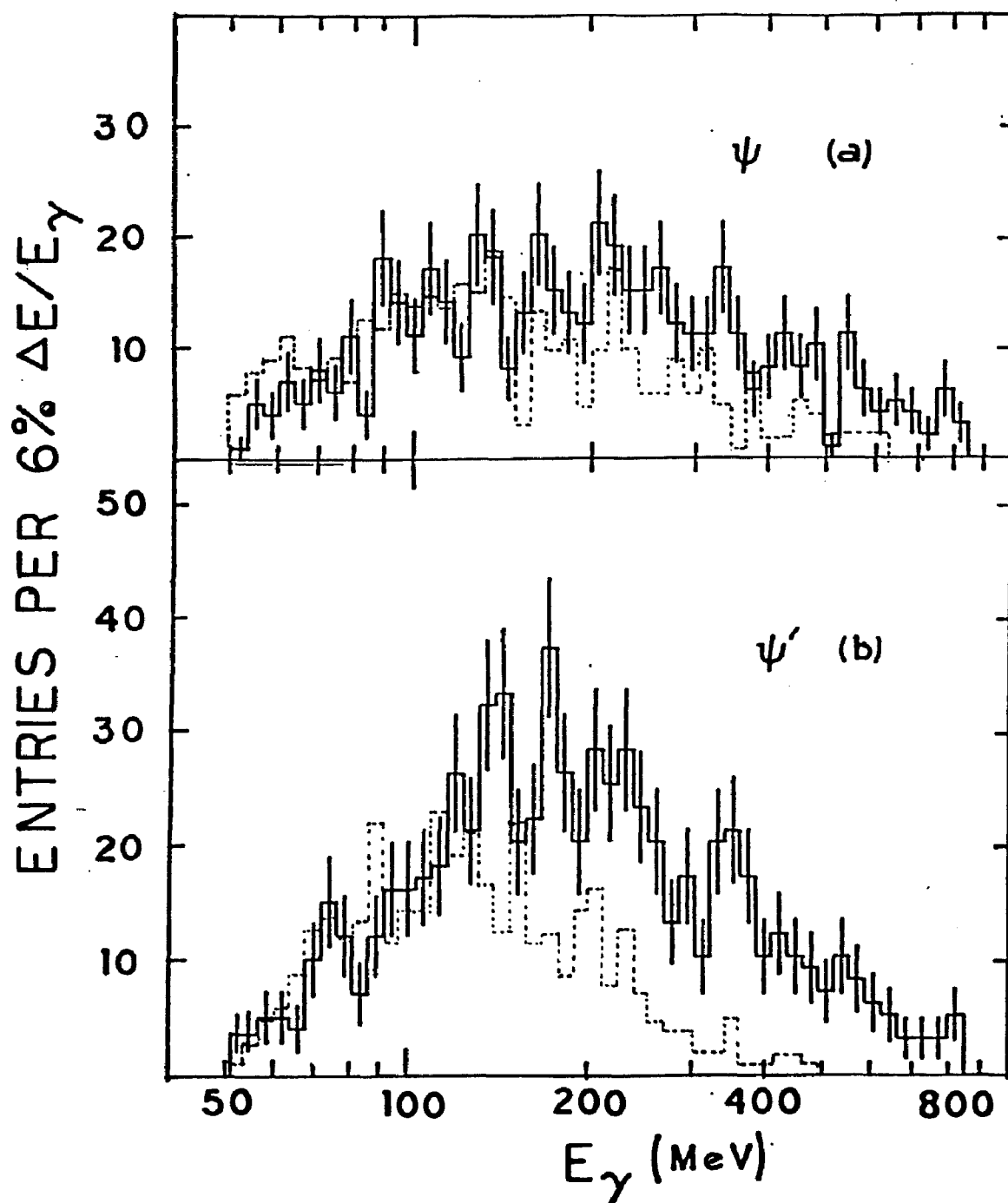


Fig. V-23 The photon spectra associated with spectrometer triggers for the ψ (a) and ψ' (b) decays. The dotted lines are the spectra from possible π_0 candidates, i.e. those events where there are two photons in the same NaI array.

The resulting spectra are shown in Fig. V-23. One sees that the ψ spectra are nearly smooth, within statistical errors, but there is considerable structure in the ψ' results, similar to the inclusive distribution. The interesting feature is that there now appears to be an enhancement at around 75 MeV, though the statistical significance is not greater than 3 standard deviations. The peaks around 120 MeV and 170 MeV are consistent with the results of the inclusive data. The peak at about 240 MeV is much broader than expected from the energy resolution of the NaI arrays, this may indicate the presence of decays to the $\chi(3455)$ which is unobserved in the inclusive spectrum, in addition to the decays to the $\chi(3415)$ which is clearly seen in the inclusive distribution. The structure between 300 and 400 MeV is consistent with the radiative decays of the χ states to the ψ , also observed inclusively. In lieu of a Monte Carlo simulation, the photon spectra from events which have two photons entering a single stack are shown in Fig V-23. This provides a fairly good fit to the ψ data and also to the lowest energy part of the ψ' data. Note, however, the presence of the 75 MeV peak in the semi-inclusive distribution is absent from the photon spectra for possible π^0 candidates. Even with different

cuts on the semi-inclusive data³¹, the 75 MeV peak still persists, indicating it may not arise from statistical fluctuations.

Due to the poor knowledge of the acceptance for the different energy gamma rays associated with spectrometer hadrons, branching ratios for the decay of the ψ^0 to χ states can only be guessed at from these data. If the contribution from the η decays is included with the potential π^0 photon contribution, one arrives at branching ratio on the order of $10\% \pm 5\%$ for all three transitions to the χ states seen in the inclusive distribution.

In Fig. V-24, the momentum distribution of the hadrons associated with photons in different energy regions is shown. There appear to be some significant changes in the shape of the spectra for hadrons accompanied by different energy photons. This, to some extent is governed by kinematics, and by the variations in the decay spectrum of the χ states. The latter effect could be expected to be small, since the hadrons' spectra from the ψ and ψ^0 decays are quite similar.

Fig. V-25 displays the observed charged multiplicity distributions associated with the different ranges of gamma ray energies from the ψ^0 decays. The average behavior

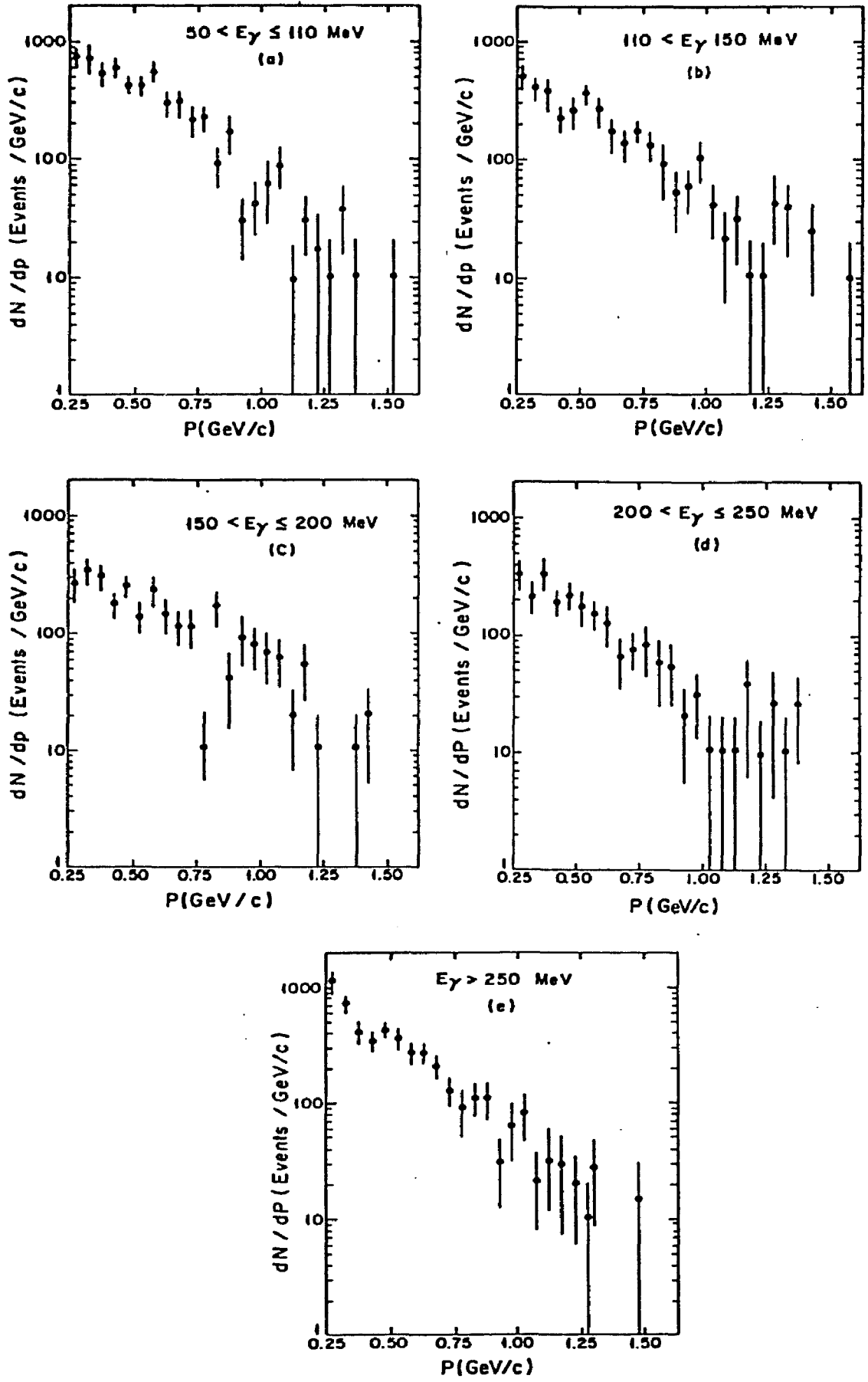


Fig. V-24 The momentum distributions associated with photons in the listed energy ranges from the ψ' decays. These data are for hadrons that have all the corrections applied to them. The errors contain both the statistical and appropriate systematic uncertainties.

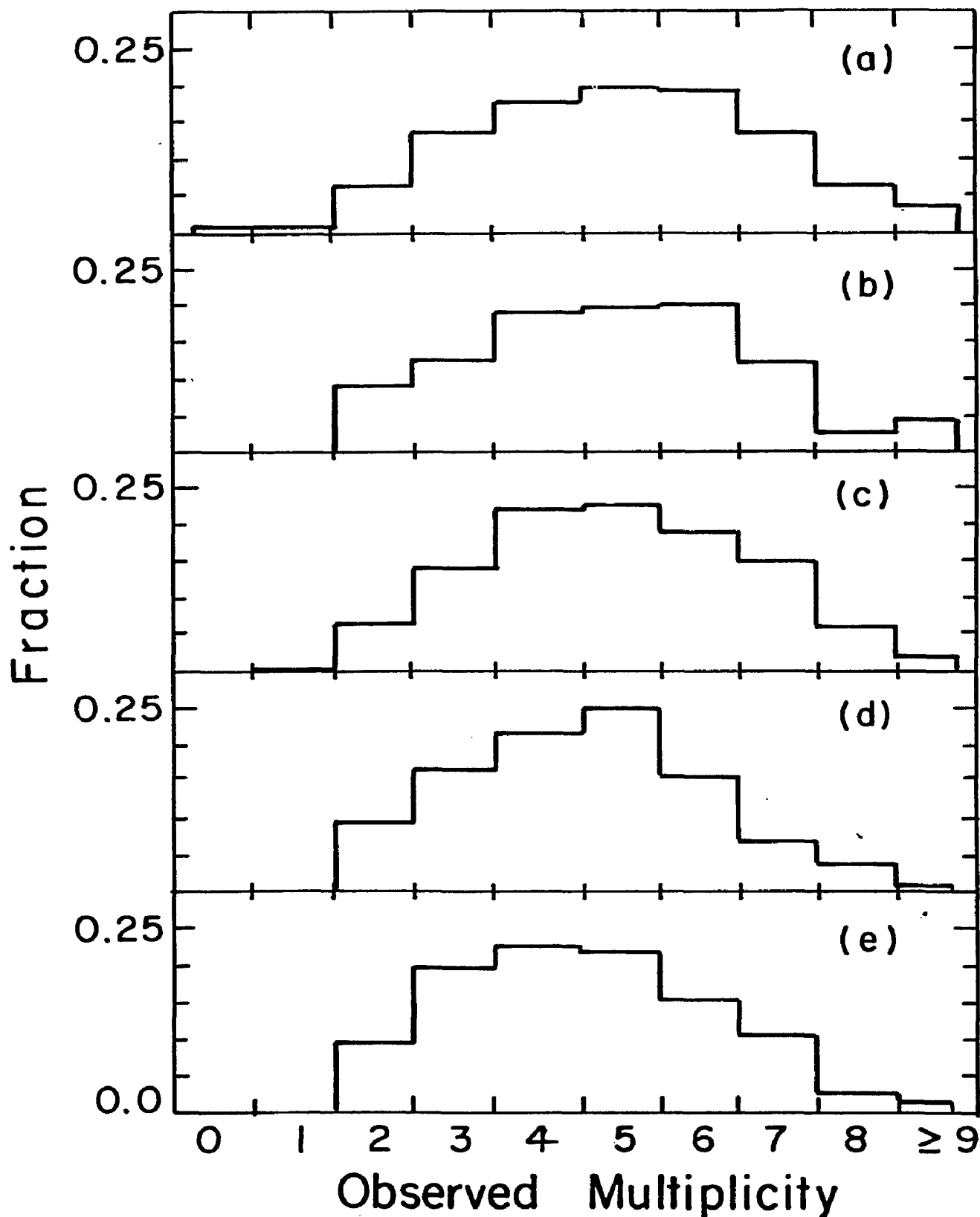


Fig. V-25 The observed charged multiplicities for the spectrometer-associated photon spectrum from the ψ' decays. The photon energy ranges are: (a) 50-110 MeV, (b) 110-150 MeV, (c) 150-200 MeV, (d) 200-250 MeV, and (e) above 250 MeV.

follows that of the multiplicity associated with the inclusive hadron spectra, namely that the average multiplicity tends to decrease with increasing energy of the inclusively measured particle.

4. Discussion

If the radiative transitions shown in Fig. 0-1 are assumed to come from electric or magnetic dipole transitions, then the emission probability for a photon from the decays of the quark-anti quark system can be calculated as in the positronium case³². The results for the E1 transitions from the 2^3S to the 1^3P states is given by:

$$\Gamma_J = \frac{4\alpha}{27} e_Q^2 (2J + 1) k^3 |\langle 1P | r | 2S \rangle|^2,$$

where e_Q is the quark's electric charge, k is the photon's energy. The matrix element can be chosen for the harmonic oscillator case. This gives

$$|\langle 1P | r | 2S \rangle|^2 = \xi^{-2},$$

where ξ is a scale parameter of the wave function, and is determined by the reduced mass and the parameters of the potential. For the harmonic oscillator case, $\xi = \sqrt{\mu \omega_0}$, with the reduced mass, μ , set to $M_Q/2 = 1.5/2$ GeV, and the

oscillator spacing, ω_0 set to the average of the 1S-1P and 1S-2S spacing; $\omega_0 = 0.33$ GeV, then $\xi = 0.52$ GeV. Using the observed level spacings of the ψ' to χ state transitions the expected decay rates for $e_Q = 2/3$ are:

$$\Gamma(\psi' \rightarrow 2^{++}) = 19 \text{ keV}, \quad \Gamma(\psi' \rightarrow 1^{++}) = 27 \text{ keV},$$

$$\Gamma(\psi' \rightarrow 0^{++}) = 31 \text{ keV}$$

while the observed widths for the inclusive data are:

$$\Gamma(\psi' \rightarrow \chi(3550)) = 16 \pm 6, \quad \Gamma(\psi' \rightarrow \chi(3515)) = 16 \pm 6,$$

$$\Gamma(\psi' \rightarrow \chi(3410)) = 16 \pm 7,$$

in keV for the assumed width of the ψ' as 228 ± 56 keV. It appears that the radiative decays of the ψ' to the χ states are in reasonable agreement with the results of the simple charmonium model.

For the transitions from the 3P states to the 3S state, the dipole matrix element is

$$|\langle 1S | r | 1D \rangle| = \frac{3}{2} \xi^{-2}.$$

From this, one can calculate the dipole transition rate. However, the selection rules for an oscillator, summarized

in sum rule expressions such as the Bethe-Salpeter dipole sum rule³³, set limits on the allowed dipole contribution. The transition rates are then³⁴

$$\Gamma(2^{++} \rightarrow \psi) = 320 \text{ keV}, \quad \Gamma(1^{++} \rightarrow \psi) = 200 \text{ keV}, \quad \Gamma(0^{++} \rightarrow \psi) = 90 \text{ keV}.$$

Taking the observed product of branching fractions from the ψ^* to the ψ via the χ states, we can obtain the total widths of the various χ states.

$$\Gamma(\chi(3550)) = 818 \pm 490 \text{ keV}, \quad \Gamma(\chi(3515)) = 420 \pm 204 \text{ keV},$$

$$\Gamma(\chi(3410)) = 697 \pm 403 \text{ keV}.$$

For the magnetic dipole transitions from the ψ^* and ψ to the corresponding 1S states, the expected rates are

$$\Gamma(^3S_1 \rightarrow ^1S_0) = \frac{4\alpha}{3m} e^2 k^3 (2J + 1).$$

Here, $m = 1.65 \text{ GeV}$ and J is the spin of the final state. For the upper limit listed on p. 215 for the $\psi \rightarrow ^1S_0$ radiative decay, the upper limit on this transition is 1.2 keV, which gives the maximum splitting allowed of 90 MeV. For the ψ^* case, the possible photon line at 75 MeV may be interpreted as the $^2^1S_0$ state. In this case, the decay rate is expected to be 0.7 keV, in reasonable agreement with the observed branching fraction into this possible state of

2.5 ± 2.0 keV.

Another alternative for the presence of a 75 MeV line is the transition between the 2^{++} P state at 3550 MeV and the so-far unobserved 1^{+-} state. However, the Doppler broadening of this line would be over 80 MeV, far larger than the observed width of 10 MeV. Note that the observed width is consistent with the expected energy resolution at this energy.

In conclusion, we see that the radiative decays of the simple charmonium model are in reasonable agreement with the data. The possible state at 3.62 GeV corresponding to the 75 MeV photon may be the 1S_0 partner of the ψ' .

J. Conclusions

From the inclusive hadron distribution, it appears that the gross features of the psion decays can be described by the statistical or thermodynamical models. In the latter case, the "temperature" of the psions is about 165 MeV, almost the same as that found in hadron-hadron collisions. The statistical nature of the decay is also apparent in the multiplicity distributions where the averaged charged multiplicity as a function of the spectrometer particle's momentum is fairly well described by the invariant-phase

space Monte Carlo simulation. Further, on comparing the hadronic spectra from the ψ decays with the non-resonant e^+e^- hadronic spectra, we see a surprisingly similar pattern. In the non-resonant case, the statistical decay contribution appears to dominate the low momentum end of the spectra, since the exponential behavior of the spectra is almost identical to that of the resonance decay spectra. The similarity between the slopes of the on and off resonance spectra appears to end at about 1 GeV/c, indicating that the quark-parton contribution may give a substantial contribution above this momentum.

The relative populations of the different hadronic species are also nearly the same on and off resonance. This again indicates that the same mechanism responsible for the decays of the massive resonances also plays a major role in the decays of the virtual photon from e^+e^- annihilation.

From the two-body decays of the resonances, there appears to be a substantial number of massive resonances in the resulting debris. In addition to the well-known meson resonances, a number of higher mass resonances that are relatively narrow may have been observed in the resonance decays. However, the presence of kinematically produced peaks in the recoiling mass spectra can not be totally ruled

out. Additionally, the SU(3) character of the ψ appears to be fairly well established as a singlet state with a small (10-20%) octet component indicating some SU(3) breaking.

The decays of the resonances into quark-antiquark pairs with possibly some other hadrons has been ruled out at the .05% branching fraction level.

The inclusive photon distribution from the ψ' decays shows monochromatic lines that are consistent with the expectations from the charmonium models with a linear potential between the charmed quarks. The spectra of photons from the ψ' decays where a particle is observed in the magnetic spectrometer are very similar to the inclusive spectra with the additional presence of a monochromatic photon line at about 75 MeV. This last line may correspond to the pseudoscalar partner of the ψ' . No structure is seen in the ψ gamma ray spectrum at the 1-to-2% level.

REFERENCES

CHAPTER V

1. E. Fermi, Prog. Theor. Phys. 5, 570(1950).
2. R. Hagedorn, Suppl. Nuovo Cimento 3, 147(1965).
3. G.J. Feldman and M.L. Perl, Phys. Repts. 19C, 233(1975).
4. S.D. Drell, D.J. Levy, and T.M. Yan, Phys. Rev. D1, 1617 (1970).
5. Y. Frishman, in Proceedings of the XVI International Conference on High Energy Physics, J.D. Jackson and H. Roberts, editors (National Accelerator Laboratory, Batavia, Ill., 1972), p. 119; H. Fritzsche and M. Gell-Mann in Scale Invariance and the Light Cone, Gordon and Breach, N.Y., 1971, Vol. 2, p. 1.
6. R.P. Feynman, Phys. Rev. Lett. 23, 1415(1969);
R.P. Feynman, Photon-Hadron Interactions, W.A. Benjamin, Reading, Mass., 1972.
7. J.D. Bjorken, Phys. Rev. 179, 1547(1969).
8. F. Elvekjaer and F. Steiner, Phys. Lett. 60B, 456(1976).
9. see e.g. V. Luth in Proceedings of the Summer Institute on Particle Physics, Stanford, Calif.(1977).
- 10.. B. Alper, et al., Nucl. Phys. B87, 19(1975).
11. R. Blankenbecler and S.J. Brodsky, Phys. Rev. D10, 2973(1974).
12. W. Braunschweig, et al., Phys. Lett. 63B, 115(1976).
13. T.L. Atwood, Ph.D. Thesis, Univ. of Maryland, 1977.(unpublished).
14. The values for $\langle E_{ch} \rangle$ and σ_{tot} are taken from Ref. 3.
For the ψ , $\langle E_{ch} \rangle \cdot \sigma_{tot} = 920 \text{ nb-GeV}$, for $\sqrt{s} = 4.8 \text{ GeV}$,
 $\langle E_{ch} \rangle \cdot \sigma_{tot} = 8.74 \text{ nb-GeV}$.

15. J. Cronin, et al., Phys. Rev. Lett. 31, 1426(1973).
16. D.H. Badtke, et al., to be published.
17. J. Engels, H. Satz, and K. Schilling, Phys. Lett. 49B, 171(1974).
18. see e.g. Ref. 3 and Ref. 9
19. J. Whitmore, Phys. Reports 10C, 273(1974).
20. This Monte Carlo was taken from the MADSIM code of the SLAC-LBL group. See Ref. 3 and R. Hollebeek, Ph.D. thesis, University of California at Berkely, LBL-3874, Appendix II, (unpublished) 1975.
21. R. Baldini-Celio, et al., Phys. Lett. 58B, 471 (1975).
22. K. Lane and S. Rudaz, Phys. Lett. 66B, 139(1977).
23. see e.g. D.D. Carmony, et al., Phys. Rev. D 16, 1251(1977).
24. see Appendix A and Particle Data Group, Phys. Lett. 68B, 1(1977).
25. for a recent review of quark searches, see L.W. Jones, Rev. Mod. Phys. 49, 717(1977).
26. This assumes the quarks are produced as point-like objects.
27. T. Appelquist, et al., Phys. Rev. Lett. 34, 365(1975), and E. Eichten, et al., Phys. Rev. Lett. 34, 369(1975).
28. see G. Feldman in Proceedings of the Summer Institute on Particle Physics, Stanford, Calif., (1976), p.81.
29. C. Biddick, et al., Phys. Rev. Lett. 38, 1324(1977).
30. see Ref. 20. We thank G. Feldman for providing the code.
31. K. Shinsky, SP19 Internal Memorandum, (1977).
32. see J.D. Jackson in Proceedings of the Summer Institute on Particle Physics, Stanford, Calif., (1976), p. 147.
33. H.A. Bethe, and E. Salpeter, "Quantum Mechanics of One- and Two-Electron Atoms", Springer-Verlag, N.Y., (1957).
34. E. Eichten, et al., Phys. Rev. Lett. 36, 500(1976).

PROPERTIES OF CHARMONIUM

In Tables A-1 to A-3, the known properties of the resonances studied in this work are shown. These states are thought to comprise some of the lowest-lying charmonium states (see e.g. Fig. 0-2). The decay rates that have been observed so far are taken from the "Reviews of Particle Properties"¹, the SLAC Summer School of 1976², and the Proceedings of the Hamburg Photon-Lepton Conference of 1977³.

In the notation, a K^* (892) is represented by K^* . A K^* (1420) is represented by K^{**} . Those decay modes enclosed in parentheses are derived from the unenclosed decay mode immediately preceding it. All upper limits are indicated for 90% confidence levels.

$$J^{PC} = 1^{--} \quad \text{Mass} = 3097.2 \pm 3.2 \text{ MeV}/c^2 \quad \text{Width} = 66.9 \pm 12.4 \text{ keV}$$

Second Order Electromagnetic Decays (in per cent)

Total	17 ± 3	$\pi^+\pi^-$	0.011 ± 0.007
$2\pi^+ 2\pi^-$	0.4 ± 0.1	$3\pi^+ 3\pi^-$	0.4 ± 0.2
$e^+ e^-$	6.9 ± 0.9	$\mu^+ \mu^-$	6.9 ± 0.9

Direct Decays (in per cent)

$\pi^+\pi^-\pi^0$	1.6 ± 0.6	$K^+K^-\omega$	0.03 ± 0.02
($\rho\pi$)	1.25 ± 0.2	$\phi\eta$	0.07 ± 0.04
$2\pi^+ 2\pi^-\pi^0$	4.0 ± 0.1	$f \omega$	0.30 ± 0.10
($\omega\pi\pi$)	1.0 ± 0.3	$\pi^\pm B$	0.28 ± 0.07
($\rho\pi\pi\pi$)	1.8 ± 0.45	$2K^+ 2K^-$	0.07 ± 0.03
(ρA_2)	0.9 ± 0.6	($\phi K^+ K^-$)	0.09 ± 0.04
$3\pi^+ 3\pi^-\pi^0$	2.9 ± 0.7	($\phi f'$)	0.08 ± 0.05
($\omega 2\pi^+ 2\pi^-$)	0.85 ± 0.34	$K^+ K^- 2\pi^+ 2\pi^-$	0.3 ± 0.1
$4\pi^+ 4\pi^-\pi^0$	0.9 ± 0.3	$\phi\eta'$	0.05 ± 0.04
K^+K^-	0.020 ± 0.016	$p\bar{p}$	0.22 ± 0.02
$K_S^0 K_L^0$	< 0.008	$p\bar{n}\pi^-$	0.38 ± 0.08
$K_S^0 K_L^{0*}$	0.34 ± 0.06	$p\bar{p}\pi^0$	0.10 ± 0.02
$K^0 \bar{K}^{0*}$	0.27 ± 0.06	($\Lambda\bar{\Lambda}$)	0.16 ± 0.08
$K^+ K^{*-}$	< 0.15	$p\bar{p} \pi^+ \pi^-$	0.41 ± 0.08
$K^0 \bar{K}^{0**}$	< 0.20	($\Lambda\bar{\Sigma}$)	< 0.04
$K^+ K^- \pi^+ \pi^-$	0.72 ± 0.23	$p\bar{p}\pi^+ \pi^- \pi^0$	0.11 ± 0.04
($K^0 \bar{K}^{0*}$)	< 0.5	($p\bar{p}\eta$)	0.19 ± 0.04
($K^0 \bar{K}^{0**}$)	0.67 ± 0.26	($p\bar{p}\omega$)	0.05 ± 0.01
($K^0 \bar{K}^{0**}$)	< 0.29	$\Xi^- \bar{\Xi}^-$	< 0.04
($\phi\pi\pi$)	0.21 ± 0.09		

Radiative Decays

$\gamma X(2830)$	< 1.7	$\gamma\gamma$	< 0.005
$\gamma X(2830) \rightarrow \gamma\gamma$	0.012 ± 0.005	$\gamma\pi^0$	0.0075 ± 0.0048
$\gamma\gamma$	< 0.0078	$\gamma\eta$	0.082 ± 0.019
γf^0	0.20 ± 0.07	$\gamma\eta'$	0.23 ± 0.18

Note: A decay mode listed in parentheses indicates that it was determined principally from the general mode listed before it, e.g. $\pi\rho$ from $\pi^+\pi^-\pi^0$

$$J^{PC} = 1^{--} \quad \text{Mass} = 3684 \pm 4 \text{ MeV}/c^2 \quad \text{Width} = 228 \pm 56 \text{ keV}$$

Second Order Electromagnetic Decays (in per cent)

Total	2.9 ± 0.4	$\pi^+\pi^-$	< 0.005
$2\pi^+ 2\pi^-$	0.08 ± 0.02	e^+e^-	0.93 ± 0.16
$\mu^+\mu^-$	0.77 ± 0.17		

Direct Decays (in per cent)

$\pi^+\pi^-\psi$	33.2 ± 3.3	$\pi\rho$	< 0.1
$\pi^0\pi^0\psi$	17.2 ± 2.8	K^+K^-	< 0.005
$\eta\psi$	4.2 ± 0.8	$K^+K^-\pi^+\pi^-$	0.14 ± 0.04
$2\pi^+ 2\pi^-\pi^0$	0.35 ± 0.15	$p\bar{p}$	0.023 ± 0.007
		$\Lambda\bar{\Lambda}$	< 0.04
		$\Xi^-\bar{\Xi}^-$	~ 0.02

Radiative Decays

$\gamma\psi$	< 0.15	$\gamma X(2830)$	< 1.1
$\gamma\gamma$	< 0.5	$\gamma X(2830) \rightarrow \gamma\gamma\gamma$	< 0.037
$\gamma\pi^0$	< 0.7	$\gamma X(3410)$	7.2 ± 2.3
$\gamma\eta$	< 0.04	$\gamma X(3450)$	< 1.5
$\gamma\eta'$	< 0.11	$\gamma X(3510)$	7.1 ± 1.9
		$\gamma X(3550)$	$7. \pm 2.$

Table A-2

Properties of the $\chi(3410)$

$$J^{PC} = 0^{++} \quad \text{Mass} = 3414 \pm 4 \text{ MeV}/c^2$$

Decay Modes (in per cent) *

$\gamma \psi$	46 ± 24	$\gamma\gamma$	< 0.57
$\pi^+ \pi^-$	1.0 ± 0.5	$K^+ K^-$	1.0 ± 0.5
$2\pi^+ 2\pi^-$	4.3 ± 1.7	$\pi^+ \pi^- K^+ K^-$	3.6 ± 1.5
$(\rho^0 \pi^+ \pi^-)$	1.7 ± 0.5	$(K^{0*} K^+ \pi^-)$	1.5 ± 0.4
$3\pi^+ 3\pi^-$	2.0 ± 1.0	$\pi^+ \pi^- p \bar{p}$	0.5 ± 0.2

Properties of the $\chi(3510)$

$$J^{PC} = 1^{++} \quad \text{Mass} = 3510 \pm 4 \text{ MeV}/c^2$$

Decay Modes (in per cent) #

$\gamma \psi$	70 ± 21	$\gamma\gamma$	< 0.3
$\pi^+ \pi^-$ and $K^+ K^-$	< 0.22	$K^+ K^- \pi^+ \pi^-$	0.9 ± 0.4
$2\pi^+ 2\pi^-$	1.5 ± 0.6	$(K^{0*} K^- \pi^+)$	0.32 ± 0.16
$(\rho^0 \pi^+ \pi^-)$	0.36 ± 0.30	$3\pi^+ 3\pi^-$	~ 1.8
		$\pi^+ \pi^- p \bar{p}$	~ 0.1

Properties of the $\chi(3550)$

$$J^{PC} = 2^{++} \quad \text{Mass} = 3554 \pm 5 \text{ MeV}/c^2$$

Decay Modes (in per cent) §

$\gamma \psi$	31 ± 14	$\gamma\gamma$	< 0.25
$\pi^+ \pi^-$ and $K^+ K^-$	0.33 ± 0.17	$\pi^+ \pi^- K^+ K^-$	2.1 ± 0.6
$2\pi^+ 2\pi^-$	2.3 ± 0.6	$(K^{0*} \pi^+ \pi^-)$	0.75 ± 0.41
$(\rho^0 \pi^+ \pi^-)$	0.71 ± 0.41	$3\pi^+ 3\pi^-$	~ 1.8
		$\pi^+ \pi^- p \bar{p}$	~ 0.23

*) Assuming the branching fraction for $\psi' \rightarrow \gamma \chi(3410)$ is 0.072

) Assuming the branching fraction for $\psi' \rightarrow \gamma \chi(3510)$ is 0.071

§) Assuming the branching fraction for $\psi' \rightarrow \gamma \chi(3550)$ is 0.070

REFERENCES

APPENDIX A

1. Particle Data Group, "New Particle Searches and Discoveries", Phys. Lett. 68B, 1(1977).
2. G. Feldman in Proceedings of the Summer Institute on Particle Physics, Stanford, Calif. (1976), SLAC-198, p. 81.
3. see Proceedings of the 1977 International Symposium on Lepton and Photon Interactions at High Energy, Hamburg, Germany, (to be published).

DIMENSIONS OF THE APPARATUS

In the following table, the dimensions of all the counters and chambers used in this experiment are listed. The coordinate system is defined such that the positive Z axis is through the center of the spectrometer, the positive Y axis points upwards, and the positive X axis points in the direction of the electron bunch's travel. All dimensions refer to the active area of the device.

The solid angle subtended by the active area of the devices is also shown. This is the purely geometrical solid angle and does not account for the effect of the magnetic field on the trajectories of the charged particles in the spectrometer.

The thickness of each detector in terms of radiation lengths and nuclear collision lengths is also calculated and displayed in the table. These values were derived from the equivalent amounts of elements, such as hydrogen, carbon, aluminum, and iron, which comprise the various materials in the detectors.

Table B-1

Device	X (cm)	Y (cm)	Z (cm)	$\Delta\Omega/4\pi$ (ster)	Radiation Lengths	Nucl. Col Lengths
Beam pipe	150	7.6	--	0.999	0.094	0.016
Polymer	± 27.5	± 11.5	0	0.905	0.089	0.031
AIX	± 12.5	± 5.5	16.7	0.060	0.00051	0.00031
AMX	± 12.4	± 5.5	19.1	0.048	"	"
AOY	± 12.5	± 5.3	21.5	0.038	"	"
AIY	± 12.3	± 5.5	23.8	0.033	"	"
UIX	± 21.1	18.3	± 17.4	0.174	"	"
UMX	± 21.1	20.6	± 17.4	0.153	"	"
UOX	± 21.1	23.0	± 17.4	0.134	"	"
BIX	± 12.4	± 5.5	-17.0	0.058	"	"
BMX	± 12.5	± 5.8	-19.4	0.050	"	"
BOX	± 12.3	± 5.0	-21.8	0.038	"	"
B-NaI Cryst.	19.8	25.4	-38.2(m)	0.095	9.8	1.01
B2X	± 44.8	± 24.25	-68.9	0.058	0.00051	0.00031
B2Y	± 39.1	± 14.0	-73.5	0.028	"	"
B-Shower Counter	± 91.4	± 45.7	-89.4 (f) -103.6(b)	0.106 0.086	7.0	0.41
B-Hadron Filter	± 137.2	± 83.3	-138.2(f) -218.4(b)	0.119 0.061	40.0	6.8
LIX	± 21.2	-18.5	± 17.4	0.172	0.00051	0.00031
LMX	± 21.1	-20.9	± 17.4	0.150	"	"
LOX	± 21.1	-23.3	± 17.4	0.132	"	"
S1 Cnt.	19.1	6.4	29.2	0.038	0.044	0.036
A2Y	± 16.8	± 8.25	39.3	0.026	0.00051	0.00031
A2X	± 16.75	± 8.4	41.5	0.024	"	"
A3X	± 64.4	± 28.6	201.9	0.0136	"	"
A3Y	± 70.7	± 28.0	222.5	0.0120	"	"
A4X	± 86.8	± 37.25	333.6	0.0089	"	"
A4Y	± 87.5	± 36.4	352.6	0.0079	"	"
A5X	± 114.8	± 57.2	480.9	0.00873	"	"
S2 Cnt.	± 139.7	± 71.1	495.3	0.0123	0.044	0.036
A6X	± 148.2	± 57.2	513.3	0.00978	0.06	0.02
A-Shower Counter	± 171.5	± 68.6	522.5(f) 536.7(b)	0.0129 0.0123	7.0	0.41
A-Hadron Filter	± 171.5	± 83.8	572.0(f) 653.3(b)	0.0133 0.0103	40.0	6.8
Upper NaI	33.1	50.8	30.4(m)	0.102	19.6	2.03
Lower NaI	33.1	-50.8	30.4(m)	0.102	19.6	2.03
Cherenkov Counter	45.7(f) 76.2(b)	20.3 30.5	43.2 193.2	0.105 0.018	0.51	0.37

Notation: All proportional chambers are designated by the three letter code, XYZ, where X indicates the chamber's location, i.e. A means spectrometer side, B means the conjugate side, U means upper chambers, L means lower chambers; Y designates the relative position of the chamber with respect to the beam pipe, i.e., I means inner, M means middle, O means outer, and numbers indicate increasing distances; Z designates the type of chamber, i.e. whether the sense wires are along the X or Y direction. A \pm sign before a coordinate indicates the plane of the active elements, while the absence of this sign indicates a distance from the interaction region. For the Cherenkov, shower and hadron filter counters, the front(f) and back(b) dimensions are listed, For the sodium iodide arrays, the dimensions at the middle(m) of the arrays are shown.

NUCLEAR ABSORPTION CORRECTIONS

The correction to the number of observed hadrons from nuclear interactions in the material comprising the detectors was computed from the measured nuclear absorption cross sections¹ for aluminum, iron, carbon and hydrogen. The materials comprising the various pieces of the apparatus were reduced to the equivalents of these elements².

Using these values, the attenuation due to absorption effects is given by:

$$N(x) = N_0 \exp\left[-\sum_{j=1}^n f_i \sigma_i d_i x\right]$$

where $N(x)$ is the number of incident particles surviving when N_0 particles strike a slab of thickness x , composed of n different elements, each of which has a density d_i , representing a fraction f_i of the slab, and having a cross section σ_i for an absorption reaction. The secondaries emitted in the absorption process are neglected since their momentum is sufficiently small so that they cannot trigger the apparatus if they interact in the material before the magnet chambers. This effect has been verified by the Monte Carlo program described in Section IV-B. Since over 99% of the total material traversed by a particle in the spectrometer's triggering part lies in front of the first

magnet chamber, a nuclear interaction will prevent that particle from triggering the spectrometer.

The resulting multiplicative correction factor that must be applied to the hadrons is then $N_0/N(x)$. Since these correction factors are highly dependent on the particle's momentum, they were evaluated at 50 MeV/c intervals and interpolated by a cubic spline fit. These correction factors are shown in Figs. C-1, 2, and 3 for the three species of stable hadrons.

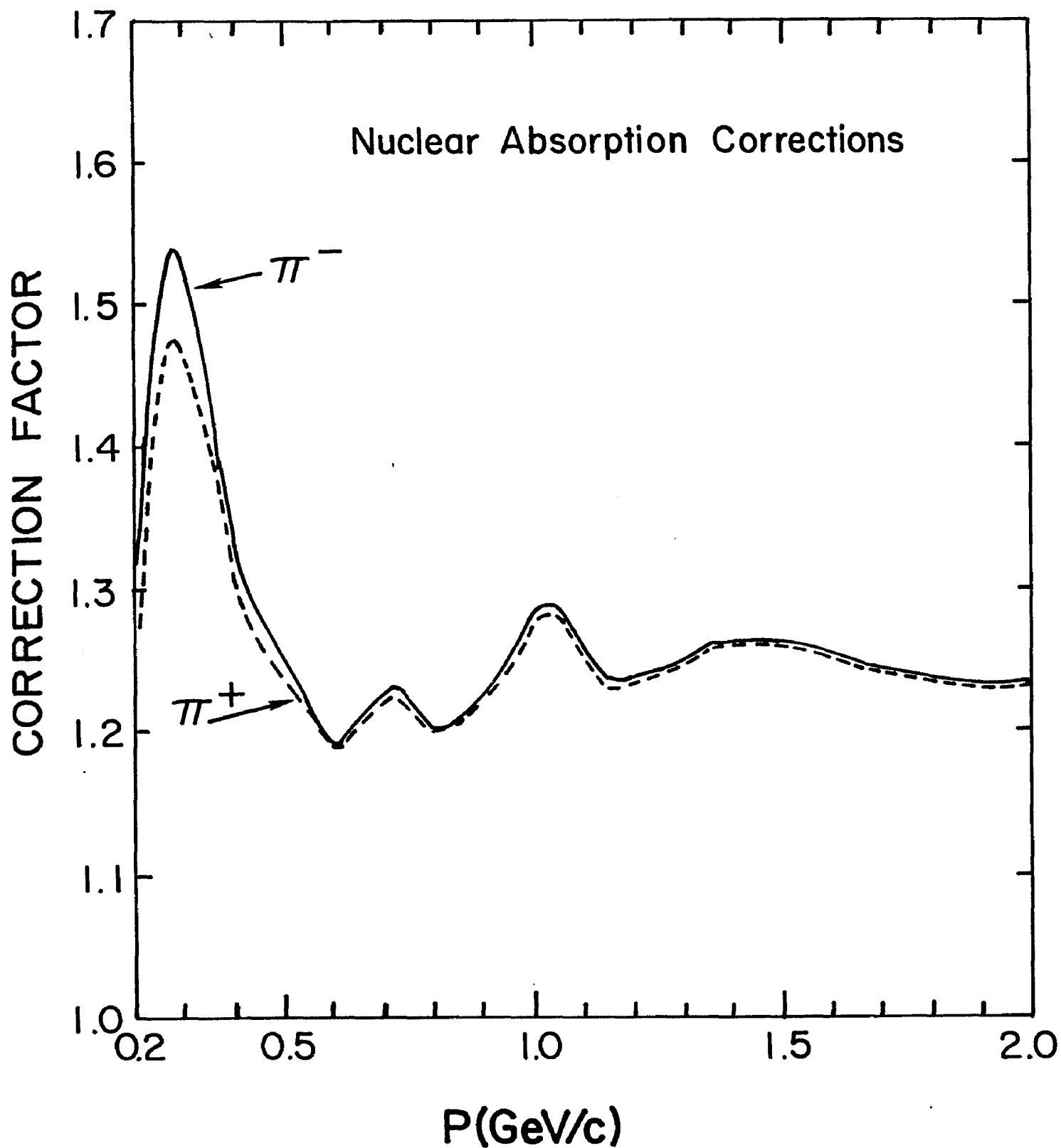


Fig. C-1 The calculated nuclear absorption correction for the pions entering the spectrometer. The number of observed pions is multiplied by this correction factor to get the number of incident pions.

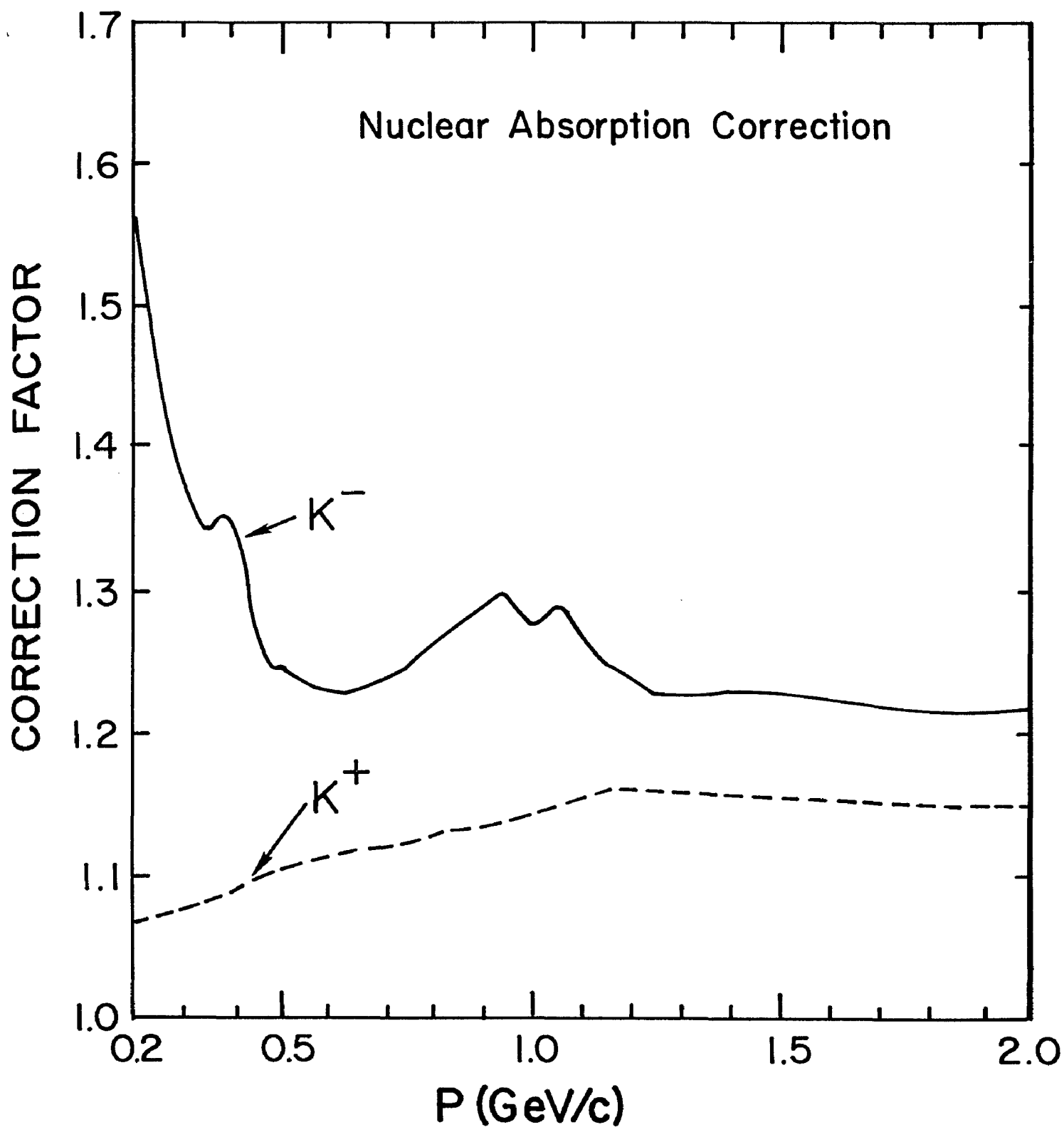


Fig. C-2 The calculated nuclear absorption correction for the kaons entering the spectrometer.

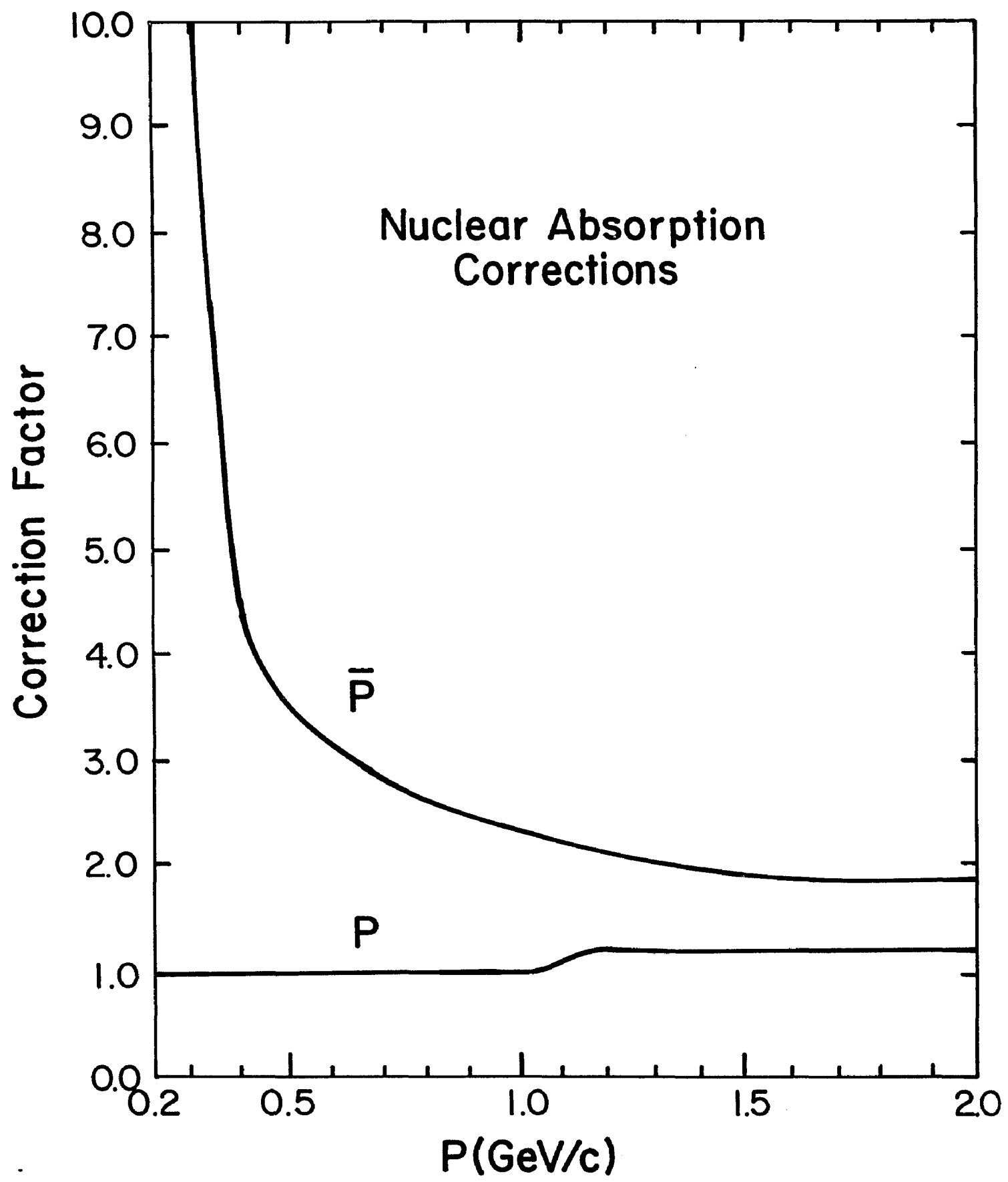


Fig. C-3 The calculated nuclear absorption correction for the protons and antiprotons entering the spectrometer.

REFERENCES

APPENDIX C

1. High Energy Reactions Analysis Group, CERN, #72-1(1972);
High Energy Reactions Analysis Group, CERN, #75-1(1975);
J.W. Cronin, R. Cool, and A. Abashian, Phys. Rev. 107, 1121
(1957); R.L. Martin, Phys. Rev. 87, 1052(1954);
M.J. Longo, B.J. Moyer, Phys. Rev. 125, 701(1962).
2. D.H. Badtke, Ph.D. Thesis, University of Maryland,
Appendix F, 1978 (unpublished).